frontiers | Research Topics

Risk assessment and resilience of extreme weather-induced disasters

Edited by
Lingling Shen, Wentao Yang, Yanfang Sang, Qi Zhang, Kaushal Gnyawali and Xiya Zhang

Published in
Frontiers in Earth Science

ISSN 1664-8714
ISBN 978-2-8325-6426-4
DOI 10.3389/978-2-8325-6426-4

About Frontiers

Frontiers is more than just an open access publisher of scholarly articles: it is a pioneering approach to the world of academia, radically improving the way scholarly research is managed. The grand vision of Frontiers is a world where all people have an equal opportunity to seek, share and generate knowledge. Frontiers provides immediate and permanent online open access to all its publications, but this alone is not enough to realize our grand goals.

Frontiers journal series

The Frontiers journal series is a multi-tier and interdisciplinary set of open-access, online journals, promising a paradigm shift from the current review, selection and dissemination processes in academic publishing. All Frontiers journals are driven by researchers for researchers; therefore, they constitute a service to the scholarly community. At the same time, the *Frontiers journal series* operates on a revolutionary invention, the tiered publishing system, initially addressing specific communities of scholars, and gradually climbing up to broader public understanding, thus serving the interests of the lay society, too.

Dedication to quality

Each Frontiers article is a landmark of the highest quality, thanks to genuinely collaborative interactions between authors and review editors, who include some of the world's best academicians. Research must be certified by peers before entering a stream of knowledge that may eventually reach the public - and shape society; therefore, Frontiers only applies the most rigorous and unbiased reviews. Frontiers revolutionizes research publishing by freely delivering the most outstanding research, evaluated with no bias from both the academic and social point of view. By applying the most advanced information technologies, Frontiers is catapulting scholarly publishing into a new generation.

What are Frontiers Research Topics?

Frontiers Research Topics are very popular trademarks of the *Frontiers journals series*: they are collections of at least ten articles, all centered on a particular subject. With their unique mix of varied contributions from Original Research to Review Articles, Frontiers Research Topics unify the most influential researchers, the latest key findings and historical advances in a hot research area.

Find out more on how to host your own Frontiers Research Topic or contribute to one as an author by contacting the Frontiers editorial office: frontiersin.org/about/contact

Risk assessment and resilience of extreme weather-induced disasters

Topic editors

Lingling Shen — Beijing Meteorological Information Center, China
Wentao Yang — University of Leeds, United Kingdom
Yanfang Sang — Key Laboratory of Water Cycle and Related Land Surface Processes, Institute of Geographic Sciences and Natural Resources (CAS), China
Qi Zhang — Nanjing University of Information Science and Technology, China
Kaushal Gnyawali — University of British Columbia, Okanagan Campus, Canada
Xiya Zhang — Institute of Urban Meteorology, China Meteorological Administration, China

Citation

Shen, L., Yang, W., Sang, Y., Zhang, Q., Gnyawali, K., Zhang, X., eds. (2025). *Risk assessment and resilience of extreme weather-induced disasters*. Lausanne: Frontiers Media SA. doi: 10.3389/978-2-8325-6426-4

Table of contents

frontiers | Frontiers in Earth Science

TYPE Editorial
PUBLISHED 21 May 2025
DOI 10.3389/feart.2025.1623074

OPEN ACCESS

EDITED AND REVIEWED BY
Gordon Woo,
Risk Management Solutions, United Kingdom

*CORRESPONDENCE
Yan-Fang Sang,
sangyf@igsnrr.ac.cn

RECEIVED 05 May 2025
ACCEPTED 14 May 2025
PUBLISHED 21 May 2025

CITATION
Sang Y-F, Shen L, Zhang X and Yang W (2025) Editorial: Risk assessment and resilience of extreme weather-induced disasters.
Front. Earth Sci. 13:1623074.
doi: 10.3389/feart.2025.1623074

Editorial: Risk assessment and resilience of extreme weather-induced disasters

Yan-Fang Sang[1,2,3]*, Lingling Shen[4], Xiya Zhang[5] and Wentao Yang[6]

[1]Key Laboratory of Water Cycle and Related Land Surface Processes, Institute of Geographic Sciences and Natural Resources Research, Chinese Academy of Sciences, Beijing, China, [2]Key Laboratory of Compound and Chained Natural Hazards, Ministry of Emergency Management of China, Beijing, China, [3]Yarlung Zangbo Grand Canyon Water Cycle Monitoring and Research Station, Linzhi, China, [4]Beijing Meteorological Information Center, Beijing, China, [5]Institute of Urban Meteorology, China Meteorological Administration, Beijing, China, [6]School of Geography, Faculty of Environment, University of Leeds, Leeds, United Kingdom

KEYWORDS

extreme weather, risk assessment, resilience management, natural disasters, sustainable development

Editorial on the Research Topic
Risk assessment and resilience of extreme weather-induced disasters

Introduction

Extreme weather events include unexpected, unusual, severe, or unseasonable rainstorms, droughts, and extreme temperatures, among others. They are important triggering factors that cause various natural hazards, including mountain flash floods (Figure 1), landslides, debris flows, urban flooding waterlogging, and agro-meteorological hazards, etc (Field et al., 2012; Sang et al., 2018; Sajadi, et al., 2022; Ren et al., 2024; Shi, et al., 2024). Such extreme weather-induced hazards pose a significant global threat to sustainable socioeconomic development. For instance, flooding generated by heavy rainstorms has become a serious "urban disease" in many cities worldwide, posing a serious threat to the safety of people's lives and property and the normal operation of cities (Yang et al., 2020). Because of climate change, the frequency and intensity of extreme weather events and related disasters will worsen (Stott, 2016). Thereby, it is vital to focus on risk assessment and resilience management of extreme weather-induced disasters (Easterling et al., 2000), to inform policymaking and mitigate natural disasters. This is the motivation for proposing this Research Topic.

In this Research Topic, scholars contributed their latest findings on useful methods and techniques for forecasting, providing early warning and assessing the risks of extreme weather-induced disasters. Moreover, they provided in-depth scientific insights and improved our understanding of the resilience and mitigation of extreme weather-induced disasters. Their solid scientific contributions will significantly promote research on extreme weather-induced disasters.

FIGURE 1
Mountain flash flood disaster in a small basin in Southwest China on 18–19 August 2020, following extreme rainstorms.

Overview of the articles

As guest editors, we would like to thank the authors who submitted very interesting articles for this Research Topic. Thanks to the valuable collaboration between the reviewers and authors, eight articles are featured in this Research Topic, which are briefly summarized below.

In the first study, "*Objective identification and forecast method of PM2.5 pollution based on medium- and long-term ensemble forecasts in Beijing-Tianjin-Hebei region and its surrounding areas*", Liu et al. developed an objective identification and forecast method for $PM_{2.5}$ pollution (OIF-$PM_{2.5}$) in the Beijing-Tianjin-Hebei region and its surrounding areas. The authors reported that the observed $PM_{2.5}$ pollution ratio increased with the aggravating $PM_{2.5}$ pollution. Statistical results indicated that the OIF-$PM_{2.5}$ method is highly reliable for forecasts with a leading forecasting time of 1–15 days.

In the second article by Assi et al.,"*Homeowner flood risk and risk reduction from home elevation between the limits of the 100- and 500-year floodplains*", the authors proposed a systematic approach to predicting flood risk for single-family homes using the average annual loss in the shaded X Zone–the area immediately outside the Special Flood Hazard Area (i.e., the 500-year floodplain) in the United States. The results enhanced the understanding of flood risk and the benefits of elevating homes above the first floor in the shaded X Zone.

The third article "*Gaps in the governance of floods, droughts, and heatwaves in the United Kingdom*" was contributed by Carvalho and Spataru. The authors presented the current state of the art of flood, drought, and heatwave governance in the United Kingdom, with a focus on pre-emergency phases and the lack of indicators for the assessment of the effectiveness of adaptation to all three disasters. Gaps and challenges are discussed, along with providing actions for adapting to and building resilience against these three types of disasters.

In the fourth contribution "*Analysis of urban necessities reserve index and reserve quantity under emergency conditions*", Jiang et al. assessed urban safety, and classified the emergency materials of urban necessities in Shanghai, by establishing a corresponding reserve list. To better handle emergencies, the authors provided countermeasures and suggestions for optimizing the material structure of emergency reserves, managing material reserves at different levels, reasonably planning the amount of emergency materials, reducing the cost of reserves and improving the efficiency of emergency reserves.

The fifth study "*Sedimentary records of giant landslide-dam breach events in western Sichuan, China*" was contributed by Ma et al. The authors conducted a detailed investigation of large-scale landslide-dammed lake outburst deposits in two typical River Basins on the Western Sichuan Plateau in China. They found that the sedimentary characteristics of outburst deposits (ODs) explain the hydrodynamic changes during the propagation of outburst floods, and are important records for distinguishing ODs and "*normal*" floods.

The sixth study, by Liu et al., is titled "*A comparative study of regional rainfall-induced landslide early warning models based on RF, CNN and MLP algorithms*". The authors focused on Fujian Province in China, and proposed a four-step process for building a regional landslide early warning model based on machine learning. The process includes data integration and cleaning, sample set construction, model training and validation, and practical application. This study will be valuable for landslide disaster warning research.

In the seventh contribution "*Construction and preliminary analysis of landslide database triggered by heavy storm in the parallel range-valley area of western Chongqing, China, on 8 June 2017*", Liu and Xu identified landslide disasters triggered by extreme rainfall events in the parallel range-valley area of western Chongqing, China, and established a historical landslide database. This database provides scientific support for investigating landslide mechanisms in western Chongqing and mitigating the associated risks.

The eighth study "*Exploring Bayesian network model with noise filtering for rainfall-induced landslide susceptibility assessment in Fujian, China*" was contributed by Zhou et al. The researchers employed a Bayesian network to analyze the factors influencing landslides in Fujian Province, China, which is prone to typhoons and landslides. They introduced a progressive noise filtering method to mitigate the mislabeling effects of non-landslide points. This study provides useful guidance for reliable landslide susceptibility mapping in the study area.

For this Research Topic, further critical and constructive debate, viewpoints and opinions are welcome: they will contribute to more

resilient and sustainable strategies and practices for adapting to extreme weather-induced disasters. We suggest you freely use and discuss these articles—including their methods, solid datasets, key findings and propositions, to promote research on extreme weather-induced disasters.

Author contributions

Y-FS: Writing – review and editing, Writing – original draft. LS: Writing – review and editing. XZ: Writing – review and editing. WY: Writing – review and editing.

Funding

The author(s) declare that financial support was received for the research and/or publication of this article. This work is financially supported by the National Natural Science Foundation of China (Grants 42471029, 2311530063), and the Science and Technology Projects of Xizang Autonomous Region (Grants XZ202501ZY0004, XZ202401JD0001).

Conflict of interest

The authors declare that the research was conducted in the absence of any commercial or financial relationships that could be construed as a potential conflict of interest.

Generative AI statement

The author(s) declare that no Generative AI was used in the creation of this manuscript.

Publisher's note

References

Easterling, D. R., Meehl, G. A., Parmesan, C., Changnon, S. A., Karl, T. R., and Mearns, L. O. (2000). Climate extremes: observations, modeling, and impacts. *Science* 289 (5487), 2068–2074. doi:10.1126/science.289.5487.2068

Field, C. B., Barros, V., Stocker, T. F., and Dahe, Q. (2012). *Managing the risks of extreme events and disasters to advance climate change adaptation: special report of the intergovernmental panel on climate change* (Cambridge University Press).

Ren, Z., Sang, Y. F., Cui, P., Chen, D., Zhang, Y., Sun, S., et al. (2024). Temporal scaling characteristics of sub-daily precipitation in Qinghai-Tibet Plateau. *Earth's Future* 465, 133177. doi:10.1029/2024ef004417

Sajadi, P., Sang, Y. F., Gholamnia, M., Bonafoni, S., and Mukherjee, S. (2022). Evaluation of the landslide susceptibility and its spatial difference in the whole Qinghai-Tibetan Plateau region by five learning algorithms. *Geosci. Lett.* 9 (1), 9–25. doi:10.1186/s40562-022-00218-x

Sang, Y. F., Singh, V. P., Hu, Z., Xie, P., and Li, X. (2018). Entropy-aided evaluation of meteorological droughts over China. *J. Geophys. Research-Atmospheres* 123 (2), 740–749. doi:10.1002/2017jd026956

Shi, J., Sang, Y. F., Sun, S., Aghakouchak, A., Hu, S., and Dash, S. S. (2024). Development of a leaf area index-based relative threshold method for identifying agricultural drought areas. *J. Hydrology* 641, 131846. doi:10.1016/j.jhydrol.2024.131846

Stott, P. (2016). How climate change affects extreme weather events. *Science* 352 (6293), 1517–1518. doi:10.1126/science.aaf7271

Yang, M. Y., Sang, Y. F., Sivakumar, B., Chan, F., and Pan, X. (2020). Challenges in urban stormwater management in Chinese cities: a hydrologic perspective. *J. Hydrology* 591, 125314. doi:10.1016/j.jhydrol.2020.125314

frontiers | Frontiers in Earth Science

TYPE Original Research
PUBLISHED 05 January 2023
DOI 10.3389/feart.2022.1022565

OPEN ACCESS

EDITED BY
Lingling Shen,
Beijing Meteorological Information Center, China

REVIEWED BY
Ying Zhou,
Beijing University of Technology, China
Duanyang Liu,
Chinese Academy of Meteorological Sciences, China

*CORRESPONDENCE
Xiaoqin Rao,
raoxq@cma.gov.cn
Qiying Chen,
chenqy@cma.gov.cn

SPECIALTY SECTION
This article was submitted to Geohazards and Georisks, a section of the journal Frontiers in Earth Science

RECEIVED 18 August 2022
ACCEPTED 01 November 2022
PUBLISHED 05 January 2023

CITATION
Liu C, Rao X, Chen Q, Zhang B and Zhang B (2023), Objective identification and forecast method of $PM_{2.5}$ pollution based on medium- and long-term ensemble forecasts in Beijing-Tianjin-Hebei region and its surrounding areas. *Front. Earth Sci.* 10:1022565. doi: 10.3389/feart.2022.1022565

Objective identification and forecast method of $PM_{2.5}$ pollution based on medium- and long-term ensemble forecasts in Beijing-Tianjin-Hebei region and its surrounding areas

Chao Liu[1], Xiaoqin Rao[1]*, Qiying Chen[2]*, Bihui Zhang[1] and Bo Zhang[1]

[1]National Meteorological Centre, Beijing, China, [2]CMA Earth System Modeling and Prediction Centre, Beijing, China

Accurate long-term forecasts of $PM_{2.5}$ pollution are essential to mitigating health risks and formulating pollutant control strategies for decision-makers in China. In this study, an objective identification and forecast method for $PM_{2.5}$ pollution (OIF-$PM_{2.5}$) is developed based on medium- and long-term ensemble forecasts of $PM_{2.5}$ in Beijing-Tianjin-Hebei region and its surrounding areas. The results show that the observed $PM_{2.5}$ pollution ratio increases with the aggravating $PM_{2.5}$ pollution. For example, the ratio of meteorological stations with heavy pollution is 4.4 times that of light pollution and 3.9 times that of moderate pollution. In addition, the correlation coefficients between observations and forecasts are above 0.60 for all forecast leading times. Statistical results show that the average accuracy for forecasts with the leading times of 1–3 days, 4–7 days, and 8–15 days are 74.1%, 81.3%, and 72.9% respectively, indicating that the OIF-$PM_{2.5}$ method has a high reliability in forecasts with the leading times of 1–15 days. The OIF-$PM_{2.5}$ method is further applied in a severe $PM_{2.5}$ pollution episode in the December of 2021, and the average forecast precision in forecasts with the leading times of 6–8 days reaches as high as 100%, showing a certain reference value for $PM_{2.5}$ forecasts.

KEYWORDS

PM 2.5 pollution, ensemble forecast, forecast technology, objective identification and forecast method for PM2.5 pollution, beijing-tianjin-hebei region and its surrounding areas

1 Introduction

In terms of economy, urbanization and population growth, the Beijing-Tianjin-Hebei region (BTH) and its surrounding areas are among the most developed regions in China. Meanwhile, severe and frequent $PM_{2.5}$ (fine particulate matter with an aerodynamic diameter ≤2.5 μm) pollution in this region has attracted more and more attention in recent years due to its complex impacts on visibility, human health and ecological environment (Liu et al., 2019; Li et al., 2021a; Cheng et al., 2021; Sawlani et al., 2021; Zhang et al., 2021). The Chinese government launched the "Air Pollution Prevention and Control Action plan" in 2013 and "2017 Air Pollution Prevention and Management Plan for the Beijing-Tianjin-Hebei Region and its Surrounding Areas" to solve the severe $PM_{2.5}$ pollution. A series of control measures have been implemented to reduce pollutant emissions, e.g., eliminating industries with high pollution and emission, optimizing industrial and energy structures and restricting vehicle use (Zhang et al., 2014; Chen et al., 2021; Liu et al., 2021). Nonetheless, heavy $PM_{2.5}$ pollution episodes are still frequent in BTH and its surrounding areas, especially during autumn and winter due to unfavorable meteorological conditions (Zhang et al., 2018; Li et al., 2019; Bei et al., 2020). Accurate $PM_{2.5}$ pollution forecasts can reduce the air pollutant exposure to sensitive groups and provide necessary reference for making pollution policies and starting control measures in advance, especially before some importance events such as the Asia-Pacific Economic Cooperation Summit 2014 and 70th anniversary of the founding of the People's Republic of China. Therefore, medium- and long-term $PM_{2.5}$ forecast is critically important.

Various methods have been used for air pollution forecasting. In general, the forecasting methods can be categorized into three groups: empirical method, statistical approaches and numerical simulations (Zhai and Chen, 2018; Liu and Chen, 2019). The empirical method, also known as a knowledge-based procedure, is based on previous observations, which requires a comprehensive understanding of the pollution dispersion/transport mechanisms and physical-chemical processes (Garner and Thompson, 2012; Yuval et al., 2012). Furthermore, the empirical method is highly dependent on pollution sources and meteorological factors, and previous studies (Zhou et al., 2019; Wu et al., 2020; Samal et al., 2021) have demonstrated that it performs poorly when compared with statistical approaches. Statistical approaches consist of multiple linear regression (Dimitriou and Kassomenos, 2014; Jeong et al., 2021; Liu et al., 2022), Kalman filtering, artificial neural network (Zhou et al., 2020; Bera et al., 2021), long short-term memory (Gao and Li, 2021), support vector machine (Wang et al., 2017) and other hybrid methods (Liu et al., 2020; Huang et al., 2021). It is found that they can successfully forecast the $PM_{2.5}$ for their capacity of nonlinear mapping. In addition, the deep learning technology has sparked a lot of interest (Pak et al., 2020; Menares et al., 2021; Yang et al., 2021) and proven its superiority in several fields. Deep learning technology is proposed for analyzing the characteristics of historical data. However, all of these statistical approaches only focus on the historical data, which ignore the atmospheric dispersion and transport mechanisms. Furthermore, most of them could only provide short-term forecasts that usually range from 24 to

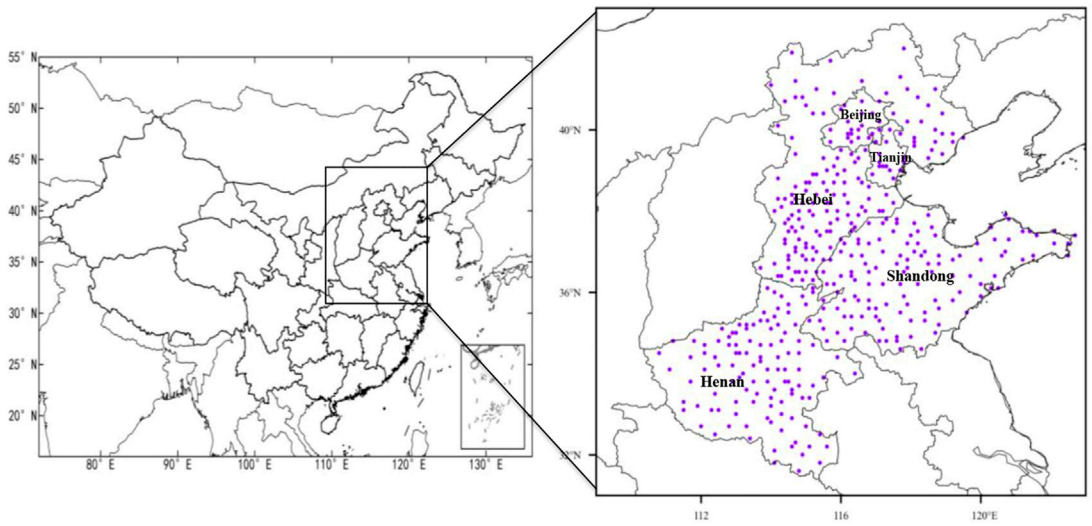

FIGURE 1
Locations of the meteorological stations in Beijing-Tianjin-Hebei (BTH) and its surrounding areas.

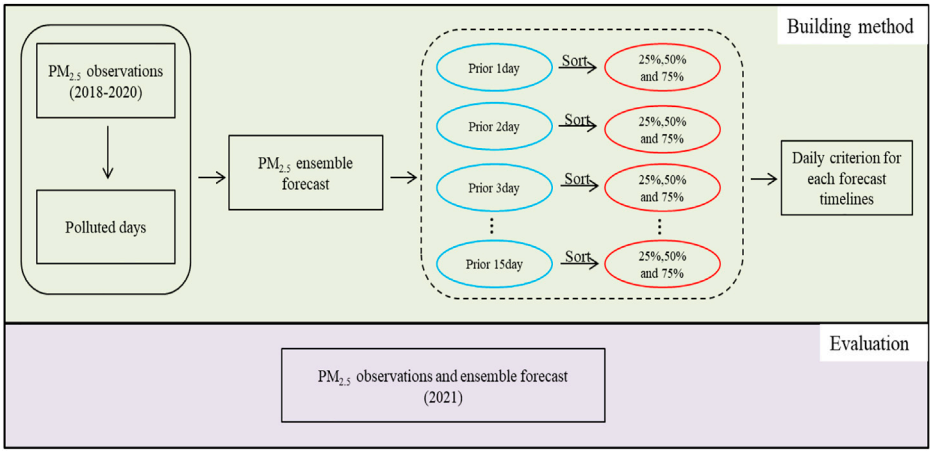

FIGURE 2
The technical flowchart for the objective identification and forecast of $PM_{2.5}$ pollution.

TABLE 1 Accuracy index categories.

Polluted day	Forecasted $PM_{2.5}$ pollution ratio	
	≥25th percentile	< 25th percentile
Yes	NA	NC
NO	NB	ND

72 h (Jiang et al., 2021), while most planning and monitoring actions have a greater demand for long-term forecasts. Numerical simulations, such as the Community Multiscale Air Quality Modeling System and the Comprehensive Air quality Model with extensions, can simulate the chemical and physical processes of $PM_{2.5}$ pollution (Cai et al., 2017; Liu et al., 2018) and thus provide a better understanding of the transformations and distributions of $PM_{2.5.}$ Although numerical models can provide reliable medium-term forecasts, there may be some systematic errors in short-term forecasts. Such models tend to be sensitive to initial and boundary fields (Feng et al., 2020).

Over the past decades, ensemble forecast products have been a major contributor to improving weather forecasts (Yang et al., 2015; Zhao et al., 2022). These products take into account the uncertainty of initial states and process description in numerical weather forecasting models. Ensemble forecasts include several members, representing a set of possible atmospheric conditions in the future. In contrast to deterministic weather forecasts, ensemble forecasts increase the lead time of high-quality forecasts to more than several days. The Observing-system Research and Predictability Experiment (THORPEX) Interactive Grand Global Ensemble (TIGGE) is a database of ensemble forecasts in medium and long ranges conducted by different forecasting centers established for scientific research (Tao et al., 2014). Among all TIGGE data, the European Centre for Medium-Range Weather Forecasts (ECMWF) have presented advantages in the number of ensemble members and spatial resolutions than other forecasting systems (Sagar et al., 2017), consisting of 51 members with a resolution of approximate 0.5° for the whole globe (Zhao et al., 2016). Regarding these advantages, the ECMWF ensemble forecasts are widely applied in forecasting precipitation (Cong et al., 2021), temperature (Verkade et al., 2013), tropical cyclone track (Nishimura and Yamaguchi, 2015) and water deficit depth (Zhao et al., 2016). Based on the ECMWF ensemble forecasts, Schumacher et al. (2011) studied a low-vortex induced rainstorm event in southern United States, and investigated the impact of disturbances in upstream weather systems on precipitation forecasts. Besides, Schauwecker et al. (2021) also conducted a research on the forecast performance of ECMWF Integrated Forecasting System ensemble median run in a heavy precipitation event over Switzerland. The uncertainty in atmospheric forecasts mainly arises from the parameters, initial states and model structure. In the past few years, researchers have proposed various techniques to tackle the uncertainties in ensemble forecasts from different aspects (Demeritt et al., 2007; Yu and Meng, 2016; Ali et al., 2018). For these uncertainties, the forecasting skill can be enhanced by post-processing through multiple-modeling, statistical methods and data assimilation (Li et al., 2021b; Whan et al., 2021; Zhao et al., 2022). However, there are few studies on ensemble forecasting post-processing techniques in the field of $PM_{2.5}$ forecasting.

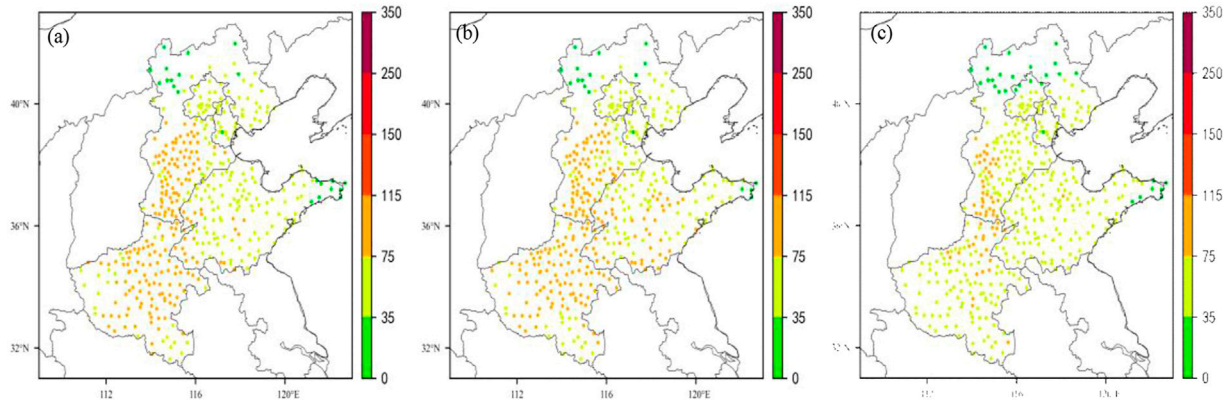

FIGURE 3
Observations of $PM_{2.5}$ concentrations in BTH and its surrounding areas in **(A)** 2018, **(B)** 2019 and **(C)** 2020.

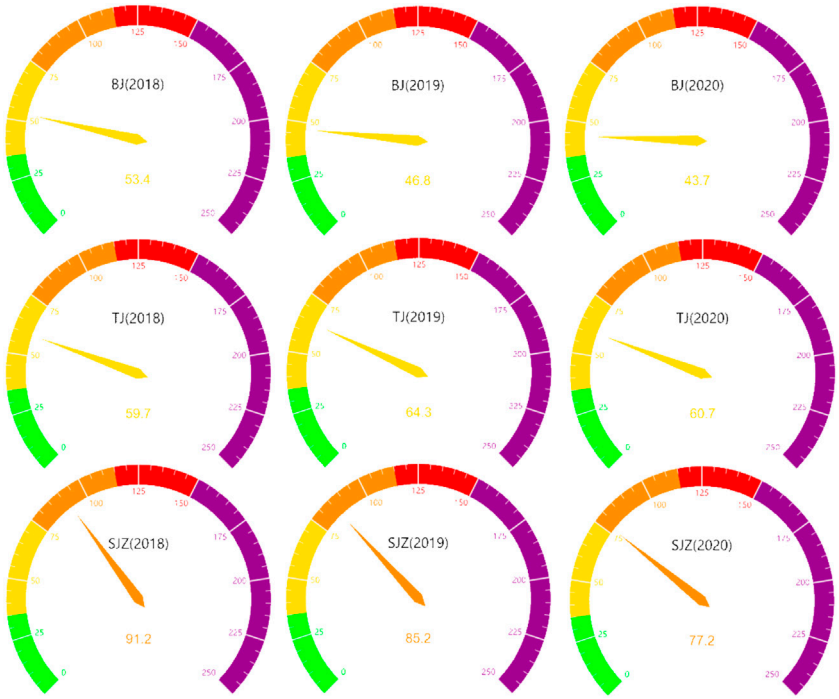

FIGURE 4
Observations of $PM_{2.5}$ concentrations in Beijing, Tianjin and Shijiazhuang.

In this study, objective identification and forecast method of $PM_{2.5}$ pollution (OIF-$PM_{2.5}$) is established based on the medium- and long-term ensemble forecasts with the leading times of 1–15 days. Besides, this method is evaluated by the forecast precision and its applicability is assessed in a $PM_{2.5}$ pollution episode in BTH and its surrounding areas. The remainder of this paper is organized as follows. Section 2 describes the study area, data and method. Section 3 presents the results and discussions, including the characteristics of $PM_{2.5}$ pollution, the performance of $PM_{2.5}$ ensemble forecast and the evaluation of OIF-$PM_{2.5}$ method. Finally, Section 4 gives the conclusions.

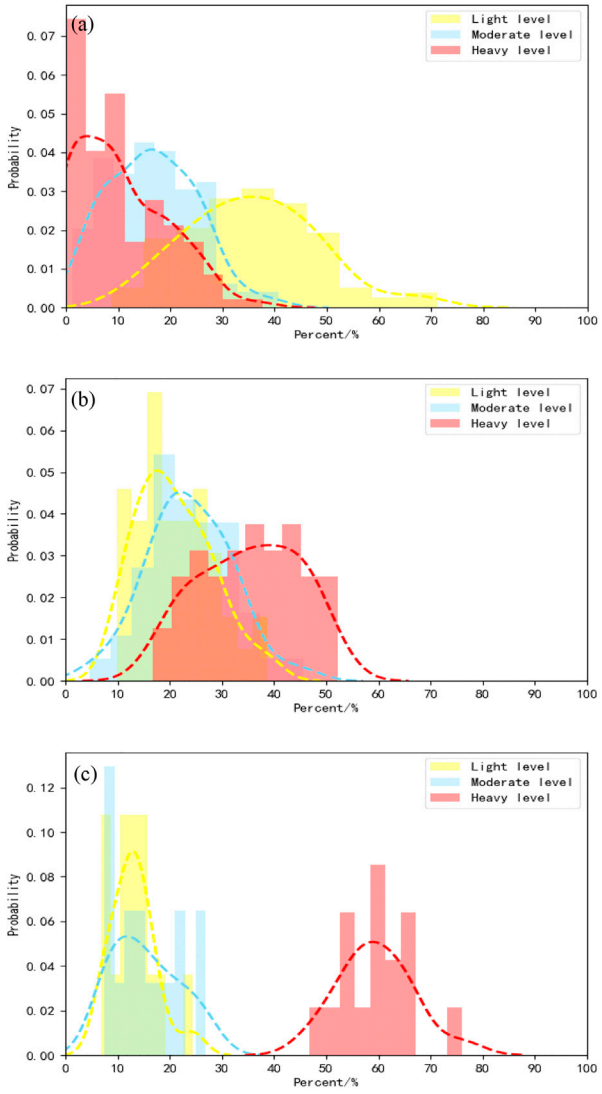

FIGURE 5
Distributions of observed $PM_{2.5}$ pollution ratios under **(A)** light pollution, **(B)** moderate pollution and **(C)** heavy pollution in BTH and its surrounding areas.

TABLE 2 Average $PM_{2.5}$ pollution ratios at different polluted levels in BTH and its surrounding areas.

Polluted level	$PM_{2.5}$ pollution ratio (unit: %)		
	Light	Moderate	Heavy
Light	35.8 ± 12.8	16.6 ± 8.4	10.4 ± 8.8
Moderate	20.9 ± 7.2	23.8 ± 8.2	35.3 ± 9.6
Heavy	13.1 ± 4.3	15.4 ± 6.4	59.5 ± 7.2

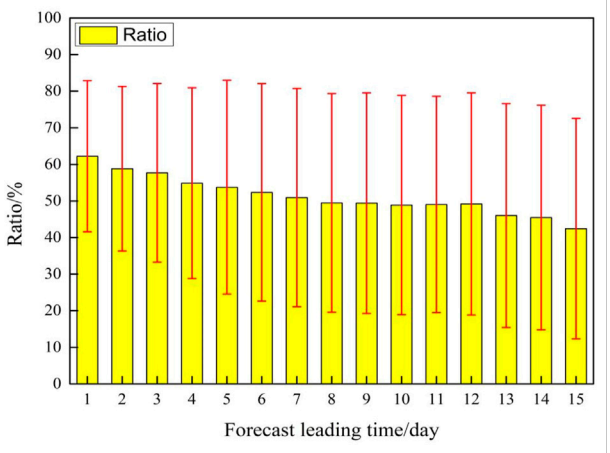

FIGURE 6
Forecasted $PM_{2.5}$ pollution ratios with different forecast leading times.

2 Data and methods

2.1 Study areas

The BTH and its surrounding areas include two municipalities (Beijing and Tianjin) as well as the provinces of Hebei, Henan and Shandong. This region is home to the majority of energy-intensive and polluting industries (Tong et al., 2019). In addition, the unfavorable geographical conditions with the Yanshan Mountains to its north and the Taihang Mountains to its west are conducive to the accumulation of pollutants (Bei et al., 2020).

2.2 $PM_{2.5}$ observations

The medium- and long-term ensemble forecasts of $PM_{2.5}$ are established based on ground observations from meteorological stations in China. The daily $PM_{2.5}$ observations are obtained through the neighboring-point interpolation algorithm conducted on data from 417 meteorological stations set up by the China National Environmental Monitoring Centre. All observed samples are divided into two groups of training dataset and testing dataset. The OIF-$PM_{2.5}$ is established by using the training dataset of the autumns and winters (January, February, March, October, November and December) from 2018 to 2020, and the testing dataset contains the data of the autumn and winter of 2021. The locations of meteorological stations in the study area is presented in Figure 1.

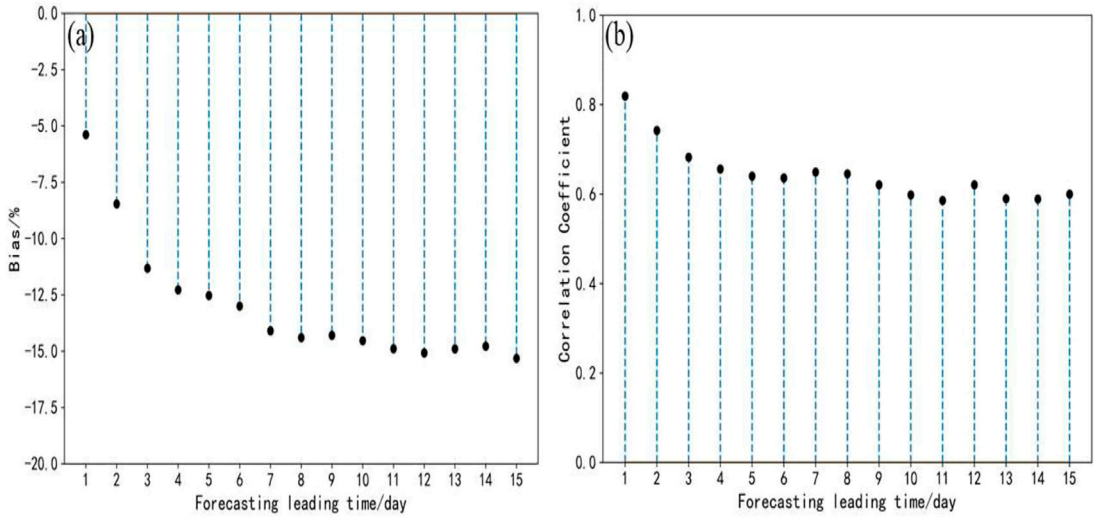

FIGURE 7
(A) Biases (forecast minus observation) of $PM_{2.5}$ pollution ratios and **(B)** correlation coefficients between observations and forecasts with different forecast leading times.

TABLE 3 The first, second and third quartiles of forecasted $PM_{2.5}$ pollution ratios with different forecast leading times.

Forecast leading time (unit: day)	First quartile (unit: %)	Second quartile (unit: %)	Third quartile (unit: %)
1	47.6	69.4	79.9
2	42.2	66.2	78.6
3	37.5	64.7	77.1
4	35.7	63.8	75.9
5	32.8	60.4	76.2
6	31.5	58.2	75.4
7	28.3	58.3	74.9
8	26.8	57.1	73.6
9	24.1	55.8	75.0
10	21.8	55.1	73.7
11	22.3	53.3	72.0
12	19.2	54.6	72.6
13	19.4	51.2	71.4
14	18.6	49.3	70.1
15	17.8	48.8	69.8

2.3 $PM_{2.5}$ ensemble forecast

Based on regional pollution characteristics, topography and climate differences, the $PM_{2.5}$ ensemble forecast products are made by using the ECMWF ensemble products. These products contain meteorological factors such as horizontal and vertical diffusion capacities and dry and wet deposition conditions. Furthermore, the forecast equations of daily $PM_{2.5}$ at each station is set up based on meteorological factors and pollution characteristics in different regions. Finally, the ensemble average forecast, control forecast and 51-members ensemble forecast products are obtained, forming 1–15-day forecast products. In this study, the ensemble average forecast is used to establish the OIF-$PM_{2.5}$.

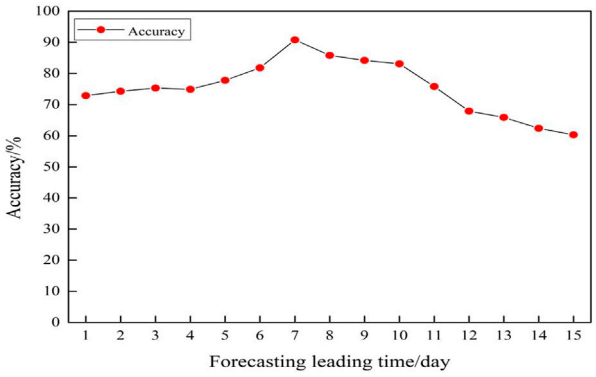

FIGURE 8
Values of accuracy under different forecast leading times.

2.4 Methods

The OIF-$PM_{2.5}$ technical flowchart is presented in Figure 2. In this study, the performance of $PM_{2.5}$ ensemble forecast in varying forecasting time ranges is considered. The 25th, 50th and 75th percentiles of forecasted $PM_{2.5}$ pollution ratios are chosen as the identification thresholds for each forecasting time range corresponding to each polluted day ($PM_{2.5} \geq 75\ \mu g\ m^{-3}$) in the training dataset. Here, the forecasted $PM_{2.5}$ pollution ratio is defined as the ratio of the number of stations with $PM_{2.5} \geq 75\ \mu g\ m^{-3}$ in the ensemble forecast to the total number of stations in this region in each day.

To evaluate the performance and precision of the OIF-$PM_{2.5}$ method, the 25th percentile is selected as the criterion, and the accuracy as the statistical index. The principle of the accuracy (AC, unit:%) index is listed in Table 1, where NA, NB, NC, and ND variables represent different categories. NA variable represents the forecasted $PM_{2.5}$ pollution ratio exceeds the 25th percentile on the polluted day, and NC variable means the forecasted $PM_{2.5}$ pollution ratio exceeds the 25th percentile on the polluted day is lower than the 25th percentile on the polluted day. Consequently, NB and ND variables represent the forecasted $PM_{2.5}$ pollution ratio are higher or lower than the 25th percentile on non-polluted day, respectively.

$$\mathrm{AC} = \frac{NA + ND}{NA + NB + NC + ND} \times 100\%. \quad (1)$$

3 Results

3.1 Characteristics of $PM_{2.5}$ pollution

The spatial distributions of average $PM_{2.5}$ concentrations in BTH and its surrounding areas from 2018 to 2020 are shown in

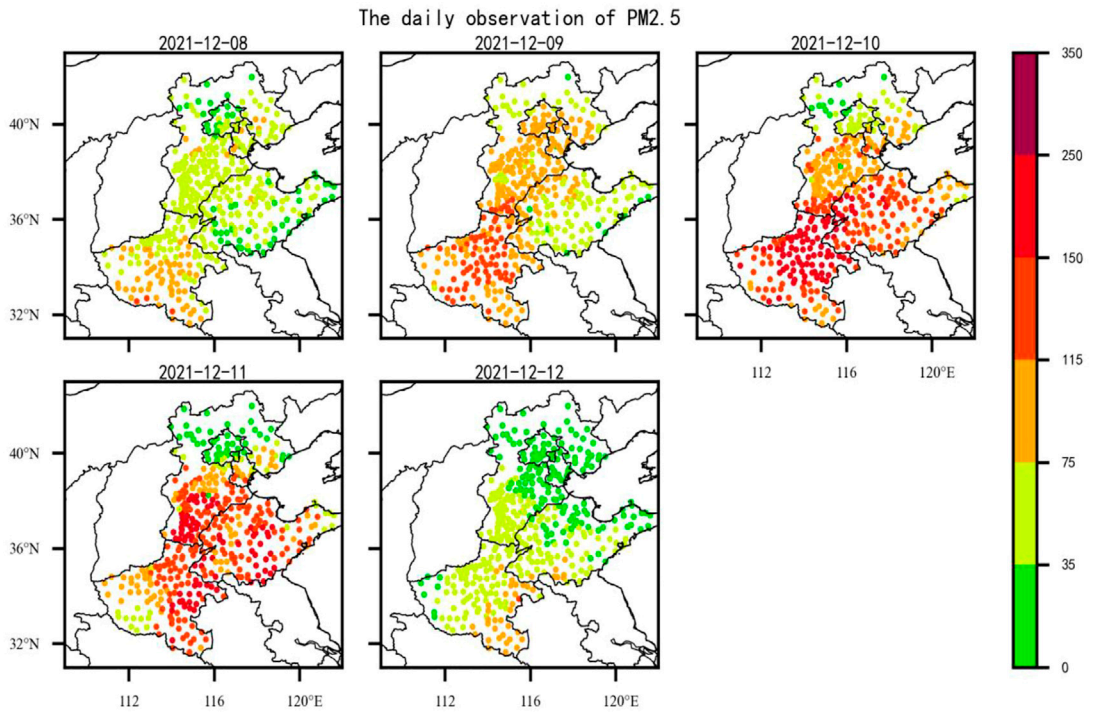

FIGURE 9
Distributions of daily $PM_{2.5}$ concentrations from December 8 to 12 of 2021 in BTH and its surrounding areas.

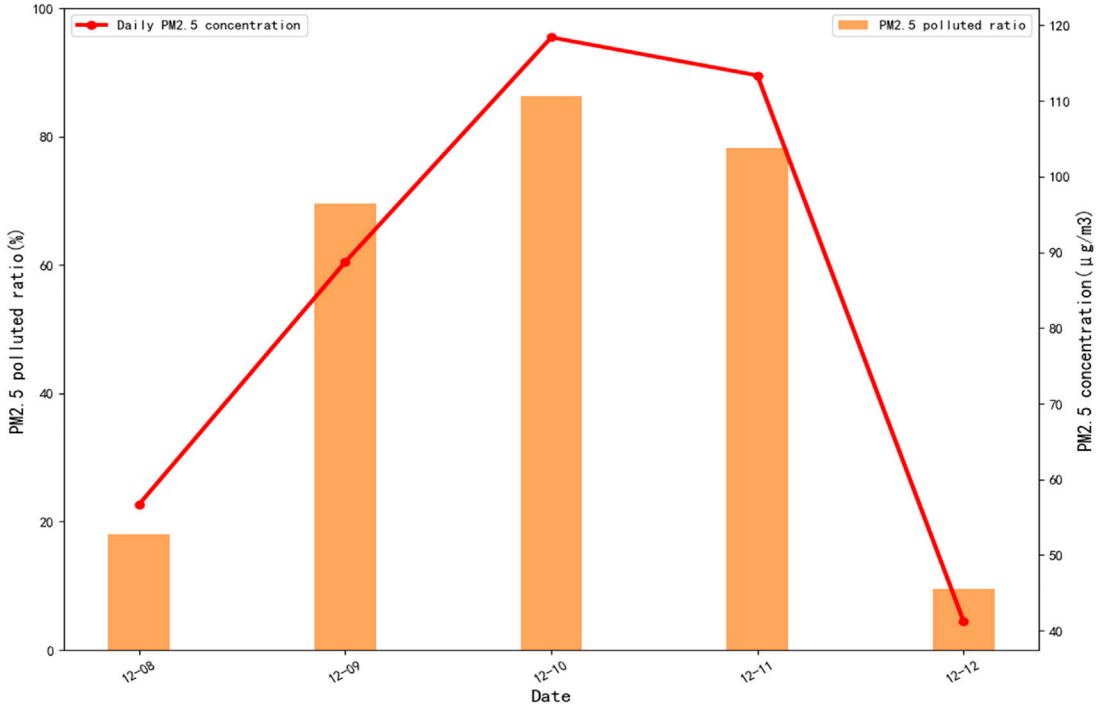

FIGURE 10
Daily $PM_{2.5}$ concentrations and $PM_{2.5}$ pollution ratios from December 8 to 12 of 2021 in BTH and its surrounding areas.

Figure 3. It is worth noting that the $PM_{2.5}$ concentrations in northern Hebei are below the threshold for the daily average of the China Ambient Air Quality Standard (GB 3095–2012) for $PM_{2.5}$ (Grade I:35 μg m^{-3}). However, the $PM_{2.5}$ pollution in 2018 and 2019 is heavy in the south and light in the north of the BTH and its surrounding areas, with the main pollution belts concentrated in southern Hebei, central-eastern Henan and western Shandong. In 2020, the $PM_{2.5}$ level is low in Beijing, Tianjin, Northern Hebei and Shandong, while slightly polluted in Southern Hebei and Northern Henan. In addition, Beijing, Tianjin and Shijiazhuang are selected for comparison (Figure 4). It can be seen that the $PM_{2.5}$ concentrations of Beijing decrease from 53.4 μg m^{-3} in 2018 to 43.7 μg m^{-3} in 2020, while those in Tianjin fluctuate between 59.7 μg m^{-3} and 64.3 μg m^{-3} within the same period. In other words, the $PM_{2.5}$ concentrations of 2020 are 1.2 times and 1.7 times the $PM_{2.5}$ Grade I in Beijing and Tianjin, respectively. What's more, the $PM_{2.5}$ concentrations in Shijiazhuang decrease from 91.2 μg m^{-3} in 2018 to 77.2 μg m^{-3} in 2020 by 15.3%, which is the largest decrease among the three cities. However, the magnitude of $PM_{2.5}$ concentrations in 2020 in Shijiazhuang is 2.2 times the $PM_{2.5}$ Grade I.

The probability distributions and averages of observed $PM_{2.5}$ pollution ratios under different polluted levels in BTH and its surrounding areas are given in Figure 5, Table 2, respectively. As can be seen, when the average $PM_{2.5}$ concentration reaches the light level, the ratio of the number of stations with light pollution is the highest within the range of 34%–40%, and the distribution curve follows the law of normal distribution. However, the average $PM_{2.5}$ pollution ratios for moderate pollution and heavy pollution are 16.6% and 10.4%, respectively. What's more, the highest ratio of the number of stations with heavy pollution rapidly increases to 35.3% under the level of moderate pollution, which is 1.7 times that of light pollution and 1.5 times that of moderate pollution. In addition, the number of stations with heavy pollution are more than half of the total in this region. Nevertheless, the heavy $PM_{2.5}$ pollution ratio is 4.4 times that of light pollution and 3.9 times that of moderate pollution. In general, the ratio of polluted meteorological stations is increasing as the $PM_{2.5}$ pollution aggravates in this region.

3.2 Performance of $PM_{2.5}$ ensemble forecasts

Some studies (Wang and Huang, 2006; Zhao et al., 2021) have revealed that the performance of forecasting products vary with the forecast leading times. The forecasted $PM_{2.5}$ pollution

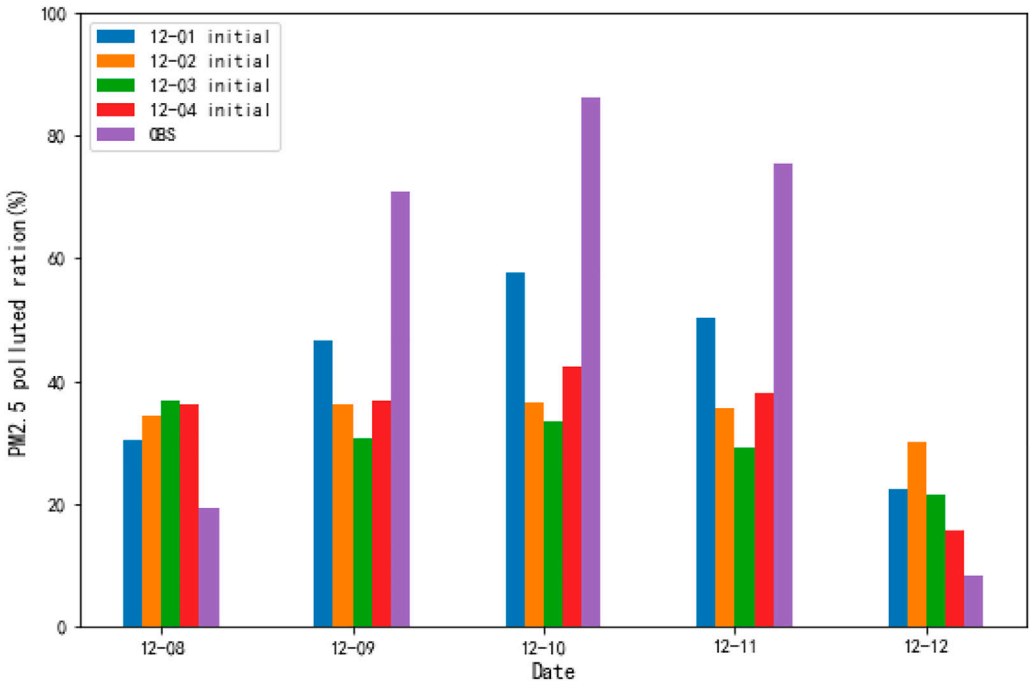

FIGURE 11
$PM_{2.5}$ pollution ratios for forecasts under different forecast initial times and observations from December 8 to 12 of 2021 in BTH and its surrounding areas.

ratios with different forecast leading times are analyzed based on the training dataset (Figure 6). For $PM_{2.5}$ ensemble forecasts, the ratio of stations being polluted decreases with the increasing forecast leading times, which is consistent with other forecasting products. The averages of forecasted $PM_{2.5}$ pollution ratios with the forecast leading times of 1–3 days, 4–7 days and 8–15 days are 59.5%, 52.9% and 47.4%, respectively. That is, the $PM_{2.5}$ pollution processes at more than 50% meteorological stations in this region can be forecasted by 8 days in advance.

As illustrated in Figure 7A, the bias (forecast minus observation) of $PM_{2.5}$ pollution ratio increases with the increasing forecast leading time, and the biases are all negative, that is, the forecasted ratios are lower than the observed ones. The biases of $PM_{2.5}$ pollution ratio with the forecast leading times of 1–6 days are less than −13%; however, the bias remains between −14.1% and −15.4% when the forecast leading time is more than 7 days. Besides, the correlation coefficients of the ratios between the observations and forecasts are more than 0.68 with the forecast leading times being 1–3 days, while above 0.60 for other leading times (Figure 7B). In general, although the forecasted ratios are lower than the observed ones, the correlation between them remains high values, indicating a good performance of the $PM_{2.5}$ ensemble forecasts.

The forecasted $PM_{2.5}$ pollution ratios of the autumns and winters from 2018 to 2020 are calculated, and the corresponding 25th, 50th and 75th percentiles are given in Table 3. The 25th percentiles of the forecasted $PM_{2.5}$ pollution ratios are below 50% for all forecast leading times, which are below 20% for the leading times of 12–15 days. Besides, the 25th percentiles exceed 30% with the forecast leading times of 1–6 days, with the ratios being 47.6% and 42.2% for the leading times of 1 day and 2 days, respectively. The 50th percentiles are below 70% for all forecast leading times, which are over 60% with the forecast leading times of 1–5 days. Besides, the differences of the 50th percentiles among different forecast leading times are smaller than those of the 25th percentiles. The 75th percentiles of the forecasted $PM_{2.5}$ pollution ratios are above 70% for most of the forecast leading times, which exceed 75% with the leading times of 1–6 days. In addition, the differences of the 75th percentiles among different forecast leading times are further reduced when compared with those of the 50 percentiles, being only 10.1% between the 1-day and 15-day forecast leading times. In summary, the forecasts of $PM_{2.5}$ pollution ratio with different leading times are indicative of the occurrence of regional $PM_{2.5}$ pollution events to some extent.

3.3 Evaluation of the OIF-$PM_{2.5}$ method and its application

3.3.1 Performance of the OIF-$PM_{2.5}$ method

In this study, the accuracy for forecasts in the autumn and winter of 2021 is examined. As illustrated in Figure 8, the accuracy of the OIF-$PM_{2.5}$ method show a trend of first increase and then decrease, being over 60% for different forecast leading times. The highest accuracy of 90.8% is achieved for the forecasts with the leading time of 7 days. In addition, the average accuracy for forecast leading times of 1–3 days, 4–7 days and 8–15 days are 74.1%, 81.3% and 72.9%, respectively. It is well documented that the ECMWF has better predictability for ensemble forecasts with the leading times of 4–7 days (Huang and Niu, 2017). The evolution of accuracy with different forecast leading times is consistent with that reported in Tao et al. (2017). It indicates that the OIF-$PM_{2.5}$ method has a high reliability in forecasts with the forecast leading times of 1–15 days.

3.3.2 Application in a $PM_{2.5}$ pollution process

A regional $PM_{2.5}$ pollution event occurred in BTH and its surrounding areas from December 8 to 12, 2021 (Figures 9, 10). Most of the region was dominated by $PM_{2.5}$ pollution of light level on December 9, with the daily average $PM_{2.5}$ concentration being 88.7 μg m^{-3} and the pollution ratio being 69.5%. In addition, the atmospheric dispersion conditions worsened in this region during December 10–11. The areas with high $PM_{2.5}$ concentrations were mainly located in southern Hebei, central and eastern Henan, and central and Western Shandong, with the regional averaged $PM_{2.5}$ concentrations reaching 118.3 μg m^{-3} on December 10 and 113.4 μg m^{-3} on December 11. In addition, the $PM_{2.5}$ pollution ratio increased to 86.3% on December 10 and 78.2% on December 11, indicating the significant expansion and enhancement of the $PM_{2.5}$ pollution. Eventually, the $PM_{2.5}$ concentrations decreased gradually from North to South due to the cold air on December 12, and the air quality reached the excellent and good level in most of the region.

Using different forecast initial times, the OIF-$PM_{2.5}$ method is applied to this pollution episode, and the forecast results are shown in Figure 11. It can be seen that the forecasted $PM_{2.5}$ pollution ratios for different initial times are consistent with the observations, which is of indicative significance for the evolution of pollution process. For the most polluted period of the pollution process, the pollution ratio of stations on December 10 is 57.7% with the forecast initial time being December 1, which even exceeds the 50th percentile (55.8%). In addition, the values of accuracy under different forecast leading times are also calculated. The results show that the average accuracy reaches 90% (100%) under the leading times of 4–11 days (6–8 days), indicating that the forecast stability of the OIF-$PM_{2.5}$ method is more stable and is of reference value for forecasts.

4 Conclusion and discussion

Based on the medium- and long-term ensemble forecasts of $PM_{2.5}$ concentrations, the OIF-$PM_{2.5}$ method is developed in this study. Specifically, different percentiles of forecasted $PM_{2.5}$ pollution ratios for each forecast leading time from 2018 to 2020 are determined and analyzed. The OIF-$PM_{2.5}$ method is further evaluated and applied in a $PM_{2.5}$ pollution episode in 2021. The main conclusions are as follows.

The observed $PM_{2.5}$ pollution ratio increases with the aggravation of $PM_{2.5}$ pollution in this region. For example, the heavy pollution ratio is 4.4 times the light pollution ratio and 3.9 times the moderate pollution ratio. Besides, the correlation coefficients between the observed ratios and forecasted ratios are above 0.60 for all forecast leading times in ensemble forecast products. Furthermore, the statistical results show that the average accuracy for forecasts with the leading times of 1–3 days, 4–7 days and 8–15 days in are 74.1%, 81.3% and 72.9%, respectively, indicating that the OIF-$PM_{2.5}$ method has a high reliability in forecasts with the leading times of 1–15 days. The OIF-$PM_{2.5}$ method is further applied in a severe $PM_{2.5}$ pollution episode in the December of 2021. It is revealed that the average accuracy for the forecasts with the leading times of 6–8 days reaches as high as 100%, showing a certain reference value.

The findings of this paper help to understand the $PM_{2.5}$ concentration forecasts with the forecast leading times of 1–15 days, which can help to minimize the adverse effects of high $PM_{2.5}$ pollution for society and public health. Moreover, it will help decision makers to formulate pollutant control strategies and take precautions.

Data availability statement

The raw data supporting the conclusion of this article will be made available by the authors, without undue reservation.

Author contributions

Conceptualization, XR; Methodology, BOZ; Data curation and formal analysis and writing—original draft preparation, CL; writing—review and editing, CL and QC; Visualization, BOZ; Funding acquisition: BHZ and QC. All authors have read and agreed to the published version of the manuscript.

Funding

This study was supported by the National Key R & D Program Pilot Projects of China (2019YFC0214602), National Key R & D

Program Pilot Projects of China (2021YFC3000900) and National Meteorological Centre forecaster funding (Y202127).

Conflict of interest

The authors declare that the research was conducted in the absence of any commercial or financial relationships that could be construed as a potential conflict of interest.

Publisher's note

All claims expressed in this article are solely those of the authors and do not necessarily represent those of their affiliated organizations, or those of the publisher, the editors and the reviewers. Any product that may be evaluated in this article, or claim that may be made by its manufacturer, is not guaranteed or endorsed by the publisher.

References

Ali, M., Deo, R. C., Down, N. J., and Maraseni, T. (2018). An ensemble-ANFIS based uncertainty assessment model for forecasting multi-scalar standardized precipitation index. *Atmos. Res.* 207 (15), 155–180. doi:10.1016/j.atmosres.2018.02.024

Bei, N. F., Li, X. P., Tie, X. X., Zhao, L. N., Wu, J. R., Li, X., et al. (2020). Impact of synoptic patterns and meteorological elements on the wintertime haze in the Beijing-Tianjin-Hebei region, China from 2013 to 2017. *Sci. Total Environ.* 772 (20), 135210. doi:10.1016/j.scitotenv.2019.135210

Bera, B., Bhattacharjee, S., Sengupta, N., and Saha, S. (2021). $PM_{2.5}$ concentration prediction during COVID-19 lockdown over Kolkata metropolitan city, India using MLR and ANN models. *Environ. Challenges* 4, 100155. doi:10.1016/j.envc.2021.100155

Cai, S. Y., Wang, Y. J., Zhao, B., Wang, S. X., Chang, X., and Hao, J. M. (2017). The impact of the "air pollution prevention and control action plan" on $PM_{2.5}$ concentrations in jing-jin-ji region during 2012–2020. *Sci. Total Environ.* 580 (15), 197–209. doi:10.1016/j.scitotenv.2016.11.188

Chen, J. D., Gao, M., Li, D., Li, L., Song, M. L., and Xie, Q. J. (2021). Changes in $PM_{2.5}$ emissions in China: An extended chain and nested refined laspeyres index decomposition analysis. *J. Clean. Prod.* 294 (20), 126248. doi:10.1016/j.jclepro.2021.126248

Cheng, M. T., Tang, G. Q., Lv, B., Li, X. R., Wu, X. R., Wang, Y. M., et al. (2021). Source apportionment of $PM_{2.5}$ and visibility in Jinan, China. *J. Environ. Sci.* 102, 207–215. doi:10.1016/j.jes.2020.09.012

Cong, J., Wu, Z. L., Ma, Y. X., Xu, S., Wang, Y., Sun, M. N., et al. (2021). Improving numerical forecast of the rainstorms induced by Mongolia cold vortex in North China with the frequency matching method. *Atmos. Res.* 262, 105791. doi:10.1016/j.atmosres.2021.105791

Demeritt, D., Cloke, H., Pappenberger, F., Thielen, J., Bartholmes, J., and Ramos, M. H. (2007). Ensemble predictions and perceptions of risk, uncertainty, and error in flood forecasting. *Environ. Hazards* 7 (2), 115–127. doi:10.1016/j.envhaz.2007.05.001

Dimitriou, K., and Kassomenos, P. (2014). A study on the reconstitution of daily PM_{10} and $PM_{2.5}$ levels in Pariswith a multivariate linear regression model. *Atmos. Environ.* 98, 648–654. doi:10.1016/j.atmosenv.2014.09.047

Feng, L. W., Li, Y. Y., Wang, Y. M., and Du, Q. Y. (2020). Estimating hourly and continuous ground-level $PM_{2.5}$ concentrations using an ensemble learning algorithm: The ST-stacking model. *Atmos. Environ.* 223, 117242. doi:10.1016/j.atmosenv.2019.117242

Gao, X., and Li, W. D. (2021). A graph-based LSTM model for $PM_{2.5}$ forecasting. *Atmos. Pollut. Res.* 12 (9), 101150. doi:10.1016/j.apr.2021.101150

Garner, G. G., and Thompson, A. M. (2012). The value of air quality forecasting in the mid-atlantic region. *Weather, Clim. Soc.* 4 (1), 69–79. doi:10.1175/wcas-d-10-05010.1

Huang, G. Y., Li, X. Y., Zhang, B., and Ren, J. D. (2021). $PM_{2.5}$ concentration forecasting at surface monitoring sites using GRU neural network based on empirical mode decomposition. *Sci. Total Environ.* 768 (10), 144516. doi:10.1016/j.scitotenv.2020.144516

Huang, W., and Niu, R. Y. (2017). The medium-term multi-model integration forecast experimentation for heavy rain based on support vector machine. *Meteorol. Mon.* 43 (9), 1110–1116. (in Chinese).

Jeong, J. L., Park, R. J. L., Yeh, S. W., and Roh, J. W. (2021). Statistical predictability of wintertime $PM_{2.5}$ concentrations over East Asia using simple linear regression. *Sci. Total Environ.* 776, 146059. doi:10.1016/j.scitotenv.2021.146059

Jiang, S., Yu, Z. G., Anh, V. V., and Zhou, Y. (2021). Long- and short-term time series forecasting of air quality by a multi-scale framework. *Environ. Pollut.* 271, 116381. doi:10.1016/j.envpol.2020.116381

Li, F., Yan, J. J., Wei, Y. C., Zeng, J. J., Wang, X. Y., Chen, X. Y., et al. (2021a). $PM_{2.5}$-bound heavy metals from the major cities in China: Spatiotemporal distribution, fuzzy exposure assessment and health risk management. *J. Clean. Prod.* 286 (1), 124967. doi:10.1016/j.jclepro.2020.124967

Li, W. T., Pan, B. X., Xia, J. J., and Duan, Q. Y. (2021b). Convolutional neural network-based statistical post-processing of ensemble precipitation forecasts. *J. Hydrology* 605, 127301. doi:10.1016/j.jhydrol.2021.127301

Li, X., Gao, Z. Q., Li, Y. B., Gao, C. Y., Ren, J. Z., and Zhang, X. Y. (2019). Meteorological conditions for severe foggy haze episodes over north China in 2016–2017 winter. *Atmos. Environ.* 199 (15), 284–298. doi:10.1016/j.atmosenv.2018.11.042

Liu, C., Hua, C., Zhang, H. D., Zhang, B. H., Wang, G., Zhu, W. H., et al. (2019). A severe fog-haze episode in Beijing-Tianjin-Hebei region: Characteristics, sources and impacts of boundary layer structure. *Atmos. Pollut. Res.* 10 (4), 1190–1202. doi:10.1016/j.apr.2019.02.002

Liu, H., and Chen, C. (2019). Prediction of outdoor $PM_{2.5}$ concentrations based on a three-stage hybrid neural network model. *Atmos. Pollut. Res.* 11 (3), 469–481. doi:10.1016/j.apr.2019.11.019

Liu, H., Long, Z. H., Duan, Z., and Shi, H. P. (2020). A new model using multiple feature clustering and neural networks for forecasting hourly $PM_{2.5}$ concentrations, and its applications in China. *Engineering* 6 (8), 944–956. doi:10.1016/j.eng.2020.05.009

Liu, T., Lau, A. K. H., Sandbrink, K., and Fung, J. C. H. (2018). Time series forecasting of air quality based on regional numerical modeling in Hong Kong. *J. Geophys. Res. Atmos.* 123, 4175–4196. doi:10.1002/2017jd028052

Liu, Z. J., Szpiro, A. A., Workalemahu, T., Young, M. T., Kaufman, J. D., and Enquobahrie, D. A. (2022). Associations of perinatal exposure to $PM_{2.5}$ with gestational weight gain and offspring birth weight. *Environ. Res.* 204, 112087. doi:10.1016/j.envres.2021.112087

Liu, Z. Y., Qi, Z. L., Ni, X. F., Dong, M. T., Ma, M. Y., Xue, W. B., et al. (2021). How to apply O3 and PM2.5 collaborative control to practical management in China: A study based on meta-analysis and machine learning. *Sci. Total Environ.* 772, 145392. doi:10.1016/j.scitotenv.2021.145392

Menares, C., Perez, P., Parraguez, S., and Fleming, Z. L. (2021). Forecasting $PM_{2.5}$ levels in Santiago de Chile using deep learning neural networks. *Urban Clim.* 38, 100906. doi:10.1016/j.uclim.2021.100906

Nishimura, M., and Yamaguchi, M. (2015). Selective ensemble mean technique for tropical cyclone track forecasts using multi-model ensembles. *Trop. Cyclone Res. Rev.* 4 (2), 71–78.

Pak, U., Ma, J., Ryu, U., Ryom, K., Juhyok, U., Pak, K., et al. (2020). Deep learning-based $PM_{2.5}$ prediction considering the spatiotemporal correlations: A case study of beijing, China. *Sci. Total Environ.* 699 (10), 133561. doi:10.1016/j.scitotenv.2019.07.367

Sagar, S. K., Rajeevan, M., Rao, S. V. B., and Mitra, A. K. (2017). Prediction skill of rainstorm events over India in the TIGGE weather prediction models. *Atmos. Res.* 198 (1), 194–204. doi:10.1016/j.atmosres.2017.08.017

Samal, K. K. R., Panda, A. K., Babu, K. S., and Das, S. K. (2021). Multi-output TCN autoencoder for long-term pollution forecasting for multiple sites. *Urban Clim.* 39, 100943. doi:10.1016/j.uclim.2021.100943

Sawlani, R., Agnihotri, R., and Sharma, C. (2021). Chemical and isotopic characteristics of $PM_{2.5}$ over New Delhi from September 2014 to May 2015: Evidences for synergy between air-pollution and meteorological changes. *Sci. Total Environ.* 763, 142966. doi:10.1016/j.scitotenv.2020.142966

Schauwecker, S., Schwarb, M., Rohrer, M., and Stoffel, M. (2021). Heavy precipitation forecasts over Switzerland – an evaluation of bias-corrected ECMWF predictions. *Weather Clim. Extrem.* 34, 100372. doi:10.1016/j.wace.2021.100372

Schumacher, R. S. (2011). Ensemble-based analysis of factors leading to the development of a multiday warm-season heavy rain event. *Mon. Weather Rev.* 139 (9), 3016–3035. doi:10.1175/mwr-d-10-05022.1

Tao, Y. M., Duan, Q. Y., Ye, A. Z., Gong, W., Di, Z. H., Xiao, M., et al. (2014). An evaluation of post-processed TIGGE multimodel ensemble precipitation forecast in the Huai river basin. *J. Hydrology* 519, 2890–2905. doi:10.1016/j.jhydrol.2014.04.040

Tao, Y. W., Dai, K., and Dong, Q. (2017). Extreme analysis and ensemble prediction verification on cold wave process in January 2016. *Meteorol. Mon.* 43 (10), 1176–1185. (in Chinese). doi:10.7519/j.issn.1000-0526.2017.10.002

Tong, D., Geng, G. N., Jiang, K. J., Cheng, J., Zheng, Y. X., Hong, C. P., et al. (2019). Energy and emission pathways towards $PM_{2.5}$ air quality attainment in the Beijing-Tianjin-Hebei region by 2030. *Sci. Total Environ.* 692, 361–370. doi:10.1016/j.scitotenv.2019.07.218

Verkade, J. S., Brown, J. D., Reggiani, P., and Weerts, A. H. (2013). Post-processing ECMWF precipitation and temperature ensemble reforecasts for operational hydrologic forecasting at various spatial scales. *J. Hydrology* 501 (25), 73–91. doi:10.1016/j.jhydrol.2013.07.039

Wang, P. F., and Huang, G. (2006). A study on the dependency of maximum prediction time on computation precision and time step size in numerical model. *Clim. Environ. Res.* 11 (3), 395–403. (in Chinese). doi:10.3878/j.issn.1006-9585.2006.03.17

Wang, P., Zhang, H., Qin, Z. D., and Zhang, G. S. (2017). A novel hybrid-Garch model based on ARIMA and SVM for $PM_{2.5}$ concentrations forecasting. *Atmos. Pollut. Res.* 8 (5), 850–860. doi:10.1016/j.apr.2017.01.003

Whan, K., Zscheischler, J., Jordan, A. I., and Ziegel, J. F. (2021). Novel multivariate quantile mapping methods for ensemble post-processing of medium-range forecasts. *Weather Clim. Extrem.* 32, 100310. doi:10.1016/j.wace.2021.100310

Wu, H. P., Liu, H., and Duan, Z. (2020). $PM_{2.5}$ concentrations forecasting using a new multi-objective feature selection and ensemble framework. *Atmos. Pollut. Res.* 11 (7), 1187–1198. doi:10.1016/j.apr.2020.04.013

Yang, J., Yan, R., Nong, M. Y., Liao, J. Q., Li, F. P., and Sun, W. (2021). $PM_{2.5}$ concentrations forecasting in Beijing through deep learning with different inputs, model structures and forecast time. *Atmos. Pollut. Res.* 12 (9), 101168. doi:10.1016/j.apr.2021.101168

Yang, T. H., Yang, S. C., Ho, J. Y., Lin, G. F., Hwang, G. D., and Lee, C. S. (2015). Flash flood warnings using the ensemble precipitation forecasting technique: A case study on forecasting floods in taiwan caused by typhoons. *J. Hydrology* 520, 367–378. doi:10.1016/j.jhydrol.2014.11.028

Yu, H. Z., and Meng, Z. Y. (2016). Key synoptic-scale features influencing the high-impact heavy rainfall in Beijing, China, on 21 July 2012. *Tellus A Dyn. Meteorology Oceanogr.* 68, 31045. doi:10.3402/tellusa.v68.31045

Yuval, Broday, D. M., and Alpert, P. (2012). Exploring the applicability of future air quality predictions based on synoptic system forecasts. *Environ. Pollut.* 166, 65–74. doi:10.1016/j.envpol.2012.03.010

Zhai, B. X., and Chen, J. G. (2018). Development of a stacked ensemble model for forecasting and analyzing daily average $PM_{2.5}$ concentrations in Beijing, China. *Sci. Total Environ.* 635, 644–658. doi:10.1016/j.scitotenv.2018.04.040

Zhang, H., Xie, B., Zhao, S. Y., and Chen, Q. (2014). $PM_{2.5}$ and tropospheric O_3 in China and an analysis of the impact of pollutant emission control. *Adv. Clim. Change Res.* 5 (3), 136–141. doi:10.1016/j.accre.2014.11.005

Zhang, Q. Q., Ma, Q., Zhao, B., Liu, X. Y., Wang, X. Y., Jia, B. X., et al. (2018). Winter haze over north China plain from 2009 to 2016: Influence of emission and meteorology. *Environ. Pollut.* 242, 1308–1318. Part B. doi:10.1016/j.envpol.2018.08.019

Zhang, W. H., Hai, S. F., Zhao, Y. H., Sheng, L. F., Zhou, Y., Wang, W. C., et al. (2021). Numerical modeling of regional transport of $PM_{2.5}$ during a severe pollution event in the Beijing–Tianjin–Hebei region in November 2015. *Atmos. Environ.* 254, 118393. doi:10.1016/j.atmosenv.2021.118393

Zhao, G. J., He, N., Hao, C., Li, J., and Li, S. (2021). Evaluation of models and objective methods for temperature in Beijing area. *Meteorological Sci. Technol.* 49 (6), 870–877. (in Chinese). doi:10.19517/j.1671-6345.20200409

Zhao, J. F., Xu, J. W., Xie, X. M., and Lu, H. Q. (2016). Drought monitoring based on TIGGE and distributed hydrological model in Huaihe River Basin, China. *Sci. Total Environ.* 553 (15), 358–365. doi:10.1016/j.scitotenv.2016.02.115

Zhao, P. C., Wang, Q. J., Wu, W. Y., and Yang, Q. C. (2022). Extending a joint probability modelling approach for post-processing ensemble precipitation forecasts from numerical weather prediction models. *J. Hydrology* 605, 127285. doi:10.1016/j.jhydrol.2021.127285

Zhou, Y. L., Chang, F. J., Chang, L. C., Kao, I. F., Wang, Y. S., and Kang, C. C. (2019). Multi-output support vector machine for regional multi-step-ahead $PM_{2.5}$ forecasting. *Sci. Total Environ.* 651 (1), 230–240. doi:10.1016/j.scitotenv.2018.09.111

Zhou, Y. L., Chang, F. J., Chen, H., and Li, H. (2020). Exploring copula-based bayesian model averaging with multiple ANNs for $PM_{2.5}$ ensemble forecasts. *J. Clean. Prod.* 263 (1), 121528. doi:10.1016/j.jclepro.2020.121528

frontiers | Frontiers in Earth Science

TYPE Original Research
PUBLISHED 18 April 2023
DOI 10.3389/feart.2023.1051546

OPEN ACCESS

EDITED BY
Lingling Shen,
Beijing Meteorological Information Center, China

REVIEWED BY
Guy Jean-Pierre Schumann,
University of Bristol, United Kingdom
Hossein Hamidifar,
Shiraz University, Iran

*CORRESPONDENCE
Ayat Al Assi,
aalass1@lsu.edu

RECEIVED 22 September 2022
ACCEPTED 03 April 2023
PUBLISHED 18 April 2023

CITATION
Al Assi A, Mostafiz RB, Friedland CJ, Rohli RV and Rahim MA (2023), Homeowner flood risk and risk reduction from home elevation between the limits of the 100- and 500-year floodplains. *Front. Earth Sci.* 11:1051546. doi: 10.3389/feart.2023.1051546

Homeowner flood risk and risk reduction from home elevation between the limits of the 100- and 500-year floodplains

Ayat Al Assi[1,2,3]*, Rubayet Bin Mostafiz[2,3,4], Carol J. Friedland[2,3], Robert V. Rohli[3,4] and Md Adilur Rahim[2,3,5]

[1]Bert S. Turner Department of Construction Management, Louisiana State University, Baton Rouge, LA, United States, [2]LaHouse Resource Center, Department of Biological and Agricultural Engineering, Louisiana State University Agricultural Center, Baton Rouge, LA, United States, [3]Coastal Studies Institute, Louisiana State University, Baton Rouge, LA, United States, [4]Department of Oceanography & Coastal Sciences, College of the Coast & Environment, Louisiana State University, Baton Rouge, LA, United States, [5]Engineering Science Program, Louisiana State University, Baton Rouge, LA, United States

Floods inflict significant damage even outside the 100-year floodplain. Thus, restricting flood risk analysis to the 100-year floodplain (Special Flood Hazard Area (SFHA) in the United States of America) is misleading. Flood risk outside the SFHA is often underestimated because of minimal flood-related insurance requirements and regulations and sparse flood depth data. This study proposes a systematic approach to predict flood risk for a single-family home using average annual loss (AAL) in the shaded X Zone—the area immediately outside the SFHA (i.e., the 500-year floodplain), which lies between the limits of the 1.0- and 0.2-percent annual flood probability. To further inform flood mitigation strategy, annual flood risk reduction with additional elevation above an initial first-floor height (FFH_0) is estimated. The proposed approach generates synthetic flood parameters, quantifies AAL for a hypothetical slab-on–grade, single-family home with varying attributes and scenarios above the slab-on-grade elevation, and compares flood risk for two areas using the synthetic flood parameters vs existing spatial interpolation-estimated flood parameters. Results reveal a median AAL in the shaded X Zone of 0.13 and 0.17 percent of replacement cost value (V_R) for a one-story, single-family home without and with basement, respectively, at FFH_0 and 500-year flood depth <1 foot. Elevating homes one and four feet above FFH_0 substantially mitigates this risk, generating savings of 0.07–0.18 and 0.09–0.23 percent of V_R for a one-story, single-family home without and with basement, respectively. These results enhance understanding of flood risk and the benefits of elevating homes above FFH_0 in the shaded X Zone.

KEYWORDS

flood risk, average annual loss (AAL), flood mitigation strategy, special flood hazard area (SFHA), shaded X Zone

1 Introduction

Flood is considered the costliest natural hazard worldwide (Wang & Sebastian, 2021). Between 1980 and 2021, the United States of America was affected by 36 catastrophic floods that caused a total $173.3 billion (consumer price index adjusted) in direct losses (NOAA, 2022). FEMA's floodplain maps are used to determine flood risk zones and their base flood

elevations (BFEs), which have been used to define flood risk regions around the United States of America (Xian et al., 2015). FEMA's 100-year floodplain–the area that has at least a one-percent chance of experiencing flood in a given year–has been used to define high-risk flood zones, known as the Special Flood Hazard Area (SFHA). Many efforts have been made to quantify flood risk (Habete & Ferreira, 2017; Armal et al., 2020; Mostafiz et al., 2021a), determine minimum first-floor elevation requirements (American Society of Civil Engineers (ASCE), 2014; FEMA, 2019) and identify the benefit of applying mitigation strategies in the SFHA (Rath et al., 2018), including regulations on development such as the mandatory purchase of flood insurance for those with a federally-backed mortgage (Wing et al., 2022).

Areas outside the SFHA, generally known in the United States of America as X Zones, have received significantly less attention because they have been considered as moderate-to-low flood risk areas, with less than a one-percent annual chance of flood occurrence (Technical Mapping Advisory Council, 2015). However, average annual flood losses outside the SFHA have mounted to $19.1 billion and are projected to increase by 21.2 percent in the United States of America by 2050 because of climate change (Wing et al., 2022). Thus, significantly more attention must be devoted to understanding flood risk in these areas in order to reduce flood losses.

The area between the limits of the one-percent (bordering the SFHA) and 0.2-percent (bordering the "non-shaded X Zone") annual flood probability inundation areas—the 500-year floodplain, known in the United States of America as the "shaded X Zone"—is particularly preferred for dense development and is considered an area of likely population growth (Association of State Floodplain Managers, 2020). Clearly, it is important to assess the flood risk outside the SFHA, particularly in the shaded X Zone. Notable examples of research on flood hazards in the shaded X Zone include that of Hagen and Bacopoulos (2012), who identified tropical storm characteristics that induce flooding in Florida's Big Bend Region. Likewise, Ferguson and Ashley (2017) evaluated residential development in Atlanta, Georgia. Kiaghadi et al. (2020) investigated the relation between hurricane events and the housing price depreciation in Miami-Dade County. Goldberg and Watkins (2021) analyzed flood risk among three watersheds in the lower St. Johns River basin landscape, and Hemmati et al. (2021) examined how flood risk assessment affects residents' location choices. However, there is a dearth of research focusing on flood risk evaluation for residential buildings in the shaded X Zone. Without a better understanding of flood risk for areas in the shaded X Zone, the true costs and benefits of flood mitigation strategies cannot be realized (Mostafiz et al., 2022c).

Flood risk is assessed as the product of flood occurrence probability and the associated consequences (Šugareková & Zeleňáková, 2021). Average annual loss (AAL) has been used in past research to represent flood risk (Hallegatte et al., 2013; Armal et al., 2020; Rahim et al., 2021; 2022; Mostafiz et al., 2022a; Bowers et al., 2022; Wing et al., 2022; Yildirim & Demir, 2022; Al Assi et al., 2023b; Friedland et al., 2023) in terms of costs associated with direct building loss, direct contents loss, and indirect losses such as use loss while the building is being renovated (Al Assi et al., 2023a). AAL is calculated as the integral of flood loss as a known function of the flood probability (or flood return period), and the Gumbel distribution function is one of the most widely accepted probability functions (Singh et al., 2018; Patel, 2020). The Gumbel parameters are the regression coefficients (slope and y-intercept, respectively) in the relationship between flood depth above the ground (d) and the double natural logarithm of probability of non-exceedance probability (P) (Gnan et al., 2022a; 2022b).

Calculating flood risk in the shaded X Zone can be challenging due to data limitations. As the shaded X Zone lies between the limits of the one-percent and 0.2-percent annual chance of flood, land in this zone is by definition unflooded until the 100-year flood event is exceeded. Therefore, in the shaded X Zone, d is zero or null (i.e., d would be negative and is therefore undefined) for flood events with return periods less than 100 years. Given that return period depth grids typically include the 10-, 50-, 100-, and 500-year events, all locations within the shaded X Zone have a d value that is therefore zero or "null" for return periods shorter than the 500-year event. Thus, locations within the shaded X Zone have a d value for only one return period (i.e., 500 years), with the consequence that the Gumbel flood parameters cannot be generated from the Gumbel distribution for any location within the shaded X Zone. Without the Gumbel parameters, annual flood risk (or even the probable range of annual flood risk) cannot be estimated in the shaded X Zone. Further, although flood loss has been often observed in the shaded X Zone, risk reduction from elevation cannot be estimated due to the lack of flood risk estimates. Therefore, comparison of benefits and costs to support mitigation decision making in the shaded X Zone is not possible.

To overcome these challenges, this paper presents a systematic approach to 1) provide a meaningful estimate of the range of expected annual flood risk in the shaded X Zone; and 2) calculate the reduction in annual flood risk via elevation for homes in the shaded X Zone. The lack of flood hazard data in the shaded X Zone is addressed by developing a library of combinations of synthetic, regression-derived Gumbel parameters that meet the mathematical definition of the shaded X Zone. These are used here by hypothetical type of single-family homes in the United States of America (i.e., one vs two-plus stories, with vs without basement) as input to the framework methodology presented in Al Assi et al. (2023a). The results of two case studies are compared with the results generated from the Gumbel regression parameters produced using Mostafiz et al.'s (2021b, 2022b) method, which extrapolated the Gumbel parameters in the shaded X Zone using spatial interpolation, to confirm the results of this method for a range of 500-year flood depths in inland and coastal areas.

The contribution of this research is a novel conceptualization and implementation of annual flood risk assessment in the shaded X Zone–a location where little flood risk information has been generated. This improved risk assessment provides a clearer perception of the advantages of applying mitigation strategies in those areas. The methodology and results generated in this paper will benefit homeowners, builders, developers, community planners, and other partners in the process of enhancing resilience to the flood hazard via risk-informed construction techniques.

2 Background

Recent catastrophic events and studies regarding projected trends under environmental change scenarios reveal that the area

outside the presently designated SFHA is subjected to rapidly increasing flood risk. For example, in 2005 Hurricane Katrina inflicted severe damage outside the SFHA across Louisiana, Mississippi, and Alabama, including massive structural damage (Xian et al., 2015). Likewise, only 7 years later Hurricane Sandy caused flooding far above the BFE and beyond the SFHA in New York and New Jersey (FEMA, 2013). Only 5 years later, amazingly, 68 percent of the 31,000 homes that Hurricane Harvey flooded in the Houston, Texas, area were outside the SFHA (Kousky et al., 2020b). In the next year, 24 percent of the area flooded and 43 percent of the residential structures damaged in North Carolina by Hurricane Florence were outside the SFHA (Pricope et al., 2022). And in 2019, 62 percent of the 1,000+ Texas homes flooded in Tropical Storm Imelda were outside the SFHA (Kousky et al., 2020b). Kennedy et al. (2020) reported that Hurricane Michael in Florida caused major wave and surge damage in X Zones. In a more general sense, a trained model to predict flood damage probability in the conterminous United States of America using a suite of geospatial predictors and the location of historical reported flood damage revealed that an astounding 68 percent of flood damage was outside of FEMA's high-risk zone (Collins et al., 2022). Significant attention has been devoted to reducing flood damage exacerbated by climate change and sea level rise (Botzen & van den Bergh, 2008; Hino & Hall, 2017; Kousky et al., 2020a; Xian et al., 2017). Therefore, a need exists to evaluate flood risk in the shaded X Zone more comprehensively through improved assessment of economic consequences to better identify and mitigate the risk.

Recent studies show that using the refined numerical integration method shows promising results to predict AAL because it accounts for losses across the full range of exceedance probabilities, and it addresses the limitations of other approaches (Gnan et al., 2022a). This refined numerical integration method models the annual probability of exceedance for the expected flood depth using available flood depth data. The Gumbel distribution is used to determine the annual probability of exceedance at each given depth. AAL is then estimated using trapezoidal Riemann sums to aggregate the area under the loss-exceedance probability curve (Meyer et al., 2009; Gnan et al., 2022a).

Specifically, the refined numerical integration method has been used to estimate annual flood risk for multiple home elevation scenarios above the initial first-floor height to determine flood risk reduction (Gnan et al., 2022a). Optimizing the effectiveness of the elevation strategy using such scenarios is important for maximizing the benefit of federal government grants, such as from FEMA or the U.S. Department of Housing and Urban Development (HUD), for elevating such homes, to as many people as possible. These elevation scenarios conform to or surpass the National Flood Insurance Program (NFIP) requirement that the minimum lowest-floor elevation is at the BFE, which is approximately equal to the 100-year flood elevation (E_{100}) (FEMA, 2019). However, because ASCE (2014) national technical standard stipulates that adding one foot above E_{100} as the minimum recommended elevation requirement for residential buildings in the United States of America, higher elevation scenarios must also be considered in assessing flood risk and risk reduction.

Elevating above FFH_0 is often cost-effective (Taghinezhad et al., 2021), especially at the time of construction (Rath et al., 2018). It is already well-established that increasing first-floor heights in A and V Zones (i.e., inundation and high-velocity zones within the SFHA, respectively in the United States of America) at the time of construction is wise, with costs recoverable in as few as 6 and 3 years, respectively, through insurance premium reduction (Rath et al., 2018). The value of implementing a "smart" flood risk mitigation strategy (Taghinezhad et al., 2020) applies equally to homes in the shaded X Zone, especially now that it is becoming apparent that these homes are not as flood safe as was recently assumed, by using the refined numerical integration technique. Flood risk reduction in dollars, represented as the difference between the AAL before and after applying the mitigation strategy, can be promulgated as a means of increasing awareness for homeowners and communities in the shaded X Zone regarding the flood risk and the importance of considering the mitigation strategies to decrease that risk.

3 Methodology

The computational framework to quantify AAL in the shaded X Zone consists of three major steps (Figure 1). First, synthetic flood parameters are generated based on shaded X Zone properties. Second, AAL is quantified using the computational framework developed by Al Assi et al. (2023a). In that approach, AAL is partitioned to homes (I = 1 through n) separately for building, contents, and use, with the AAL reduction calculated for M increases of increment J in first-floor height above the FFH_0 (Al Assi et al., 2023a). Third, the results are confirmed using two separate areas by comparing the AAL computed from synthetic data in this framework against that calculated using the flood parameters generated through the Mostafiz et al. (2021b) method.

3.1 Generate synthetic flood parameters

This research uses the two-parameter Gumbel distribution function to estimate flood depth. Equation (1) shows the cumulative distribution function (CDF) of the Gumbel distribution, which represents the annual non-exceedance probability (p).

$$F(d) = p(X \le d) = exp\left[-exp\left(-\left(\frac{d-u}{a}\right)\right)\right] \tag{1}$$

Solving Eq. (1) for d yields:

$$d = u - a\ln\left[-\ln(p)\right] \tag{2}$$

In Eqs (1), (2), d is flood depth, u represents the location parameter or y-intercept of the Gumbel-generated regression line (noting that Eq. (2) takes the form $y = b + mx$ where x is $-\ln\left[-\ln(p)\right]$; m is a,; b is u) of d as a function of the double natural logarithm of p, and a is the scale parameter or slope of the same Gumbel-generated regression line. p is expressed as a function of flood return period (T) by:

$$p = 1 - \frac{1}{T} \tag{3}$$

To overcome the absence of u and a values in shaded X Zone, synthetic values of u and a are generated to estimate the range of these parameters expected in the shaded X Zone.

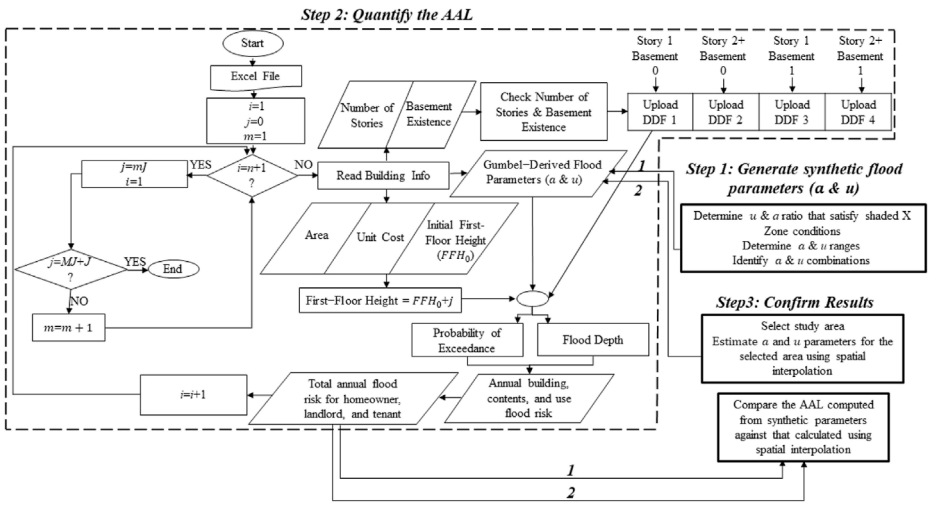

FIGURE 1
Computational framework to quantify and confirm AAL in the shaded X Zone.

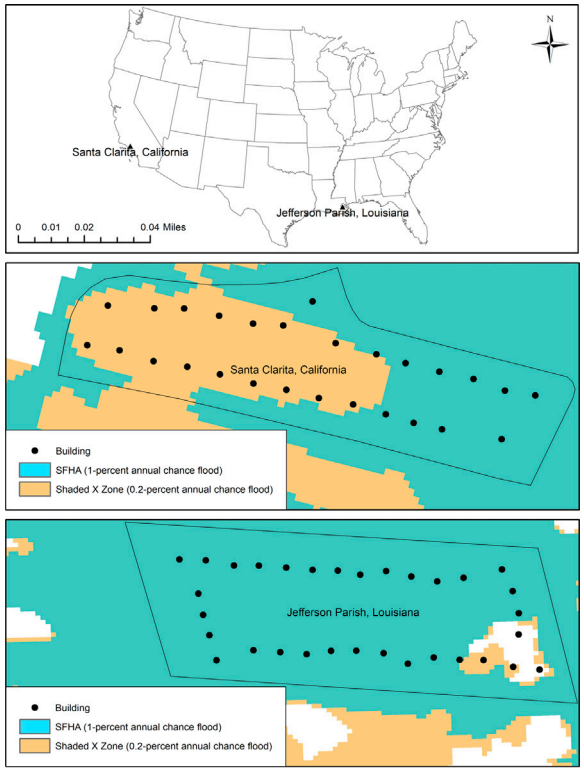

FIGURE 2
Case study areas in Santa Clarita, California, and Jefferson Parish, Louisiana, highlighting the homes situated in the Special Flood Hazard Area (SFHA) and shaded X Zone.

Generating the synthetic, unique u and a for the shaded X Zone begins with substituting for p from Eq. (3) into Eq. (2), for the 100 (i.e., T)-year return period, for which d is assumed to be less than or equal to zero in the shaded X Zone, as shown in Eq. (4):

$$0 \geq u - a \ln\left[-\ln\left(1 - \frac{1}{100}\right)\right] \tag{4}$$

Likewise, if it is assumed that a point within the shaded X Zone does flood within the 500 (i.e., T)-year flood, the generalized Eq. (2) can be expressed for this specific scenario as:

$$0 < u - a \ln\left[-\ln\left(1 - \frac{1}{500}\right)\right] \tag{5}$$

Solving Eqs (4)–(5) yields the ratio between u and a in the shaded X Zone:

$$-6.214 < \frac{u}{a} \leq -4.600 \tag{6}$$

Thus, the range of the ratio of u to a in the shaded X Zone is known, but the range of u and the range of a remain unknown. By definition, a (i.e., the slope of the Gumbel-generated regression) must be positive because longer-return-period flood events always have higher d than shorter-return-period d. The upper limit of a is assumed to occur in coastal areas. Therefore, this study updates d values from flood events in Bohn's (2013) data set that expresses stillwater elevation at 10-, 50-, 100-, and 500-year return periods for 13 counties along the Gulf and Atlantic coasts (Supplementary Table S1). This data set is then used to identify the upper limit of a (Supplementary Table S2).

Because a is positive, by Eq. (6), u must be negative. A negative u meets expectations, as this value represents the y-intercept of the Gumbel-generated regression, with an equivalent return period of 1.58 years. The maximum allowable value of u is therefore determined, subject to the restraints of Eq. (6).

Each combination of u and a values within the acceptable range of each variable, as described above, at increments of 0.1 feet for each, is initially considered as potentially acceptable values to describe the d vs return period relationship. Those simultaneous combinations that have a u vs a ratio that falls outside the range of acceptability (Eq. (6)) are discarded. The

TABLE 1 Descriptive statistics for synthetic flood parameters in the shaded X Zone.

Flood parameter	Minimum	25th	50th	75th	Maximum
u	− 28.58	− 21.58	− 17.58	− 12.48	− 0.48
a	0.10	2.30	3.30	4.00	4.60

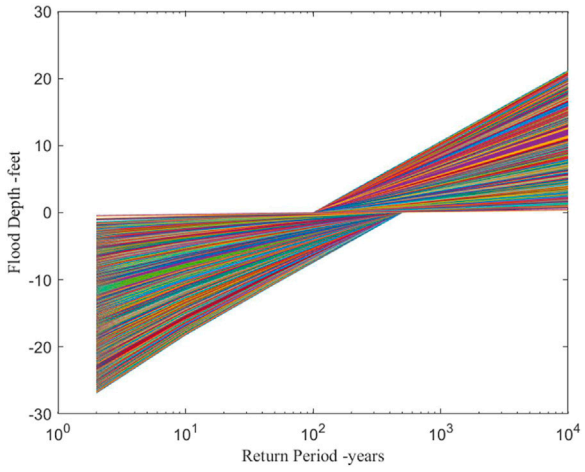

FIGURE 3
Flood depth-return period relationship for synthetic data.

remaining combinations of u and a are used to calculate d, with the result considered potentially acceptable for inclusion, as described in the next section.

Each combination of u and a that is derived and potentially acceptable is used to determine possible d values at the 2-, 10-, 50-, 100-, 500-,1,000-, 5,000-, and 10,000-year return periods (Eq. (2)), noting that d values for the 100-year and shorter return periods are negative or zero. A plot of d vs the double natural logarithm of return period based on these calculations is then used to confirm the assumption that d is less than or equal to zero for the 100-year and more than zero for the 500-year flood events, in addition to visualizing d at longer return periods (i.e., 500-, and 1,000- year).

3.2 Quantify annual flood risk and flood risk reduction

3.2.1 Refined numerical integration method

AAL represents the sum of the expected annual flood risk to a building (AAL_B), its contents (AAL_C), and its loss of use while unoccupied due to flood (AAL_U). While AAL_B, AAL_C, and AAL_U likely differ based on owner-occupant category (i.e., homeowner, landlord, tenant), this study considers only AAL from the perspective of a homeowner.

The method of Gnan et al. (2022a, 2022b, 2022c) is used to calculate AAL_B and AAL_C as a proportion of home replacement cost value (V_R) by integrating the flood loss over all probabilities of exceedance, as shown in Eqs. (7)–(8):

$$AAL_{B/V_R} = \int_{P_{min}}^{P_{max}} L_B(P)dP \tag{7}$$

$$AAL_{C/V_R} = \int_{P_{min}}^{P_{max}} L_C(P)dP \tag{8}$$

where L_B and L_C represent the building and contents losses as a proportion of V_R, which is the unit replacement cost per square foot (C_R) multiplied by the home area (A):

$$V_R = A \times C_R \tag{9}$$

By contrast, AAL_U is calculated from the number of months that the building is inoperable, as shown in Eq. (10):

$$AAL_{U\ (\text{months})} = \int_{P_{min}}^{P_{max}} L_U(P)dP \tag{10}$$

where L_U represents the use loss in months.

Then, the three components of AAL are converted to absolute currency values (in USD) for building (AAL_B), contents (AAL_C), and use (AAL_U), as described by Eqs (11)–(13):

$$AAL_{B\$} = AAL_{B/V_R} \times V_R \tag{11}$$

$$AAL_{C\$} = AAL_{C/V_R} \times V_R \tag{12}$$

$$AAL_{U\$} = AAL_{U(\text{months})} \times R_I \tag{13}$$

where R_I is the monthly rent incurred by the homeowner, calculated by assuming that 1 year of rent is equal to one-seventh of V_R (Amoroso & Fennell, 2008; Eq. (14)).

$$R_I = \frac{V_R}{84\,month} \tag{14}$$

These values are then summed to give the total AAL as a proportion of V_R (AAL_{T/V_R}) as shown in Eqs (15–16):

$$AAL_{T/V_R} = \left(AAL_{B/V_R} + AAL_{C/V_R} + \frac{AAAL_U}{84}\right) \tag{15}$$

$$AAL_{T\$} = AAL_{T/V_R} \times V_R \tag{16}$$

To quantify the economic benefit of elevating above FFH_0, AAL is calculated with and without elevation, to reveal the annual flood risk reduction, as generally expressed by Eq. (17):

$$\Delta AAL = AAL_{FFH_0} - AAL_{FFH} \tag{17}$$

3.2.2 Data processing

The MATLAB algorithm developed by Al Assi et al. (2023a) is utilized here to analyze all simultaneously valid u and a combinations; these combinations remain constant by home type (i.e., one or two-or-more stories, with and without basement). The input data include number of stories (1 or 2+), basement existence (0 = No, 1 = Yes), living area in square feet (A), unit cost per square

TABLE 2 Descriptive statistics of flood depth at long return periods using synthetic data in the shaded X Zone.

Return period	Minimum (feet)	25th (feet)	50th (feet)	75th (feet)	Maximum (feet)
500-year	0.003	1.003	2.196	3.749	7.400
1,000-year	0.110	2.942	4.387	6.236	10.593
5,000-year	0.272	6.986	9.879	12.376	17.999
10,000-year	0.341	8.654	12.224	15.093	21.187

footage (C_R, in USD/sf), FFH_0, and flood parameters (u; a). United States Army Corps of Engineers (USACE, 2000) depth damage functions (DDFs) are incorporated by home type (i.e., number of stories and basement existence). The AAL reduction is calculated for each additional elevation J through MJ feet (Figure 1) above FFH_0.

3.3 Confirm results

Spatial interpolation is used to characterize the flood hazard (u; a) in the shaded X Zone (Mostafiz et al., 2021b; 2022b) for a known location where multiple return period flood depth data are available. The flood parameters (u; a) are used to calculate annual flood risk by using Eq. (2) and (7)–(17) and confirming the result produced from the synthetic data.

4 Case study

Jefferson Parish, Louisiana, and Santa Clarita, California, are selected as these areas have multiple return period (10–, 50–, 100–, and 500–years) flood depth data, which are needed to estimate flood parameters using spatial interpolation (Figure 2). Flood depth grids were developed at a scale of 3.048 m x 3.048 m, by FEMA through its Risk Mapping, Assessment and Planning (Risk MAP) program (FEMA, 2021). To demonstrate all possible scenarios for synthetic and estimated flood parameters to quantify annual flood risk and flood risk reduction in the shaded X Zone, a hypothetical slab-on-grade, single-family home with 2000 sq. ft. of living area is used, with the four scenarios of home type (i.e., one or two-or-more stories, with and without basement) calculated separately. Each combination in the collection of synthetic and estimated Gumbel parameters is input to evaluate the range of annual flood risk for each home type. C_R is assumed to be $135 according to the projected 2022 average construction cost of single-family homes in the United States of America (Doheny, 2021), and FFH_0 is assumed to be 0.5 feet above the ground for slab-on grade foundations. This assumption is made because there is no regulatory BFE in the shaded X Zone and it is assumed that most homes are built on non-elevated slab foundations. The flood damage initiation point in the DDF is assigned at a fixed flood depth of zero in the structure, as suggested by Pistrika et al. (2014). Annual flood risk for homes with basements is calculated in the same way; thus, it is assumed that the basement is not flooded until water is above the FFH. The annual flood risk reduction is calculated for each additional first-floor height of 1–4 feet above FFH_0.

5 Results

5.1 Generate synthetic flood parameters

The ratio of flood parameters (Eq. (6)) along with the updated stillwater elevation for coastal data are used to determine the flood parameters' range and combinations that satisfy shaded X Zone properties. The analysis updating the results of Bohn (2013) suggests that the maximum a is 4.60 (Eq. (18)). Thus, the range of u, subject to the constraints of Eq. (6), is shown in Eq. (19).

$$0 < a \leq 4.60 \tag{18}$$

$$-28.58 \leq u < 0 \tag{19}$$

A total of 1740 combinations of u and a satisfies the flood parameter ratio for the shaded X Zone (Eq. (6)). Table 1 shows the descriptive statistics for u and a values resulting from all possible combinations. Because the dataset is very large and is not normally distributed, percentiles are provided along with the minimum and maximum values. Possible values of u and a fall between – 28.58 and – 0.48 feet and between 0.10 and 4.60, respectively.

The flood depth-return period relationships generated at the 2-, 10-, 50-, 100-, 500-, 1,000-, 5,000- and 10,000-year return periods for these 1740 scenarios are shown in Figure 3. The d at return periods less than or equal to 100-year is negative or zero, and d at 500-year and longer return periods is positive, as expected. Descriptive statistics of d at the 500-, 1,000-, 5,000-, and 10,000-year return periods are shown in Table 2.

5.2 Quantify annual flood risk and flood risk reduction

For the 1740 scenarios of valid u and a combinations, annual flood risk and flood risk at additional elevations above FFH_0 are calculated as a proportion of V_R by using FFH_0 = 0.5 foot, and the corresponding DDF for each home type. The results are presented for the shaded X Zone for homes without and with basement by categories of 500-year flood depths for one- and two-plus-story homes (Table 3; Table 4, respectively), and by categories of a for one- and two-plus-story homes (Table 5; Table 6, respectively). The annual flood risk reduction is considered as the mean avoided AAL, calculated at each additional increment above FFH_0 for

TABLE 3 Descriptive statistics of annual flood risk as a proportion of V_R (i.e., AAL_{T/V_R}) for slab-on-grade one-story single-family home with and without basement using synthetic data, categorized based on 500-year flood depth.

500-year Flood Depth (feet)	FFH (feet)	Total average annual loss as a proportion of V_R (i.e., AAL_{T/V_R}) x10^{-4}									
		One Story without Basement					One Story with Basement				
		Min	25th	50th	75th	Max	Min	25th	50th	75th	Max
<1	FFH_0	0.82	10.68	13.31	15.08	18.17	1.40	14.59	17.20	19.15	27.55
	FFH_0 +1	0.00	5.19	8.56	11.24	14.55	0.00	7.17	11.16	13.84	17.36
	FFH_0 +2	0.00	2.53	5.78	8.50	11.65	0.00	3.58	7.43	10.46	13.90
	FFH_0 +3	0.00	1.26	3.87	6.39	9.37	0.00	1.74	4.98	7.87	11.15
	FFH_0 +4	0.00	0.62	2.59	4.84	7.54	0.00	0.86	3.31	5.96	8.97
1–2	FFH_0	14.97	18.17	19.84	21.65	31.96	20.27	22.88	25.16	27.40	45.40
	FFH_0 +1	4.64	11.50	13.70	15.28	18.17	7.17	15.20	17.47	19.12	21.68
	FFH_0 +2	1.11	6.84	9.48	11.58	14.55	1.72	9.16	12.04	14.16	17.40
	FFH_0 +3	0.27	3.95	6.58	8.83	11.65	0.41	5.35	8.37	10.79	13.90
	FFH_0 +4	0.06	2.30	4.64	6.77	9.37	0.10	3.08	5.88	8.27	11.15
2–3	FFH_0	22.68	24.97	27.30	29.88	41.31	27.16	30.89	33.84	38.61	55.47
	FFH_0 +1	14.97	18.05	19.60	21.17	24.43	20.27	22.62	24.37	26.39	32.81
	FFH_0 +2	7.35	12.34	14.22	15.57	18.17	10.33	15.89	17.74	19.24	21.68
	FFH_0 +3	3.60	8.12	10.17	11.91	14.55	5.06	10.56	12.78	14.51	17.36
	FFH_0 +4	1.76	5.34	7.38	9.23	11.65	2.48	6.95	9.29	11.10	13.90
3–4	FFH_0	28.36	32.48	35.47	39.51	51.05	33.74	39.53	43.54	49.93	65.86
	FFH_0 +1	22.68	24.66	26.39	28.23	34.25	27.16	30.20	32.59	35.19	44.19
	FFH_0 +2	15.22	18.18	19.55	21.07	23.07	20.27	22.48	24.11	25.94	29.65
	FFH_0 +3	8.99	13.13	14.66	15.88	18.17	12.08	16.50	18.04	19.48	21.68
	FFH_0 +4	5.32	9.41	10.93	12.22	14.55	7.14	11.81	13.51	14.86	17.36
4–5	FFH_0	35.23	40.96	44.44	48.88	59.42	41.92	49.55	54.05	60.40	74.38
	FFH_0 +1	28.36	31.71	33.88	36.17	43.07	33.74	38.44	41.36	44.86	53.93
	FFH_0 +2	22.68	24.15	25.74	27.44	31.22	27.16	29.49	31.62	33.51	39.09
	FFH_0 +3	16.19	18.37	19.63	21.05	22.68	20.56	22.48	23.95	25.65	28.32
	FFH_0 +4	11.09	13.84	15.09	16.21	18.16	14.23	17.06	18.33	19.72	21.68
5–6	FFH_0	43.77	50.36	54.01	57.89	64.94	52.08	60.56	65.35	70.67	79.41
	FFH_0 +1	35.23	39.59	42.00	44.44	49.61	41.92	47.70	50.93	54.08	60.66
	FFH_0 +2	28.36	30.94	32.52	34.50	37.88	33.74	37.48	39.51	41.67	46.32
	FFH_0 +3	22.68	23.88	25.30	26.87	28.92	27.10	29.17	30.88	32.47	35.37
	FFH_0 +4	16.63	18.59	19.72	21.06	22.68	20.74	22.50	23.87	25.45	27.33
6–7.4	FFH_0	54.37	60.77	64.34	67.47	73.65	64.69	72.90	77.56	81.62	87.62
	FFH_0 +1	43.77	48.23	50.74	53.38	59.30	52.08	58.05	61.04	64.09	70.55
	FFH_0 +2	35.23	38.29	40.13	42.55	47.74	41.92	46.03	48.19	50.90	56.80
	FFH_0 +3	28.35	30.28	31.73	33.82	38.43	33.74	36.22	38.07	40.36	45.72
	FFH_0 +4	22.79	23.84	25.15	26.97	30.93	27.16	28.70	30.18	32.32	36.80

TABLE 4 As in **Table 3**, except for two-plus-story home.

500-year Flood Depth (feet)	FFH (feet)	Total average annual loss as a proportion of V_R (i.e., AAL_{T/V_R}) x10^{-4}									
		Two-plus-story without Basement					Two-plus-story with Basement				
		Min	25th	50th	75th	Max	Min	25th	50th	75th	Max
<1	FFH_0	0.63	7.94	9.97	11.46	14.06	1.11	12.14	14.11	15.47	21.80
	FFH_0 +1	0.00	3.84	6.44	8.58	11.26	0.00	6.10	9.10	11.34	14.22
	FFH_0 +2	0.00	1.87	4.32	6.48	9.03	0.00	3.02	6.07	8.57	11.38
	FFH_0 +3	0.00	0.93	2.89	4.87	7.26	0.00	1.49	4.06	6.46	9.16
	FFH_0 +4	0.00	0.46	1.93	3.69	5.84	0.00	0.75	2.70	4.89	7.36
1–2	FFH_0	11.08	13.73	15.01	16.40	23.61	15.88	19.06	20.69	22.20	35.60
	FFH_0 +1	3.46	8.58	10.31	11.64	14.06	5.66	12.65	14.35	15.51	17.75
	FFH_0 +2	0.83	5.06	7.12	8.82	11.26	1.36	7.62	9.83	11.70	14.22
	FFH_0 +3	0.20	2.93	4.95	6.77	9.03	0.33	4.43	6.86	8.92	11.38
	FFH_0 +4	0.05	1.71	3.47	5.17	7.26	0.08	2.68	4.82	6.82	9.15
2–3	FFH_0	17.19	18.98	20.71	22.41	30.59	22.29	25.69	27.67	31.33	43.47
	FFH_0 +1	11.08	13.63	14.86	16.12	18.10	15.88	19.00	20.20	21.58	25.71
	FFH_0 +2	5.43	9.21	10.75	11.87	14.06	8.10	13.26	14.67	15.74	17.75
	FFH_0 +3	2.66	6.07	7.68	9.10	11.26	3.97	8.88	10.55	12.01	14.22
	FFH_0 +4	1.30	3.99	5.58	7.04	9.03	1.94	5.82	7.67	9.26	11.38
3–4	FFH_0	21.99	24.80	26.93	29.84	38.12	27.69	33.11	35.99	40.78	51.91
	FFH_0 +1	17.19	18.68	20.05	21.45	25.58	22.29	25.57	27.02	28.84	34.83
	FFH_0 +2	11.28	13.77	14.87	16.06	17.56	15.94	19.08	20.13	21.28	23.37
	FFH_0 +3	6.66	9.92	11.15	12.12	14.06	9.47	13.98	15.10	16.02	17.75
	FFH_0 +4	3.94	7.08	8.35	9.41	11.26	5.60	10.00	11.26	12.39	14.22
4–5	FFH_0	27.32	31.35	33.89	36.93	44.85	34.40	41.82	45.05	49.86	59.20
	FFH_0 +1	21.99	24.33	25.87	27.53	32.51	27.69	32.86	34.67	36.96	42.92
	FFH_0 +2	17.19	18.48	19.62	20.97	23.56	22.29	25.56	26.47	27.67	31.11
	FFH_0 +3	12.15	14.02	15.03	16.12	17.56	16.28	19.48	20.33	21.25	22.54
	FFH_0 +4	8.30	10.53	11.55	12.40	14.06	11.23	14.77	15.62	16.38	17.75
5–6	FFH_0	33.94	38.82	41.44	44.17	49.57	42.74	52.07	55.12	58.75	63.95
	FFH_0 +1	27.32	30.50	32.22	34.03	37.86	34.40	41.29	43.30	45.41	48.84
	FFH_0 +2	21.99	23.80	25.05	26.42	28.91	27.69	32.81	33.85	35.03	37.30
	FFH_0 +3	17.19	18.38	19.44	20.67	22.21	22.29	25.70	26.41	27.50	28.48
	FFH_0 +4	12.58	14.30	15.20	16.23	17.56	16.54	20.12	20.76	21.41	22.20
6–7.4	FFH_0	42.17	46.99	49.60	52.07	57.12	53.09	69.62	70.37	71.14	71.91
	FFH_0 +1	33.94	37.34	39.03	41.26	45.99	42.74	56.05	56.66	57.28	57.90
	FFH_0 +2	27.32	29.48	30.88	32.80	37.02	34.40	45.12	45.62	46.11	46.62
	FFH_0 +3	21.99	23.32	24.49	26.18	29.80	27.69	36.32	36.72	37.12	37.52
	FFH_0 +4	17.45	18.40	19.41	20.81	23.99	22.29	29.23	29.56	29.87	30.20

TABLE 5 As in **Table 3** but categorized based on the a parameter.

a	FFH (feet)	Total average annual loss as a proportion of V_R (i.e., AAL_{T/V_R}) x10^{-4}									
		One Story without Basement					One Story with Basement				
		Min	25th	50th	75th	Max	Min	25th	50th	75th	Max
<1	FFH_0	0.82	5.30	8.05	12.65	25.04	1.40	8.11	12.52	19.43	37.47
	FFH_0 +1	0.00	0.77	1.84	3.29	8.26	0.00	1.27	2.83	5.03	12.36
	FFH_0 +2	0.00	0.11	0.46	0.92	2.72	0.00	0.18	0.72	1.39	4.07
	FFH_0 +3	0.00	0.02	0.11	0.26	0.90	0.00	0.02	0.17	0.40	1.34
	FFH_0 +4	0.00	0.00	0.02	0.08	0.29	0.00	0.00	0.04	0.12	0.44
1–2	FFH_0	5.87	11.27	16.73	24.98	43.53	8.66	15.72	23.17	34.75	58.45
	FFH_0 +1	2.16	5.60	8.43	12.72	25.75	3.19	7.81	11.70	17.64	34.58
	FFH_0 +2	0.80	2.83	4.28	6.84	15.23	1.17	3.89	5.93	9.32	20.45
	FFH_0 +3	0.29	1.31	2.18	3.66	8.99	0.43	1.86	3.06	5.05	12.08
	FFH_0 +4	0.11	0.62	1.16	1.99	5.32	0.16	0.88	1.59	2.72	7.14
2–3	FFH_0	9.39	15.63	23.10	34.75	56.76	12.56	20.15	30.26	45.05	71.71
	FFH_0 +1	5.70	10.38	15.50	23.05	40.24	7.59	13.43	20.06	29.92	50.85
	FFH_0 +2	3.46	6.93	10.30	15.39	28.52	4.61	8.92	13.33	19.87	36.04
	FFH_0 +3	2.10	4.59	6.87	10.24	20.21	2.79	5.93	8.87	13.25	25.54
	FFH_0 +4	1.27	3.05	4.57	6.87	14.32	1.69	3.97	5.89	8.87	18.10
3–4	FFH_0	11.96	19.03	28.25	42.42	67.22	15.04	23.41	35.07	52.27	81.63
	FFH_0 +1	8.57	14.21	21.23	31.75	52.05	10.78	17.52	26.24	39.15	63.22
	FFH_0 +2	6.14	10.66	15.90	23.76	40.30	7.73	13.13	19.62	29.26	48.95
	FFH_0 +3	4.40	7.97	11.89	17.80	31.20	5.54	9.82	14.70	21.96	37.90
	FFH_0 +4	3.15	5.94	8.90	13.33	24.15	3.97	7.35	11.08	16.44	29.34
4–4.6	FFH_0	14.00	21.38	31.85	47.66	73.65	16.95	25.65	38.44	57.28	87.62
	FFH_0 +1	10.91	16.95	25.35	37.78	59.30	13.20	20.33	30.24	45.45	70.55
	FFH_0 +2	8.49	13.43	20.05	30.27	47.74	10.29	16.13	24.07	36.01	56.80
	FFH_0 +3	6.62	10.65	15.90	23.78	38.42	8.01	12.78	19.18	28.65	45.72
	FFH_0 +4	5.15	8.44	12.62	18.83	30.93	6.24	10.13	15.13	22.66	36.80

each single-family home type (Table 7; Table 8). Because the data set is not normally distributed, the percentiles are provided along with the minimum and maximum values to describe the annual flood risk (Tables 3–6) and flood risk reduction (Tables 7 and 8) at each category.

5.3 Confirm results

Table 9 demonstrates u and a parameters, and the 500-year flood depths, in the shaded X Zone located in Jefferson Parish, Louisiana, and Santa Clarita, California, using spatial interpolation (Mostafiz et al., 2021b). The a parameter and 500-year flood depth for Jefferson Parish are less than 1 while these values range from 0.97 to 1.37 and 1.00–1.70 feet, respectively, in Santa Clarita. The AAL (i.e., annual flood risk) results for a hypothetical home located in Jefferson Parish and Santa Clarita, calculated through spatially interpolated and synthetic parameters, are summarized in Table 10 and Table 11, respectively.

6 Discussion

The derivation of the synthetic flood parameters (i.e., u; a) for the shaded X Zone (Table 1) for establishing the relationship between flood depth and return period (Figure 3) is useful for providing decision-makers (e.g., construction specialists and

TABLE 6 As in Table 4 but categorized based on a parameter.

a	FFH (feet)	Total average annual loss as a proportion of V_R (i.e., AAL_{T/V_R}) x10^{-4}									
		Two-plus-story without Basement					Two-plus-story with Basement				
		Min	25th	50th	75th	Max	Min	25th	50th	75th	Max
<1	FFH_0	0.63	3.93	6.03	9.43	18.57	1.11	6.40	9.87	15.33	29.50
	FFH_0 +1	0.00	0.54	1.29	2.41	6.12	0.00	1.00	2.24	3.96	9.73
	FFH_0 +2	0.00	0.06	0.33	0.67	2.02	0.00	0.14	0.57	1.09	3.20
	FFH_0 +3	0.00	0.00	0.07	0.20	0.66	0.00	0.02	0.13	0.32	1.06
	FFH_0 +4	0.00	0.00	0.02	0.06	0.22	0.00	0.00	0.03	0.10	0.35
1–2	FFH_0	4.35	8.33	12.38	18.47	32.24	6.81	12.32	18.20	27.26	45.81
	FFH_0 +1	1.60	4.15	6.23	9.39	19.07	2.51	6.12	9.19	13.90	27.10
	FFH_0 +2	0.59	2.10	3.17	5.05	11.28	0.92	3.06	4.66	7.30	16.02
	FFH_0 +3	0.22	0.97	1.61	2.71	6.66	0.34	1.46	2.20	3.95	9.47
	FFH_0 +4	0.08	0.46	0.86	1.47	3.94	0.12	0.69	1.25	2.13	5.60
2–3	FFH_0	6.96	11.68	17.32	25.95	42.68	9.81	15.92	23.79	35.55	56.87
	FFH_0 +1	4.22	7.73	11.55	17.20	30.26	5.95	10.61	15.81	23.53	40.32
	FFH_0 +2	2.56	5.16	7.69	11.51	21.45	3.61	7.02	10.52	15.70	28.58
	FFH_0 +3	1.55	3.43	5.14	7.65	15.20	2.19	4.68	6.97	10.50	20.26
	FFH_0 +4	0.94	2.29	3.41	5.15	10.77	1.33	3.12	4.64	6.98	14.35
3–4	FFH_0	9.01	14.41	21.47	32.22	51.49	11.95	18.81	28.05	42.09	66.00
	FFH_0 +1	6.46	10.80	16.13	24.08	39.87	8.56	14.09	21.05	31.40	51.12
	FFH_0 +2	4.63	8.12	12.09	18.07	30.87	6.14	10.51	15.74	23.47	39.59
	FFH_0 +3	3.32	6.05	9.05	13.57	23.90	4.40	7.87	11.79	17.61	30.64
	FFH_0 +4	2.38	4.53	6.77	10.11	18.50	3.15	5.89	8.85	13.17	23.72
4–4.6	FFH_0	10.75	16.49	24.50	36.84	57.12	13.74	20.92	31.22	46.62	71.91
	FFH_0 +1	8.37	13.07	19.60	29.18	45.99	10.70	16.58	24.76	37.02	57.90
	FFH_0 +2	6.52	10.36	15.54	23.31	37.02	8.33	13.14	19.65	29.56	46.62
	FFH_0 +3	5.08	8.21	12.28	18.36	29.80	6.49	10.42	15.57	23.28	37.52
	FFH_0 +4	3.95	6.52	9.70	14.53	23.99	5.06	8.26	12.37	18.45	30.20

TABLE 7 Annual flood risk reduction by FFH elevation for one-story single-family home with and without basement using synthetic data.

FFH (feet)	Total average annual loss reduction as a proportion of V_R (i.e., $\Delta\ AAL_{T/V_R}$) x 10^{-4}									
	One Story without Basement					One Story with Basement				
	Min	25th	50th	75th	Max	Min	25th	50th	75th	Max
FFH_0	0	0	0	0	0	0	0	0	0	0
FFH_0 +1	0.82	4.81	7.20	10.78	18.22	1.39	6.11	9.14	13.66	26.07
FFH_0 +2	0.82	8.09	12.14	18.15	28.78	1.39	10.28	15.45	23.07	38.56
FFH_0 +3	0.82	10.37	15.62	23.46	36.79	1.39	13.17	19.79	29.63	47.15
FFH_0 +4	0.82	12.08	18.10	27.27	43.33	1.39	15.28	22.93	34.36	53.90

TABLE 8 Annual flood risk reduction by FFH elevation for two-plus-story single-family home with and without basement using synthetic data.

FFH (feet)	Total average annual loss reduction as a proportion of V_R (i.e., $\Delta\ AAL_{T/V_R}$) x10^{-4}									
	Two-plus-story without basement					Two-plus-story with basement				
	Min	25th	50th	75th	Max	Min	25th	50th	75th	Max
FFH_0	0	0	0	0	0	0	0	0	0	0
FFH_0 +1	0.63	3.65	5.45	8.18	13.46	1.11	4.88	7.30	10.94	20.48
FFH_0 +2	0.63	6.15	9.20	13.79	21.46	1.11	8.20	12.34	18.46	30.20
FFH_0 +3	0.63	7.90	11.82	17.82	27.82	1.11	10.55	15.80	23.71	37.08
FFH_0 +4	0.63	9.16	13.67	20.70	33.20	1.11	12.21	18.31	27.44	42.87

TABLE 9 Flood parameters and 500-year flood depth for the shaded X Zone located in Jefferson Parish, Louisiana, and Santa Clarita, California, using spatial interpolation.

Location	u	a	500-Year flood depth (feet)
Jefferson	−1.09	0.19	0.10
	−0.85	0.18	0.30
Santa Clarita	−6.84	1.34	1.40
	−6.13	1.26	1.70
	−6.19	1.28	1.70
	−6.02	1.25	1.70
	−5.71	1.15	1.40
	−5.63	1.08	1.00
	−4.89	0.97	1.10
	−4.93	1.01	1.30
	−5.35	1.04	1.10
	−5.87	1.14	1.20
	−7.02	1.35	1.30
	−7.13	1.37	1.30
	−6.45	1.32	1.60
	−6.37	1.31	1.70

regional planners) sufficient information across a range of return periods. Results suggest that generating u; a is obviate the need for representing the relationship between flood depth vs building, contents, and use loss separately, as in most conventional DDF-based flood risk analyses. Instead, the approach shown here provides estimates for total loss (i.e., building, contents, and use) for wide range of 500-year flood depths (Table 2) and thus the flood risk assessment (Tables 3; 4, 5,; 6) in the shaded X Zone. The applications are even more valuable for risk assessment for construction with long expected life spans and/or grave consequences for flooding, such as sites of cultural or historical importance, hospitals, nursing homes, and bridges, in which partitioning the loss into its components is less important than estimating the long-term total loss.

Another strength of this approach is that it overcomes complications associated with the changing value of assets over time. This is because the total annual flood risk (building, contents, and use) for single-family homes in the shaded X Zone is expressed proportionally to V_R. It is anticipated that providing the results in this format will garner more attention to the long-term flood risk in the shaded X Zone with the actionable outcome of increasing awareness of the benefits of applying mitigation actions.

The results show that the median AAL at FFH_0 falls between only 0.097 and 0.172 percent of V_R, for a single-family home with 500-year flood depth less than one foot, regardless of home type. These results are mainly affected by the unique DDFs based on home type (Mostafiz et al., 2021c).

Not surprisingly, flood depth is the primary factor involved flood risk, with greater depth causing more damage. Thus, elevating the home is the primary strategy for flood risk reduction, but the improvements vary by 500-year flood depth. For example, while the flood risk reduction is approximately 36, 57, 71, and 81% for one through four feet above FFH_0, respectively, when the 500-year flood depth less than 1 foot for all home types (Tables 3; 4), that risk is reduced by less and less with additional feet of elevation in 500-year categories (i.e., 1–2 feet above FFH_0, 2–3 feet, *etc.*,; Tables 3; 4).

The AALs for the case study subsets of Jefferson Parish (Louisiana) and Santa Clarita (California) generated by spatial interpolation-estimated flood parameters are within the range of AAL results using synthetic flood parameters. In the case of Jefferson Parish, the mean AAL values of $39, $61, $30, and $49 for one-story without basement, one-story with basement, two-plus-story without basement, and two-plus-story with basement single-family home, respectively, calculated using the spatial interpolation-estimated flood parameters, are between the minimum and 25th percentile AAL for the appropriate 500-year flood depth and a values. For Santa Clarita, the mean AAL values of $584, $839, and $658 for one-story without basement, one story with basement, and two-plus-story with basement single-family home, respectively, calculated using the spatial interpolation-estimated flood parameters, are between the 75th quartile and maximum AAL for the appropriate 500-year flood

TABLE 10 Average annual loss (i.e., annual flood risk) by type of single-family home in Jefferson Parish, Louisiana, and Santa Clarita, California, implementing spatial interpolation parameters.

Location	Average annual loss ($)			
	One-story without Basement	One-storyWith Basement	Two-plus-story without Basement	Two-plus-story with Basement
Jefferson	23	36	18	30
	54	86	41	68
Santa Clarita	567	803	419	629
	715	1,020	528	800
	712	1,015	526	796
	721	1,030	532	808
	594	859	439	674
	429	627	317	492
	483	717	358	563
	573	844	424	664
	471	690	348	542
	501	726	370	570
	525	742	388	582
	523	738	387	578
	657	933	485	731
	708	1,005	523	788

TABLE 11 Descriptive statistics of average annual loss ($; i.e., annual flood risk) by type of single-family home, after implementing synthetic flood parameters, by 500-year flood depth and *a* parameter.

		Average annual loss ($)									
		One Story without Basement					One Story with Basement				
		Min	25th	50th	75th	Max	Min	25th	50th	75th	Max
500-year flood depth	<1	22	288	359	407	490	38	394	464	517	744
	1–2	404	491	536	585	863	547	618	679	740	1,226
a parameter	<1	22	143	217	341	676	38	219	338	525	1,012
	1–2	155	304	452	674	1,175	234	424	626	938	1,578
		Two-plus-story without Basement					Two-plus-story with Basement				
		Min	25th	50th	75th	Max	Min	25th	50th	75th	Max
500-year flood depth	<1	17	214	269	309	380	30	328	381	418	589
	1–2	299	370	405	443	638	429	514	559	599	961
a parameter	<1	17	106	162	254	501	30	173	267	414	797
	1–2	117	225	334	499	870	184	333	491	736	1,237

depth and *a* values, while the mean AAL value of $432 for two-plus-story without basement single-family home is between the 50th and 75th quartiles. While both techniques lead to similar results, the spatial interpolation method requires multiple return period flood depth data and is computationally intensive. Additional work to confirm the range of areas for which synthetic flood parameters is appropriate will further justify the use of this technique.

7 Conclusion

Although areas outside the SFHA may be highly susceptible to destructive and unanticipated floods at return periods beyond 100 years, they are often overlooked in flood risk assessments, often because they seldom have sufficient data to predict flood parameters. The increased need to have meaningful data outside the SFHA to understand flood hazard risk motivated this new approach to estimate AAL within the shaded X Zone using synthetic flood parameters. The derivation of synthetic flood hazard parameters enables the estimation of flood risk values in the shaded X Zone to assist stakeholders in minimizing flood risk. The major findings are:

- The synthetic data approach improves understanding of flood risk in the shaded X Zone for 1740 scenarios that include a wide range of 500-year flood depths.
- Flood depth-return period relationships provide vital information regarding flood depths at longer return periods that can be used to enhance flood resilience.
- For the analyzed synthetic data, the median AAL for all four types of single-family homes (one- and two-plus-story, each without and with basement) in the shaded X Zone falls between 0.10 and 0.78 percent of V_R for the full range of 500-year flood depths between 0.003 feet and 7.400 feet and a values between 0.10 and 4.60.
- The median value of AAL reduction falls between 0.06 and 0.23 percent of V_R when elevating by an additional 1 and 4 feet, respectively, above FFH_0.
- For case study areas within Jefferson Parish (Louisiana) and Santa Clarita (California), AAL values calculated from spatial interpolation-estimated flood parameters fall within the range of those computed from synthetic flood parameters.

Although this study provides an important first step for predicting and enhancing community understanding of the flood risk in the shaded X Zone, some cautions need to be considered. First, the numerical results will differ from those suggested here in areas where the a parameter exceeds 4.60. Also, the spatial interpolation-estimated flood parameters derived here require depth grids for 10-, 50-, 100-, and 500-year events; these results would be refined if 200- or 250- year depth grids are available. Furthermore, location-specific and recent inflationary trends may result in C_R being much higher than the assumed $135/sf, but AAL could be updated easily for future work. Despite these cautions, this research contributes to the mitigation of the damage and loss experienced outside the SFHA and to improved awareness of the magnitude of flood risk in this region and the benefit of applying mitigation strategies.

Data availability statement

The original contributions presented in the study are included in the article/Supplementary Material; further inquiries can be directed to the corresponding author.

Author contributions

AA developed the methodology, analyzed the data, interpreted the findings, and developed the initial text. RM selected the case study area, prepared the input data, and supervised the research. CF supervised the research, provided insight and recommendation for the research, and reviewed and edited the manuscript. RR reviewed and edited the writing of the manuscript and provided insight and recommendations for the research. MR reviewed and edited the manuscript.

Funding

This research was funded by the USDA National Institute of Food and Agriculture, Hatch project LAB 94873, accession number 7008346, U.S. Department of Homeland Security (Award Number: 2015-ST-061-ND0001-01), the Louisiana Sea Grant College Program (Omnibus cycle 2020–2022; Award Number: NA18OAR4170098; Project Number: R/CH-03; Omnibus cycle 2022–2024; Award Number: NA22OAR4710105; Project Number: R/CH-05), the Gulf Research Program of the National Academies of Sciences, Engineering, and Medicine under the Grant Agreement number: 200010880 "The New First Line of Defense: Building Community Resilience through Residential Risk Disclosure," and the U.S. Department of Housing and Urban Development (HUD; 2019–2022; Award No. H21679CA, Subaward No. S01227-1). The publication of this article is supported by the LSU AgCenter LaHouse Resource Center.

Conflict of interest

The authors declare that the research was conducted in the absence of any commercial or financial relationships that could be construed as a potential conflict of interest.

Publisher's note

All claims expressed in this article are solely those of the authors and do not necessarily represent those of their affiliated organizations, or those of the publisher, the editors and the reviewers. Any product that may be evaluated in this article, or claim that may be made by its manufacturer, is not guaranteed or endorsed by the publisher.

Author disclaimer

Any opinions, findings, conclusions, and recommendations expressed in this manuscript are those of the author and do not necessarily reflect the official policy or position of the funders.

Supplementary material

The Supplementary Material for this article can be found online at: https://www.frontiersin.org/articles/10.3389/feart.2023.1051546/full#supplementary-material

References

Al Assi, A., Mostafiz, R. B., Friedland, C. J., Rahim, M. A., and Rohli, R. V. (2023a). Flood risk assessment for residences at the neighborhood scale by owner/occupant type and first-floor height. *Front. Big Data* 5, 997447. doi:10.3389/fdata.2022.997447

Al Assi, A., Mostafiz, R. B., Friedland, C. J., Rohli, R. V., Taghinezhad, A., and Rahim, M. A. (2023b). Cost-effectiveness of federal CDBG-DR Road Home Program mitigation assistance in Jefferson Parish, Louisiana. *Nat. Hazards*. doi:10.1007/s11069-023-05904-3

American Society of Civil Engineers (Asce) (2014). Flood resistant design and construction. *ASCE Stand.* 24–14, 1–75. doi:10.1061/9780784413791

Amoroso, S. D., and Fennell, J. P. (2008). "A rational benefit/cost approach to evaluating structural mitigation for wind damage: Learning "the hard way" and looking forward," in *Structures congress 2008* (Vancouver, Canada: ASCE). doi:10.1061/41016(314)249

Armal, S., Porter, J. R., Lingle, B., Chu, Z., Marston, M. L., and Wing, O. E. J. (2020). Assessing property level economic impacts of climate in the US, new insights and evidence from a comprehensive flood risk assessment tool. *Climate* 8 (10), 116–120. doi:10.3390/cli8100116

Association of State Floodplain Managers (2020). Flood mapping for the nation A cost analysis for completing and maintaining the nation's NFIP flood map inventory. https://webapps.usgs.gov/infrm/estBFE/.

Bohn, F. H. (2013). Design flood elevations beyond code requirements and current best practices. LSU Master's Theses. Lsu Press, Baton Rouge, Louisiana, https://digitalcommons.lsu.edu/gradschool_theses/69.

Botzen, W. J. W., and van den Bergh, J. C. J. M. (2008). Insurance against climate change and flooding in The Netherlands: Present, future, and comparison with other countries. *Risk Anal.* 28 (2), 413–426. doi:10.1111/j.1539-6924.2008.01035.x

Bowers, C., Serafin, K. A., and Baker, J. (2022). A performance-based approach to quantify atmospheric river flood risk. *Nat. Hazards Earth Syst. Sci.* 22 (4), 1371–1393. doi:10.5194/nhess-22-1371-2022

Collins, E. L., Sanchez, G. M., Terando, A., Stillwell, C. C., Mitasova, H., Sebastian, A., et al. (2022). Predicting flood damage probability across the conterminous United States. *Environ. Res. Lett.* 17 (3), 34006. doi:10.1088/1748-9326/ac4f0f

Doheny, M. (2021). *Square foot costs with RSMeans Cost data*, 42. Gordian. Rockland, MA, USA.

Fema (2013). Designing for flood levels above the BFE after hurricane Sandy. http://www.region2coastal.com/.

Fema (2019). National flood insurance program flood mitigation measures for multi-family buildings. https://floodawareness.org/wp-content/uploads/2020/08/16-J-0218_Multi-FamilyGuidance_06222020.pdf.

Fema (2021). Risk mapping, assessment and planning (risk MAP). https://www.fema.gov/flood-maps/tools-resources/risk-map.

Ferguson, A. P., and Ashley, W. S. (2017). Spatiotemporal analysis of residential flood exposure in the Atlanta, Georgia metropolitan area. *Nat. Hazards* 87 (2), 989–1016. doi:10.1007/s11069-017-2806-6

Friedland, C. J., Lee, Y. C., Mostafiz, R. B., Lee, J., Mithila, S., Rohli, R. V., et al. (2023). FloodSafeHome: Evaluating benefits and savings of freeboard for improved decision-making in flood risk mitigation. *Front. Commun.* 8, 1060901. doi:10.3389/fcomm.2023.1060901

Gnan, E., Friedland, C. J., Mostafiz, R. B., Rahim, M. A., Gentimis, T., Taghinezhad, A., et al. (2022b). Economically optimizing elevation of new, single-family residences for flood mitigation via life-cycle benefit-cost analysis. *Front. Environ. Sci.* 10, 889239. doi:10.3389/fenvs.2022.889239

Gnan, E., Friedland, C. J., Rahim, M. A., Mostafiz, R. B., Rohli, R. V., Orooji, F., et al. (2022a). Improved building-specific flood risk assessment and implications of depth-damage function selection. *Front. Water* 4, 919726. doi:10.3389/frwa.2022.919726

Gnan, E., Mostafiz, R. B., Rahim, M. A., Friedland, C. J., Rohli, R. V., Taghinezhad, A., et al. (2022c). Freeboard life-cycle benefit-cost analysis of a rental single-family residence for landlord, tenant, and insurer. Nat. Hazards Earth Syst. Sci. *Discuss. Prepr.* [Preprint]. doi:10.5194/nhess-2022-222

Goldberg, N., and Watkins, R. L. (2021). Spatial comparisons in wetland loss, mitigation, and flood hazards among watersheds in the lower St. Johns River basin, northeastern Florida, USA. *Nat. Hazards* 109 (2), 1743–1757. doi:10.1007/s11069-021-04896-2

Habete, D., and Ferreira, C. M. (2017). Potential impacts of sea-level rise and land-use change on special flood hazard areas and associated risks. *Nat. Hazards Rev.* 18 (4), 4017017. doi:10.1061/(asce)nh.1527-6996.0000262

Hagen, S. C., and Bacopoulos, P. (2012). Coastal flooding in Florida's big bend region with application to sea level rise based on synthetic storms analysis. *Terr. Atmos. Ocean. Sci.* 23 (5), 481–500. doi:10.3319/tao.2012.04.17.01(wmh)

Hallegatte, S., Green, C., Nicholls, R. J., and Corfee-Morlot, J. (2013). Future flood losses in major coastal cities. *Nat. Clim. Change* 3 (9), 802–806. doi:10.1038/nclimate1979

Hemmati, M., Mahmoud, H. N., Ellingwood, B. R., and Crooks, A. T. (2021). Unraveling the complexity of human behavior and urbanization on community vulnerability to floods. *Sci. Rep.* 11 (1), 20085. doi:10.1038/s41598-021-99587-0

Hino, M., and Hall, J. W. (2017). Real options analysis of adaptation to changing flood risk: Structural and nonstructural measures. *ASCE-ASME J. Risk Uncertain. Eng. Syst. Part A Civ. Eng.* 3 (3), 4017005. doi:10.1061/ajrua6.0000905

Kennedy, A., Copp, A., Florence, M., Gradel, A., Gurley, K., Janssen, M., et al. (2020). Hurricane Michael in the area of Mexico beach, Florida. *J. Waterw. Port, Coast. Ocean Eng.* 146 (5), 5020004. doi:10.1061/(asce)ww.1943-5460.0000590

Kiaghadi, A., Govindarajan, A., Sobel, R. S., and Rifai, H. S. (2020). Environmental damage associated with severe hydrologic events: A LiDAR-based geospatial modeling approach. *Nat. Hazards* 103 (3), 2711–2729. doi:10.1007/s11069-020-04099-1

Kousky, C., Palim, M., and Pan, Y. (2020a). Flood damage and mortgage credit risk: A case study of hurricane Harvey. *J. Hous. Res.* 29 (1), S86–S120. doi:10.1080/10527001.2020.1840131

Kousky, C., Shabman, L., Linder-Baptie, Z., and Peter, E. S. (2020b). Perspectives on flood insurance demand outside the 100-year floodplain. https://riskcenter.wharton.upenn.edu/wp-content/uploads/2020/05/Perspectives-on-Flood-Insurance-Demand-Outside-the-100-Year-Floodplain.pdf.

Meyer, V., Haase, D., and Scheuer, S. (2009). Flood risk assessment in European river basins-concept, methods, and challenges exemplified at the Mulde River. *Integr. Environ. Assess. Manag.* 5 (1), 17–26. doi:10.1897/ieam_2008-031.1

Mostafiz, R. B., Assi, A. A., Friedland, C. J., Rohli, R. V., and Rahim, M. A. (2022a). "A numerically-integrated approach for residential flood loss estimation at the community level", in *EGU general assembly 2022* EGU (Vienna, Austria, 23–27. doi:10.5194/egusphere-egu22-10827

Mostafiz, R. B., Bushra, N., Rohli, R. V., Friedland, C. J., and Rahim, M. A. (2021a). Present vs. future property losses from a 100-year coastal flood: A case study of grand isle, Louisiana. *Front. Water* 3, 763358. doi:10.3389/frwa.2021.763358

Mostafiz, R. B., Friedland, C. J., Rahman, M. A., Rohli, R. V., Tate, E., Bushra, N., et al. (2021c). Comparison of neighborhood-scale, residential property flood-loss assessment methodologies. *Front. Environ. Sci.* 9, 734294. doi:10.3389/fenvs.2021.734294

Mostafiz, R. B., Friedland, C., Rahim, M. A., Rohli, R. V., and Bushra, N. (2021b). A data-driven, probabilistic, multiple return period method of flood depth estimation. In *American geophysical union fall meeting* Agu Fall Meeting Abstracts, Illinois, CH, USA, https://www.authorea.com/doi/full/10.1002/essoar.10509337.1

Mostafiz, R. B., Rahim, M. A., Friedland, C. J., Rohli, R. V., Bushra, N., and Orooji, F. (2022b). A data-driven spatial approach to characterize the flood hazard. *Front. Big Data* 5, 1022900. doi:10.3389/fdata.2022.1022900

Mostafiz, R. B., Rohli, R. V., Friedland, C. J., and Lee, Y.- C. (2022c). Actionable information in flood risk communications and the potential for new web-based tools for long-term planning for individuals and community. *Front. Earth Sci.* 10, 840250. doi:10.3389/feart.2022.840250

NOAA (2022). National centers for environmental information (NCEI) U.S. Billion-dollar weather and climate disasters. https://www.ncei.noaa.gov/access/billions/summary-stats/US/1980-2021.doi:10.25921/stkw-7w73

Patel, M. B. (2020). Flood frequency analysis using Gumbel distribution method at garudeshwar weir, narmada basin. *Int. J. Trend Res. Dev.* 7 (1), 36–38. http://www.ijtrd.com/papers/IJTRD21899.pdf.

Pistrika, A., Tsakiris, G., and Nalbantis, I. (2014). Flood depth-damage functions for built environment. *Environ. Process.* 1 (4), 553–572. doi:10.1007/s40710-014-0038-2

Pricope, N. G., Hidalgo, C., Pippin, J. S., and Evans, J. M. (2022). Shifting landscapes of risk: Quantifying pluvial flood vulnerability beyond the regulated floodplain. *J. Environ. Manag.* 304, 114221. doi:10.1016/j.jenvman.2021.114221

Rahim, M. A., Friedland, C. J., Rohli, R. V., Bushra, N., and Mostafiz, R. B. (2021). "A data-intensive approach to allocating owner vs. NFIP portion of average annual flood losses," in *AGU 2021 fall meeting, 13–17 december* (New Orleans, LA, USA. AGU, https://www.authorea.com/doi/full/10.1002/essoar.10509884.1.

Rahim, M. A., Gnan, E. S., Friedland, C. J., Mostafiz, R. B., and Rohli, R. V. (2022). "An improved micro scale average annual flood loss implementation approach", EGU, in *EGU general assembly 2022* (Vienna, Austria, 23–27. doi:10.5194/egusphere-egu22-10940

Rath, W., Kelly, C. P., and Beahm, K. A. (2018). Floodplain building elevation standards current requirements & enhancement options for connecticut shoreline municipalities. *University of Connecticut Center for Energy & Environmental Law*. University of Connecticut, Storrs, CT, USA, https://circa.

uconn.edu/wp-content/uploads/sites/1618/2018/03/Floodplain-Building-Elevation-Standards.pdf.

Singh, P., Sinha, V. S. P., Vijhani, A., and Pahuja, N. (2018). Vulnerability assessment of urban road network from urban flood. *Int. J. Disaster Risk Reduct.*, 28, 237–250. doi:10.1016/j.ijdrr.2018.03.017

Šugareková, M., and Zeleňáková, M. (2021). Flood risk assessment and flood damage evaluation – The review of the case studies. *Acta Hydrol. Slovaca* 22 (1), 156–163. doi:10.31577/ahs-2021-0022.01.0019

Taghinezhad, A., Friedland, C. J., and Rohli, R. V. (2021). Benefit-cost analysis of flood-mitigated residential buildings in Louisiana. Hous. *Soc.* 48 (2), 185–202. doi:10.1080/08882746.2020.1796120

Taghinezhad, A., Friedland, C. J., Rohli, R. V., and Marx, B. D. (2020). An imputation of first-floor elevation data for the avoided loss analysis of flood-mitigated single-family homes in Louisiana, United States. *Front. Built Environ.* 6, 138. doi:10.3389/fbuil.2020.00138

Technical Mapping Advisory Council (TMAC) (2015). TMAC annual report 2015. https://www.fema.gov/sites/default/files/documents/fema_tmac_2015_annual_report.pdf.

Usace (2000). "Economic guidance memorandum (EGM) 01-03, generic depth damage relationships. 1–3", in *Memorandum from USACE (United States Army Corps of Engineers)* OCLC, (Washington, DC, USA.

Wang, Y., and Sebastian, A. (2021). Community flood vulnerability and risk assessment: An empirical predictive modeling approach. *J. Flood Risk Manag.* 14 (3), 12739. doi:10.1111/jfr3.12739

Wing, O. E. J., Lehman, W., Bates, P. D., Sampson, C. C., Quinn, N., Smith, A. M., et al. (2022). Inequitable patterns of US flood risk in the Anthropocene. *Nat. Clim. Change* 12 (2), 156–162. doi:10.1038/s41558-021-01265-6

Xian, S., Lin, N., and Hatzikyriakou, A. (2015). Storm surge damage to residential areas: A quantitative analysis for hurricane Sandy in comparison with FEMA flood map. *Nat. Hazards* 79 (3), 1867–1888. doi:10.1007/s11069-015-1937-x

Xian, S., Lin, N., and Kunreuther, H. (2017). Optimal house elevation for reducing flood-related losses. *J. Hydrology*, 548, 63–74. doi:10.1016/j.jhydrol.2017.02.057

Yildirim, E., and Demir, I. (2022). Agricultural flood vulnerability assessment and risk quantification in Iowa. *Sci. Total Environ.* 826, 154165. doi:10.1016/j.scitotenv.2022.154165

frontiers | Frontiers in Earth Science

TYPE Review
PUBLISHED 18 May 2023
DOI 10.3389/feart.2023.1124166

OPEN ACCESS

EDITED BY
Wentao Yang,
University of Leeds, United Kingdom

REVIEWED BY
Fabio Matano,
National Research Council (CNR), Italy
Maxim A. Dulebenets,
Florida Agricultural and Mechanical University, United States

*CORRESPONDENCE
Priscila Carvalho,
priscila.carvalho@ucl.ac.uk

RECEIVED 14 December 2022
ACCEPTED 24 April 2023
PUBLISHED 18 May 2023

CITATION
Carvalho P and Spataru C (2023), Gaps in the governance of floods, droughts, and heatwaves in the United Kingdom.
Front. Earth Sci. 11:1124166.
doi: 10.3389/feart.2023.1124166

Gaps in the governance of floods, droughts, and heatwaves in the United Kingdom

Priscila Carvalho* and Catalina Spataru

Island and Coastal Research Lab, UCL Energy Institute, Bartlett School of Energy, Environment and Resources, University College London, London, United Kingdom

Disaster risk reduction (DRR) and equitable resilience have cross-cutting challenges relevant to the Sustainable Development Goals (SDGs), Sendai Framework (SF) and Climate Change Adaptation (CCA). The capacity of governments to assess, prevent, prepare, respond, and recover from disasters depends on effective laws, planning, policies, governance instruments, equity indicators, harmonized standards, and a holistic approach to cross-sectoral issues and multi-scalar challenges. The principle of subsidiarity guides the United Kingdom (UK) approach to disaster governance, with decisions taken at lowest level and coordinated at different scales (national, sub-national, local). Cross-scale work needed to address large-scale issues and enable the pooling of resources, happens at a sub-national tier created especially for this purpose. At national level, there is a government lead department for each risk identified in the National Risk Assessment, with Department for Environment, Food and Rural Affairs (DEFRA) serving as the lead for floods and droughts, while the Department of Health and Social Care is the lead for heatwaves. In this paper we present the current state of the art of the governance of floods, droughts, and heatwaves in the UK, with a focus on pre-emergency phases and the shortage of indicators for assessment of the effectiveness of adaptation for all three disasters, which also compromise the realization and monitoring of targets across all three agendas. The governance of floods counts with the most developed legal framework of the three. Droughts are mainly dealt by the water sector, while heatwaves are treated exclusively as a health issue, leaving gaps with regards to the multiple risks these disasters pose to livelihoods and other sectors. Gaps and challenges that remain are related to siloed institutional approaches, lack of adaptation indicators, lack of cross-sectoral resilience standards, and lack of policy instruments and metrics to promote equitable resilience. Commonly, actions have mainly focused on the response and recovery strategies instead of risk reduction and adaptation to address rising vulnerabilities and exposure.

KEYWORDS

climate adaptation, equitable resilience, governance, risk reduction, sdgs, sendai framework

Introduction

Despite current global and national policy commitments to mitigate and adapt to climate change, Earth's mean temperature is projected to rise by approximately 2.7°C above pre-industrial levels by the end of the century (Climate Action Tracker, 2022). This increase is expected to result in more extreme weather events and recurring hazards. Six major storms took place in the UK in 2022, which saw some of the highest wind speeds in over 30 years

(Met Office, 2022c). These northerly winds led to widespread damage in Northeast England and Scotland, including power line damages and trees uprooted, with almost a million customers losing power (Met Office, 2021; OFGEM, 2022). The last decade was the warmest on record (WMO, 2022). The UK's average land temperature increased by about 1.2°C from pre-industrial levels (Climate Change Committee, 2021). Sea levels have risen by 16 cm since 1900 and could reach up to 30 cm by 2050, increasing flood risks along a third of England's coast (Climate Change Committee, 2021). The year of 2020 was the third warmest and fifth wettest in history, which led to extensive flooding, particularly in the Northern England and Wales (Kendon et al., 2020). The economic damages of the 2019/20 floods reached £333 million, but flood defences reduced costs that would have been at least fourteen times greater without such protection (ibid.). There are £200 billion worth of assets at risk of flooding (Environment Agency, 2021a). The latest UK Climate Change Risk Assessment (2022) identified that around 3.2 million properties are at risk of surface water flooding in England (DEFRA, 2022). Increased flooding poses significant challenges to various aspects of infrastructure, including energy systems, transportation networks, water management, waste disposal, and digital communication systems. Storm Arwen in 2022 caused significant disruptions for a water company, leading to power outages at 140 wastewater sites and water treatment assets serving 17,500 properties, leaving them without water (Joint Committee on the National Security Strategy, 2022). In 2018, the 'Beast from the East' created substantial travel disruptions, complicating the efforts of an energy company's engineers to visit gas sites and address technical faults (ibid.).

Annual average rainfall is increasing since 1980s in the UK and in the last decade, the summers were 20% wetter than in the decade before (1990–2000) (Climate Change Committee, 2021). There are about 6.4 million people living under flood prone areas in the UK (Sayers et al., 2017). From this total, around 1.8 million people are exposed to significant risks of floods and estimates show this number could reach 2.6 million people by 2050 in a two-degree scenario (Climate Change Committee, 2016). The socially vulnerable neighbourhoods are over-represented in areas prone to costal and tidal flood (33% of all people exposed to this risk −590,000–are within the 20% most vulnerable neighbourhoods in the UK) (Sayers et al., 2017). Saline intrusion, coastal squeeze, coastal building damage are high risks associated with coastal flooding and erosion damage. By 2080, 10.8 million people could be exposed to significant risks of floods in the UK, with the most vulnerable neighbourhoods seeing the highest rise to 1.4 million people (ibid.).

Higher maximum temperature and longer warm spells have also been the reality in the United Kingdom. England recorded 2,556 excess deaths across three heatwave periods in summer 2020. Notable heatwaves were registered in 1976, 1990, 1995, 2003, 2006 (Met Office, 2018), 2019, 2020 and 2022 (Met Office, 2022a). In 2003, the United Kingdom hit a record high of 38.5° (Public Health England, 2020). In 2019, the United Kingdom broke the 2003 record at 38.7° (Met Office, 2019). In 2022 a new record was set at 40.3° (Met Office, 2022a). Close to 12 million people are in danger of the risks of heatwaves, with most vulnerable more at risk than others (e.g., elderly people and pre-existing health conditions) (The Climate Coalition, 2021). Heat related mortality of elderly people increased by 21% between 2004 and 2018 (ibid.). It could rise by 250% without climate action and affect an additional 7.5 million people aged 65 years and above by 2070 (ibid.). Heatwaves cause the loss of life, but also the loss of productivity and overheating in buildings, which has implication for health (Arbuthnott and Hajat, 2017). There are no specific policies addressing the overheating of buildings and the lack of prevention and preparedness measures will continue to expose to the most vulnerable, locking in major risks to wellbeing (Climate Change Committee, 2021). Today, the best practice is to follow the thermal comfort guidance of the Chartered Institution of Building Services Engineers but estimates show that more than 20% of buildings exceed maximum temperature for a normal United Kingdom summer, which will certainly aggravate with additional extreme heat (Brimicombe et al., 2021).

Higher temperatures increase evaporation, causing soils to become dryer which can potentially worsen drought impacts. Even though droughts are the least frequent of the three disasters in the United Kingdom, there are recent and notable events registered in England between 1972 and 74, 1975-76, 1988-89, 1990-92, 1995-97, 2004-06, 2010-12 (Met Office, 2013) and 2022 (Environment Agency, DEFRA and Double, 2022). Droughts represent risks to food security, land, insects, trade, economic growth, carbon uptake, fish deaths, reduced breeding of birds and poisonous algae. They are characterized for being a slow on-set type of disaster, which vary in timeframe, impacts and nature (environmental drought, agricultural drought, and water supply drought) (Environment Agency, 2017). Areas most at risk of droughts are in the southern parts of the United Kingdom (Environment Agency, DEFRA and Double, 2022). In 2022 large areas were moved into drought status (Devon and Cornwall/Isles of Silly; Solent and South Downs; Thames; Hertfordshire and North London; Kent and South London; East Anglia; Lincolnshire and Northamptonshire; East Midlands; and Yorkshire) (ibid.). Many areas of England are predicted to have water shortage by 2050 due to prolonged hot and dry weather, impacting river flows and soil dryness (Environment Agency and Bevan, 2019). Without further investment in water storage and transfer infrastructure, coupled with efforts to reduce water demand, the probability of facing a severe drought before 2050 is of around 25% (Joint Committee on the National Security Strategy, 2022).

Floods, heatwaves, and droughts are critically linked and have compounding impacts. Heatwaves can exacerbate droughts and wildfires, which can lead to dryer soils that are not able to retain the heavy rainfall that usually come at the end of dry periods, aggravating impacts of floods. The negative consequences for people, environment, critically interlinked resources, and systems of provision are unquestionable. However, the increasing risks of droughts, floods and heatwaves are managed in fragmented and siloed ways and count with different stages of governance maturity, lacking indicators for adaptation and equitable resilience. There are asymmetries in the capacity to assess, prevent, prepare, respond, and recover from each of these disasters, which will continue to expose the most vulnerable to their impacts. The governance of floods counts with the most developed framework when compared to heatwaves and droughts, including in terms of laws, plans, policies, regulations, knowledge and information and prevention mechanisms. DEFRA is the lead government department for floods and droughts (DEFRA, 2015), while the Department of Health and

Social Care is the lead department for heatwaves (Public Health England, 2020). Heatwaves are treated as a health issue and together with droughts their main governance instrument is a national plan, leaving gaps and challenges with regards to the risks these disasters pose to livelihoods, resources, and sectors in other domains (e.g., land, water, energy, transport, food and building sector). Siloed institutional approaches, lack of adaptation and equity indicators, and better integrated resilience strategies, sustainability and risk reduction policies represent gaps and challenges for managing multi-hazard risks. Compared to the Sendai Framework and Climate Change Adaptation for which the United Kingdom is still developing data approaches to measure many domestic objectives (PHE, 2017; Climate Change Committee, 2021), the SDGs count with a high number of indicators to measure progress on the ground (180 of the total of 244) (DFID, 2019). In general adaptation is not following the increasing risks the United Kingdom is facing, which means it is less prepared now than it was 5 years ago (Climate Change Committee, 2021), raising environmental justice concerns. Loss of assets, income and livelihood suffered by disadvantaged groups in context of climate hazard aggravate inequalities and consequently the exposure and vulnerability of these same groups to the risks of floods, droughts, and heatwaves.

Disaster risk reduction under the Sendai Framework refers to a wide range of opportunities for risk abatement and disaster management, including prevention, preparedness, and part of the recovery process, giving particular emphasis to the reduction of vulnerability. Targets A-D of the Sendai Framework form the basis of monitoring and reporting on disaster loss data, including on reduction of disaster mortality, number of affected people, disaster economic loss and damage to critical infrastructure (UNISDR, 2015b). About 60% of the Sendai reporting countries (from a total of 87 in the last review) have a national database for monitoring disaster losses, but the United Kingdom did not report to have one (UNISDR, 2017). Under the Paris Agreement, climate change adaptation (CCA) strategies and outcomes also aim to reduce vulnerability to expected impacts of climate change. The United Kingdom actions and indicators for CCA are developed through its National Adaptation Strategy and National Adaptation Plan, completed impacts, vulnerability, and adaptation assessments, established meteorological observations, climate projects and services, monitoring and reporting. At national level, the adaptation indicator framework has been reviewed by the Climate Change Committee in 2021 covering trends of risk factors, adaptation actions and climate impacts, and many gaps in the following areas: natural environment, business, infrastructure, people, and the built environment (Climate Change Committee, 2021). The United Kingdom does not have measurable targets to assess progress towards climate change adaptation and at least 34 areas of adaptation priorities do not present strong progress (ibid.). Adaptation is yet to be mainstreamed into policy and practice, while most adaptation priorities lack account of the impacts under different warming scenarios (ibid.).

Climate change adaptation and disaster risk reduction are key to manage risks and impacts of floods, droughts and heatwaves and support equitable resilience in benefit of the Sustainable Development Goals (SDGs). On the other hand, if development follows a more sustainable path, reducing pressure on resources such as water (SDG 6), energy (SDG 7), food (SDGs 2), ocean (SDG 14), land (SDG 15), it can reduce risks and address the drivers of vulnerabilities that aggravate impacts of floods, droughts, and heatwaves. There are 25 targets and 35 indicators under the Sustainable Development Goals, which can help monitor the Sendai Framework and risk reduction and resilience (UNISDR, 2015a). The United Kingdom has data for 27 out of the 35 indicators, with actions that span across the Resilience Capabilities Programme, the 25 Year Environment Plan, Environment Bill, citizenship curriculum and abstraction plans (DFID, 2019). Gaps remain with respect to lack of disaggregated data and missing data for direct economic loss in relation to global GDP, damage to critical infrastructure and number of disruptions to services attributable to disasters (Climate Change Committee, 2021). Even though the global targets share common objectives on reduction of risk and vulnerability to communities, the development basis of adaptation, risk reduction and equitable resilience are not the reality. There is a need for better integrated approaches towards implementation of the global targets of the SDGs, CCA and SF that crosscut and intersect the latter objectives, addressing the drivers of vulnerability as drivers of disaster risk, and strengthening resilience across scales and sectors, with a focus on equity and justice.

We present a review on the United Kingdom's risk assessment and governance of floods, droughts, and heatwaves in the context of the three global policy frameworks (SDGs, Climate Change Adaptation and Sendai Framework). We advocate that for these frameworks to build on each other and advance fair processes and outcomes in the implementation of targets relevant for risk reduction and resilience, environmental justice has a role to play. It serves well the purpose of addressing the inequitable outcomes for people and places in relation to climate impacts and risks associated with increasing frequency and magnitude of floods, droughts, and heatwaves. Section 2 contains a review of the risk assessment approach; Section 3 contains the governance review of the three disasters in the United Kingdom. Conclusions are driven about which one counts with the most or least developed framework to safeguard that collectively and individually, everyone can prepare, respond, and recover, while having their essential needs met (e.g., housing, energy, water, transport, telecommunication). Section 4 covers the criteria and approach for risk management across national critical sectors in the United Kingdom with a focus on the three disasters. We identify the lack of data on the vulnerability of infrastructure to extreme weather and the gaps towards improved resilience. The discussion and conclusions on Section 5 focuses on the environmental justice implications of disparate governance approaches towards these disasters, including main conclusions and prospects to advance research and practice in the field of risk reduction and resilience to floods, droughts, and heatwaves.

Shortcomings in risk assessment of floods, droughts, and heatwaves

The United Kingdom produces every 2 years a classified assessment of the risks of civil emergencies that have the potential to cause significant disruption due to threats to human welfare, environment, or security (Cabinet Office, 2017). This

TABLE 1 Comparison of risk assessment criteria under the national risk registry.

Fatalities	Number of fatalities directly attributable to the emergency	2017
Casualties	illness or injury over the period following the onset of the emergency	2017
Social disruption	Levels of disruption to people's lives, from an inability to gain access to healthcare or schools to interruptions in supplies of essential services such as food, water, transport, healthcare*etc.*	2017
Economic damage	Such as lost tourism or working hours, with effects measured for the economy overall and not just the cost of repairs	2017
Psychological impact	Widespread anxiety, loss of confidence in the Government, outrage that communities may experience	2017
Human welfare	Fatalities directly attributable to the incident, causalities resulting from the incident (illness, injury and psychological impacts), evacuation and shelter requirements	2020
Behavioral	Changes to people's behavior or public outrage	2020
Essential services	Levels of disruption to people's lives, from an inability to gain access to healthcare or schools to interruptions in supplies of essential services such as food, water, transport, healthcare*etc.*	2020
Economic damage	Such as lost tourism or working hours, with effects measured for the economy overall and not just the cost of repairs	2020
Environmental impact	Widespread anxiety, loss of confidence in the Government, outrage that communities may experience	2020
Security	Law enforcement and the criminal justice system	2020
International	Damages to international relations	2020

Source (Cabinet Office, 2017; Cabinet Office, 2020).

"National Risk Assessment" (NRA) analyses the key risks over a five-year period, as a way of providing the government and local responders with the means to plan, prioritise and proportionately prepare for eventualities. The risk assessment considers environmental hazard risks and others (e.g., pandemics) in terms of likelihood, scale and extent of consequences, prioritizing the eminent emergencies and the ways of responding to them (Cabinet Office, 2020). The public has access to this assessment through the National Risk Register (NRR), which serves as a resource for individuals and organizations to prepare. The NRA helps the local level to identify potential risks and prepare plans for either preventing or mitigating the impact of incidents locally. This work is coordinated through in England and Wales, Regional Resilience Partnerships in Scotland, and Emergency Preparedness Groups in Northern Ireland (Cabinet Office, 2013c). These multi-agency partnerships are made up of representatives from local public services, including the emergency services, local authorities, NHS, and the environmental agencies. They also draw on the support by other organizations such as Highways England and public utility companies. Local Resilience Forums (LRF) are the building block for emergency planning and response activities, while the Civil Contingencies Secretariat in the Cabinet Office is responsible for providing guidance on the preparation and work coordinated by local partners. At the local level, Community Risk Registers (CCR) are published by the Local Resilience Forums to provide an overview of the risks based on local conditions, infrastructure, and geography (Cabinet Office, 2020). Local Resilience Forums should follow a uniform process of risk assessment developing Community Risk Register (CRR), but discrepancies and errors have been identified, which compromises a nationally consistent picture of local risks (Deeming, 2017).

The NRR published in 2020 includes floods, droughts, and heatwaves under the 'reasonably worst-case scenario' due their likelihood assessment and impact (Cabinet Office, 2020). For risks to be included in the NRA they need to have at least 20,000 chances of occurring in the United Kingdom in the next 5 years; and have an expected impact that reaches a minimum threshold that typically translates into significant damage to human welfare (ibid.). Likelihood scores between one and five are developed for each risk, and under each step on the scale, the probability of an event happening in the next 5 years increases approximately tenfold (ibid.). For some risks, data such as historical analysis and numeric modelling are used to inform estimates of likelihood. Scientific expertise also informs the development and review of risks (ibid.). Where possible, a combination of this analysis and expert judgement is used to estimate the approximate likelihood of an event occurring. The NRR of 2020 has 38 civil emergency risks compared to the 21 risks highlighted in the previous NRR of 2017 (Cabinet Office, 2017). The impacts of risks under the NRR of 2017 were assessed according to the five criteria (fatalities, causalities, social disruption, economic damage, psychological impact), while in the NRR 2020 spans across seven criteria (human welfare, behavioral, essential services, economic damage, environmental impact, security and international) (Table 1). The expansion of the assessment framework reflects the growing complexities of risks and is a step forward towards a more comprehensive understanding of their likelihood and impacts, which can inform more effective risk management and mitigation strategies. There are new challenges in terms of data collection, analysis, and interpretation, including with regards to cross-sectoral collaboration and coordination. Overall, there is a growing need for more integrated and holistic approaches to risk management across critical sectors and resilience building.

Under the 2020 NRR, heatwaves are the most likely to happen (25–125 in 500) and has an impact score of three (Cabinet Office, 2020). Droughts are the least likely to happen (1–5 in 500) and has the same impact score as heatwaves (ibid.). Coastal flooding and river flooding are in between the two in terms of likelihood (5–25 in 500) but are considered to have the highest impact of all three. The United Kingdom faces an adaptation deficit (Joint Committee on the

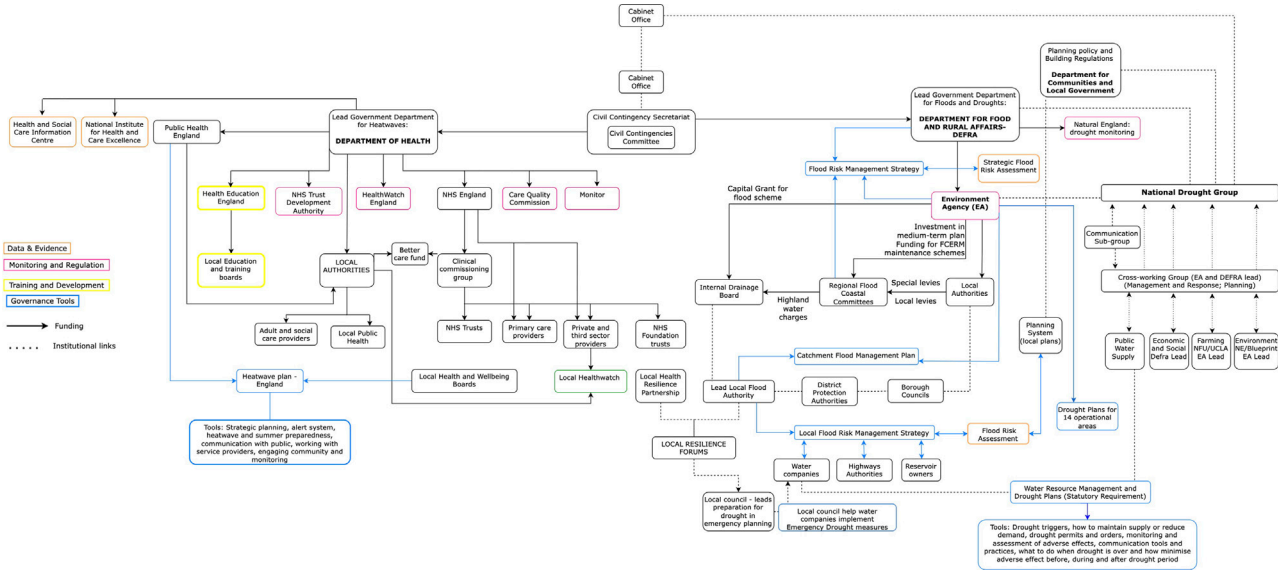

FIGURE 1
Cross-scale governance of floods, droughts and heatwaves.

National Security Strategy, 2022) so questions remain about the degree of preparedness to the compounding impacts of these latter disasters, including the United Kingdom's progress towards the SDGs, SF and CCA targets. The United Kingdom's Adaptation Committee found in its 2021 Independent Assessment that the country is unprepared for even the best-case climate change scenario, with the gap between risk levels and adaptation efforts widening since 2017 (CCC, 2021). Major adaptation deficit impacts all the United Kingdom's Critical National Infrastructure (CNI), including energy, transport, water, waste and digital communication (Joint Committee on National Security Strategy, 2022). The growing potential for incidents like the August 2020 train derailment in Stonehaven, Scotland, where heavy rainfall washed debris onto the track, causing a collision that resulted in fatalities, raises concerns (RAIB, 2022). Shortcomings were identified in the Network Rail's risk management processes, including weather forecasting accuracy, risk assessment dependability, resource deployment, and real-time monitoring of rainfall events (ibid.). The latter poses risk to effective emergency evacuation planning, which is crucial for maintaining safety and efficiency in transportation networks during impending natural hazards (Dulebenets et al., 2019a).

Every 5 years, the United Kingdom Government presents a Climate Change Risk Assessment (CCRA) to Parliament, based on an independent analysis by the Adaptation Committee, a sub-committee of the Climate Change Committee. In June 2021, the committee identified eight urgent action areas, including climate-related risks to the power system. The CCRA highlighted that, by 2050, the financial cost of infrastructure risks in a 2°C global warming scenario would be "very high," with economic costs exceeding £1 billion per annum (UK Climate Change Risk Assessment, 2022). There are still gaps in defining methodologies for risk assessment that National Critical Infrastructure (CNI) stakeholders from both government and operators can apply in practice (Climate Change Committee, 2021). Clarifying these methodologies and their related data requirements is crucial for prioritizing investments in resilience and addressing climate-related risks more effectively (United Kingdom Readiness for Storms, 2022). Unawareness of cascading risks may lead to delayed or absent mitigation actions and increased casualties during disasters, highlighting the need for cross-regulator collaboration due to the interconnectedness of various sectors and their shared risks (House of Lords Risk Assessment and Risk Planning Committee, 2021).

Asymmetries and gaps in the governance of floods, droughts, and heatwaves in the United Kingdom

Every risk of civil emergency has a government lead department at national level that is responsible for the day-to-day coordination, support and oversight of risks and management of response by central government (Civil Contingencies Secretariat, 2004; DEFRA, 2015). Figure 1 has an overview of the governance structure for floods, droughts, and heatwaves. The Department of Health and Social Care (DHSC) is the lead government department for heatwaves (Figure 1). The Department for Food and Rural Affairs (DEFRA) is the lead for floods and droughts, providing funding for risk management through grants to the Environment Agency, local authorities, and drainage boards. New or revised flood policies are prepared with other parts of government such as the Treasury, the Cabinet Office (for emergency response planning) and the Department for Communities and Local Government (e.g., for land-use and planning policy). These national policies are delivered by Risk Management Authorities (RMAs). RMAs have their own mandates with respect to risk management but should co-operate and share information in compliance with the national and local Flood and Coastal Erosion Risk Management Strategies.

TABLE 2 Phases of the integrated emergency management in the UK[a].

Phases	Description
Anticipation	Horizon-scanning for identification of risks and potential emergencies
Assessment	Analysis of likelihood of occurrence and impact of emergencies. Risk knowledge (National Risk Registry)
Prevention	Measures to stop a disaster event and/or prevent its harmful effects on communities and infrastructure (e.g., safety standards, flood defense, land use regulations, building codes, preventive healthcare, education and provisions of basic needs and services)
Preparedness	Measures to limit the impact of a disaster, including through quick and orderly reaction and structured response (e.g., warning systems, evacuation, rescue and relief, counter-disaster plans, stockpiling of supplies, resource trade-off and/or conflict plans, community drills, education and awareness)
Response	Measures and decisions to deal with a disaster as soon as it happens, split in two objectives: (i) crisis management that includes measures to avert a disaster, with protective actions that can mitigate its effects, prevent damage or disruption and secure livelihoods (e.g., fighting fires, search and rescue, health advice; and (ii) impact management that includes steps to stop incident from escalating (restoring utility services, providing shelter)
Recovery	Measure to rebuild, restore and rehabilitate the communities impacted by a disaster, which can take months or years (e.g., reconstruction of infrastructure and restoration of people's wellbeing - physical, mental, emotional, social and economic)

[a]Information source retrieved from (Deeming, 2017).

According to the principle of subsidiarity that guides the United Kingdom's governance of civil emergencies, decisions should be taken at the lowest appropriate level with co-ordination at the highest level (HM Government, 2004). Most incidents are best managed by local authorities, affected industries and emergency responders. Category 1 responders at local level (emergency services, local authorities, NHS bodies) have the duty to maintain plans for preventing emergencies, reducing, controlling, and mitigating its effects, while acting when emergencies happen by observing the formal arrangements to warn, inform and advise the public accordingly (Cabinet Office, 2012). The latter should involve Category 2 responders, which include electricity distributers and transmitters, gas distributers, water and sewerage undertakers, telecommunication providers, transport organizations, health bodies and government agencies) and other relevant voluntary organizations when developing plans. The local tier also provides the building block of the response to disasters (Cabinet Office, 2013a). The United Kingdom has developed a concept of operations specifically to guide how different levels should respond and recover from emergencies by working together (UK Cabinet Office, 2013). The Strategic and Recovery Co-ordinating Groups act as the local mechanism during the response and recovery phases of disasters (ibid.). To improve the overall co-ordination and communication between the central government and local responders, and other organizations, a sub-national tier was created as a key element of the civil protection framework (Cabinet Office, 2012). Under this tier, local responders, and central government work in partnership to ensure a coordinated planning and response, either through multi-agency setting or directly between two or more responders (ibid.). This cross-boundary work to address large-scale issues aims to enable the pooling of resources, avoidance of duplication of work by LRF and support for emergencies crossing local resilience areas (Cabinet Office, 2013a). The Department for Communities and Local Government has a Resilience and Emergencies Division, which provides the platform for multi-LRF cooperation (ibid.). The governance model in which United Kingdom civil protection is delivered to protect people, businesses and infrastructure from floods, droughts and heatwaves is the Integrated Emergency Management in Table 2, which entails six key phases–anticipation, assessment, prevention, preparation, response, and recovery (Cabinet Office, 2013b).

Legislation plays a crucial role in the governance of disaster risk reduction and equitable resilience. Table 3 has a snapshot of key laws and plans that apply directly or indirectly to the reduction of risks to floods, droughts, and heatwaves, with consideration of which global policy agendas they relate to. They set out the norms and frameworks for disaster risk governance, implementing strategies and creating specific accountabilities and liabilities for public officials, private sectors, and society. By regulating risk-related decisions, actions and responsibilities, the law sets out how the integration and coordination of local and national disaster risk management and practices should happen, including the distribution of resources and powers among different sectors and institutions (Mehryar and Surminski, 2020). In the United Kingdom, the Civil Contingencies Act provides an overarching framework for reducing risks to civil emergencies, including floods, droughts, and heatwaves, putting a duty on emergency planners and responders to identify and assess the risks affecting the area in which they operate (HM Government, 2004). Whereas the Act is responsible for setting the duties for civil protection, the details of what the duties entail, how they should be conducted and delivered is set under Regulations. Neither the Act or Regulations impose a statutory duty for authorities to take a more proactive approach towards reducing the likelihood of threats, so responders can decide how to treat risks beyond the emergency plans that are required by the Act, leaving prevention and pre-emption out (Deeming, 2017).

Actions to manage the risks of floods and coastal erosion are set under the Flood and Water Management Act (2010), which is the principal legislation guiding preparedness and response to floods in the United Kingdom. It includes the building sector, natural processes, water levels, river or watercourse, shoreline, regulatory instruments, financial support, forecast and warning, information dissemination and education. The potential and/or confirmed harmful consequences of floods for health, social and economic welfare of individuals and communities, infrastructure, and the environment (including cultural heritage) form the basis of risk

TABLE 3 Mapping key documents for managing floods, droughts, and heatwaves with global frameworks.

Key Legal Documents	Floods Droughts Heatwaves	Sendai Framework Priorities	SDGs	Climate Change Adaptation
Water Act 2003	Droughts	1, 2, 3, 4	SDG 2, 3, 6, 11	Article 7
Drought Plans 2003 onwards	Droughts	2	SDG 6, 13	Article 7
Civil Contingencies Act 2004	All	1, 2, 4	SDG 11, 13, 15,	Article 7
Heatwave Plan for England 2004 onwards	Heatwave	2	SDG 11, 13	Article 7
Climate Change Act 2008	All	1, 2, 3, 4	SDG 13	Articles 2, 7
Flood Risk Regulation 2009	Flood	3, 4	SDG 11, 13, 15	Article 7
Flood and Water Management Act 2010	Flood	1, 2, 3, 4	SDG 11	Article 7
Equality Act 2010	All		SDG 5	Article 8, 11, 12,
Water Act 2010	Drought	2	SDG 6	Article 7
Health and Social Care Act 2012	Heatwave	1, 2	SDG 3	Article 11
First National Adaptation Programme 2013-18	Flood and droughts	4	SDG 13	Article 7 and 15
Resilience and Capabilities Programme (2013)	All	4	SDG 11	Article 11
National Guidance on Risk Assessment (2013)	All	1	SDG 13	Article 11
Flood RE Insurance Scheme 2016 - 2039	Flood	3, 4	SDG 13	Article 7
Drought Response Plan 2017	Drought	2	SDG 11, 13	Article 7
Second National Adaptation Plan (2018-23)	All	2	SDG 11, 13	Article 7
Community Resilience Development Framework 2019	All	1, 2, 3	SDG 13	Article 7
National Risk Register 2020	All	1, 2, 3	SDG 13	Article 4, 7
Environment Bill 2021	All	4	SDG 6, 11, 12, 13, 14, 15	Article 4, 7, 8
Flood risks and management plans 2021-27	Flood	1, 2, 3	SDG 13	Article 7, 11
Adverse Weather and Health Plan 2023-24	All	1, 2, 3	SDG 13	Article 7

Source: Paris Agreement, Sendai Framework, SDGs, UK Government.

assessments and risk management strategies. England and Wales need to prepare national and local (FCERMS) (Environment Agency, 2020). At national level, the Environment Agency is responsible for developing, applying, and monitoring these strategies, while 'Lead Local Authorities' are responsible for local flood risk management strategies. The FCERMS sets out who are the flood and coastal erosion risk management authorities at national and local scales (Environment Agency, Lead Local Flood Authorities, District and Borough Councils, Coast protection authorities, water and sewerage companies, Internal Drainage Boards, and Highways Authorities), including their functions, objectives, and measures proposed to achieve those objectives. For example, how and when the latter should be implemented, their costs and benefits, as well as how they will be paid. The FCERMS strategy for England was first published in 2011 and the latest revision was made available in 2020. Between 2015 and 2021 more than £2.6 billion of government funding has been allocated to FCERMS (Environment Agency, 2021b). Between 2021 and 2027, the government has committed to double its expenditure on FCERM to £5.2 billion, reaching the highest amount ever allocated for protection against flood risks (ibid.). Another £200 million have also been allocated to advance resilience programme (ibid.). It is predicted that an additional 336,000 properties will be safeguarded, and twenty-five local areas will be able to advance their actions and plans to protect themselves against flood and coastal erosion risks (ibid.). However, the lack of clear standards for flood protection across the United Kingdom means that measures such as flood defences are usually put in place only after severe disasters have occurred (Cabinet Office, 2016). A reactive approach is also true in relation to key legislation and policy instruments that have been developed through time to manage the risks not only of floods, but also of droughts, and heatwaves. Tables 4 shows that key measures from the last 2 decades have been put in place after major disasters happened (e.g., series of floods in 2007 that triggered the United Kingdom Flood and Management Act 2010; Head Office

TABLE 4 Review of hazards and the legal framework (2000–2020).

Year	Hazards	United Kingdom general acts, statutory instruments, plans and programmes
2000	Most widespread and severe flood events in October/November led to 10,000 properties flooded across 700 locations, with widespread disruption of road and rail services (cost of £1bn) (Environment Agency, 2001)	
2001	Highest sunshine value ever recorded since 1909 in England and Wales (2.60 h per day)	Civil Contingencies Secretariat established; Emergency Planning Review (Hodgkin and Sasse, 2022)
2002	Flooding in the end of December 2002 saw areas get 125%–150% of December's average rainfall	
2003	Heatwave that led to 2,000 excess deaths over a 10-day period in August	Water Act
2004	Flooding in North Cornwall	Civil Contingency Act; Southern, Wessex and Anglian Flood Defense Committee Order (The Wessex Regional Flood Defence Committee Order, 2004); Heatwave Plan for England (Public Health England, 2020)
2004–06	Drought with severe impacts in east England. Fish deaths, reduced breeding and green algae identified (Met Office, 2022b)	Southern Regional Flood Defense Committee Order
2005	Flooding in North Yorkshire and Carlie and Stormy spells	First national Risk Assessment. Drought Plan Regulations 2005; Civil Contingencies Act 2004 (Amendment of List of Responders) Order 2005; Civil Contingencies Act 2004 (Contingency Planning) Regulations 2005; Wessex Regional Flood Defence Committee Order; Anglian Regional Flood Defence Committee (Abolition) Order; Social Fund Cold Weather Payments (General) Amendment Regulations
2006	Heatwave with about 680 excess deaths (Met Office, 2018)	Northwest Regional Flood Defence Committee Order; Severn-Trent Regional Flood Defence Committee Order; Mid Kent Water (Non-Essential Use) Drought Order; Southern Water Services (Kent Medway, Kent Thanet and Sussex Hastings) (Non-Essential Use) Drought Order; Southern Water Services (Sussex North and Sussex Coast) (Non-Essential Use) Drought Order; Sutton and East Surrey Water plc (Non-Essential Use) Drought Order
2007	Flooding in Lake District, Cumbria. Floods had an economic cost of £3.9bn (Environment Agency, 2021a)	The Flood Defence (Mimmshall Brook Works) Order 2007
2008	Heavy Rainfall and flooding	First National Risk Register. Planning Act; Climate Change Act; National Risk Register; Civil Contingencies Act 2004 (Amendment of List of Responders) Order
2009	Heatwave with around 300 excess summer deaths	The Flood Risk Regulations; Flood Defence (Robertsbridge Works) Order
2010	2,500+ heat related deaths. Severe flooding in Cornwall. winter of 2010/11 had coldest December in the United Kingdom series dating back to 1910 (Christidis and Stott, 2021)	Flood and Water Management Act; Water Act (provides statutory definition of flooding); Flood Risk Management Functions Order; Flood Risk (Cross Border Areas) Regulations
2010–12	England and Wales drought. Driest 18 months for over 100 years. Two dry winters led to low groundwater level and reservoir stocks hit lowest records, requiring 7 water companies to impose temporary use bans in England. Ended in 2012 with wettest April to September for over 100 years	
2011	Exceptionally warm and dry spring	National Flood and Coastal Erosion Risk Management Strategy for England; The Incidental Flooding and Coastal Erosion (England) Order; The Thames Regional Flood Defence Committee (Amendment) Order
2012	Overall, 2012 was the wettest on record since 1910 (CEH 2012), except for 2000 (Met Office, 2013)	Health and Social Care Act; Public Health England was created and is main body managing heatwaves; National Drought Group; Head Office Drought Plan
2013	March 2013 was the coldest after 1962 in the national record dating back to 1910 and colder than the preceding winter months (according to the Met Office, National Climate Information Centre)	The Flood and Water Management Act (Commencement No. 2, Transitional and Savings Provisions) (England) Order; National Guidance on Risk Assessment; Resilience Capabilities Programme
2013/14	Wettest winter in the region since the beginning of the record in 1948. The period from December 2013 to February 2014 was the stormiest for at least 20 years according to the Met Office (Met Office 2014)	Flood risk maps for each river basin district
2014	The annual Central England temperature (CET) value for 2014 the highest in the 356-year series. At approximately 0.06 °C above the previous 2006 record, it cannot be entirely certain that 2014 was the warmest on record	Water Act; Heatwave Plan for England
2014/15	winter 2014/15 was the sunniest in the United Kingdom since 1930	

(Continued on following page)

TABLE 4 (*Continued*) Review of hazards and the legal framework (2000–2020).

Year	Hazards	United Kingdom general acts, statutory instruments, plans and programmes
2015	Dry early autumn, The United Kingdom provisionally set a record for the greatest 24 h rainfall recorded	National Security and Strategic Defence Review; The Flood Reinsurance (Scheme and Scheme Administrator Designation) Regulations 2015
2016	Strong winds and floodings from storm Angus; and exceptional warmth in September	Flood RE-Re-insurance Scheme (2039)
2017	In Britain the United Kingdom Met Office reported that Wednesday, June 21 was the hottest June day in more than 40 years when temperatures reached 34.5°C at Heathrow	Drought Response Framework for England; National Drought Group
2018	Cold spell in the country in early March 2018. Extremely cold conditions steered a massive Arctic airmass toward the British Isles at the end of February 2018, where it collided with winter storm Emma in the first days of March	The Environment Agency (Teggsnose Reservoir and Langley Bottoms Reservoir) Drought Order 2018
2019	A new highest ever maximum temperature of 38.7 °C was measured in Cambridge. (Met Office, 2019)	The Floods and Water (Amendment, *etc.*) (EU Exit) Regulations
2020	Storm Ciara, Dennis, and Jorge led to flood problems	Agriculture Act; Fisheries Act; Environment Bill

Drought Plan after droughts of 2010–12; and first Heatwave Plan for England in 2004 after the excess deaths of heat in 2003).

The most important legislation and governance mechanisms implemented to manage droughts include: "Water Act 2003", "Flood and Water Management Act 2010", "Water Use (Temporary Bans) Order 2010", "Head Office Drought Plan 2012", "Drought Response Framework for England 2017", drought plans for each of the six regions of the Environment Agency in England, and drought plans for all water companies (Environment Agency, 2012). Accordingly, water companies hold statutory obligation to develop such plans and manage water supply to customers to guarantee supply. DEFRA is responsible for policy and oversight by central government, while the Environment Agency has the duty to safeguard water sources and guarantee there is enough for everyone at reasonable costs and protecting the environment. Drought permits, rota cuts, standpipes and early actions by farmers are some of the key instruments to manage the risks related to severe drought periods. These only come into play when droughts become an emergency, with threats of restrictions to public water supply.

For heatwaves the main governance instruments are a Heatwave Plan and the system for heatwave alert. The plan has been in place since 2004 and is updated every year (Public Health England, 2020). In 2012, the heatwave plan changed significantly to reflect the changes in the healthcare system and align it with Cold Weather Plan and the Public Health Outcomes Framework (ibid.). The plan is primarily for health and social care services and other public agencies and professionals who interact with those most at risk from excessive heat, such as the elderly and people with different disabilities. Responsibilities are set for the DHSC, NHS, Met Office, and community health services. The key measures to manage the heatwave risks include mortality monitoring, defining critical infrastructure, awareness, preparedness, and the resilience capability programme. However, the social processes and structures which influence vulnerability in high temperatures is yet reflected in strategies and there is no longer-term preventive approach.

The United Kingdom legal framework informing multi-hazard risk assessment and governance of floods, droughts and heatwaves counts with many laws, plans, policies, regulations, and programme which were enacted after catastrophic events took place, as shown in Table 4. Consequently, the existing measures often emphasize response and recovery strategies, which are crucial for addressing the immediate impacts of disasters. However, they lack focus on addressing the root causes of vulnerability and promoting long-term resilience to climate hazards. For example, the plans that serve as main policy instrument to manage droughts and heatwaves are essentially response plans. The heatwave plan is criticized for falling short of social, environmental, and technical risk considerations (Abeling, 2017) and insufficient efforts beyond health sector (Brimicombe et al., 2021). The drought plans set the actions that should be carried out by the Environment Agency, water companies, DEFRA, and local councils when a drought occurs. However, it falls short of considerations of disruptions due to network failures, water quality incidents and dependencies across sectors (NIC, 2020). Estimated impacts of climate change calls for more preventative and proactive approaches to manage the cascading risks of hazards and promote equitable resilience (e.g., water transfer networks to prepare for future droughts; sustainable resource management; addressing drivers of vulnerability). Better understanding of the physical, economic, and environmental factors that increase the susceptibility of an individual, assets, and resources to the compounding impacts of hazard will be key to prevent and prepare the most vulnerable to climate change. Laws, plans, policies, and regulations that address risk reduction and adaptation proactively are also key, so that community preparedness, cross-sector collaboration, public awareness and integrated approaches to multi-disaster risk assessment and governance can be advanced.

The asymmetries and gaps in the governance of hazard and disaster risks, and lack of adaptation indicators challenge the understanding about sufficient funding, policies and planning being allocated towards the right actions to protect the most vulnerable. Consequently, environmental justice concerns are raised (e.g., distribution, recognition, participation, and capability). Low-income and vulnerable communities live in areas with higher exposure to climate hazards, such as flood-prone zones or urban heat islands and have fewer resources to adapt to or recover from extreme weather events. Areas that are prone to coastal and

TABLE 5 A combined framework for equitable resilience.

Elements of Equitable Resilience Ensor et al. (2019)	Indicator categories of resilience in social ecological and socio-ecological systems Bahadur et al. (2013)	Environmental justice dimensions Menton et al. (2020)
Recognise subjectivities, inclusion, and representation	Community involvement and inclusion of local knowledge	Procedural justice
	High diversity	All justice dimensions
	High degree of equity	All justice dimensions
	Social capital, values, and structures	Distributional justice
Working across scales	Effective governance institutions	Procedural and distributional justice
	Learning	Recognitional and capabilities justice
Transformative change	Non-equilibrium system dynamics	Distributional justice
	Preparedness and planning	All justice dimensions
	Acceptance of uncertainty and change	Capabilities

tidal flooding in the United Kingdom are over-represented by socially vulnerable neighbourhoods (Sayers et al., 2017). The authors also highlighted that socially deprived communities are at a higher risk of flooding due to a range of factors, including inadequate infrastructure, substandard housing, and limited access to resources and support. Similarly, in the case of floods, these communities may be more likely to live in lower-quality housing that is less resilient to water damage and may not have the financial means to recover from the impacts of flooding. During heatwaves, low-income households may lack access to adequate cooling systems or green spaces that can help mitigate heat stress. Droughts adversely affect agriculture and food production, resulting in higher food prices and potential food shortages. These factors can place an additional burden on already vulnerable communities, exacerbating existing inequalities and health disparities.

The SDGs (Menton et al., 2020), Sendai and CCA do not explicitly mainstream environmental justice within their targets and neither does the United Kingdom have targeted interventions to address the issues of environmental justice. However, distributive justice concerns are on the rise regarding the ways in which the burdens of disasters, the benefits of adaptation and responsibilities are allocated between different individuals and groups. Recognitional justice concerns are also growing due to risks to personal dignity of individuals and collective identities (ibid.) across different phases of risk management. Recognitional justice across all phases of risk management has the potential to ensure that perspectives, needs, and priorities of all communities, are adequately considered in the development and implementation of DR3 policies, strategies, and actions. The capabilities approach to justice concerns the distribution of goods and resources (ibid.) in ways that will support people to flourish based on the multi-dimensions of wellbeing. The latter is particularly relevant in the context of disaster risk management, where the distribution of resources and opportunities is crucial to helping communities build resilience and recover from disasters. Procedural justice concerns the institutional processes in which the unfair distribution of goods and burdens, lack of recognition and lack of capabilities are perpetuated through exclusion and inequitable participation in decision-making processes (Schlosberg and Collins, 2014). In the context of disasters, this can manifest in several ways, such as inadequate representation of vulnerable groups in emergency planning and response efforts, limited access to resources and support, and disparities in disaster recovery outcomes.

The four key elements to build equitable resilience are based on recognizing subjectivities, inclusion, and representation, working across scales, and promoting transformative change (Ensor et al., 2019). These four elements are closely connected to the categories of resilience in socio-ecological systems applied to climate, disaster, and development contexts developed by Bahadur et al. (2013). The latter indicators include absorptive capacity, adaptive capacity, transformative capacity, equity, and ecosystem services (ibid.). We recommend that equitable resilience metrics be developed for the United Kingdom, combining the four key elements identified by Ensor et al. (2019), with the 10 categories of resilience in socio-ecological systems, and the dimensions of environmental justice (Table 5). Risk reduction, risk management and resilience happen in the context of unequal power dynamics, complex resource trade-offs and shifting vulnerabilities stemming for diverse sources and with distinct impacts. Developing equitable resilience metrics will be key to promote resilience-building efforts that can engage with drivers of vulnerability.

Sectoral resilience to floods, droughts, and heatwaves

The United Kingdom's infrastructure faces risks from high temperatures, flooding, drought, coastal erosion (Climate Change Committee, 2021). Flood is considered the most impactful to energy, transport, water, waste, and digital communication, with the number of assets exposed to risks likely to double by 2080 (ibid.). Drought is the most impactful to water, food, and land, with major impacts on biodiversity, agriculture, and forestry. Heatwaves are the most impactful on crops, livestock, productivity loss (2010 heatwave reached a total of £770 million), building sector, transport infrastructure and disruption (ibid.). Some flood protection measures have been implemented by electricity supply, transmission, and distribution companies, reducing risks of interruption of supply, but for other disasters and non-primary

TABLE 6 Lead Government Department (LGD) with Responsibilities on Resilience per Sector.

LDGs	Sector
Department for Business, Energy and Industrial Strategy	Chemicals
Department for Business, Energy and Industrial Strategy	Civil Nuclear
Department for Digital, Culture, Media and Sport Department for Business, Energy and Industrial Strategy	Communications
Ministry of Defence	Defence
Department of Health and Social Care	Emergency Services
Department for Transport	
Home Office	
Department for Business, Energy and Industrial Strategy	Energy
HM Treasury	Finance
Department for Environment, Food and Rural Affairs	Food
Cabinet Office	Government
Department of Health and Social Care	Health
UK Space Agency	Space
Department for Transport	Transport
Department for Environment, Food and Rural Affairs	Water

Source: (Cabinet Office, 2020).

substations, gaps remain (DEFRA, 2020). For the Critical National Infrastructure (CNI), the Cabinet Office commissions Lead Government Departments (LDGs) (Table 6) to produce Sector Security Resilience Plans (SSRP) (Cabinet Office, 2019). These latter plans are prepared through consultations with infrastructure owners and operators, regulators, and government agencies (ibid.). They assess security and resilience considering the risks to each sector, including some activities necessary to mitigate and respond to these risks. However, the lack of understanding of infrastructure interdependencies and the potential for cascading climate risks underscores the need for greater clarity regarding the roles and responsibilities of both state and non-state actors (Environment Agency, 2022). DEFRA leads the Government department for climate adaptation in the United Kingdom, while the Cabinet Office is responsible for overseeing the resilience of Critical National Infrastructure (CNI) and LGDs for each of the 13 CNI sectors (Joint Committee on the National Security Strategy, 2022) (Table 6). Under the support of the Cabinet Office, the LDGs are tasked with resourcing and overseeing the preparedness levels to the potential consequences of each risk in the National Security Risk Assessment (ibid.). Relevant departments also produce National Policy Statements for England and relevant reserved matters, to guide significant infrastructure project decisions (e.g., on ports and waste water), including adaptation requirements (ibid.). Consequently, there are issues involving the allocation of responsibilities for CNI resilience and climate adaptation across Government (ibid.).

The elements of infrastructure considered critical across the sectors are assets, facilities, systems, networks or processes and the essential workers, so any losses involving them have major detrimental impact on accessibility, security, and affordability of essential services (PHE, 2017). Higher storm wind may greatly impact power lines, data cables, offshore structures and wind turbines. The National Infrastructure Commission (NIC) has identified six key aspects of resilience: anticipate, resist, absorb, recover, adapt, and transform (NIC, 2020). The latter is in line with concept of resilience as an ability to "bounce back" after adversity. However, more broadly, the "bounce back" approach adopted within the United Kingdom's civil emergency framework entails risks of perpetuating inequalities and vulnerabilities that feed future disasters (Deeming, 2017). The focus on rapid recovery and restoration of normalcy after a disaster can result in the neglect of vulnerable groups and their needs. This can lead to further marginalization and social exclusion, exacerbating existing inequalities and increasing the risk of future disasters. An example of this can be seen in the United Kingdom's response to the 2015 floods, where the focus was primarily on repairing damaged infrastructure and restoring, without sufficient consideration for the needs of vulnerable groups (ibid.). As a result, some communities were left without access to necessities like food, water, and shelter for extended periods of time, and were more likely to experience long-term negative impacts from the disaster.

The NIC provides expert advice on infrastructure challenges involving energy, transport, water and wastewater, waste, flood and risk management and digital communications, including on framework under development for resilience standards. Land, agriculture, schools, and hospitals are out of the scope of the NIC's expert work, which does not support the critical links between these and those that are part of NIC's work (e.g., energy and water). The NIC recommends the implementation of a

framework for resilience, protecting everywhere equally, but providing a higher standard in urban areas due to services being overwhelmed when compared to rural areas (ibid.). Regulators should be responsible for setting out the initial plans for stress test, as well as the costs and benefits of different resilience standards, dependencies with standards and other sectors, and the range of shocks and stresses that infrastructure services should be resilient to (NIC, 2020). Government should partner with critical infrastructure operators from the public and the private sectors to agree on a common resilience vision for critical infrastructure nationwide and on shared and achievable resilience objectives (ibid.). Questions remain about how the measures and standards will help deliver on cross-sectoral resilience and equity aspects. The latter are hard to answer without data on vulnerability of infrastructure to extreme weather, limited engagement with suppliers on climate change, little assurance for key supply chains and business opportunities from climate change adaptation that are not well reflected in national plans or strategies (Foulkes et al., 2017).

The United Kingdom's National Adaptation Plan sets out the perspectives on resilience of core sectors. One of the main requirements is for all infrastructure projects to leave the environment in a measurable better state than found (UK NAP). For business, there is a lack of indicators that support understanding of effectiveness of adaptation over time and today most of them are self-reported, which may not be representative for different sizes or sectors (ibid.). The lack of data on interdependent risks and resilience actions by infrastructure providers makes it hard to assess whether actions by operators are really reducing risk towards the cascading failures caused by climate-related disruptions. The latter is aggravated by lack of data on how climate risks are being considered in the design and selection of places for new infrastructure as early as early as possible and through the whole life cycle of the asset. When it comes to ports and airports, resilience standards are left to individual operations, with very limited data to assess the frequency of interruptions due to extreme weather events and actions taken to lower those risks. There remains a lack of data to assess the vulnerability of local roads to specific climate risks and to assess progress in managing the impact of climate risks on local roads. In May 2020, the Government announced a £1.7 billion Transport Infrastructure Investment Fund for local roads and motorways (and railways). It is not yet clear what proportion of this additional funding will go towards reactive repair and what resources will be allocated to adaptation and increasing climate resilience. The rail sector remains at increasing risk of river and surface waterflooding under a continuation of planned adaptation action, and increased heat risk causing rails to buckle, overhead cables to sag and signals to fail.

Discussion and conclusion

Risk assessment is a developed area in the United Kingdom. However, at national level, long term adaptation plans and risk assessment (Climate Change Risk Assessments) and shorter term ones like the National Risk Assessment (NRA) are not aligned. Across scales, national and local assessments face discrepancies and a full picture of local risks is not clear. LRFs play a crucial role in developing local risk assessment but are currently underfunded and facing issues to oversee local climate risks. The overall lack of participation of local communities in risk assessment procedures is problematic and raises issues of trust. People's trust affects their response to instructions during emergencies (Dhellemmes et al., 2021). These shortcomings will increasingly impact the United Kingdom's adaptation to climate change and capacity to develop robust evacuation and shelter planning. These plans need to account for the specific risks faced by local communities and the complexities involved in assessing people's reactions to evacuation orders (ibid.). Considering that evacuation and shelter planning in the United Kingdom is based on local risk assessments, the National Resilience Planning Assumptions, and the National Risk Assessment, the identified discrepancies and likely impacts this bring to evacuation plans represent a gap within the broader emergency planning and preparedness in the United Kingdom, which can aggravate climate injustices. Effective evacuation at local level is crucial for vulnerable populations, who due to factors such as age, reduced cognitive functions, mobility, and declining vision, are disproportionately affected by disasters (Abioye et al., 2020). Unfortunately, these groups have also been identified as the most difficult to evacuate (ibid.) and effective allocation of evacuees among emergency shelters is a challenge, compounded by limited capacity and the specific needs of certain groups (e.g., individuals with disabilities, who require placement in special-needs shelters) (Dulebenets et al., 2019b). There are growing concerns in the United Kingdom about the capacity and accessibility of emergency shelters, particularly for vulnerable populations such as individuals with disabilities or the elderly.

Legislation, planning, policies, regulations, tools, governance instruments, collaborations and partnerships exist to support the United Kingdom to prepare and respond to multi-disaster risks and develop its evolving frameworks to implement and monitor the targets of the three global frameworks–SDGs, CCA and SF. However, the United Kingdom faces an adaptation deficit, which compromise targets of risk reduction and resilience across all three agendas and environmental justice. Comparing to heatwaves and droughts, floods count with most developed legal framework and highest allocation of resources. The latter has a dedicated legislation (Flood and Water Management Act, 2010), specific policy (Flood and Coastal Erosion Risk Management Policy, 2020), and strategies developed by local resilience forums, as well as a plethora of actors with distinct responsibilities to help mitigate flood risks. Flooding is the only disaster of the three that is explicitly reflected in the adaptation plans and counts with a growing budget for prevention and preparedness. Between 2021 and 2027, the government has allocated the highest amount to manage floods risks (£5.2bn), with an additional 336,000 properties being safeguarded, and twenty-five local areas able to advance their actions and plans against flood and coastal erosion risks (ibid.). Flood insurance schemes, flood defense and regional flood defense committees serve well the purpose of prevention and preparedness to risks. By 2024, a new national assessment of flood risk will compose the reforms to the United Kingdom's planning system, aimed at safeguarding that future flood risks are considered in decision-making, including through policies and mechanisms that can ensure that effectively (DEFRA, 2022). For the protection against coastal flooding and coastal erosion, an additional £1 million is allocated for the work conducted between Environment Agency and coastal authorities updating the Shoreline Management Plans that will set the priority areas of action and funds for

adaptation. A roadmap to accelerate the uptake of property flood resilience is also being developed together with several changes to the Flood RE Scheme, so that additional funds (above the cost of a claim) are available to flooded properties above the cost of a claim (CCRA, 2022). There is also a strong commitment to develop national set of indicators to monitor trends and understand impacts of flood and coastal erosion risk management policies, with aim to safeguard that communities can build resilience (ibid.).

Heatwaves count with a heatwave plan as the main national policy instrument for managing the risks of extreme heat. A drought Plan is one of the key national policy instruments for managing drought risks. Both plans are essentially an emergency response plan. More preventative approaches that can improve community resilience to risks of droughts and heatwaves will need to consider the factors that can influence an individual's vulnerability to the risks of each type of disaster. For heatwaves, quality of housing and built environment, local urban geography, lifestyle, income, employment, tenure, social networks, and self-perception of risk can influence the level of exposure and sensitivity to extreme heat and capacity to anticipate, prevent, prepare, respond, and recover. For droughts, actions to help lessen impacts includes building a water transfer network, plans to deliver additional supply and reduce demand in case of serious or prolonged droughts, reduce network failures, water quality incidents, and assess dependencies across sectors. Many risks are ignored for warmer scenarios, which are aggravated in the context of missing indicators and lack of specific laws, regulations, policies, instruments, and institutions relevant to heatwave and its impacts beyond health. Altogether, it compromises equitable risk reduction and resilience to all three disasters in the United Kingdom. There are important governance mechanisms, lessons and best practices developed to manage flood risks, which are replicable to enhance the management of the other two types of disasters beyond plans. For example, advanced flood maps that inform planning and land-use, strategy for local flood authorities to manage local risks, asset recovery and business continuity through affordable national insurance, public-private flood reinsurance schemes and analysis of impacts of disasters that translate into lessons learned replicable.

In terms of its Critical National Infrastructure better indicators, analytical tools and cross-sectoral approaches are needed that enable the assessment of vulnerability of infrastructure and impacts from disruption due to extreme weather.

The United Kingdom can expect to face warmer and wetter winters, hotter and drier summers, and rising sea levels, according to the independent Climate Change Committee looking forward to 2050. Allocating resources to adaptation and increasing climate resilience instead of following a reactive repair is necessary. Despite progress made with key sectors conducting individual risk assessments, adaptation gaps are identified across all of them. The current regulatory model for Critical National Infrastructure in the United Kingdom is based on a vertical structure, where each sector is regulated and operated separately, which mirrors the departmental oversight system, contributing to fragmented approaches to climate adaptation (Climate Change Committee, 2021; Joint Committee on the National Security Strategy, 2022). As a result, formal connections between sectors are lacking, creating gaps in preparedness and response to climate risks. This will further increase inequalities and result in long-term consequences for social and economic wellbeing. To enhance collaboration on interdependencies and improve oversight of adaptation and resilience, various mechanisms have been proposed, such as creating a statutory forum for CNI regulators, setting clear resilience standards for CNI operators, and implementing a stress testing program against extreme weather and climate change effects. Infrastructure needs urgent adapted to cope with the potential rapid effects of climate change, presenting a significant challenge for the government, operators, and regulators when it comes to all three disasters we focused on: floods, droughts and heatwaves.

Limitations of study and future research

The National Risk Register has many listed risks, but we focus on floods, droughts and heatwaves and leave many other climate related hazard risks out of the in-depth review and analysis. Consequently, limiting the insights and understanding of gaps in relation other types of hazards (e.g., extreme cold temperatures). Considering that approximately 75 local authorities (one-fifth of the country) have 50% of their population living in flood-prone areas (Sayers *et* al, 2017), further analysis of preparedness and climate adaptation with focus on local level represents another limitation of this study. We recommend that future research focuses on the preparedness of local authorities, considering the barriers they face to manage the risk of hazards and disasters at local level (e.g., underfunded LRFs). Other areas for future research, with a focus on the United Kingdom include.

- Climate change adaptation of national infrastructure.
- Cross-sectoral resilience and preparedness considering cascading impacts of climate related hazards on critically interlinked sectors (e.g., energy and water).
- Development of equitable resilience metrics for the United Kingdom.
- Improving analytical tools and methods for risk assessment across scales and distinct timeframes.
- Public education campaigns on disaster risk reduction and climate change adaptation.
- Public engagement and acceptance of adaptation measures and resilience standards for critical national infrastructure, given consumers will bear costs of high levels of investment to advance these.
- Assessment of existing emergency evacuation plans and their limitations in protecting areas with vulnerable population when multiple infrastructure assets and sectors are affected by hazards.

Author contributions

Both authors contributed to all sections of the article and approved the submitted version.

Funding

This research was funded by Belmont Forum's first disaster-focused funding call Belmont Collaborative Research Action 2019: Disaster Risk, Reduction and Resilience (DR32019) which was supported by the Ministry of Science and Technology (MOST) of Chinese Taipei in partnership with funders from Brazil (FAPESP),

Japan (JST), Qatar (QNRF), UK (UKRI), US (NSF), CNR (Italy). This research was funded by UKRI grant EP/V002945/.

Conflict of interest

The authors declare that the research was conducted in the absence of any commercial or financial relationships that could be construed as a potential conflict of interest.

Publisher's note

All claims expressed in this article are solely those of the authors and do not necessarily represent those of their affiliated organizations, or those of the publisher, the editors and the reviewers. Any product that may be evaluated in this article, or claim that may be made by its manufacturer, is not guaranteed or endorsed by the publisher.

References

Abeling, T. (2017). 'According to plan? Disaster risk knowledge and organizational responses to heat wave risk in London, UK'. *Ecosyst. Health Sustain.* 1 (3), 1–8. doi:10.1890/ehs14-0022.1

Abioye, O. F., Dulebenets, M. A., Ozguven, E. E., Moses, R., Boot, W. R., and Sando, T. (2020). 'Assessing perceived driving difficulties under emergency evacuation for vulnerable population groups'. *Socio-Economic Plan. Sci.* 72, 100878. doi:10.1016/j.seps.2020.100878

Arbuthnott, K., and Hajat, S. (2017). 'The health effects of hotter summers and heat waves in the population of the United Kingdom: A review of the evidence'. *Environ. Health A Glob. Access Sci. Source* 16 (1), 1–13. doi:10.1186/s12940-017-0322-5

Bahadur, A., Ibrahim, M., Tanner, T., Ibrahim, M., and Tanner, T. (2013) Characterising resilience: Unpacking the concept for tackling climate change and development, *Clim. Dev.* 5(1), 55–65. doi:10.1080/17565529.2012.762334

Brimicombe, C., Porter, J. J., Di Napoli, C., Pappenberger, F., Cornforth, R., Petty, C., et al. (2021). 'Heatwaves: An invisible risk in UK policy and research'. *Environ. Sci. Policy* 116, 1–7. doi:10.1016/j.envsci.2020.10.021

Cabinet Office (2012). *Chapter 2 Co-operation - revision to emergency preparedness, civil Contingencies act enhancement programme*. London: Cabinet Office.

Cabinet Office (2013a). *Emergency response and recovery, non statutory guidance accompanying the civil Contingencies act 2004*. London: Cabinet Office. doi:10.1016/b978-159749172-3/50012-8

Cabinet Office (2013b). *Expectations and indicators of good practice set for category 1 and 2 responders*. London: Cabinet Office.

Cabinet Office (2013c). *The role of local resilience forums, guidance*. London: Cabinet Office. Available at: https://www.gov.uk/government/publications/the-role-of-local-resilience-forums-a-reference-document (Accessed: 3 December 2022).

Cabinet Office (2016). *National flood resilience review*. London: Cabinet Office.

Cabinet Office (2017). *National risk register of civil emergencies*. London: Cabinet Office. Available at: www.official-documents.gov.uk (Accessed: 10 March 2021).

Cabinet Office (2019). *Public summary of sector security and resilience plans*. London: Cabinet Office.

Cabinet Office (2020). *National risk register 2020*. London: Cabinet Office.

Christidis, N., and Stott, P. A. (2021). 'The influence of anthropogenic climate change on wet and dry summers in Europe'. *Sci. Bull.* 66 (8), 813–823. doi:10.1016/j.scib.2021.01.020

Civil Contingencies Secretariat (2004). *'The lead government department and its role – guidance and best practice'*. London: Cabinet Office. [Preprint]. Available at: https://www.gov.uk/government/uploads/system/uploads/attachment_data/file/61355/lead-government-departments-role.pdf.

Climate Action Tracker (2022). *2100 Warming Projections: Emissions and expected warming based on pledges and current policies*. Germany: Climate Analytics and NewClimate Institute. Available at: https://climateactiontracker.org/global/temperatures/.

Climate Change Committee (2016). *UK climate change risk assessment*. London. Available at: https://www.gov.uk/government/publications/uk-climate-change-risk-assessment-2017 (Accessed: 1 December 2022).

Climate Change Committee (2021). *Independent assessment of UK climate risk*. Available at: https://www.theccc.org.uk/publication/independent-assessment-of-uk-climate-risk/ (Accessed: 1 December 2022).

Deeming, H. (2017). *Disaster risk reduction and the Sendai framework - what does it mean for UK resilience practitioners? emergency planning College*. Available at: https://www.epcresilience.com/EPC.Web/media/documents/Papers/OP21-Disaster-Risk-Reduction-Jun-2017.pdf.

DEFRA (2020). *Flood and coastal erosion risk management: Policy Statement*. London. Available at: https://www.gov.uk/government/publications/flood-and-coastal-erosion-risk-management-policy-statement.

DEFRA (2015). *Flooding in England: Lead government department plan*. Available at: https://assets.publishing.service.gov.uk/government/uploads/system/uploads/attachment_data/file/399931/pb14297-flood-lead-department-plan.pdf.

DEFRA (2022). *UK climate change risk assessment*. doi:10.1108/ijccsm.2012.41404baa.006

DFID (2019). *Voluntary national review progress towards the sustainable development Goals*.

Dhellemmes, A., Leonard, G. S., Johnston, D. M., Vinnell, L. J., Becker, J. S., Fraser, S. A., et al. (2021). 'Tsunami awareness and preparedness in Aotearoa New Zealand: The evolution of community understanding',. *Int. J. Disaster Risk Reduct.* 65, 102576. doi:10.1016/j.ijdrr.2021.102576

Dulebenets, M. A., Abioye, O. F., Ozguven, E. E., Moses, R., Boot, W. R., and Sando, T. (2019a). 'Exact and heuristic solution algorithms for efficient emergency evacuation in areas with vulnerable populations. *Int. J. Disaster Risk Reduct.* 39. doi:10.1016/J.IJDRR.2019.101114

Dulebenets, M. A., Pasha, J., Abioye, O. F., Kavoosi, M., Ozguven, E. E., Moses, R., et al. (2019b). 'Exact and heuristic solution algorithms for efficient emergency evacuation in areas with vulnerable populations'. *Int. J. Disaster Risk Reduct.* 39, 101114. doi:10.1016/j.ijdrr.2019.101114

Ensor, J., Forrester, J., and Matin, N. (2019). What is equitable resilience? *World Dev.* 109. doi:10.1016/j.worlddev.2018.04.020

Environment Agency and Bevan, S. J. (2019) *Escaping the jaws of death: Ensuring enough water in 2015, speech by sir james bevan, chief executive of the environment agency waterwise conference*. means that in the,water during the summer months. Available at: https://www.gov.uk/government/speeches/escaping-the-jaws-of-death-ensuring-enough-water-in-2050#:~:text=It. (Accessed: 2 December 2022).

Environment Agency (2001). *Lessons learned autumn 2000 floods*. Bristol: Environment Agency. Available at: https://assets.publishing.service.gov.uk/government/uploads/system/uploads/attachment_data/file/292917/geho0301bmxo-e-e.pdf (Accessed: 8 December 2022).

Environment Agency (2012). *Head Office drought plan*. Bristol: Environment Agency.

Environment Agency (2017). *Drought response: Our framework for England, environment agency*. Bristol: Environment Agency. Available at: https://assets.publishing.service.gov.uk/government/uploads/system/uploads/attachment_data/file/625006/LIT_10104.pdf.

Environment Agency (2020). *National flood and coastal erosion risk management strategy for England*. Bristol: Environment Agency. Available at: https://www.gov.uk/government/publications/national-flood-and-coastal-erosion-risk-management-strategy-for-england.

Environment Agency (2021a). *Living better with a changing climate*. Bristol: Environment Agency.

Environment Agency (2021b). *National flood and coastal erosion risk management strategy for England: Executive summary - GOV.UK, GOV.UK*. Available at: https://www.gov.uk/government/publications/national-flood-and-coastal-erosion-risk-management-strategy-for-england–2/national-flood-and-coastal-erosion-risk-management-strategy-for-england-executive-summary (Accessed: 10 March 2021).

Environment Agency (2022). *Written evidence submitted by the environment agency*. Bristol: Environment Agency. Available at: https://committees.parliament.uk/writtenevidence/43545/pdf/.

Environment Agency, DEFRA and Double (2022). *National Drought Group agrees further steps to manage drought now and in the long term, Press Release*.

Flood and Water Management Act 2010, c29 (2010). United Kingdom: UK Public and General Acts. Available at: https://www.legislation.gov.uk/ukpga/2010/29/contents.

Foulkes, C., Wynn, S., Wilson, L., Mohan, C., Elizabeth, E., and Wheeler, K. (2017). *Research to provide update indicators of climate change risk and adaptation action in England*. The Climate Change Committeee, 203. (10486936).

HM Government (2004). *Civil Contingencies act 2004*.

Hodgkin, R., and Sasse, T. (2022). *Managing extreme risks - how the new goverment can learn from Covid to be better prepared for the next crisis*. Available at: www.instituteforgovernment.org.uk (Accessed: 8 December 2022).

House of Lords Risk Assessment and Risk Planning Committee (2021). *Preparing for Extreme Risks: Building a Resilient Society, HL Paper 110*. London. Available at: https://committees.parliament.uk/publications/8082/documents/83124/default/.

Joint Committee on the National Security Strategy (2022). *Readiness for storms ahead? Critical national infrastructure in an age of climate change*. London. Available at: https://committees.parliament.uk/publications/30507/documents/175976/default/.

Kendon, M., McCarthy, M., Jevrejeva, S., Matthews, A., Sparks, T., and Garforth, J. (2020). 'State of the UK climate 2019'. *Int. J. Climatol.* 40 (S1), 1–69. doi:10.1002/joc.6726

Mehryar, S., and Surminski, S. (2020). *The role of national laws in managing flood risk and increasing future flood resilience*. Working Paper 334, Working Pa(365).

Menton, M., Larrea, C., Latorre, S., Martinez-Alier, J., Peck, M., Temper, L., et al. (2020). 'Environmental justice and the SDGs: From synergies to gaps and contradictions'. *Sustain. Sci.* 15 (6), 1621–1636. doi:10.1007/s11625-020-00789-8

Met Office (2013). *England and Wales drought 2010 to 2012*. London. Available at: https://www.metoffice.gov.uk/binaries/content/assets/metofficegovuk/pdf/weather/learn-about/uk-past-events/interesting/2012/england-and-wales-drought-2010-to-2012–met-office.pdf.

Met Office (2018). *State of the UK climate 2017: Supplementary report on climate extremes*. Available at: https://www.metoffice.gov.uk/binaries/content/assets/metofficegovuk/pdf/weather/learn-about/uk-past-events/state-of-uk-climate/soc_supplement-002.pdf (Accessed: 8 December 2022).

Met Office (2021). *Storm Arwen, 26 to 27 November 2021*. London. Available at: https://www.metoffice.gov.uk/binaries/content/assets/metofficegovuk/pdf/weather/learn-about/uk-past-events/interesting/2021/2021_07_storm_arwen.pdf.

Met Office (2019). *'New official highest temperature in UK confirmed'*. London: Press Office, 2. 29 July.

Met Office (2022a) *Record high temperature verified*, *Press Office*, 28 July, p. 2. Available at: https://www.metoffice.gov.uk/about-us/press-office/news/weather-and-climate/2022/record-high-temperatures-verified.

Met Office (2022b). *UK and global extreme events – drought, climate science*. Available at: https://www.metoffice.gov.uk/research/climate/understanding-climate/uk-and-global-extreme-events-drought (Accessed: 2 December 2022).

Met Office (2022c). *UK storm season 2021/22, UK Storm Centre*.

NIC (2020). *Anticipate, react, recover*.

OFGEM (2022). *Ofgem publishes full report following six-month review into networks' response to Storm Arwen, Press Release*. Available at: https://www.ofgem.gov.uk/publications/ofgem-publishes-full-report-following-six-month-review-networks-response-storm-arwen#:~:text =Today%2C 9 June 2022%2C Ofgem,response to severe weather events.

PHE (2017). *Public health England and the Sendai framework for disaster risk reduction 2015-2030*. London: PHE publications. Available at: https://assets.publishing.service.gov.uk/government/uploads/system/uploads/attachment_data/file/653164/PHE_and_the_Sendai_Framework.pdf.

Public Health England (2020). *Heatwave plan for England Protecting health and reducing harm from severe heat and heatwaves*. London.

RAIB (2022). *Rail Accident Report*. Derby. Available at: https://assets.publishing.service.gov.uk/media/62274fe0e90e0747a49c94ca/R022022_220310_Carmont.pdf.

Sayers, P. B., Horritt, M., Penning Rowsell, E., and Fieth, J. (2017). *Present and future flood vulnerability, risk and disadvantage A UK assessment prepared for joseph rowntree foundation, climate change and communities programme*. Available at: http://www.sayersandpartners.co.uk/flood-disadvantage.html.

Schlosberg, D., and Collins, L. B. (2014). From environmental to climate justice: Climate change and the discourse of environmental justice. *Wiley Interdiscip. Rev. Clim. Change* 5 (3), 359–374. doi:10.1002/wcc.275

The Climate Coalition (2021) *The climate coalition report: How climate change threatens our health*. Available at: https://www.theclimatecoalition.org/health-report (Accessed: 2 December 2022).

The Wessex Regional Flood Defence Committee Order (2004). *The wessex regional flood defence committee order 2004*. Available at: https://www.legislation.gov.uk/uksi/2004/3164/data.pdf (Accessed: 9 December 2022).

UK Cabinet Office (2013). "Responding to emergencies the UK central government response concept of operations," in *Central government of England*, 1–80.

UK Climate Change Risk Assessment, 2022 and CCRA, 2022: DEFRA (2022). *UK Climate Change Risk Assessment*. London. doi:10.1108/ijccsm.2012.41404baa.006

UK Readiness for Storms: Joint Committee on the National Security Strategy (2022). *Readiness for storms ahead? Critical national infrastructure in an age of climate change*. London. Available at: https://committees.parliament.uk/publications/30507/documents/175976/default/.

UNISDR (2015a). *Disaster risk reduction and resilience in the 2030 agenda for sustainable development*.

UNISDR (2015b). *Sendai framework for disaster risk reduction 2015-2030*.

UNISDR (2017). *Disaster-related data for sustainable development - Sendai framework data readiness review*. Available at: https://www.preventionweb.net/files/53080_entrybgpaperglobalsummaryreportdisa.pdf. (Accessed: 3 December 2022).

WMO (2022). *Eight warmest years on record witness upsurge in climate change impacts, press release number: 06112022*. Geneva: WMO. Available at: https://public.wmo.int/en/media/press-release/eight-warmest-years-record-witness-upsurge-climate-change-impacts.

frontiers | Frontiers in Earth Science

TYPE Original Research
PUBLISHED 13 May 2024
DOI 10.3389/feart.2024.1414763

OPEN ACCESS

EDITED BY
Xiya Zhang,
China Meteorological Administration, China

REVIEWED BY
Yulong Cui,
Anhui University of Science and Technology, China
Adolfo Quesada-Román,
University of Costa Rica, Costa Rica
Zhao Zhou,
Xi'an University of Science and Technology, China

*CORRESPONDENCE
Junxue Ma,
sdnj2mjx@163.com

RECEIVED 09 April 2024
ACCEPTED 29 April 2024
PUBLISHED 13 May 2024

CITATION
Ma J, Chen J and Xu C (2024), Sedimentary records of giant landslide-dam breach events in western Sichuan, China.
Front. Earth Sci. 12:1414763.
doi: 10.3389/feart.2024.1414763

Sedimentary records of giant landslide-dam breach events in western Sichuan, China

Junxue Ma[1,2]*, Jian Chen[3] and Chong Xu[1,2]

[1]National Institute of Natural Hazards, Ministry of Emergency Management of China, Beijing, China, [2]Key Laboratory of Compound and Chained Natural Hazards Dynamics, Ministry of Emergency Management of China, Beijing, China, [3]School of Engineering and Technology, China University of Geosciences Beijing, Beijing, China

Introduction: Landslide-dammed lake outburst floods (LLOFs) are common natural disasters in high-mountain regions, posing serious safety threats to residents' livelihoods and properties and causing major damage to engineering facilities. Giant landslides and river damming events commonly occur in the Eastern Tibetan Plateau in southwestern China. Dam failure generate LLOFs that form outburst deposits (ODs). This phenomenon is particularly common in some giant ancient landslide-dammed lakes.

Methods: This study conducted a detailed investigation of the sedimentary characteristics of large-scale landslide-dammed lake outburst deposits in the Diexi Reach of the Upper Minjiang River and Tangjiashan Reach of the Tongkou River Basin, West Sichuan Plateau, China. Meanwhile, typical evidence of high-energy ODs was recorded.

Results and Discussion: The longitudinal distribution of these ODs is similar to an elongated fan-shaped terrace along the river channel, presenting a distinctive sedimentary disordered–sub-ordered–ordered sequence from upstream to downstream. Several typical units of "*sedimentary facies*" are developed in the OD profiles, such as boulder units deposited by high-energy outburst flood (OF) events and the gravel and sand units representing pulsating-flow sedimentary environments during the recession stage. The grain size frequency curves are bimodal, and the granularity accumulated curves are upward convex, which reflect that the detrital characteristics of the sediment source area are mainly composed of coarse gravel and boulders. This indicates that the coarse gravel sediment gradually become decreased from upstream to downstream. Moreover, the OD hydrodynamic intensity displays a gradual weakening, and sediment sorting is improved. From upstream to the downstream, the mean particle-size and sorting of the ODs gradually decrease. The skewness become larger, and the kurtosis of the ODs is distributed in all the types. In addition, the different combinations of quartz sand surface microtextures indicate the transformation from high-to low-energy impacts over a short distance, which is controlled by flood hydrodynamics and regime.

Significance: These sedimentary characteristics of ODs explain the hydrodynamic changes during the propagation of OFs, and are also important records for distinguishing between ODs, and "*normal*" floods.

KEYWORDS

landslide-dammed lake, dam breach, outburst floods (OFs), outburst deposits (ODs), sedimentary characteristics, western Sichuan of China

1 Introduction

Catastrophic flood events are the most destructive natural disasters in the world (O'Connor et al., 2002; Herget and Fontana, 2019; Wang H. et al., 2022), and their complete frequencies and magnitudes cannot be captured by direct observation or measurement (Baker, 2008; Korup and Clague, 2009; Wang et al., 2023a; Benito et al., 2023). It is crucial to reconstruct flood records on the scale of millennia or thousands of years based on geological, geomorphological and chronological flood indicators (Carling, 2013; Chen et al., 2018; Ma et al., 2018; Baker et al., 2022; Baker and Carling, 2022; O'Connor et al., 2022; Quesada-Román et al., 2022). Affected by global warming, the hydrological and climatic changes in the Tibetan Plateau are intensifying, which increases the risk and occurrence of dammed lake OFs (Korup and Montgomery, 2008; Roe et al., 2017; Shugar et al., 2020; Bazai et al., 2021; Taylor et al., 2023). In recent years, an increasing number of studies on catastrophic flood events have been conducted in the Tibetan Plateau (Herget and Fontana, 2019; Baker et al., 2022; O'Connor et al., 2022; Yang et al., 2022). In most of the catastrophic flood cases, dammed lake OFs account for the largest number and widest distribution (Carling, 2013; Srivastava et al., 2017; Liu et al., 2019; Borgohain et al., 2020; Fan et al., 2020; Ma et al., 2022; Yang et al., 2022; Wang et al., 2023b).

There are more than 200 dammed lake OFs known on Earth, with peak discharges exceeding 108 m^3/s, and their peak discharges are more than 100 times that of the known maximum meteorological flood (O'Connor et al., 2002). In the research by O'Connor et al. (2022), of the 241 cases of dammed lake OFs on Earth with precise peak flow records, 25 were caused by landslide-dammed lake outburst floods (LLOFs). Among these LLOFs, the high mountainous areas of the Tibetan Plateau in southwest China have the highest distribution. These LLOFs often have profound and lasting impacts on regional geomorphological evolution (Korup and Montgomery, 2008; Korup, 2012; Liu et al., 2018; Fan et al., 2020; Ma et al., 2022). Moreover, the outburst floods (OFs) will also cause a large influx of freshwater resources into the ocean, which is closely related to the fluctuations of the Quaternary climate (Teller et al., 2002). Therefore, reconstructing historical floods on the Tibetan Plateau and analyzing their sensitivity to climate conditions will contribute to a better understanding of the impact of future climate change on extreme hydrological events (Knox, 2000; Benito et al., 2015; Støren et al., 2016; Harrison et al., 2018; Baker et al., 2022). In addition, the study of dammed lake OFs has profound significance for river evolution, mountain environmental changes, and human civilization development (Baker, 2008; Peng and Zhang, 2013; Liu et al., 2019; Fan et al., 2020; Wang et al., 2023b; Taylor et al., 2023).

For modern dammed lake OFs, there are usually historical or detailed data records, such as the 1933 Diexi Earthquake (25 August 1933, Ms.7.5), which resulted in 11 landslide-dammed lakes in the Diexi area, Sichuan, China, which breached on October 9 and killed approximately 2,500 people (Li et al., 1986). Another example is the Tangjiashan dammed lake induced by the Wenchuan Earthquake in 2008 (Cui et al., 2012; Peng and Zhang, 2013; Chen et al., 2015; Wang Z. et al., 2022) and the Baige dammed lake in Jinsha River in 2018 (Tian et al., 2020; Zhong et al., 2020; Liu et al., 2021; Zhang et al., 2023), both of which have detailed data on the OFs. However, there are no records of ancient OF events, particularly those that occurred during the geologic era, which need to be deduced using geomorphology, hydrology, sedimentology, meteorology, and other methods. The OF sediments (outburst deposits, ODs) formed in the lower reaches of the dams are become the most direct evidence of OFs induced by dammed lakes. Analyzing the distribution and sedimentary characteristics of ODs is of great significance for the paleohydrological reconstruction of dammed lake OFs (Dai et al., 2005; Carling, 2013; Chen et al., 2013; Wang P. et al., 2014; Ma et al., 2022; Wang et al., 2023a; Wang et al., 2023b).

Currently, research cases and data on landslide-dammed lakes and LLOFs mainly focus on the causes and processes of landslide damming, lake evolution, dam stability and breach mechanism, hazard assessment and mapping, geomorphic consequences, and sedimentary and controlling effects of the LLOFs on mountain topographic and climatic features (Costa and Schuster, 1988; Huggel et al., 2002; Ermini and Casagli, 2003; Korup et al., 2010; Peng and Zhang, 2012; Walder et al., 2015; van Gorp et al., 2016; Zheng et al., 2021; Wu et al., 2022). Theoretical and model experimental studies have mostly been conducted (Chang and Zhang, 2010; Schmocker et al., 2014; Shi et al., 2015; Jiang et al., 2018; Jiang and Wei, 2019; Zhou et al., 2019; Zhu et al., 2019; Zhong et al., 2021). However, there are still some unresolved problems in the study of the relationship between the sedimentation process of ODs and the dynamic characteristics of flood evolution. The theoretical system is not yet perfect, and there are conflicts among many pieces of evidence. Therefore, new sedimentary evidence is needed to support these issues (Lord and Kehew, 1987; Cutler et al., 2002; Borgohain et al., 2020; Wang et al., 2023a). An abundance of ODs was discovered to be preserved in the Diexi Reach of the Upper Minjiang River and Tangjiashan Reach of the Tongkou River Basin (Ma et al., 2018; Jiang and Wei, 2020; Jiang et al., 2021; Ma et al., 2022). These ODs were formed by LLOFs induced by a giant ancient landslide-dammed lake and the Tangjiashan dammed lake, respectively, and they have good comparability in terms of deposition distribution, sedimentary characteristics and profile structures. From ancient to modern times, these two cases present distinct contrasts and distinctive features, providing important sedimentary evidence for the giant landslide-dam breach events in Western Sichuan, China. The main purposes of this study are as follows: i) to explore the geomorphological and sedimentary characteristics of the ODs in the Diexi Reach of the Upper Minjiang River and Tangjiashan Reach of the Tongkou River Basin; ii) to analyze the hydraulic characteristics of the LLOFs; and iii) to explore the discrimination indicators between dammed lake OF events and other "normal flood" events. This study has a good practical significance for flood disaster prediction and mitigation of dammed-lakes' failures at present and in the future at the southeastern margin of the Tibetan Plateau.

2 Regional settings

The West Sichuan Plateau acts as a transition zone between the Tibetan Plateau (the First Gradient Terrain, and the altitude is more than 3,500 m) and the Sichuan Basin (the Second Gradient Terrain, and the altitude is between 1,000 and 2,000 m)

(Figure 1A), with a vertical drop of more than 2,000 m between the two terrains. This region is in the "*Tethys–Himalayas–Tectonic Zone*," surrounded by triangular geological structures composed of the Songpan–Ganzi geosynclinal fold belt (NWW direction), the West Qinling geosynclinal fold belt (EW direction), and the Longmenshan–Minshan fault zone (NE direction). Some complex tectonic structures have developed in this area, such as the well-known "*NS-Trending Tectonic Zone*" (Wang et al., 2011; Zhang, 2013) and several groups of major active fault zones—the Longmenshan–Minshan, Minjiang, Huya, and Yingxiu–Beichuan fault zones (Figure 1A). The study area is characterized by frequent fault activities, frequent earthquakes and poor stability. Several historical large-magnitude earthquakes have occurred in the past 2,000 years, including some large-scale ancient seismic activities (Ran et al., 2008; Wang et al., 2011).

The Diexi Reach belongs to the middle section of the Upper Minjiang River, located between Songpan County (upstream) and Maoxian County (downstream) in A'ba Prefecture, Sichuan Province, with distances of 80 km and 60 km, respectively (Figure 1A). Deep incisions along the Upper Minjiang River resulted from intense tectonic uplift at the West Sichuan Plateau in the southeastern margin of the Tibetan Plateau since the late Cenozoic (Li et al., 1986; Burchfiel et al., 1995; Xue et al., 1998; Gao et al., 2002). This region is characterized by high mountains and deep valleys with heights of ~3,000 and 1,500 m, respectively. Owing to the deep incisions, U- or V-shaped gorges are the main features of the valleys, with steep slopes, mostly above 60°. The valleys are relatively wide, ranging from tens of meters to several hundred meters. Many small canyons are distributed on both sides of the river, mostly alternating between mountains and rivers. According to the regional geological survey report of the Sichuan Provence (RGSTS, 1975), the lithology in the area mainly consists of sandstone, phyllite, limestone, and griotte. It is evident that these rocks have experienced different degrees of regional metamorphism (Figure 1B). The drought phenomenon in this region is relatively serious, belonging to the subtropical plateau–continent monsoon climate, with an average annual rainfall of only 420 mm. The Minjiang River is a perennial hydrographic system in this region, with an annual average flow of 21.178 billion m^3, which is mainly supplied by atmospheric precipitation (Ma et al., 2022). In addition, the Diexi Haizi dammed lakes, caused by the 1933 Diexi Earthquake are composed of Shanghaizi (or Dahaizi) Lake and Xiahaizi (or Xiaohaizi) Lake, with a maximum width of 692 m, ~80 m in depth and length of more than 10 km (Figure 1C). The total catchment area on the Diexi Haizi is approximately 3.15 km^2, among which, the catchment areas of the Shanghaizi and Xiahaizi Lakes are 1.8 and 1.35 km^2, respectively, and the corresponding volumes are 7×10^7 and 5×10^7 m^3, respectively (Figure 1C).

The Tangjiashan dammed lake is located in the Tongkou Reach of the Fujiang River. The landslide dam is approximately 6.5 km away from Beichuan County downstream and approximately 74.5 km from the Diexi dammed lake. The Tangjiashan Reach is a V-shaped valley with a steep right bank (40°–60°) and a gentle left bank (~30°) terrain, and many small gullies are developed. The water level in the Tangjiashan Reach is approximately 0.5–4.0 m, with a water surface elevation of approximately 664.7 m (dry season) and width of <300 m before the 2008 Wenchuan Earthquake occurred (Cui et al., 2012; Chen et al., 2015). The Tangjiashan region has a subtropical monsoon climate with an uneven distribution of rainfall and an average annual rainfall of 1,335 mm, which is concentrated in summer (May to September). The inflow during the formation stage of the barrier lake is approximately 80 m^3/s (Bo et al., 2015; Wang Z. et al., 2022). The landslide dam in the Tangjiashan Reach is a long strip with a length of 803.4 m along the river and a maximum width of 611.8 m in the transverse direction. The top width of the landslide dam is approximately 300–310 m, and the lowest and highest points of the dam crest have elevations of 752.1 m and 793.9 m, respectively. The estimated volume is approximately 20.37 million m^3, and the catchment area of the Tangjiashan dammed lake is 3,550 km^2. On 21 May 2008, the lake water elevation reached 711.0 m, with a volume of approximately 72.5 million m^3. A relatively wide new river channel was formed after the completion of discharge, with a curved shape protruding toward the right bank. The length and bottom width of the new central river channel are approximately 890 m and 100 m, respectively, with a depth of 40–60 m (Cui et al., 2012; Chen et al., 2015; Zhao et al., 2018; Xiong et al., 2022).

3 Materials and methods

3.1 Sedimentological investigation

Previous studies have commonly used slack water deposits (SWDs) (Jarrett and England, 2002) as paleo-stage indicators (PSIs) of ancient floods (Guo et al., 2017; Ruiz-Bellet et al., 2017). Paleoflood SWD-PSI is a type of suspended sediment with a sharp decrease in flow velocity under high water level stagnation (or backwater) environments, usually consisting of fine-grained sand, clay and silt with parallel bedding (Guo et al., 2023; Mao et al., 2023). It is considered to be a complete paleoflood deposit with significant precise water level indicators (Baker and Carling, 2022; Benito et al., 2022). SWDs are widely used for reconstructing smaller-scale paleoflood events (Benito et al., 2003; Baker, 2008; Huang et al., 2010; Wang L. et al., 2014; Mao et al., 2016). However, SWDs in the alpine canyon river system in a large-magnitude and high-energy OF environment are difficult to preserve but instead form ODs mainly composed of coarse gravel (Carling, 2013). The OF induced by a giant landslide-dammed lake is a typical "*Megaflood*" (Baker and Carling, 2022; O'Connor et al., 2022), which forms an abundance of ODs on the bank and riverbed downstream of the dam (Wang P. et al., 2014; Chen et al., 2018; Ma et al., 2018).

Typical large-scale landslide-dammed lake ODs were discovered in the Diexi Valley of the Upper Minjiang River and the Tangjiashan Valley of the Tongkou River. The sedimentary characteristics of these ODs are significantly different from those of mountain river facies, normal floods, alluvial fan, and debris flow. In this study, we focused on examining and analyzing the geomorphologic environment and sedimentary sequences of the ODs in the Diexi Valley of the Upper Minjiang River and the Tangjiashan Valley of the Tongkou River, including the following: i) investigating the outcropping sequence strata and geomorphic characteristics of ODs, such as exposed sites, channel expansions and constraints, channel bends, channel branching, and obstacle shadows; ii) recording the sedimentary characteristics of profile outcrops, including bed geometry, bed thickness, bed contacts, color, grain size, texture, and internal

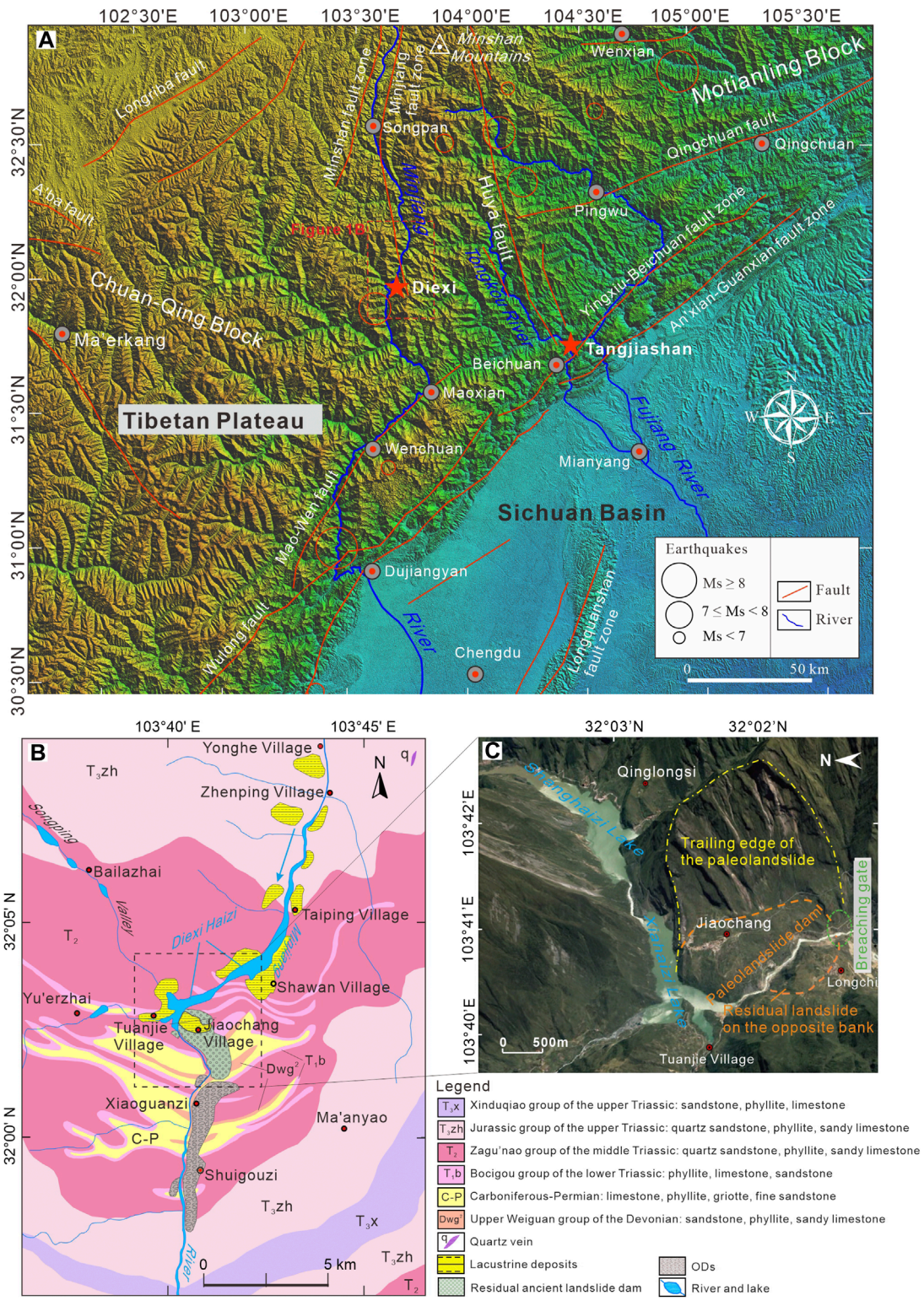

FIGURE 1
Study area. **(A)** Map showing the study area and outline of the active tectonics in the East Tibetan Plateau; **(B)** Lithologies of the exposed bedrocks in the Diexi region of the Upper Minjiang River, and the distribution of the Diexi ancient landslide-dammed lake, lacustrine sections, and ODs (modified from Ma et al. (2022)); **(C)** Topography of the Diexi paleo landslide area. The base image was captured and modified from *"Google Earth"* (date: 9 January 2016). The Diexihaizi lakes are modern dammed lakes induced by the Ms. 7.5 Diexi Earthquake that occurred in 1933.

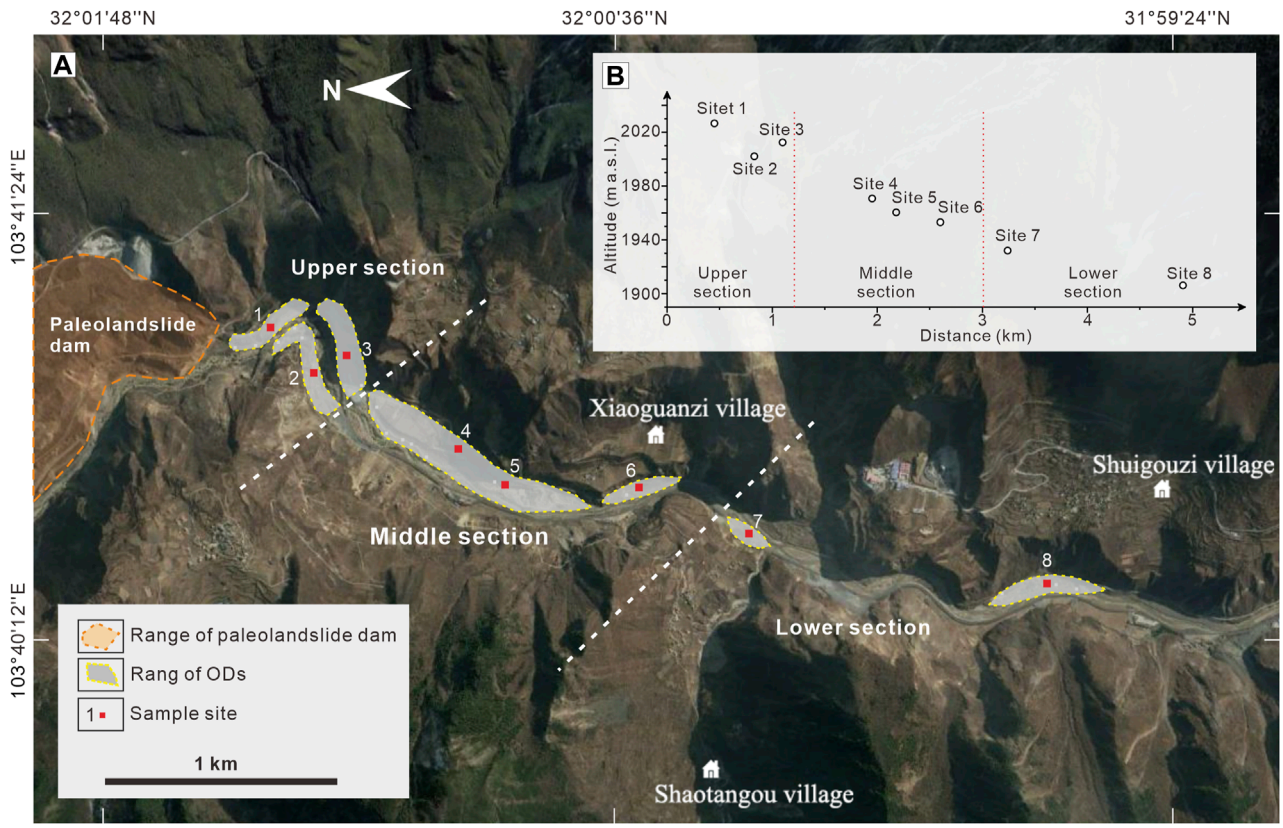

FIGURE 2
(A) Locations of the ODs sections and sampling sites. The base image was captured and modified from *"Google Earth"* (date: 9 January 2016); **(B)** Scatter plot of the altitude and relative distance of sampling sites.

sedimentary structures, to determine the hydrodynamics during the OF stage.

3.2 Sampling

In sedimentology, studying grain size characteristics is the most important aspect of the sedimentary characteristics of clastic sediments. Grain sizes can reflect the transporting dynamic environment and are one of the main characteristics of the deposits. In this study, the ODs distributions in the Diexi Reach of the Upper Minjiang River in the vertical direction were divided into upper, middle, and lower sections (Figure 2). 3 sets of grain size samples were collected from per ODs profile, and each set contained 3 samples from different layers, with approximately 1 kg per sample. A total of 72 grain size samples were collected. Table 1 shows the characteristics of the sampling sits.

3.3 Granularity experiment

The ODs grain size characteristics were tested by laboratory sieving analysis with a set of standard sieves measuring 4, 2, 1, 0.5, 0.25, 0.125, and 0.0625 mm. Then, an arithmetic method of moments is utilized to determine the grain size parameters (mean particle size, sorting coefficient, skewness, and kurtosis) of the ODs in the study area (McManus, 1988). These are quantitative indicators which effectively reflects the grain-size characteristics and sedimentary environments (Gao and Collins, 1994; Blott and Pye, 2001; Blott and Pye, 2012). Meanwhile, approximately 300 g of fine ODs was collected from per grain size sample for the surface microstructure analysis of quartz sand using a scanning electron microscope (model: Zeiss supra 55). In previous researches, microtextures have been recombined into several microstructure families (Mahaney and Kalm, 2000; Costa et al., 2012; Molén, 2014), which are used to distinguish depositional environments such as desert and glacial sediments (Bellanova et al., 2016). In this study, the comprehensive surface microstructure analysis of ODs quartz sand was performed to classified different characteristics (Immonen, 2013; Chen et al., 2019).

4 Results

4.1 Sedimentary records of landslide-dam breach events

4.1.1 The Diexi Reach in the Upper Minjiang River

In this study, several typical sedimentary and geomorphological features were discovered in the Diexi Reach of the Upper Minjiang

TABLE 1 Descriptions and locations of the ODs sections and sampling sites.

Sampling site	Distance from the relict landslide dam (km)	Exposed length (m)	Maximum thickness (m)	Top elevation (m)	Sample height above channel bottom (m)	Location	
						Latitude/N	Longitude/E
1	0.45	120	9.3	2024.7	8.4	32°01′24.86″	103°41′08.84″
2	0.8	150	25	2032.9	6.0	32°01′20.81″	103°40′57.71″
3	1.2	78	18	2027.2	13.2	32°01′11.38″	103°40′58.11″
4	1.6	25	4.2	1972.8	8.4	32°00′57.56″	103°40′45.00″
5	2.0	110	8.5	1964.3	8.5	32°00′48.91″	103°40′40.22″
6	2.6	60	3.4	1949.4	5.2	32°00′30.36″	103°40′37.12″
7	3.2	30	2.2	1929.2	4.7	32°00′11.77″	103°40′33.35″
8	4.9	62	4.9	1893.5	1.9	31°59′23.22″	103°40′25.27″

River. A relict paleolandslide dam in Jiaochang Village of Diexi Town, lacustrine deposits with a length of approximately 30 km upstream, and an abundance of outburst sediments at approximately 5 km downstream of the Minjiang River were well preserved (Figure 3), indicating that a distinct damming incident had occurred in the Upper Minjiang River that formed a giant paleodammed lake, and that the dammed lake subsequently breached and caused a large OF in the late Pleistocene (Ma et al., 2018).

Eight ODs sections (Table 1) were discovered on both riverbanks at the downstream reach of the Diexi paleo-dam (Figure 4A). The lithology of the exposed ODs are detailed in Figures 4B–I. These deposits present distinctive sedimentary sequences and characteristics. From upstream to downstream, a depositional model in a disordered–sub-ordered–ordered sequence is shown in the distribution of sedimentary profiles. The deposits profile at site 1 (near the breaching gate) are mixed and disordered, without obvious bedding and sedimentary structures (Figure 4B). The gravel in this profile section poorly arranges, with a maximum size of 3.5 m in diameter and "*Floating Clasts*" characteristics (Russell and Knudsen, 1999; Carling, 2013). The profile and flat surface of the gravel are slightly inclined downstream, with an inclination angle of approximately 7°–9°. Approximately 300 m downstream from the breaching gate, several sedimentary layers appear in the ODs profile, and large boulders are clustered (Figure 4D). Sedimentary layers and bedding characteristics become more obvious in the middle and lower sections than that in the upper section, and a special sedimentary structural unit with a rhythmic interbedding of coarse and fine gravel layers appeared. The bedding is nearly horizontal or slightly inclined downstream. The coarse- and fine-grained layers composed of rhythmic units represent the various "*cycles*" at site 7 in the lower section (Figure 4H).

These special sedimentary features explain the hydrodynamic changes of the OFs, and are also important indicators for distinguishing the ODs from the other types of sediments in the study area. Some typical "*sedimentary facies*" units of boulder (Bcm), coarse gravel (Gm), fine gravel (Gfm), fine sand-gravel (Grm), and sand (St, Sp, and Sh) can be identified from these depositional profiles (Figures 4B–I) and are described as follows:

- Bcm: clast-supported massive coarse boulder gravel layer, with gravel, cobbles, and sand matrix;
- Gm: clast-supported massive coarse gravel layer, with boulders, cobbles, and sand matrix;
- Gfm: massive clast-supported fine gravel layer;
- Grm: massive matrix-supported fine granule-gravel layer;
- St: trough cross-bedded sand layer, with fine gravel;
- Sp: planar cross-bedded sand layer, with fine gravel;
- Sh: massive to thinly laminated medium-coarse sand layer, with fine gravel.

The large boulders in the Bcm units were usually clustered within all of the profiles were laterally extensive, which were approximately horizontal throughout. This unit could be continuously traced between every two profiles, with massive and clast-supported structures. In addition, large numbers of subrounded to rounded boulders were commonly distributed on the riverbed, usually forming ODs terraces, which were mostly covered with bushes and grass, indicating a low water level stage after a high-energy flood flow. The gravel units (Gm, Gfm, and Grm) underlay and overlay the Bcm units, with a lateral expansion from several to tens of meters, which were typically structured by matrix-supported or massive, medium-coarse sandy or silty sand matrices. Sand units (St, Sp, and Sh) were found to exist among the Bcm and gravel units in several sections, forming thin layers or lenses with a maximum thickness of 0.5 m and appearing at different levels. The sand units were horizontally stratified, and contained scattered pebbles.

4.1.2 The Tangjiashan Reach in the Tongkou River

Tangjiashan ODs are distributed from downstream of the landslide dam to Beichuan County, with a length of approximately 5 km (Figure 5). Based on the Google Earth image on 25 December 2015, and field investigations, it was found that the ODs in the reach

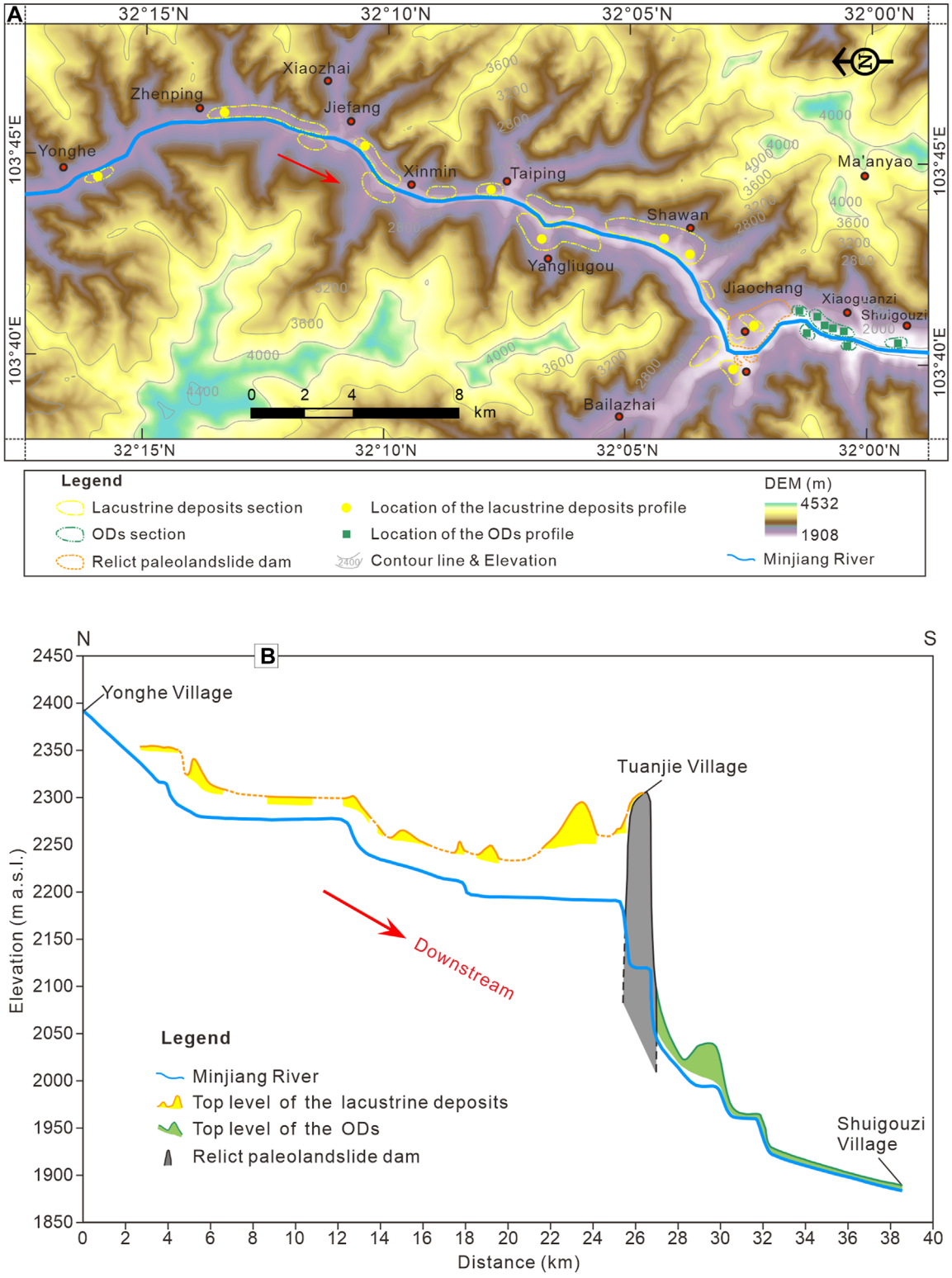

FIGURE 3
Sedimentary geomorphology features in the Diexi Reach of the Upper Minjiang River. **(A)** Spatial characteristics of sedimentary distribution and topography; **(B)** Longitudinal profile showing the relict paleolandslide dam in Jiaochang Village of Diexi Town, lacustrine deposits in the upstream, and ODs along the downstream of Minjiang River.

from Tangjiashan to Beichuan can be divided into the upper, middle, and lower sections by the first right turning point of the river channel and the Kuzhuba suspension bridge (Figure 5A). The sedimentary characteristics of the ODs in the three sections are different and form a corresponding relationship with river channel bending. In addition, there were significant distribution changes in the middle

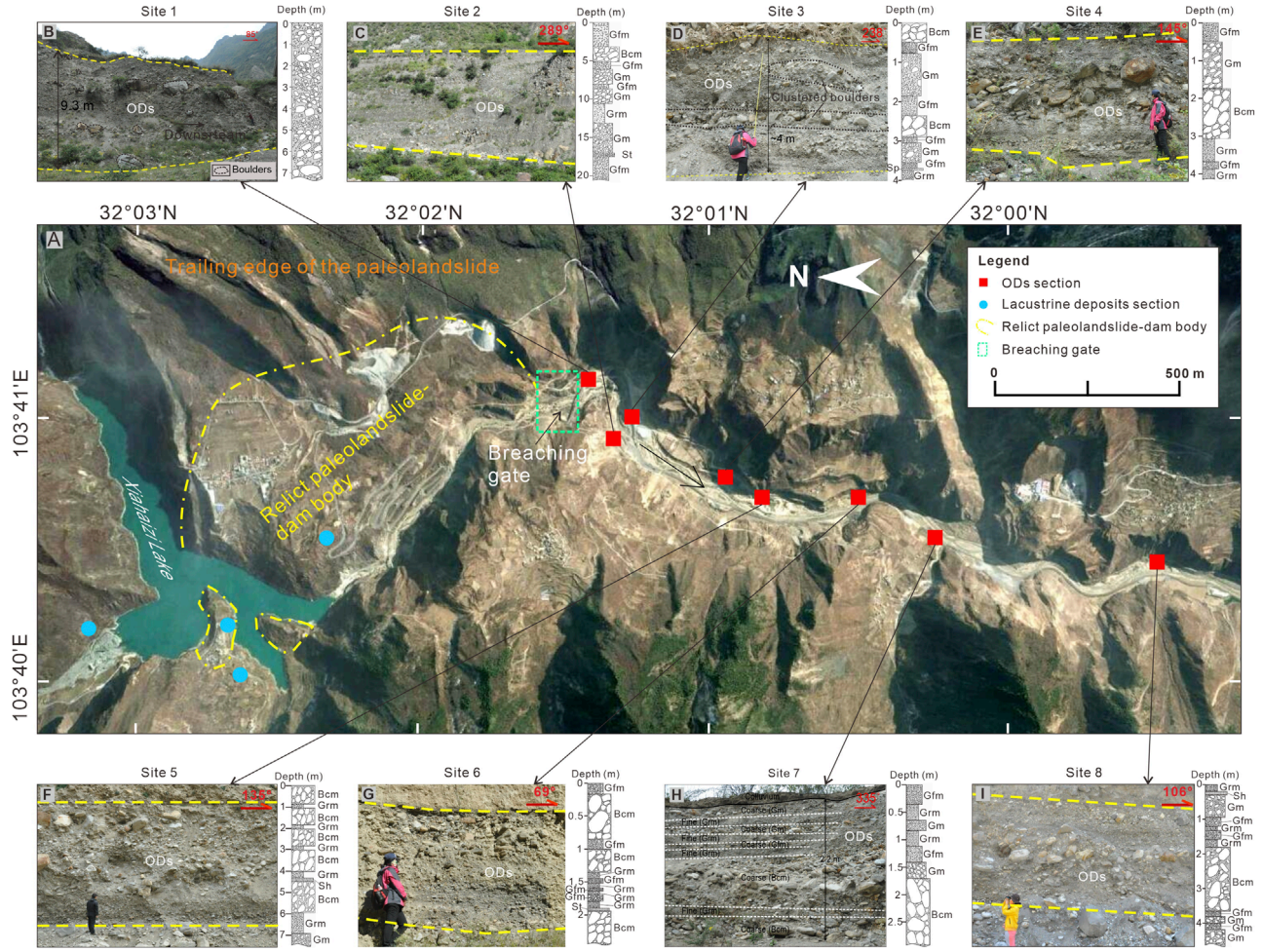

FIGURE 4
Distribution and lithologic columns of the ODs sections of the Diexi paleolandslide-dammed lake. **(A)** Geomorphological characteristics of the Diexi region, and locations of the ODs sections. The base image was captured and modified from "*Google Earth*" (date: 9 January 2016); **(B–I)** field photographs and lithologic columns of the profiles at sites of ODs 1–8, respectively.

and lower sections of the ODs in the Google Earth image on 20 March 2020 (Figure 5B), which could have been caused by human activities.

The ODs in the upper section (sites 1–4) are distributed in the river valley at a distance of 1.5 km from the landslide dam to the first river bending. Among them, ODs 1 is the largest one, which is distributed in a long strip along the left bank of the river, forming a large platform similar to an "accumulation terrace". An artificial prospecting trench with a length, width, and height of approximately 5.0, 3.0, and 1.0 m respectively, was explored at the tail of this accumulation profile, and the sedimentary characteristics were clearly visible (Figure 6A). ODs 2 is distributed on the opposite bank (right bank) of the prospecting trench, which is 1.0–2.0 m above the water surface (Figure 6B). Moreover, ODs 3 is pendant-shaped in the river channel, which is small in scale and originally part of ODs 2, separated by river flow cutting.

The middle section of the Tangjiashan ODs is distributed between the first and second major bends of the river channel downstream of the landslide dam, with a length of approximately 2.0 km, including ODs 5–7. The most typical exposed profile in this section is ODs 7 located near the Kuzhuba Hydroelectric Station, which has good continuity and integrity (Figure 5A). The planform of ODs 5 is shuttle shaped, with a prominent vertical exposed profile developed at the end. Although the upper part of the profile is covered by a pile of rubble, a certain arrangement structure can still be recognized (Figure 6C). ODs 6 is distributed on the right bank of the river bend, protruding outward, forming a flat half-moon shape. The fan-shaped ODs 7 extends along the left bank of the river. A typical vertical profile is exposed on the southeast side of the Kuzhuba Hydroelectric Station, with a thickness of approximately 4.0 m and well-developed sedimentary features (Figure 6D). Approximately 200 m upstream of the Kuzhuba suspension bridge at the end of the middle section, gravel content is lower than that of the upper and middle parts, and the gravel size decreases.

ODs 8–12 in the lower section are located at the third river bend downstream of the Tangjiashan landslide dam, with relatively scattered distributions and small scales (Figure 5A). ODs

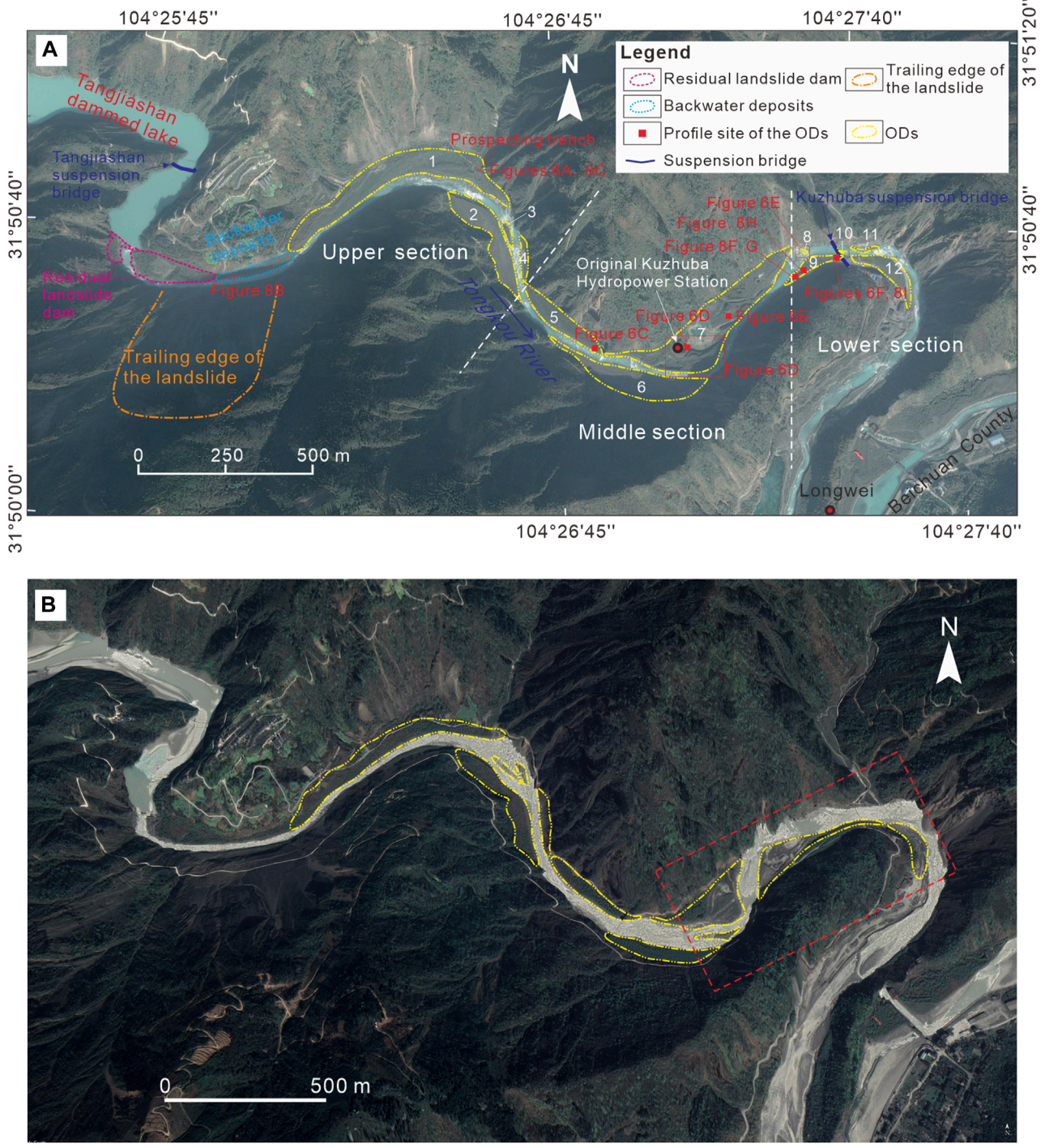

FIGURE 5
Distribution locations and geomorphological characteristics of Tangjiashan ODs in the Tongkou River Basin. **(A)** Distribution and geomorphological characteristics of the ODs in 2017, with a "*Google Earth*" image date of 25 December 2015; **(B)** Distribution and geomorphological characteristics of the ODs in 2017, with a "*Google Earth*" image date of 20 March 2020.

8, 10, and 12 lie in the river channel, forming gravel diara deposits. These gravel diara are 2.0–3.0 m thick with high gravel content and large gravel (Figure 6E). The presence of gravel diara also indicates that this location is approaching the end of the Tangjiashan ODs. ODs 9 and 12 are the two larger accumulations in the lower section, both of which have a half-moon shape. Several typical sedimentary structures develop in the profile of ODs 9 (Figure 6F).

The Tangjiashan ODs can be longitudinally divided into five depositional types: erosional residual-dam deposits, backwater deposits, and fan-apex deposits in the upper section; fan-in deposits in the middle section; and fan-margin deposits in the

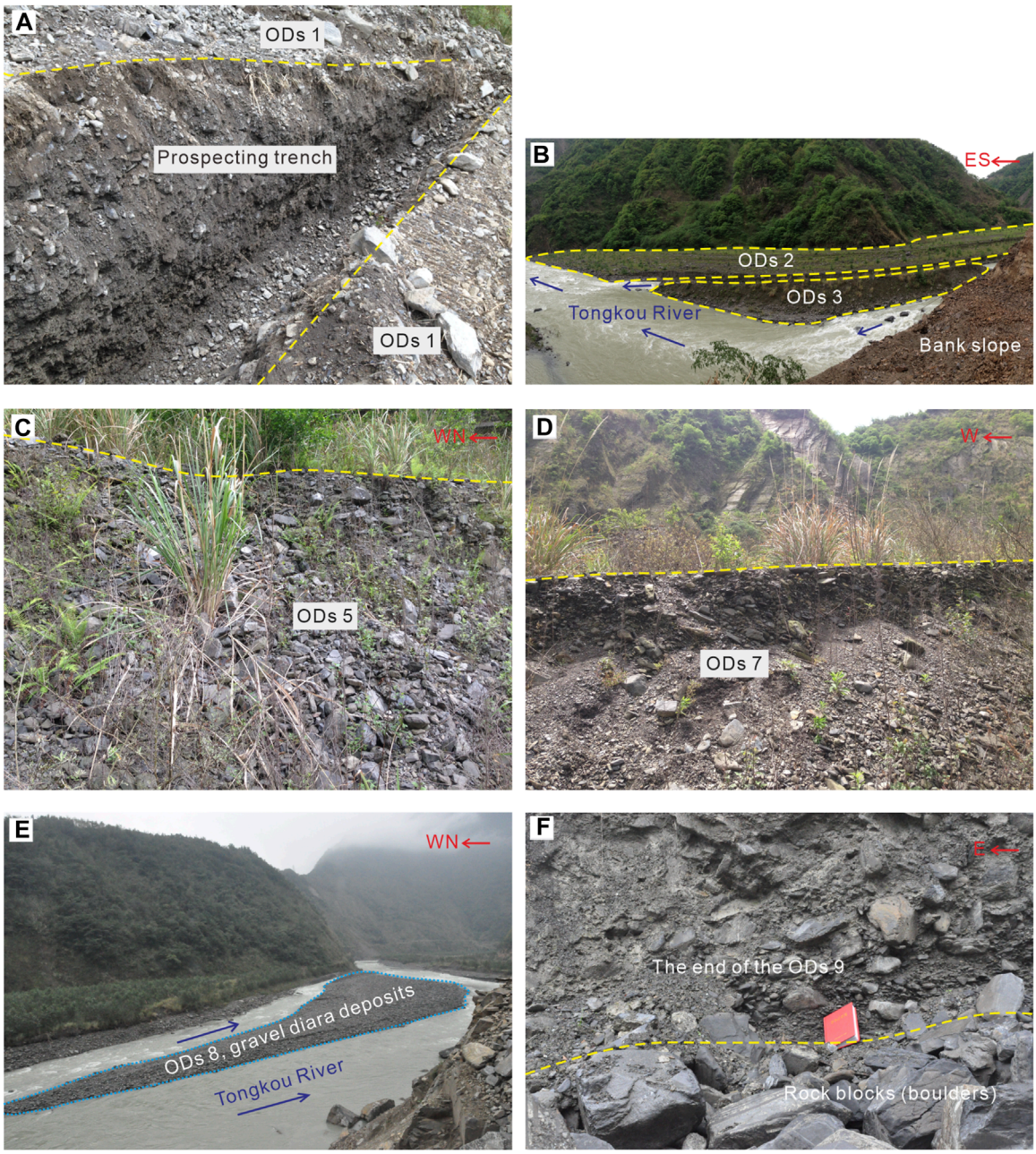

FIGURE 6
Distribution characteristics of Tangjiashan ODs. **(A)** The artificial trench at the end of ODs 1 in the upper section; **(B)** The distribution characteristics of ODs 2 and 3 in the upper section; **(C)** Profile characteristics at the end of ODs 5 in the middle section; **(D)** Profile characteristics of ODs 7 on the southeast side of the Kuzhuba Power Station in the middle section; **(E)** Gravel diara deposits in the river center of the lower section; **(F)** Profile characteristics at the end of ODs 9 in the lower section (See Figure 5 for the locations).

lower section (Figure 7). Six types of sedimentary facies, including Bcm, Gm, Gfm, Grm, and Sp/Sh, are presented in the vertical profiles of the ODs.

The erosional residual-dam deposits is an accumulation unit on the new river channel after lake discharge, which is characterized by several juxtaposed large gravel diara deposits, mainly composed of poorly sorted gravel. In addition, multiple boulders are scattered on the top residual dam, either horizontally on the diara island or in the river channel. The maximum boulder has a particle size of approximately 8 m and weighs 300 t (Figure 8A). The backwater deposits are composed of sorted sand and fine gravel, with clear horizontal bedding and varying layer thicknesses. The upper and lower parts of the backwater deposits are composed of Grm, and the middle part is composed of multilayer sand faces (St/Sh) (Figure 8B). This is due to the low flood level in the early stage of dam failure, resulting in backflow on both sides of the barrier dam (Figure 5A), which is a sign of early water level drop.

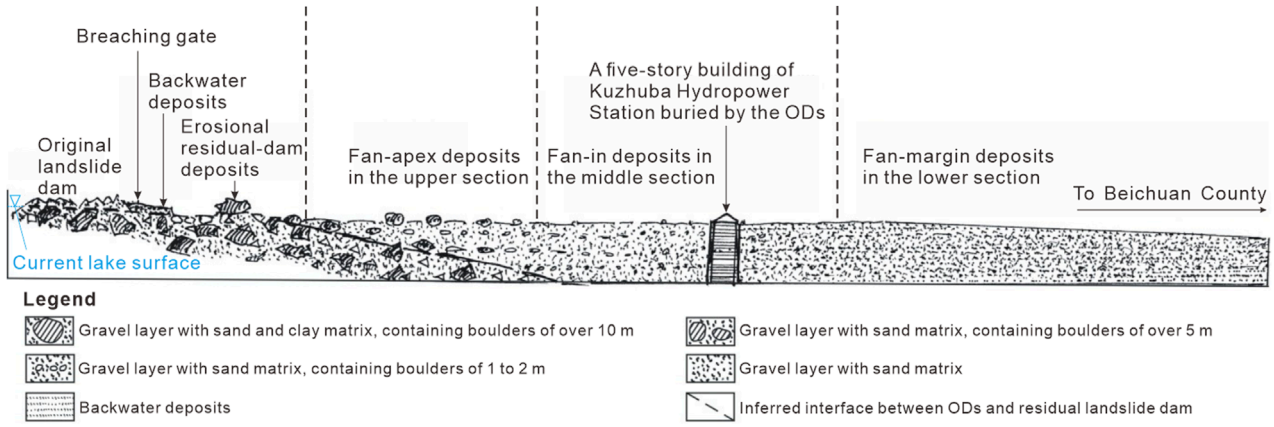

FIGURE 7
Schematic diagram of the longitudinal profile showing the Tangjiashan ODs' sedimentary characteristics. The freehand sketch was initially drawn by Cui et al. (2013).

The boulders on the riverbed and diara island of the fan-apex deposits in the upper section, with particle sizes ranging from a few centimeters to several tens of centimeters, are obviously reduced. The exposed profile of the prospecting trench shows typical sedimentary characteristics (Figure 8C). This vertical profile has obvious stratification, but does not have rhythm. The gravel in profile likely formed into imbrication structure characteristics. In addition, the ODs on the diara island and south bank of the river contain few gravel components but more silt. There are loose gravel deposits at the foot of the profile, indicating that the gravel structure in these ODs is unstable and easily scatters under river erosion or gravity.

There are almost no large boulders (particle size >1 m) on the riverbed and diara island in the middle section. A five-story building of the Kuzhuba Hydropower Station buried by the ODs 7. The estimated maximum thickness of the ODs in this section must be more than 15 m (Figure 8D). This also intuitively reflects the water depth of the Tangjiashan LLOFs at the flood stage. Figure 8E shows sedimentary characteristics of an exposed ODs 7 profile on the southeast side of the Kuzhuba Hydropower Station, with clear bedding and structures. There is a clear rhythmite-interbedded structure in the profile horizontal bedding. Five "*cycles*" could be found in this profile, illustrating that five flood peaks of the LLOF would occur in the dammed-break period. This depositional profile has developed boulder facies (Bcm) and gravel facies (Gm, Gfm and Grm). The coarser gravel layer presents gravel support-stacked, cavitation, stone-in-line and imbrication structures. Clustered gravel in the profile exhibits a "*huddling*" phenomenon. These sedimentary characteristics explain the regular changes in the hydrodynamic conditions of the OFs at the time of breaching.

The gravel diara on the riverbed of the lower section is mainly composed of fine gravel (<10 cm) and sand. The scale and quantity of gravel diara have increased, resulting in more river bifurcation. Because of the weakening of flood dynamic conditions in the lower section, the pulsating-flow characteristics were also weakened, which makes the stratification characteristics of the ODs indistinct. The exposed profile of ODs 9 in this section presents a combination pattern of an overhead gravel layer at the lower part, a cemented dense diamicts layer in the upper part, and a slightly inclined bedding layer downstream of the riverbed (Figure 8F). The lower gravel layer of this profile is composed of Gm facies and Bcm facies, with a maximum thickness of 20 cm. Because of the low sand matrix content in the Bcm facies, the gravel in the profile does not have a foundation, forming gravel support-stacked and cavitation structures (Figure 8G). The top part of the ODs 9 profile is a Bcm unit composed of a mixture of large boulders and sand, with a thickness of approximately 50 cm. ODs 9 in the middle section extends to approximately 100 m. It is inferred that the lower Bcm and Gm units should develop in an OF environment with weak hydrodynamic conditions, whereas the upper Bcm unit represents a turbidity-current flood environment with strong hydrodynamic conditions. A similar ODs profile appears approximately 50 m downstream from the above site, with a thickness of only 1.0 m, developing Bcm facies sandwiched with a lens of thin Gfm facies (Figure 8H). Most boulders in the Bcm unit are poorly rounded and disorderly arranged, showing many cavitation structures. These sedimentary characteristics indicate that this profile must have been formed by the rapid accumulation of high-energy OFs, and later eroded by low-energy floods, causing the fine-grained matrix components to be washed away.

Under the Kuzhuba suspension bridge, the sedimentary profile at the end of OFs 9 becomes more mixed (Figure 8I). Only a clearly layered Gfm unit can be distinguished at the bottom of the profile, which is mainly composed of fine gravel and sand without cavitation. The particle size of the boulders distributed in the overlying Bcm unit mostly ranges from 20 to 30 cm and are mainly plate- or sheet-shaped, with poor rounding and mixed arrangement. The sand content of the Gm unit in the upper part of the profile is higher than that of the gravel, and the flat surface of the gravel has an upstream tendency. The profile generally presents disordered sedimentary characteristics, with good cementation, which reflects the fact that when the OF reaches the lower section, its pulsatility becomes weak due to the influence of transmission distance and topography, but it still maintains a strong hydrodynamic condition.

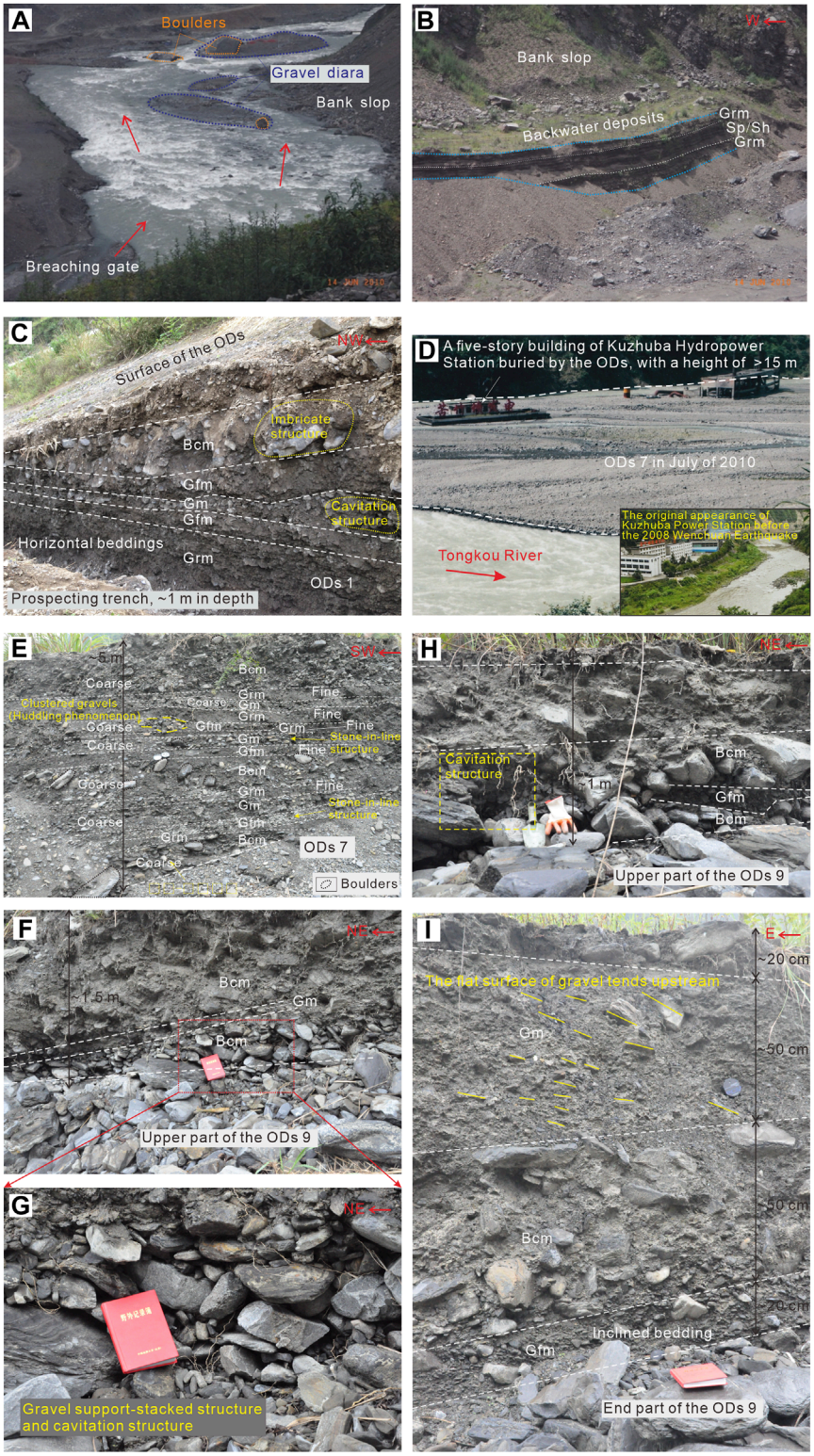

FIGURE 8
Sedimentary characteristics of Tangjiashan ODs. **(A)** Sedimentary characteristics of residual-dam deposits. The field photo was provided by Cui et al. (2013); **(B)** Sedimentary characteristics of backwater deposits. The field photo was provided by Cui et al. (2013); **(C)** Sedimentary characteristics of the prospecting trench at the end of ODs 1 in the upper section; **(D)** Comparison before and after burring of the original Kuzhuba Power Station in the middle section; **(E)** Sedimentary characteristics of the central part of ODs 7 in the middle section. **(F–H)** Sedimentary characteristics and structures of the upper part of ODs 9 in the lower section; **(I)** Sedimentary characteristics of the exposed profile at the end of ODs 9 in the lower section (See Figure 5 for the locations).

TABLE 2 Grain size proportion and sample statistics using the arithmetic moment method of the ODs in the Diexi Reach.

Section	Grain size portion (%)			Sample statistics			
	Gravel (64–2 mm)	Sand (2–0.0625 mm)	Silt and clay (<0.0625 mm)	Mean grain size (mm)	Sorting	Skewness	Kurtosis
Upper	72.01	26.68	1.31	19.57	15.65	0.06	1.42
Middle	70.46	28.04	1.50	18.60	15.91	0.06	1.19
Lower	67.12	30.96	1.92	17.21	16.02	0.06	1.11
Average	69.86	28.56	1.58	18.46	15.81	0.06	1.24

4.2 Grain size characteristics

This study determined that the main components (with a particle size of <64 mm) of the ODs in Diexi Reach are gravel (69.86%), followed by sand (28.56%), with minimal content levels of silt and clay (1.58%) (Table 2). Furthermore, from the upper to the lower sections, the gravel content displays a gradual decrease, whereas the sand content increases. The strong hydrodynamics of the OF at the time of dam failure evidently result in rapid deposition of coarse gravel components, while fine-grained components are transported downstream. The fine particles (sand, silt and clay) increased in the middle and lower sections of the ODs, which illustrates that the OF hydrodynamics decreased. The maximum granularity distribution of the ODs occurs at 4 mm, which is the peak of the particle size frequency curve (Figure 9). Furthermore, the large slope of the frequency curve between 4 and 2 mm indicates that the granularity distributes in a small interval and that the particles are relatively concentrated in gravel, which confirms that the OF is in high energy and strong hydrodynamics, resulting in gravel depositing quickly. There is a sub-peak (approximate 0.375 mm) of sand content in the upper section (Figure 9A), but not in the middle and lower sections (Figures 9B,C). However, the particle composition between 2 and 0.0625 mm (sand content) increases from upstream to downstream (Table 2), indicating that the OF energy gradually weakened, and the ODs sorting improved which was similarly charactered to that of the channel sand (Ma et al., 2018). In addition, the transport modes of the ODs in the study area include pushing, saltation, and suspension (Figure 10), which can reflect the material composition, particle sorting, and intersection of transport medium (Visher, 1969). The pushing sections of the grain size accumulated probability curves present steep-slope characteristics, which reflects the material source is coarse-grained detritals, consisting with the fact that the ODs in the study area are mainly composed of gravel components. Furthermore, the curve slopes of the saltation and suspension sections quickly flattened and are much smaller than that of the pushing sections, reflecting a rapid decrease in the content of coarse-grained components from the upper section to the lower section. From upstream to downstream, the intervals of the pushing sections gradually increase, the intervals of the suspension sections gradually decrease, and the interval differences of the saltation sections are small. These findings indicate that the coarser-grain compositions (gravel) decreased and finer-grain compositions (silt and clay) increased, which resulted from gradually weakened OF energy, stabilized sedimentary environment and, improved sorting from upstream to downstream. In the current study, the grain size characteristics in the upper section of the ODs are similar to those of the debris flow deposits, whereas the grain size characteristics in the middle and lower sections are similar to those of the channel sand sediment. However, with regard to the precise definition of this new type of sedimentary environment, further in-depth study is recommended.

The mean particle-sizes of the upper, middle, and lower segments were 19.57 mm, 18.65 mm, and 17.21 mm, respectively (Figure 11A). From which we may learn that the mean particle-size of the deposits has gradually decreased from the upper section to the lower section. This indicates that a large amount of fine particles have removed by the OF in the upper section, leaving the larger particles behind. The average sorting coefficient values are 15.65, 15.91, and 16.02 for the upper, middle, and lower sections, respectively, with an average sorting coefficient of 15.81, which is characterized by very poor sorting (Figure 11B). However, from the upper section to the lower section, the sorting coefficient value tends to become gradually smaller, which indicates that the sorting of sediment has improved. The average skewness value is 0.06 for each section, which belongs to the symmetrical type (Figure 11C). The deposits presents very coarse skewed-type characteristics, which indicates that the fine particles have easily formed into suspended matter, and then migrated to the lower section by means of pushing and suspension. For the entire study area, the kurtosis values of the sediment ranges between 1.02 and 2.15, with an average value of 1.24. The very platykurtic kurtosis (<1.7) accounts for 91.7%, therefore the ODs in the study area belongs to the very platykurtic type of sediment (Figure 11D). It is determined that the narrower the kurtosis is, the more concentrated the particle-size distribution of the samples would be, which confirms that at least a part of the sedimentary particulates are without environmental modification, and have been directly transformed into the environment in this area.

4.3 Surface mechanical microtextures of quartz grain in outburst deposits

The mechanical microtextures of ODs in the Diexi Reach of the Upper Minjiang River, such as fractured plate, conchoidal

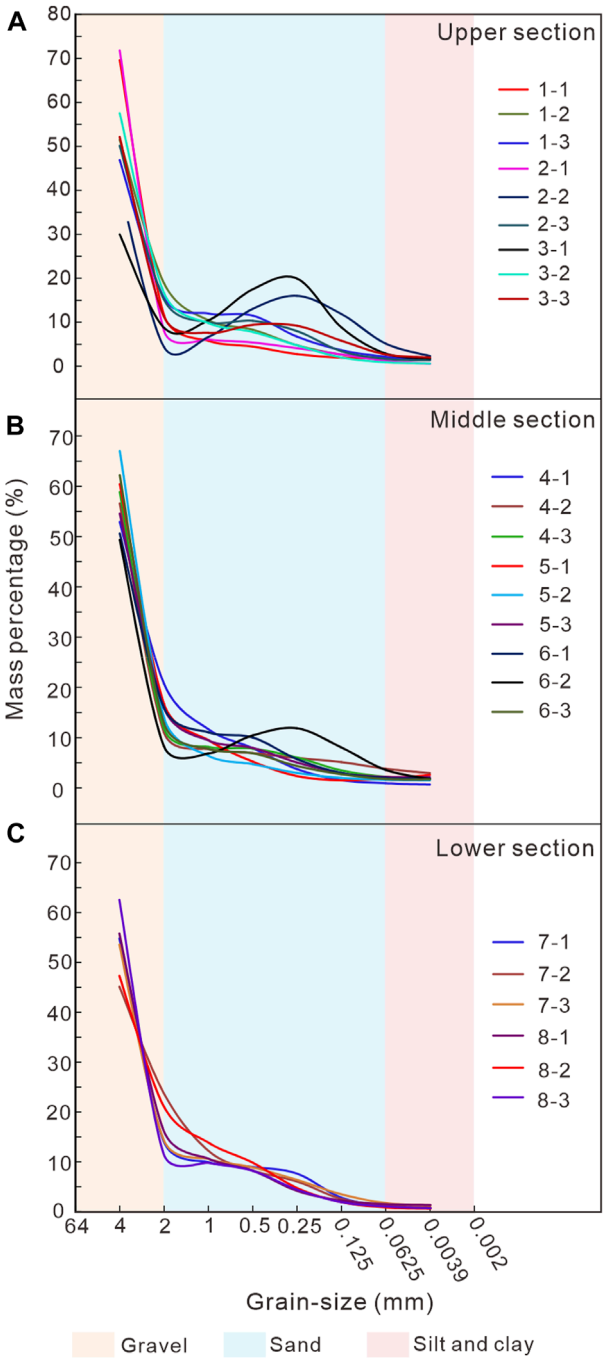

FIGURE 9
Frequency curves of the grain size samples from the ODs in Diexi region. **(A)** Frequency curve from the samples of the upper section; **(B)** Frequency curve from the samples of the middle section; **(C)** Frequency curve from the samples of the lower section.

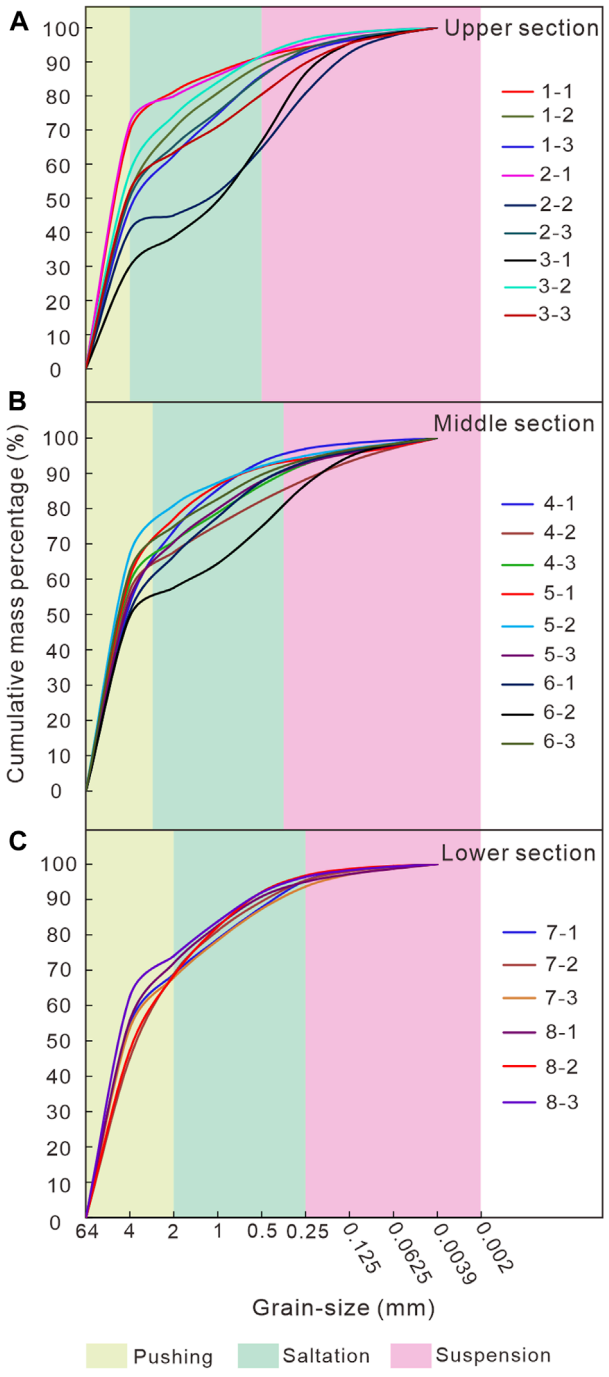

FIGURE 10
Accumulated probability curves of the grain size samples from the ODs in the Diexi region. **(A)** Accumulated probability curve from the samples of the upper section; **(B)** Accumulated probability curve from the samples of the middle section; **(C)** Accumulated probability curve from the samples of the lower section.

fracture, impact crater, and V-shaped pit, are shown in Figure 12. The quartz sand surface of in ODs presents a microtexture of the breakage block with similar large geometry size (Figures 12A,D), which is generated by strong collisions. This type of microtexture characteristic is commonly found in the upper section of the ODs. However, the middle section of the ODs is characterized by conchoidal fracture (Figures 12C,D), which usually occurs in mineral particles lacking clear joints caused by strong impact (Margolis and Krinsley, 1974; Chen et al., 2019). This study shows that the breakage block frequency in the middle and lower sections of the ODs is arranged from 25% to 33%, which is less than half of that in the upper section. From upstream to downstream, the

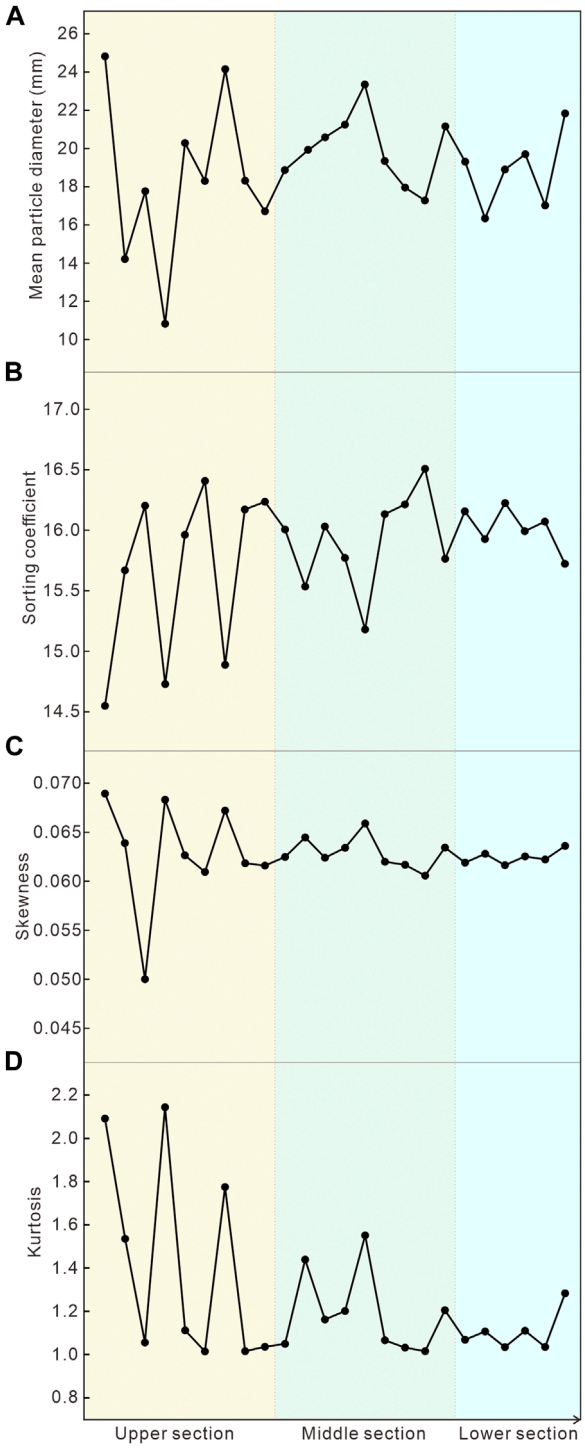

FIGURE 11
Grain size distribution curves of the ODs in the Diexi region obtained using an arithmetic moment method. **(A)** Mean grain size; **(B)** Sorting coefficient; **(C)** Skewness; **(D)** Kurtosis.

frequency of large (>100 μm) and medium (10–100 μm) conchoidal fractures shows a decreasing trend. However, the frequency of small (<10 μm) conchoidal fractures appearing in the upper and lower sections was higher than that in the middle section. Among them, the upper section has the highest frequency of 40.09% induced by inherited microtextures. The middle and lower sections have small frequencies of conchoidal fractures, with values of 27.83% and 32.08%, respectively, which reflects that the OF energy decreased.

Previous studies indicated that impact crater, V-shaped pit, triangular marks, and impact pit are typical markers observed only in the lower section of the ODs (Figure 12F), whereas impact craters are common in the three sections (Figures 12B–E). However, from the upper section to the lower section of the ODs, the frequency of impact craters did not increase or decrease significantly. In addition, scratch, groove and upturned plate microtextures were also observed in the ODs (Figures 12A–C), with a relatively low percentage of approximately 5.5%. The smooth surface (Figure 12F) with a sparse content of <6% in the lower section suggests a fast deposition rate at the flood stage.

5 Discussion

5.1 Difference between the outburst deposits and other sedimentary types

Overall, the longitudinal distribution of ODs is similar to that of an elongated fan-shaped terrace along the river channel (Figure 13). Based on the morphological characteristics and developmental locations, ODs can generally be divided into upper, middle and lower sections from upstream to downstream, which presents an obvious development regulation and distinctive sedimentary characteristics.

From the perspective of developmental characteristics, the sedimentary sequences of the ODs are between alluvial and debris flow facies (Bridge, 1984; Blair and McPherson, 1998; Moscariello et al., 2002; Ferring, 2020; Miall, 2022). The graded bedding texture in ODs is clearer than that in debris flow deposits, but there is no reverse or positive bedding rhythm in alluvial deposits. With regard to the macroscopic characteristics, the ODs profiles exhibit the accumulation characteristics of normal fluvial deposits, such as a large-scale rough sorting mechanism (Bridge, 2006; Dino et al., 2012; Miall, 2013). Meanwhile, on a microscopic level, they also exhibit the characteristics of diluted debris flow deposits (Eyles et al., 1988; Sohn et al., 1999), such as mixed sizes of gravel fragments and extremely inhomogeneous particle sizes, which reflects a rapid and erratic accumulation process (Ma et al., 2018). In terms of sediment formation conditions and distribution, ODs are also different from alluvial and debris flow deposits. On the one hand, regardless of the scale or flow magnitude of the material source, the formation conditions of ODs far exceed those of fluvial deposits, which also results in the absence of rhythmic characteristics of fluvial deposits in the ODs. On the other hand, the ODs lack the ability to maintain integrity such as debris flow deposits, which will still be affected by river transformation in the later stage. In addition, the ODs' surface is flat and has a long extension, with a leading front edge angle generally below 30°, which is different from the sharp-surface sedimentary facies of alluvial deposits and the large-angle front edge of debris flow deposits (Blair and McPherson, 1994; Bernhardt et al., 2012; Alván and von Eynatten, 2014; Chen et al., 2017).

In the microcosmic research of sediments, quartz sand surface microtextures have been widely applied in the reconstruction of sedimentary environments (Sweet and Soreghan, 2010; Vos et al.,

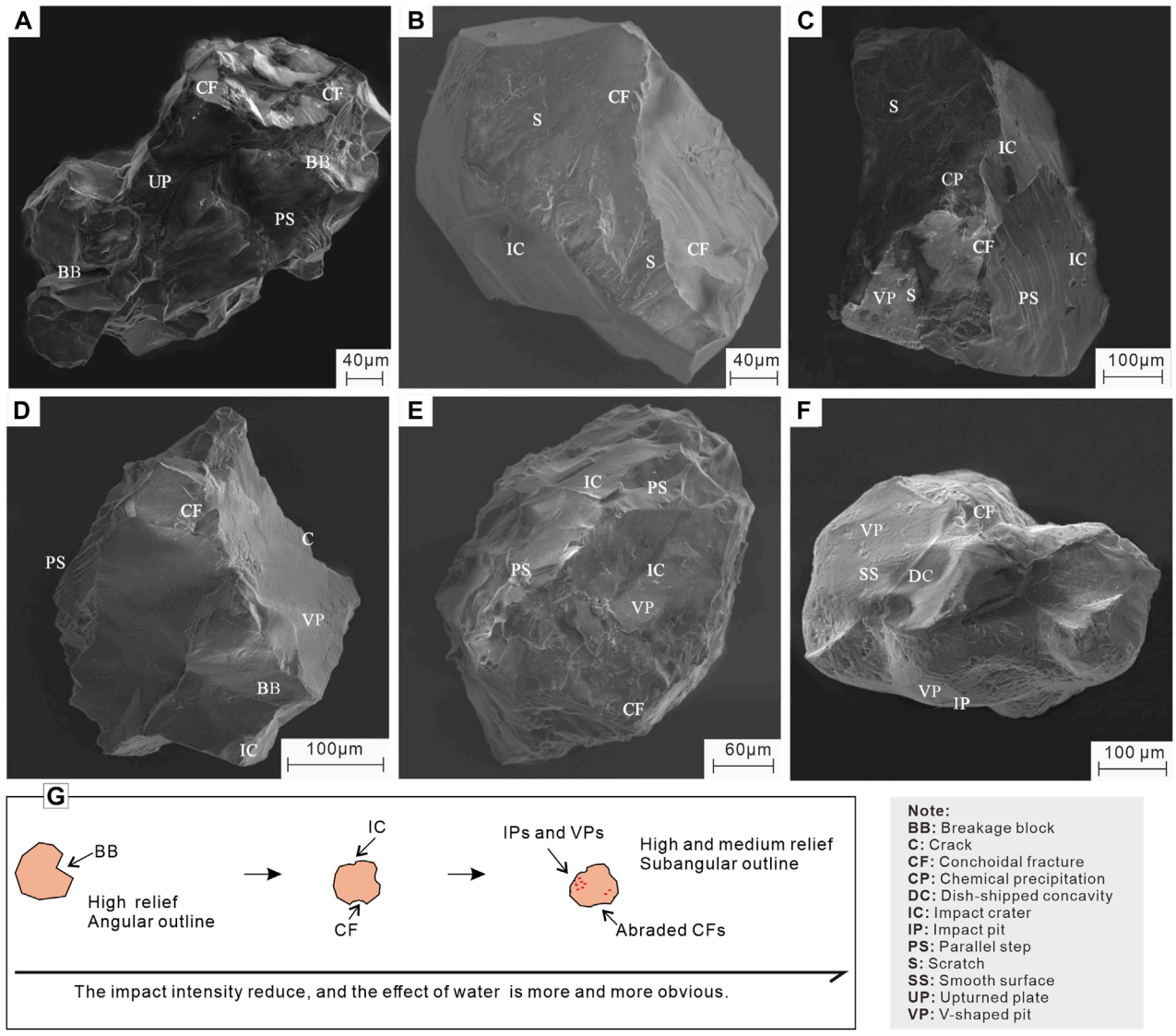

FIGURE 12
Quartz sand surface microtextures of the ODs in the Diexi region (modified from Chen et al., 2019). **(A)** Quartz sand surface microtextures (Mag = 535×) from site 2; **(B)** Quartz sand surface microtextures (Mag = 607×) from site 3; **(C)** Quartz sand surface microtextures (Mag = 396×) from site 4; **(D)** Quartz sand surface microtextures (Mag = 483×) from site 5; **(E)** Quartz sand surface microtextures (Mag = 530×) from site 7; **(F)** Quartz sand surface microtextures (Mag = 422×) from site 8; **(G)** The main surface microtextures changes of quartz sand during the transport.

2014; Gobala krishnan et al., 2015). Based on the statistical results of quartz grain surface microtextures in ODs, it indicates that the combination of mechanical microtextures changes obviously along the transporting distance of the ODs (Chen et al., 2019). Near the breaching gate, the morphology of quartz grains is controlled by the breakage blocks, which is similar to the grains of colluvial deposits (Goudie and Bull, 1984). However, the inherited microtextural features (e.g., fluvial sediments, lacustrine sediments and landslide deposits) representing these morphological modifications are uneven, which may be related to the high concentrations and rapid deposit process. As the distance increases, the quartz grains in the ODs become more similar to the grains from debris flow (Deane, 2010), which are characterized by medium conchoidal fractures and impact craters. In addition, the roundness of quartz sands and frequent V-shaped pits and impact pits also improved with transporting distance (Figure 12G). The different combinations of quartz sand surface textures indicated that the transformation process changed from high energy collisions to low energy collisions over a short distance, which was controlled by the hydrodynamic conditions or flow regime (Chen et al., 2019).

In sedimentology, based on sedimentary bedding and sorting degree, the sedimentary types can generally be divided into ordered and disordered, or ordered, sub-ordered, and disordered, and any sedimentary type can only possess one sedimentary sequence (Harms et al., 1975; Reading, 2009; Cui et al., 2013; Miall, 2022). Nevertheless, due to the influence of dynamic and medium composition changes during transportation and accumulation, the ODs will form disordered sedimentary sequence in the upper

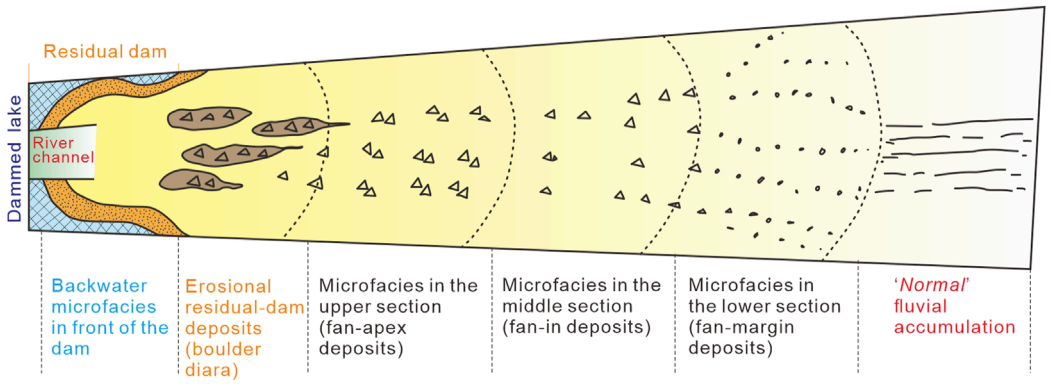

FIGURE 13
Longitudinal plane schematic diagram of the distribution of ODs along the river channel.

section, whereas sub-ordered or ordered sedimentary sequences will form in the middle and lower sections. It is completely absent in sedimentary deposits (Ma et al., 2018).

5.2 Different characteristics of the landslide-dammed lake outburst floods from "*normal*" floods

In a "*normal*" flood stage, low discharge and intensity are consistent throughout the entire basin, which should form similar sedimentary characteristics in sediments (McKee et al., 1967; Mutti et al., 2000; Wang et al., 2023a). However, the ODs exhibited inconsistent characteristics in the deposits profiles. Near the breaching gate, the OF is under large-discharge and high-energy, thus forming disorganized deposits profiles with no obvious beddings, which are similar to the characteristics of "*normal*" flood accumulation. In addition, the gravel in these profiles is disordered and mixed with some isolated boulders. Subsequently, with an increase in the transporting distance, the OF discharge and intensity decreased gradually, and the regularity of sedimentary characteristics also gradually became observable, such as the increasingly obvious stratification characteristics and the gradual reduction of gravel particle size.

Different sedimentary units in the ODs profiles record contrasting transportation mechanisms. The characteristics of massive and clast-supported structures, gravel cavitation, no or poor sorting, and profile thicknesses in the Bcm unit indicate that its formation conditions are closely related to high-energy flow (Smith, 1986; Maizels, 1997; Cutler et al., 2002). This is consistent with the transporting and sedimentation characteristics of OFs, speculating that they should be accumulated by OFs. Gm, Gfm, and Grm represent the recession stage of ODs, whereas the thin-layer Sh, St, and Sp represent a brief sedimentary period under stable weak hydrodynamic conditions after the accumulation of boulder units within the same flood peak "*cycle*". The isolated boulders in deposits profiles are transported and rapidly deposited by high-energy flood flows (Russell and Knudsen, 2002), which provides strong evidence of LLOFs. In addition, because of the high flow velocity and transport energy of the OF, most of the fine-grained components cannot be quickly deposited but are transported downstream for a longer distance. Therefore, no extremely fine sand and clay units were found in the ODs.

5.3 Reconstruction of catastrophic paleo landslide-dammed lake outburst floods

According to the statistics of large floods recorded worldwide in a previous research, the OFs caused by ice or landslide dams are much larger than that caused by rainstorms (O'Connor and Costa, 2004; Benito and Thorndycraft, 2020), and its erosive geomorphology, sedimentation process, flood magnitude, and flooding path have distinct temporal and spatial characteristics (Baker et al., 1993; Carling, 2013). The reconstruction of catastrophic paleo LLOFs is conducted on the basis of accurate identification of geomorphological evidence and chronology. The geomorphological map was completed along the flooding path during the same period as the catastrophic paleo OFs. Then, flood level indicators within ODs are identified by comparing and analyzing the evidence of different types of paleo-flood topography (O'Connor et al., 2022; Guo et al., 2023).

Hydraulic models for catastrophic paleoflood reconstruction mainly have two types: stable and unstable. The calculation of the flow surface profile in the stable hydraulic model assumes that the geomorphological indicators of the paleoflood are in close proximity to the maximum flood water level. However, it is crucial to determine the water level and flow rate of the OF in the unsteady simulating hydraulic model. In addition, the flow discharge of the OFs also depends on the water elevation and volume of the dammed lake and the breaching gate and cross-section geometry. On the basis of the sensitivity assessment between geomorphological evidence and water surface elevation changes of the OFs, the simulating model's validation was conducted (Baker et al., 1993; Carling, 2013; Benito and Thorndycraft, 2020; Benito et al., 2023). In terms of high-energy floods, such as OFs or flash floods in mountain regions, flow or boulder competence methods are applicable to estimate the hydraulics of floods using the relationships between the energy parameters of the flow and the geometric characteristics of the sediment particles being transported

by the floods (Costa, 1983; O'Connor, 1993; Ma et al., 2022). Because of the significant uncertainty of hydraulic parameters used in these empirical formulas, it is necessary to verify the rationality of calculating the results in combination with other geomorphological evidence and models (Wohl, 1992; Greenbaum et al., 2020; Ma et al., 2022). Therefore, detecting the estimated results of discharge and evaluating the topographic changes caused by OFs is important in the reconstruction of catastrophic paleo-OFs.

6 Conclusion

During the evolution of LLOFs, materials from the landslide dam and bank slopes and riverbed are transported downstream and gradually deposited, forming ODs in the river channel. This phenomenon is particularly common in some ancient landslide-dammed lakes. This study discovered the development of large-scale ODs in the Diexi Reach of the Upper Minjiang River, and thus obtained a preliminary understanding of ancient giant ODs and LLOFs. Investigations and studies were also conducted on Tangjiashan ODs. These have become important means of studying giant landslide-dam breach events. The accumulation profile has developed structural features such as imbrication, cavitation, gravel support stacking, and rhythmic interbedding. Moreover, the ODs possess some typical "*sedimentary facies*" Bcm, Gm, Gfm, Grm, and sand (St, Sp, and Sh). Among them, the Bcm units are deposited by high-energy OF events, and the gravel and sand units represent the recession stage of the flood.

This study determined that the main components (with a particle size of <64 mm) of the ODs in Diexi Reach are gravel, followed by sand, with minimal content levels of silt and clay, which mainly originate from the landslide dam. From the upper to the lower sections, the coarser-grain compositions (gravel) decreased and finer-grain compositions (silt and clay) increased, which resulted from gradually weakened OF energy, stabilized sedimentary environment and, improved sorting from upstream to downstream. The mean particle-size and sorting of the ODs all displays gradual decreases from the upper section to the lower section, which indicates that the sorting of ODs tends to improve. There is found to be a tendency for the skewness to become larger from the upstream to the downstream, and the ODs presents a very coarse skewed type. The kurtosis of the ODs is distributed in all of the types. The narrower the kurtosis is, the more concentrated the particle-size distribution of the samples would be, which indicates that at least a portion of the sedimentary particulates is without environmental modification, and is directly transformed into the environment. In addition, the different combinations of quartz sand surface microtextures indicate the transformation from high-to low-energy impacts over a short distance, which is controlled by flood hydrodynamics and regime.

Overall, the longitudinal distribution of ODs is similar to that of an elongated fan-shaped terrace along the river channel. Disordered sedimentary sequences are formed in the upper section, whereas sub-ordered or ordered sedimentary sequences are formed in the middle and lower sections, which are completely absent in sedimentary deposits. The sedimentary sequences of the ODs lie between the alluvial and debris flow facies. The graded bedding texture in ODs is clearer than that in debris flow deposits, but there is no reverse or positive bedding rhythm in alluvial deposits. With regard to the macroscopic characteristics, the ODs profiles exhibit accumulation characteristics of normal fluvial deposits. Meanwhile, on a microscopic level, they also exhibit the characteristics of diluted debris flow deposits.

The special sedimentary characteristics of ODs can explain the hydrodynamic changes during the propagation of OFs and are important indicators for distinguishing between ODs and "*normal*" floods.

Data availability statement

The raw data supporting the conclusion of this article will be made available by the authors, without undue reservation.

Author contributions

JM: Conceptualization, Data curation, Formal Analysis, Investigation, Methodology, Software, Supervision, Validation, Visualization, Writing–original draft, Writing–review and editing. JC: Data curation, Investigation, Methodology, Project administration, Supervision, Validation, Writing–review and editing. CX: Conceptualization, Formal Analysis, Funding acquisition, Project administration, Resources, Software, Supervision, Writing–original draft.

Funding

The author(s) declare that financial support was received for the research, authorship, and/or publication of this article. This research study was supported by the National Institute of Natural Hazards, Ministry of Emergency Management of China (Grant no. 2023-JBKY-57).

Conflict of interest

The authors declare that the research was conducted in the absence of any commercial or financial relationships that could be construed as a potential conflict of interest.

The author(s) declared that they were an editorial board member of Frontiers, at the time of submission. This had no impact on the peer review process and the final decision.

Publisher's note

References

Alván, A., and von Eynatten, H. (2014). Sedimentary facies and stratigraphic architecture in coarse-grained deltas: anatomy of the Cenozoic Camaná Formation, southern Peru (16°25′S to 17°15′S). *J. S. Am. Earth Sci.* 54, 82–108. doi:10.1016/j.jsames.2014.04.008

Baker, V. R. (2008). Paleoflood hydrology: origin, progress, prospects. *Geomorphology* 101 (1-2), 1–13. doi:10.1016/j.geomorph.2008.05.016

Baker, V. R., Benito, G., Brown, A. G., Carling, P. A., Enzel, Y., Greenbaum, N., et al. (2022). Fluvial palaeohydrology in the 21st century and beyond. *Earth Surf. Process. Landforms* 47 (1), 58–81. doi:10.1002/esp.5275

Baker, V. R., Benito, G., and Rudoy, A. N. (1993). Paleohydrology of late Pleistocene superflooding, altay mountains, siberia. *Science* 259 (5093), 348–350. doi:10.1126/science.259.5093.348

Baker, V. R., and Carling, P. A. (2022). "6.38 - global late quaternary megafloods," in *Treatise on geomorphology*. Editor J. F. Shroder Second edition (San Diego: Academic Press), 832–840.

Bazai, N. A., Cui, P., Carling, P. A., Wang, H., Hassan, J., Liu, D., et al. (2021). Increasing glacial lake outburst flood hazard in response to surge glaciers in the Karakoram. *Earth-Science Rev.* 212, 103432. doi:10.1016/j.earscirev.2020.103432

Bellanova, P., Bahlburg, H., Nentwig, V., and Spiske, M. (2016). Microtextural analysis of quartz grains of tsunami and non-tsunami deposits – a case study from Tiráa (Chile). *Sediment. Geol.* 343, 72–84. doi:10.1016/j.sedgeo.2016.08.001

Benito, G., Ballesteros-Cánovas, J. A., and Díez-Herrero, A. (2023). "Chapter 2 - paleoflood hydrology: reconstructing rare events and extreme flood discharges," in *Hydro-meteorological hazards, risks, and disasters*. Editors J. F. Shroder, P. Paron, and G. D. Baldassarre Second Edition (Boston: Elsevier), 33–83.

Benito, G., Harden, T. M., and O'Connor, J. (2022). "6.35 - quantitative paleoflood hydrology," in *Treatise on geomorphology*. Editor J. F. Shroder Second Edition (Oxford: Academic Press), 743–764.

Benito, G., Macklin, M. G., Panin, A., Rossato, S., Fontana, A., Jones, A. F., et al. (2015). Recurring flood distribution patterns related to short-term Holocene climatic variability. *Sci. Rep.* 5, 16398. doi:10.1038/srep16398

Benito, G., Sánchez-Moya, Y., and Sopeña, A. (2003). Sedimentology of high-stage flood deposits of the Tagus River, Central Spain. *Sediment. Geol.* 157 (1-2), 107–132. doi:10.1016/S0037-0738(02)00196-3

Benito, G., and Thorndycraft, V. R. (2020). Catastrophic glacial-lake outburst flooding of the patagonian ice sheet. *Earth-Science Rev.* 200, 102996. doi:10.1016/j.earscirev.2019.102996

Bernhardt, A., Stright, L., and Lowe, D. R. (2012). Channelized debris-flow deposits and their impact on turbidity currents: the Puchkirchen axial channel belt in the Austrian Molasse Basin. *Sedimentology* 59 (7), 2042–2070. doi:10.1111/j.1365-3091.2012.01334.x

Blair, T. C., and McPherson, J. G. (1994). Alluvial fans and their natural distinction from rivers based on morphology, hydraulic processes, sedimentary processes, and facies assemblages. *J. Sediment. Res.* 64 (3a), 450–489. doi:10.1306/D4267DDE-2B26-11D7-8648000102C1865D

Blair, T. C., and McPherson, J. G. (1998). Recent debris-flow processes and resultant form and facies of the Dolomite alluvial fan, Owens Valley, California. *J. Sediment. Res.* 68 (5), 800–818. doi:10.2110/jsr.68.800

Blott, S. J., and Pye, K. (2001). GRADISTAT: a grain size distribution and statistics package for the analysis of unconsolidated sediments. *Earth Surf. Process. Landf.* 26 (11), 1237–1248. doi:10.1002/esp.261

Blott, S. J., and Pye, K. (2012). Particle size scales and classification of sediment types based on particle size distributions: Review and recommended procedures. *Sedimentology* 59 (7), 2071–2096. doi:10.1111/j.1365-3091.2012.01335.x

Bo, W., Zhang, T., Qin, Z., Chao, W., Chen, Y.-l., and Ping, W. (2015). A case study of the Tangjiashan landslide dam-break. *J. Hydrodynamics, Ser. B* 27 (2), 223–233. doi:10.1016/S1001-6058(15)60476-0

Borgohain, B., Mathew, G., Chauhan, N., Jain, V., and Singhvi, A. K. (2020). Evidence of episodically accelerated denudation on the Namche Barwa massif (Eastern Himalayan syntaxis) by megafloods. *Quat. Sci. Rev.* 245, 106410. doi:10.1016/j.quascirev.2020.106410

Bridge, J. S. (1984). Large-scale facies sequences in alluvial overbank environments. *J. Sediment. Res.* 54 (2), 583–588. doi:10.1306/212F8477-2B24-11D7-8648000102C1865D

Bridge, J. S. (2006). "Fluvial facies models: recent developments," in *Facies models revisited*. Editors H. W. Posamentier, and R. G. Walker (McLean, VA: SEPM Society for Sedimentary Geology), 1–17.

Burchfiel, B. C., Zhiliang, C., Yupinc, L., and Royden, L. H. (1995). Tectonics of the longmen Shan and adjacent regions, Central China. *Int. Geol. Rev.* 37 (8), 661–735. doi:10.1080/00206819509465424

Carling, P. A. (2013). Freshwater megaflood sedimentation: what can we learn about generic processes? *Earth-Science Rev.* 125, 87–113. doi:10.1016/j.earscirev.2013.06.002

Chang, D. S., and Zhang, L. M. (2010). Simulation of the erosion process of landslide dams due to overtopping considering variations in soil erodibility along depth. *Nat. Hazards Earth Syst. Sci.* 10 (4), 933–946. doi:10.5194/nhess-10-933-2010

Chen, J., Dai, F., Lv, T., and Cui, Z. (2013). Holocene landslide-dammed lake deposits in the Upper Jinsha River, SE Tibetan Plateau and their ages. *Quat. Int.* 298, 107–113. doi:10.1016/j.quaint.2012.09.018

Chen, J., Zhou, W., Cui, Z., Li, W., Wu, S., and Ma, J. (2018). Formation process of a large paleolandslide-dammed lake at Xuelongnang in the upper Jinsha River, SE Tibetan Plateau: constraints from OSL and 14 C dating. *Landslides* 15, 2399–2412. doi:10.1007/s10346-018-1056-3

Chen, L., Steel, R. J., Guo, F., Olariu, C., and Gong, C. (2017). Alluvial fan facies of the yongchong basin: implications for tectonic and paleoclimatic changes during late cretaceous in SE China. *J. Asian Earth Sci.* 134, 37–54. doi:10.1016/j.jseaes.2016.10.010

Chen, R., Chen, J., Ma, J., and Cui, Z. (2019). Quartz grain surface microtextures of dam-break flood deposits from a landslide-dammed lake: a case study. *Sediment. Geol.* 383, 238–247. doi:10.1016/j.sedgeo.2019.02.010

Chen, Z., Ma, L., Yu, S., Chen, S., Zhou, X., Sun, P., et al. (2015). Back analysis of the draining process of the Tangjiashan barrier lake. *J. Hydraulic Eng.* 141 (4), 05014011. doi:10.1061/(asce)hy.1943-7900.0000965

Costa, J. E. (1983). Paleohydraulic reconstruction of flash-flood peaks from boulder deposits in the Colorado Front Range. *Geol. Soc. Am. Bull.* 94 (8), 986–1004. doi:10.1130/0016-7606(1983)94<986:PROFPF>2.0.CO;2

Costa, J. E., and Schuster, R. L. (1988). The formation and failure of natural dams. *eology Soc. Am. Bull.* 100 (7), 1054–1068. doi:10.1130/0016-7606(1988)100<1054:TFAFON>2.3.CO;2

Costa, P. J. M., Andrade, C., Dawson, A. G., Mahaney, W. C., Freitas, M. C., Paris, R., et al. (2012). Microtextural characteristics of quartz grains transported and deposited by tsunamis and storms. *Sediment. Geol.* 275, 55–69. doi:10.1016/j.sedgeo.2012.07.013

Cui, P., Dang, C., Zhuang, J., You, Y., Chen, X., and Scott, K. M. (2012). Landslide-dammed lake at Tangjiashan, Sichuan Province, China (triggered by the Wenchuan Earthquake, May 12, 2008): risk assessment, mitigation strategy, and lessons learned. *Environ. Earth Sci.* 65 (4), 1055–1065. doi:10.1007/s12665-010-0749-2

Cui, Z., Ge, D., Guan, B., Li, D., Zhang, X., Chen, J., et al. (2013). *Diamicts and environment*. Shijiazhuang, China: Hebei Science and Technology Press.

Cutler, P. M., Colgan, P. M., and Mickelson, D. M. (2002). Sedimentologic evidence for outburst floods from the Laurentide Ice Sheet margin in Wisconsin, USA: implications for tunnel-channel formation. *Quat. Int.* 90 (1), 23–40. doi:10.1016/S1040-6182(01)00090-8

Dai, F. C., Lee, C. F., Deng, J. H., and Tham, L. G. (2005). The 1786 earthquake-triggered landslide dam and subsequent dam-break flood on the Dadu River, southwestern China. *Geomorphology* 65 (3-4), 205–221. doi:10.1016/j.geomorph.2004.08.011

Deane, S. M. (2010). *Quartz grain microtextures and sediment provenance: using scanning electron microscopy to characterize tropical highland sediments from costa rica and the dominican republic*. Master of Science (Knoxville: University of Tennessee).

Dino, R., Soares, E. A. A., Antonioli, L., Riccomini, C., and Nogueira, A. C. R. (2012). Palynostratigraphy and sedimentary facies of middle miocene fluvial deposits of the amazonas basin, Brazil. *J. S. Am. Earth Sci.* 34, 61–80. doi:10.1016/j.jsames.2011.11.008

Ermini, L., and Casagli, N. (2003). Prediction of the behaviour of landslide dams using a geomorphological dimensionless index. *Earth Surf. Process. Landforms J. Br. Geomorphol. Res. Group* 28 (1), 31–47. doi:10.1002/esp.424

Eyles, N., Eyles, C. H., and McCabe, A. M. (1988). Late Pleistocene subaerial debris-flow facies of the bow valley, near banff, Canadian rocky mountains. *Sedimentology* 35 (3), 465–480. doi:10.1111/j.1365-3091.1988.tb00998.x

Fan, X., Dufresne, A., Subramanian, S. S., Strom, A., Hermanns, R., Stefanelli, C. T., et al. (2020). The formation and impact of landslide dams–State of the art. *Earth-Science Rev.* 203, 103116. doi:10.1016/j.earscirev.2020.103116

Ferring, C. R. (2020). "Alluvial settings," in *Encyclopedia of geoarchaeology*. Editors A. S. Gilbert, P. Goldberg, R. D. Mandel, and V. Aldeias (Cham: Springer International Publishing), 1–11.

Gao, Q., Cui, Z., Tao, Z., Liu, G., and Hong, Y. (2002). The property, age and formation environment of the palaeokarst in Qinghai-Xizang Plateau. *J. Geogr. Sci.* 12 (2), 144–152. doi:10.1007/BF02837468

Gao, S., and Collins, M. B. (1994). Analysis of grain size trends, for defining sediment transport pathways in marine environments. *J. Coast. Res.* 10 (1), 70–78. doi:10.1002/esp.261

Gobala krishnan, N., Nagendra, R., and Elango, L. (2015). Quartz surface microtextural studies of Cauvery River sediments, Tamil Nadu, India. *Arabian J. Geosciences* 8 (12), 10665–10673. doi:10.1007/s12517-015-1995-0

Goudie, A., and Bull, P. A. (1984). Slope process change and colluvium deposition in Swaziland: an SEM analysis. *Earth Surf. Process. Landforms* 9 (3), 289–299. doi:10.1002/esp.3290090308

Greenbaum, N., Schwartz, U., Carling, P., Bergman, N., Mushkin, A., Zituni, R., et al. (2020). Frequency of boulders transport during large floods in hyperarid areas using paleoflood analysis – an example from the Negev Desert, Israel. *Earth-Science Rev.* 202, 103086. doi:10.1016/j.earscirev.2020.103086

Guo, Y., Ge, Y., Mao, P., Liu, T., Fu, X., and Wu, S. (2023). Geomorphologic evidences and hydrologic reconstruction of holocene catastrophic flood events in the yarlung tsangpo grand canyon, eastern himalaya. *J. Hydrology* 626, 130146. doi:10.1016/j.jhydrol.2023.130146

Guo, Y., Huang, C. C., Pang, J., Zhou, Y., Zha, X., and Mao, P. (2017). Reconstruction palaeoflood hydrology using slackwater flow depth method in the Yanhe River valley, middle Yellow River basin, China. *J. Hydrology* 544, 156–171. doi:10.1016/j.jhydrol.2016.11.017

Harms, J. C., Southard, J. B., Spearing, D. R., and Walker, R. G. (1975). *Depositional environments as interpreted from primary sedimentary structures and stratification sequences*. Tulsa, Oklahoma: SEPM Society for Sedimentary Geology.

Harrison, S., Kargel, J. S., Huggel, C., Reynolds, J., Shugar, D. H., Betts, R. A., et al. (2018). Climate change and the global pattern of moraine-dammed glacial lake outburst floods. *Cryosphere* 12 (4), 1195–1209. doi:10.5194/tc-12-1195-2018

Herget, J., and Fontana, A. (2019). *Palaeohydrology: traces, tracks and trails of extreme events*. Berlin, Heidelberg: Springer.

Huang, C. C., Pang, J., Zha, X., Zhou, Y., Su, H., and Li, Y. (2010). Extraordinary floods of 4100–4000 a BP recorded at the late neolithic ruins in the jinghe river gorges, middle reach of the yellow river, China. *Palaeogeogr. Palaeoclimatol. Palaeoecol.* 289 (1-4), 1–9. doi:10.1016/j.palaeo.2010.02.003

Huggel, C., Kääb, A., Haeberli, W., Teysseire, P., and Paul, F. (2002). Remote sensing based assessment of hazards from glacier lake outbursts: a case study in the Swiss Alps. *Can. Geotechnical J.* 39 (2), 316–330. doi:10.1139/t01-099

Immonen, N. (2013). Surface microtextures of ice-rafted quartz grains revealing glacial ice in the Cenozoic Arctic. *Palaeogeogr. Palaeoclimatol. Palaeoecol.* 374, 293–302. doi:10.1016/j.palaeo.2013.02.003

Jarrett, R. D., and England, J. F. (2002). "Reliability of paleostage indicators for paleoflood studies," in *Ancient floods, modern hazards*. Editors P. K. House, R. H. Webb, V. R. Baker, and D. R. Levish, 91–109.

Jiang, X., Cheng, H., Gao, L., and Liu, W. (2021). The formation and geometry characteristics of boulder bars due to outburst floods triggered by overtopped landslide dam failure. *Earth Surf. Dyn.* 9 (5), 1263–1277. doi:10.5194/esurf-9-1263-2021

Jiang, X., Huang, J., Wei, Y., Niu, Z., Chen, F., Zou, Z., et al. (2018). The influence of materials on the breaching process of natural dams. *Landslides* 15 (2), 243–255. doi:10.1007/s10346-017-0877-9

Jiang, X., and Wei, Y. (2019). Natural dam breaching due to overtopping: effects of initial soil moisture. *Bull. Eng. Geol. Environ.* 78 (7), 4821–4831. doi:10.1007/s10064-018-01441-7

Jiang, X., and Wei, Y. (2020). Erosion characteristics of outburst floods on channel beds under the conditions of different natural dam downstream slope angles. *Landslides* 17 (8), 1823–1834. doi:10.1007/s10346-020-01381-y

Knox, J. C. (2000). Sensitivity of modern and Holocene floods to climate change. *Quat. Sci. Rev.* 19 (1-5), 439–457. doi:10.1016/S0277-3791(99)00074-8

Korup, O. (2012). Earth's portfolio of extreme sediment transport events. *Earth-Science Rev.* 112 (3-4), 115–125. doi:10.1016/j.earscirev.2012.02.006

Korup, O., and Clague, J. J. (2009). Natural hazards, extreme events, and mountain topography. *Quat. Sci. Rev.* 28 (11-12), 977–990. doi:10.1016/j.quascirev.2009.02.021

Korup, O., and Montgomery, D. R. (2008). Tibetan plateau river incision inhibited by glacial stabilization of the Tsangpo gorge. *Nature* 455 (7214), 786–789. doi:10.1038/nature07322

Korup, O., Montgomery, D. R., and Hewitt, K. (2010). Glacier and landslide feedbacks to topographic relief in the Himalayan syntaxes. *Proc. Natl. Acad. Sci. U. S. A.* 107 (12), 5317–5322. doi:10.1073/pnas.0907531107

Li, T., Schuster, R. L., and Wu, J. (1986). "Landslide dams in south-central China," in *Landslide dams: processes, risk, and mitigation*. Editor R. L. Schuster (Washington: American Society of Civil Engineers).

Liu, D., Cui, Y., Wang, H., Jin, W., Wu, C., Bazai, N. A., et al. (2021). Assessment of local outburst flood risk from successive landslides: case study of Baige landslide-dammed lake, upper Jinsha river, eastern Tibet. *J. Hydrology* 599, 126294. doi:10.1016/j.jhydrol.2021.126294

Liu, W., Carling, P. A., Hu, K., Wang, H., Zhou, Z., Zhou, L., et al. (2019). Outburst floods in China: a review. *Earth-Science Rev.* 197, 102895. doi:10.1016/j.earscirev.2019.102895

Liu, W., Hu, K., Carling, P. A., Lai, Z., Cheng, T., and Xu, Y. (2018). The establishment and influence of Baimakou paleo-dam in an upstream reach of the Yangtze River, southeastern margin of the Tibetan Plateau. *Geomorphology* 321, 167–173. doi:10.1016/j.geomorph.2018.08.028

Lord, M. L., and Kehew, A. E. (1987). Sedimentology and paleohydrology of glacial-lake outburst deposits in southeastern Saskatchewan and northwestern North Dakota. *Geol. Soc. Am. Bull.* 99 (5), 663–673. doi:10.1130/0016-7606(1987)99<663:SAPOGO>2.0.CO;2

Ma, J., Chen, J., Cui, Z., Zhou, W., Chen, R., and Wang, C. (2022). Reconstruction of catastrophic outburst floods of the Diexi ancient landslide-dammed lake in the upper Minjiang River, eastern Tibetan plateau. *Nat. Hazards* 112 (2), 1191–1221. doi:10.1007/s11069-022-05223-z

Ma, J., Chen, J., Cui, Z., Zhou, W., Liu, C., Guo, P., et al. (2018). Sedimentary evidence of outburst deposits induced by the Diexi paleolandslide-dammed lake of the upper Minjiang River in China. *Quat. Int.* 464, 460–481. doi:10.1016/j.quaint.2017.09.022

Mahaney, W. C., and Kalm, V. (2000). Comparative scanning electron microscopy study of oriented till blocks, glacial grains and Devonian sands in Estonia and Latvia. *Boreas* 29 (1), 35–51. doi:10.1111/j.1502-3885.2000.tb01199.x

Maizels, J. (1997). Jökulhlaup deposits in proglacial areas. *Quat. Sci. Rev.* 16 (7), 793–819. doi:10.1016/S0277-3791(97)00023-1

Mao, P., Guo, Y., and Liu, T. (2023). Holocene extreme palaeofloods recorded by slackwater deposits along the Jiacha Gorge of the Yarlung Tsangpo River valley, southern Tibetan Plateau. *Catena* 231, 107360. doi:10.1016/j.catena.2023.107360

Mao, P., Pang, J., Huang, C., Zha, X., Zhou, Y., Guo, Y., et al. (2016). A multi-index analysis of the extraordinary paleoflood events recorded by slackwater deposits in the Yunxi Reach of the upper Hanjiang River, China. *Catena* 145, 1–14. doi:10.1016/j.catena.2016.05.016

Margolis, S. V., and Krinsley, D. H. (1974). Processes of formation and environmental occurrence of microfeatures on detrital quartz grains. *Am. J. Sci.* 274 (5), 449–464. doi:10.2475/ajs.274.5.449

McKee, E. D., Crosby, E. J., and Berryhill, H. L. (1967). Flood deposits, bijou creek, Colorado, JUNE =)(. *J. Sediment. Res.* 37 (3), 829–851. doi:10.1306/74D717B2-2B21-11D7-8648000102C1865D

McManus, J. (1988). "Grain size determination and interpretation," in *Techniques in sedimentology*. Editor M. E. Tucker (Oxford: Blackwell Scientific Publications), 63–85.

Miall, A. D. (2013). *The geology of fluvial deposits: sedimentary facies, basin analysis, and petroleum geology*. Berlin, Heidelberg: Springer.

Miall, A. D. (2022). "Facies models," in *Stratigraphy: a modern synthesis*. Editor A. D. Miall (Cham: Springer International Publishing), 175–230.

Molén, M. O. (2014). A simple method to classify diamicts by scanning electron microscope from surface microtextures. *Sedimentology* 61 (7), 2020–2041. doi:10.1111/sed.12127

Moscariello, A., Marchi, L., Maraga, F., and Mortara, G. (2002). "Alluvial fans in the Italian alps: sedimentary facies and processes," in *Flood and megaflood processes and deposits*. Editors P. Martini, V. R. Baker, and G. Garzón, 141–166.

Mutti, E., Tinterri, R., Di Biase, D., Fava, L., Mavilla, N., Angella, S., et al. (2000). Delta-front facies associations of ancient flood-dominated fluvio-deltaic systems. *Rev. Soc. Geol. España* 13 (2), 165–190.

O'Connor, J. E. (1993). *Hydrology, hydraulics, and geomorphology of the Bonneville flood*. Boulder, CO: Geological Society of America.

O'Connor, J. E., Clague, J. J., Walder, J. S., Manville, V., and Beebee, R. A. (2022). "6.36 - outburst floods," in *Treatise on geomorphology*. Editor J. F. Shroder Second Edition (San Diego: Academic Press), 765–819.

O'Connor, J. E., and Costa, J. E. (2004). *The world's largest floods, past and present: their causes and magnitudes*. Reston, VA: U.S. Geological Survey Circular 1254.

O'Connor, J. E., Grant, G. E., and Costa, J. E. (2002). "The geology and geography of floods," in *Ancient floods, modern hazards: principles applications of paleoflood hydrology*. Editors P. K. House, R. H. Webb, and D. R. Levish (Washington: American Geophysical Union), 359–385.

Peng, M., and Zhang, L. M. (2012). Breaching parameters of landslide dams. *Landslides* 9 (1), 13–31. doi:10.1007/s10346-011-0271-y

Peng, M., and Zhang, L. M. (2013). Dynamic decision making for dam-break emergency management – Part 2: application to Tangjiashan landslide dam failure. *Nat. Hazards Earth Syst. Sci.* 13 (2), 439–454. doi:10.5194/nhess-13-439-2013

Quesada-Román, A., Ballesteros-Cánovas, J. A., George, S. S., and Stoffel, M. (2022). Tropical and subtropical dendrochronology: approaches, applications, and prospects. *Ecol. Indic.* 144, 109506. doi:10.1016/j.ecolind.2022.109506

Ran, Y., Chen, L., Chen, G., Yin, J., Chen, J., Gong, H., et al. (2008). Primary analyses of in-situ recurrence of large earthquake along seismogenic fault of the Ms 8.0 Wenchuan earthquake (in Chinese with English Abstract). *Seismol. Geol.* 30 (3), 630–643. doi:10.3969/j.issn.0253-4967.2008.03.004

Reading, H. G. (2009). *Sedimentary environments: processes, facies and stratigraphy*. Oxford: Blackwell Publishing.

RGSTS (1975). *Regional geological survey report of the People's Republic of China: images of Songpan (NO. I-48-XXXII) and Maowen (NO. H-48-II) (scale: 1:200000)*. Chengdu: Regional Geological Survey Team of the Sichuan Bureau of Geology and Mineral Resources.

Roe, G. H., Baker, M. B., and Herla, F. (2017). Centennial glacier retreat as categorical evidence of regional climate change. *Nat. Geosci.* 10 (2), 95–99. doi:10.1038/ngeo2863

Ruiz-Bellet, J. L., Castelltort, X., Balasch, J. C., and Tuset, J. (2017). Uncertainty of the peak flow reconstruction of the 1907 flood in the ebro River in xerta (NE iberian peninsula). *J. Hydrology* 545, 339–354. doi:10.1016/j.jhydrol.2016.12.041

Russell, A. J., and Knudsen, Ó. (1999). An ice-contact rhythmite (turbidite) succession deposited during the November 1996 catastrophic outburst flood (jökulhlaup), Skeiðarárjökull, Iceland. *Sediment. Geol.* 127 (1-2), 1–10. doi:10.1016/S0037-0738(99)00024-X

Russell, A. J., and Knudsen, Ó. (2002). "The effects of glacier-outburst flood flow dynamics on ice-contact deposits: november 1996 Jökulhlaup, Skeiðarársandur, Iceland," in *Flood and megaflood processes and deposits*. Editors I. P. Martini, V. R. Baker, and G. Garzón (Chichester: Wiley), 67–83.

Schmocker, L., Frank, P.-J., and Hager, W. H. (2014). Overtopping dike-breach: effect of grain size distribution. *J. Hydraulic Res.* 52 (4), 559–564. doi:10.1080/00221686.2013.878403

Shi, Z. M., Guan, S. G., Peng, M., Zhang, L. M., Zhu, Y., and Cai, Q. P. (2015). Cascading breaching of the Tangjiashan landslide dam and two smaller downstream landslide dams. *Eng. Geol.* 193, 445–458. doi:10.1016/j.enggeo.2015.05.021

Shugar, D. H., Burr, A., Haritashya, U. K., Kargel, J. S., Watson, C. S., Kennedy, M. C., et al. (2020). Rapid worldwide growth of glacial lakes since 1990. *Nat. Clim. Change* 10 (10), 939–945. doi:10.1038/s41558-020-0855-4

Smith, G. A. (1986). Coarse-grained nonmarine volcaniclastic sediment: terminology and depositional process. *Geol. Soc. Am. Bull.* 97 (1), 1–10. doi:10.1130/0016-7606(1986)97<1:CNVSTA>2.0.CO;2

Sohn, Y. K., Rhee, C. W., and Kim, B. C. (1999). Debris flow and hyperconcentrated flood-flow deposits in an alluvial fan, northwestern part of the Cretaceous Yongdong Basin, Central Korea. *J. Geol.* 107 (1), 111–132. doi:10.1086/314334

Srivastava, P., Kumar, A., Chaudhary, S., Meena, N., Sundriyal, Y., Rawat, S., et al. (2017). Paleofloods records in himalaya. *Geomorphology* 284, 17–30. doi:10.1016/j.geomorph.2016.12.011

Støren, E. W., Paasche, Ø., Hirt, A. M., and Kumari, M. (2016). Magnetic and geochemical signatures of flood layers in a lake system. *Geochem. Geophys. Geosystems* 17 (10), 4236–4253. doi:10.1002/2016GC006540

Sweet, D. E., and Soreghan, G. S. (2010). Application of Quartz Sand Microtextural Analysis to Infer Cold-Climate Weathering for the Equatorial Fountain Formation (Pennsylvanian–Permian, Colorado, U.S.A.). *J. Sediment. Res.* 80 (7), 666–677. doi:10.2110/jsr.2010.061

Taylor, C., Robinson, T. R., Dunning, S., Rachel Carr, J., and Westoby, M. (2023). Glacial lake outburst floods threaten millions globally. *Nat. Commun.* 14, 487. doi:10.1038/s41467-023-36033-x

Teller, J. T., Leverington, D. W., and Mann, J. D. (2002). Freshwater outbursts to the oceans from glacial Lake Agassiz and their role in climate change during the last deglaciation. *Quat. Sci. Rev.* 21 (8-9), 879–887. doi:10.1016/S0277-3791(01)00145-7

Tian, S., Chen, N., Wu, H., Yang, C., Zhong, Z., and Rahman, M. (2020). New insights into the occurrence of the Baige landslide along the Jinsha River in Tibet. *Landslides* 17 (5), 1207–1216. doi:10.1007/s10346-020-01351-4

Van Gorp, W., Schoorl, J. M., Temme, A. J. A. M., Reimann, T., Wijbrans, R., Maddy, D., et al. (2016). Catchment response to lava damming: integrating field observation, geochronology and landscape evolution modelling. *Earth Surf. Process. Landforms* 41 (11), 1629–1644. doi:10.1002/esp.3981

Visher, G. S. (1969). Grain size distributions and depositional processes. *J. Sediment. Res.* 39 (3), 1074–1106. doi:10.1306/74D71D9D-2B21-11D7-8648000102C1865D

Vos, K., Vandenberghe, N., and Elsen, J. (2014). Surface textural analysis of quartz grains by scanning electron microscopy (SEM): From sample preparation to environmental interpretation. *Earth-Science Rev.* 128, 93–104. doi:10.1016/j.earscirev.2013.10.013

Walder, J. S., Iverson, R. M., Godt, J. W., Logan, M., and Solovitz, S. A. (2015). Controls on the breach geometry and flood hydrograph during overtopping of noncohesive earthen dams. *Water Resour. Res.* 51 (8), 6701–6724. doi:10.1002/2014WR016620

Wang, H., Cui, P., Yang, A., Tang, J., Wen, S., Yang, Z., et al. (2023a). New evidence of high-magnitude Holocene floods in the Purlung Tsangpo River, southeastern Tibetan Plateau. *Catena* 233, 107516. doi:10.1016/j.catena.2023.107516

Wang, H., Cui, P., Zhou, L., Liu, W., Yang, A., Yao, S., et al. (2022a). Spatial and temporal distribution of landslide-dammed lakes in Purlung Tsangpo. *Eng. Geol.* 308, 106802. doi:10.1016/j.enggeo.2022.106802

Wang, H., Yang, A., Jiang, S., and Liu, N. (2023b). Reconstruction of a Holocene landslide-dammed lake in the Yalong basin, eastern Tibetan Plateau. *Front. Earth Sci.* 10, 1042581. doi:10.3389/feart.2022.1042581

Wang, L., Huang, C. C., Pang, J., Zha, X., and Zhou, Y. (2014a). Paleofloods recorded by slackwater deposits in the upper reaches of the Hanjiang River valley, middle Yangtze River basin, China. *J. Hydrology* 519, 1249–1256. doi:10.1016/j.jhydrol.2014.08.002

Wang, P., Chen, J., Dai, F., Long, W., Xu, C., Sun, J., et al. (2014b). Chronology of relict lake deposits around the Suwalong paleolandslide in the upper Jinsha River, SE Tibetan Plateau: Implications to Holocene tectonic perturbations. *Geomorphology* 217, 193–203. doi:10.1016/j.geomorph.2014.04.027

Wang, P., Zhang, B., Qiu, W., and Wang, J. (2011). Soft-sediment deformation structures from the Diexi paleo-dammed lakes in the upper reaches of the Minjiang River, east Tibet. *J. Asian Earth Sci.* 40 (4), 865–872. doi:10.1016/j.jseaes.2010.04.006

Wang, Z., Yue, G., Lin, H., and Li, M. (2022b). Numerical analysis of dynamic evolution characteristics of a large rock landslide in Tangjiashan. *Geofluids* 2022, 1–17. doi:10.1155/2022/5423743

Wohl, E. E. (1992). Bedrock benches and boulder bars: Floods in the Burdekin Gorge of Australia. *Geol. Soc. Am. Bull.* 104 (6), 770–778. doi:10.1130/0016-7606(1992)104<0770:BBABBF>2.3.CO;2

Wu, H., Trigg, M. A., Murphy, W., and Fuentes, R. (2022). A new global landslide dam database (RAGLAD) and analysis utilizing auxiliary global fluvial datasets. *Landslides* 19 (3), 555–572. doi:10.1007/s10346-021-01817-z

Xiong, X., Matsumoto, T., Shi, Z., and Zhang, F. (2022). Flume tests and corresponding numerical simulation of hydraulic/mechanical behavior of Tangjiashan landslide dam subjected to seepage loading. *Soils Found.* 62 (5), 101200. doi:10.1016/j.sandf.2022.101200

Xue, B., Wang, S., Xia, W., Wu, J., Wang, Y., Qian, J., et al. (1998). The uplifting and environmental change of Qinghai-Xizang (Tibetan) Plateau in the past 0.9 Ma inferred from core RM of Zoige Basin. *Sci. China Ser. D Earth Sci.* 41 (2), 165–170. doi:10.1007/BF02932436

Yang, A., Wang, H., Liu, W., Hu, K., Liu, D., Wu, C., et al. (2022). Two megafloods in the middle reach of Yarlung Tsangpo River since Last-glacial period: Evidence from giant bars. *Glob. Planet. Change* 208, 103726. doi:10.1016/j.gloplacha.2021.103726

Zhang, P. (2013). A review on active tectonics and deep crustal processes of the Western Sichuan region, eastern margin of the Tibetan Plateau. *Tectonophysics* 584, 7–22. doi:10.1016/j.tecto.2012.02.021

Zhang, Q., Chen, Z., Li, Y., Yu, S., Wang, L., Zhou, X., et al. (2023). Quantitative assessment on landslide dam risks and mitigation: an in-depth study on the Baige lake breach. *Environ. Earth Sci.* 82 (4), 96–20. doi:10.1007/s12665-023-10778-6

Zhao, T., Crosta, G. B., Dai, F., and Xu, N. (2018). "Generation of complex slope geometries by DEM for modeling landslides: A case study of Tangjiashan landslide," in *GeoShanghai 2018 international conference: geoenvironment and geohazard*. Editors A. Farid, and H. Chen (Singapore: Springer).

Zheng, H., Shi, Z., Shen, D., Peng, M., Hanley, K. J., Ma, C., et al. (2021). Recent advances in stability and failure mechanisms of landslide dams. *Front. Earth Sci.* 9, 659935. doi:10.3389/feart.2021.659935

Zhong, Q., Chen, S., Wang, L., and Shan, Y. (2020). Back analysis of breaching process of Baige landslide dam. *Landslides* 17 (7), 1681–1692. doi:10.1007/s10346-020-01398-3

Zhong, Q., Wang, L., Chen, S., Chen, Z., Shan, Y., Zhang, Q., et al. (2021). Breaches of embankment and landslide dams - State of the art review. *Earth-Science Rev.* 216, 103597. doi:10.1016/j.earscirev.2021.103597

Zhou, G. G. D., Zhou, M., Shrestha, M. S., Song, D., Choi, C. E., Cui, K. F. E., et al. (2019). Experimental investigation on the longitudinal evolution of landslide dam breaching and outburst floods. *Geomorphology* 334, 29–43. doi:10.1016/j.geomorph.2019.02.035

Zhu, X., Peng, J., Jiang, C., and Guo, W. (2019). A Preliminary study of the failure modes and process of landslide dams due to upstream flow. *Water* 11 (6), 1115. doi:10.3390/w11061115

frontiers | Frontiers in Public Health

TYPE Original Research
PUBLISHED 31 July 2024
DOI 10.3389/fpubh.2024.1402998

OPEN ACCESS

EDITED BY
Lingling Shen,
Beijing Meteorological Information Center, China

REVIEWED BY
Jinjun Zhang,
Beijing Emergency Medical Center, China
Jose Luis Martinez-Flores,
Popular Autonomous University of the State of Puebla, Mexico

*CORRESPONDENCE
Xiaoyang Ji
✉ j625207669@163.com

RECEIVED 18 March 2024
ACCEPTED 22 July 2024
PUBLISHED 31 July 2024

CITATION
Jiang Q, Ji X and Rong Z (2024) Analysis of urban necessities reserve index and reserve quantity under emergency conditions. *Front. Public Health* 12:1402998. doi: 10.3389/fpubh.2024.1402998

Analysis of urban necessities reserve index and reserve quantity under emergency conditions

Qijun Jiang, Xiaoyang Ji* and Zhijie Rong

School of Economics and Management, Shanghai Ocean University, Shanghai, China

While maintaining a robust reserve of daily necessities is crucial for urban safety, but there is a lack of scientific basis for determining "what to store" and "how much to store." This paper address this gap by classifying and summarizing the emergency materials of urban necessities in Shanghai, and establishing a corresponding reserve list. By constructing an index model of daily necessities reserve, this paper provides a scientific foundation for "what to store." Additionally, the reserve levels of different types of daily necessities are classified and managed, the reserve model of emergency daily necessities is constructed. This approach clarifies the scientific basis for "how much to store," overcoming the problems of subjective factors interference and the potential mismatch between the results of objective weighting method and reality. Furthermore, to better cope with emergencies, countermeasures and suggestions are put forward: optimizing the material structure of emergency reserves, managing the material reserves at different levels, scientifically and reasonably planning the amount of emergency materials, and reducing the cost of reserves and improve the efficiency of emergency reserves.

KEYWORDS

necessities of life, reserve index, reserve quantity, emergency reserve, city

1 Introduction

Global warming intensifies the instability of the climate system, with frequent extreme cold and warm events, and frequent droughts and rainstorms becoming a new normal (1). This undescores the importance of constructing an urban necessities reserve system. Under the emergency situations of natural disasters, wars, public health incidents, accidents, and other serious disasters, such system is crucial for urban residents to maintain their normal lives, and it is also an important micro-embodiment of urban resilience (2). In recent years, the State Council has repeatedly proposed to improve the reserve mechanism of residents' daily necessities in relevant documents concerning the circulation industry, emergency system, and economic system improvement (3). The efficient and accurate management of daily necessities in emergencies is a systematic work that requires considering many factors in the management process, and the storage requirements and conditions of each type of material are different (4). After the outbreak, megacities consolidated and optimized the experience model of epidemic prevention and supply, and many cities incorporated emergency supply of daily necessities into the smart governance of megacities and the construction of living materials support capacity in the strategic rear area according to the idea of "wartime supply, peacetime regulation, peacetime combination, and agile switching" (5).

To improve the emergency support ability of daily necessities in emergencies such as public health emergencies, we can focus on four key areas: technology, management, storage, and logistics. First, we can rely on scientific and technological means to achieve efficiency emergency management of daily necessities. This includes establishing a scientific and technological support system and building an integrated emergency support platform for daily necessities (6). Second, it is necessary to improve the emergency material support mechanism. This involves creating a coordinated support system, identifying and evaluate risks (7), and establishing relevant management organizations to provide emergency support for the government's emergency material allocation management (8). Third, we should also strengthen research and application of monitoring technology for emergency storage channels of daily necessities (9). We should further improve the storage system of daily necessities and establish a scientific material storage system (10). Fourth, building a robust emergency logistics system is essential. This system should encompass a command system, channel system, information management system, facilities and equipment system, and security system (11). At present, China has established a relatively well-developed urban reserve management system, and the main challenge is the reserve of daily necessities. However, the scope of daily necessities evolves with societal development, and reserve and allocation in sudden disasters constantly face new challenges (12). Under the emergency situations, the city's regular resource allocation system becomes easily disrupted. Determine the categories, storage quantities, and storage methods of daily necessities (13), and identifying approaches to ensure the supply of urban daily necessities, are urgent issues that need to be addressed.

The type, quality, and speed of the supply of necessities, as well as whether it can meet people's needs in a timely manner, can indirectly reflect the local government's ability to guarantee emergency response. Necessities of life are items that can satisfy the most basic needs of people's survival and life. Although market serves as the primary supplier of necessities goods, during emergencies, local governments play a crucial role in emergency management by issuing notices related to the supply of necessities of life, and providing green channels and policy concessions for the relevant enterprises, to ensure that the supply of essential commodities meets public needs. While the National Classification and Coding of Emergency Materials and the Catalogue of Emergency Support Key Materials provide a clear description of emergency materials, there is no well-defined judgment basis for the confirmation standards of reserve varieties and reserve quantities of urban necessities in academic circles and industries. For the reserve of daily necessities, simply having more reserves is not necessarily better. Effectively improving the reserve efficiency of urban daily necessities is an important part of reserve management. This paper deepens the research on how government can guarantee necessities of life during emergencies such as public health emergencies. Existing research on public health emergencies in China focus on the exploration of the causes and the construction of the system, with less emphasis on the effective emergency reserve management under such events. At the same time, although the stockpiling of daily necessities has been strongly advocated, there are no clear regulations on the quantity and types of daily necessities to be stockpiled in cities. Taking Shanghai as an example, this paper analyzes the reserve index and reserve quantity of various types of daily necessities based on the risk characteristics, environmental characteristics and demand characteristics of daily necessities in Shanghai, comprehensive risk probability, urban population characteristics and other factors. This analysis clarifies the importance of different types of daily necessities reserves, improves the distribution method of daily necessities in emergencies, promotes the construction of the daily necessities reserve theory in emergencies that aligns with China's national conditions and guides practical implementation, enriches the contents of emergency support such as public health, and has significance for effectively guiding the hierarchical management of daily necessities reserves, thereby improving urban residents' livelihood security.

2 Literature review

2.1 Definition and classification of daily necessities

In response to emergencies, the government stockpiles a certain amount of relief materials to ensure the supply of urban necessities (14), especially in case of inconvenient transportation, such as the closure of the city caused by emergencies and the shortage of residents' daily necessities. Local departments must then arrange and deploy resources in a timely manner to ensure the basic needs of the residents who during city closures. The necessities of life are the basic living aid materials used to ensure the emergency transfer and resettlement of personnel and meet their basic living needs in emergencies. The public's understanding of the word "necessities" can vary (15), and personal views are influenced by individual circumstances, making it difficult to reach a consensus on the definition of necessities that are completely public-oriented (16). In a broad sense, necessities of life cover the protection of food, clothing, housing, transportation, medical care, sanitation, and other aspects, including but not limited to five functional categories: temporary residence, bedding, clothing, food, medical and epidemic prevention. From an economic point of view, the demand for daily necessities are mostly inelastic, such as food and medical services (17). In other words, even during economic fluctuations, the demand for these items remains relatively constant. From the perspective of daily life, it also includes items such as sanitary cleaning products that can meet the most basic needs of people's survival and life. In 2011, Article 27 of the Emergency Management Measures for Market Supply of Necessities by the Ministry of Commerce proposed that "in the event of public health incidents which are easy to spread, such as mass diseases and animal epidemics, it is necessary to focus on the market supply of sanitary and cleaning products, protective products, grain, edible oil, salt, livestock and poultry products, and convenience foods" (18). Combining this information with the list of daily necessities outlined in the Tenth Five-Year Plan for Emergency Material Support, Shanghai List of Suggestions for Family Emergency Material Reserve and Guidelines for Disaster Relief Material Reserve Standards (19), this paper classifies the daily necessities into "clothing support, food support, temporary accommodation, sanitary products, medical drugs" and other varieties. The clothing support category includes regular clothes and warm clothes; Food security mainly includes drinking water, finished grain, convenience food, edible oil, edible salt, green leafy vegetables, radishes, potatoes, edible fungi, fruits, livestock meat, aquatic products, eggs, milk powder and liquid milk. Temporary accommodation mainly includes tents, movable tables and chairs, folding beds, bedding, pillows and moisture-proof mats.

Hygienic articles can be divided into cleaning and disinfection articles such as disinfectant alcohol, disinfectant and insecticide, daily necessities such as towels, toothbrushes, toothpaste, roll paper and garbage bags, and sanitary protection articles such as simple toilets, bath cars and garbage bins. Medical drugs are mainly emergency medical kits.

2.2 Differences in demand for daily necessities under different emergency levels

The State Emergency Management Bureau divides emergencies into four grades: I (particularly serious), II (serious), III (major), and IV (general). The emergency response is divided into four levels from high to low: I, II, III, and IV (20). Level IV refers to general public health emergencies, public health emergencies with more than 10 casualties and less than 29, with more than one case of death and critical illness, and other events jeopardizing the safety of public life, which are also reported to the people's government of the prefecture-level administrative regions. Level III refers to major public health emergencies, public health emergencies with more than 30 casualties and less than 49 casualties, more than 3 cases of death and critical illness, and other events jeopardizing the safety of public life, also reported to the People's Government of the prefecture-level administrative regions. Level II refers to major public health emergencies, cross-city (prefecture) public emergencies with serious casualties, and other events requiring emergency medical and health care rescue, and is guided by an expert group sent by the provincial government. Level I refers to particularly significant public health emergencies, public emergencies with particularly serious casualties across provinces (districts and municipalities), and other events requiring medical and health emergency rescue, with the State Council sending an expert steering group (21). Taking the sudden flood disaster as an example (22), the level of impact on daily life varies depending on the emergency response level. When the level IV emergency response occurs, the daily life of most residents are minimally affected, and it may only increase the purchase of main and non-staple foods such as meat and vegetables. When Class III and Class II emergency responses occur, there may be more than dozens of casualties, leading to changes in demand of daily necessities. On the one hand, it is reflected in the increase of food reserves of residents' families; on the other hand, it may be reflected in the increase of medication purchases due to the occurrence of casualties. When the level I emergency response occurs, not only casualties may occur, but also houses may collapse and people's production and living materials suffer huge losses. This level of emergency triggers the need for temporary necessities such as clothing, food, temporary accommodation, medical drugs, and sanitary products.

3 Materials and methods

3.1 Model construction of single variety reserve index of daily necessities

3.1.1 Screening standard of daily necessities reserve

Due to the wide variety of daily necessities, it is impractical to reserve all of them. In order to comprehensively evaluate the importance and necessity of the reserve of each item of daily necessities, it is essential to thoroughly analyse the characteristics of daily necessities, reserve costs, and other factors. By constructing the single variety reserve index of emergency daily necessities, we can scientifically answer the question of "what to store." This will allow us to optimize the category composition and allocation of daily necessities reserve, resulting in reduced costs and improved efficiency of emergency daily necessities reserves. The emergency necessities single product reserve index refers to the importance of maintain this particular product in daily necessities reserve. The higher the value, the more essential it is to have a sufficient stock of this particular product.

In recent years, Shanghai, Beijing, and Guangzhou have proposed the concept of establishing a 15-min life circle (23). The typical size of a 15-min community life circle generally ranges from 3 km^2, with a permanent population of 50,000 to 100,000 people and a population density of 10,000 to 30,000 people/km^2 (24). To understand the standard of the daily necessity reserve, we take the 15-min walking range as the spatial scale, and allocate various functions and facilities required by residents' basic life (25). Daily necessities are the most needed materials for residents to deal with emergencies, and also the basic reserve materials to meet the needs of residents' 15-min living circle. After an emergency, the emergency reserve of daily necessities can meet the basic needs of the victims. Therefore, meeting consumers' consumption demand is the most important of the screening criteria.

When planning emergency supplies, it's crucial to consider the unique challenges of emergencies and logistics. This means finding a balance between shelf life and convenient circulation of goods. To address these, it is necessary to implement a multi-item storage strategy, to meet the overall nutritional needs of the population while maintaining convenient circulation with a relatively small amount of single items (26). In addition, given the unexpected nature of the emergency and unknown duration, it is also necessary to take into account goods that have low storage requirements and extended shelf lives.

To sum up, based on the premise of "satisfying consumers' needs, diversifying commodity categories and facilitating storage," to meet the basic reserve material demand of residents' 15-min living circle and improve the energy efficiency of daily necessities reserve, this paper puts forward the following screening criteria for the selection of daily necessities single product reserve: the selected emergency materials of daily necessities must be in the list of Emergency Materials Classification and Coding, and the reserve scope should cover four aspects: eating, wearing, living and using, which can meet the requirements. The reserve of daily necessities should be closely related to the needs of life, which is universal. The chosen items should be in high demand during disasters when many residents require them. To improve the reserve efficiency, it is necessary to give priority to the economical varieties, comprehensive in function, convenient to use, and easy to reserve (27).

3.1.2 Analysis of factors affecting single variety reserve index

When a disaster occurs, emergency managers should first consider whether there are available reserve materials. If there are, it will be regarded as a direct acquisition of the materials; if not, it will be considered as internal acquisition and external acquisition of the materials. The main way of internal acquisition is direct production.

In case of emergency, the most important consideration is whether the material can be obtained through production in a timely manner. If the materials can be produced quickly during an emergency, they are considered to be available. Conversely, slow production necessitates reserve stockpiling. The primary factor for external acquisition or purchase is the market liquidity of the material. Materials with strong market liquidity are considered to be available. If the liquidity is not strong, the rational decision is to reserve the material for a rainy day. To sum up, when it is difficult to obtain a material internally and externally, the rational decision is to reserve it, and the storage cost and storage resistance of this material will further affect the storage strategy. Therefore, this study identifies four key factors for screening the single variety reserve index of daily necessities: market liquidity, production cycle, storage resistance, and storage cost of materials.

Market liquidity of reserve items. Market liquidity is the possibility and speed of market participants to reach a transaction at market price. Commercial reserves usually reserve emergency materials and equipment with large market liquidity, high storage costs, and short shelf life (28). The higher the market liquidity of materials, the easier it is for residents to buy such materials in case of emergency. Therefore, the influence of market liquidity on the reserves of such materials is negative.

Production cycle of reserved items. When an emergency happens, the demand for living materials has the characteristics of timeliness, suddenness, and universality. Therefore, when formulating the emergency material reserve strategy, the length of the production cycle of the material should be considered. Emergency materials with a long production cycle are difficult to produce quickly in response to an emergency (29), necessitating a larger reserve. Therefore, the impact of the production cycle on the reserve of such materials is positive. In the context of emergency procurement, emergency materials with large demand, short production cycles, and easy preservation are usually studied (30).

Storage resistance of reserved items. Storage resistance refers to the characteristics that materials can maintain their original quality without obvious adverse changes within a certain storage period. When considering the storage capacity of a single item, the storability of the single item is often considered to reduce the inventory cost of emergency materials and the waste caused by deterioration (31). The higher the storability of materials, the lower the risk of loss caused by storage time, and the influence of storability on the storage capacity of such materials is positive.

The reserve cost of a single item. During the storage of materials, there may be various storage expenses such as warehouse expenses, insurance expenses, inventory damage, and deterioration losses. The reserve cost may lead to the problem of overstock of inventory and capital occupation. If the materials are excessively reserved, it will increase the material reserve cost and lead to the waste of material resources. For example, to reduce the impact of disasters, the government reserves emergency materials to improve the efficiency of disaster relief, but it may not be able to meet the demand for emergency materials for unconventional emergencies due to factors such as reserve costs and management costs (32). Therefore, to improve the reserve efficiency, materials with high reserve costs need to be appropriately reduced.

3.1.3 Calculation of single variety reserve index of daily necessities

According to the above analysis, this paper comprehensively considers four factors of emergency necessities: market liquidity ∂_i, storage resistance β_i, production cycle γ_i, and reserve cost θ_i. The subjective and objective combination method of the Delphi method and entropy weight method is used to calculate the weight of each index, which solves the problem that the subjective weighting method is too subjective and the objective weighting method is quite different from the actual situation. The data sources are the China Logistics Association Report, China Statistical Yearbook, China Retail Yearbook, and China Agricultural Statistical Yearbook. The implementation effect of each influencing factor index is evaluated, and the initial data set of each index is finally obtained.

Because the storage capacity and production cycle have a positive impact on the reserve, the β_i and γ_i are positively standardized by Eq. (1). The influence of market liquidity and reserve cost on the reserve is negative, and ∂_i and θ_i are inversely standardized by Eq. (2) to get the standardized index data set.

$$X_i' = \frac{X_i - \min(X_1\ X_2, \ldots\ldots\ X_i)}{\max(X_1\ X_2, \ldots\ldots\ X_i) - \min(X_1\ X_2, \ldots\ldots\ X_i)} \quad (1)$$

$$X_i' = \frac{\max(X_1\ X_2, \ldots\ldots\ X_i) - X_i}{\max(X_1\ X_2, \ldots\ldots\ X_i) - \min(X_1\ X_2, \ldots\ldots\ X_i)} \quad (2)$$

The specific steps are as follows:

① For n indicators and m individual items, the value of the ith individual item under the kth indicator is the weight of that indicator: $P_{ik} = \frac{x_{ik}'}{\sum_{i=1}^{m} x_{ik}'}, (i = 1,2 \ldots, m;\ k = 1,2, \ldots n)$

② Entropy value of the four evaluation indicators.

The entropy values of four evaluation indexes, such as market liquidity ∂_i, storage resistance β_i, production cycle γ_i and reserve cost θ_i, are obtained by using the equation $e_k = -(lnm)^{-1} \sum_{i=1}^{m} p_{ik} \ln p_{ik}$.

The entropy weight of four evaluation indexes, such as market liquidity ∂_i, storage resistance β_i, production cycle γ_i and reserve cost θ_i, is obtained by using the equation $\omega_k = \frac{1 - e_k}{k - \sum_{k=1}^{n} e_k}$.

Substituting the standardized index data into the above equation, the entropy weights of market liquidity ∂_i, storage resistance β_i, production cycle γ_i and reserve cost θ_i are 0.21, 0.11, 0.46, and 0.21, respectively.

Considering the market liquidity ∂_i, storage resistance β_i, production cycle γ_i and reserve cost θ_i of emergency daily necessities, the single product storage index of daily necessities is calculated, as shown Eq. (3).

$$\sigma_i = k_{\partial i}\partial_i + k_{\beta i}\beta_i' + k_{\gamma i}\gamma_i' + k_{\theta i}\theta_i' + k_{\mu i}\mu_i' \quad (3)$$

Among them, $k_{\partial i}$, $k_{\beta i}$, $k_{\gamma i}$, $k_{\theta i}$, $k_{\mu i}$ respectively represent the entropy weight of liquidity, storage resistance, production cycle, and

reserve cost. Finally, the single variety reserve index of emergency materials is obtained as shown in Table 1.

It can be seen from Table 1 that the reserve index of temporary accommodation and office necessities such as tents, movable tables, and chairs, health protection articles, and bedding articles is the highest. During serious disasters, basic living facilities such as houses may be seriously damaged, and emergency materials such as emergency tents, quilts, and pillows can provide temporary accommodation and office facilities for victims and staff who carry out the rescue. Moreover, temporary accommodation materials such as emergency tents, movable tables and chairs, and bedding articles have low market liquidity, convenient purchase, good corrosion resistance, and low storage cost, and can be stored for a long time. Health protection articles also have high storage resistance. After a disaster breaks out, sanitation and disinfection are an indispensable part, so the importance of storage is the highest.

The reserve index is also high for food categorized by bottled water, ready-to-eat grain, radish, and other shelf-stable vegetables, convenience food, and other food security necessities. When typhoons, earthquakes, floods, and other natural disasters occur, there is likely a shortage of enough food and clean water, instant noodles, biscuits, bread, and other convenient foods. These food security necessities have the advantages of rapid collection, convenient transportation, resistance to damage (anti-fall, and anti-corrosion), and the reserve value is high, so the reserve is of high importance.

In the third place are sanitary necessities such as cleaning and disinfection products and daily necessities, mainly including sterilized alcohol, simple toilets, toilet paper, toothbrushes, laundry detergent, wet paper towels, towels, etc. These are the basic daily necessities for people's daily lives for survival and maintaining personal hygiene and health, and protect them from diseases. In addition, sanitary necessities generally have a long shelf life, are relatively storable, and are relatively inexpensive to store, thus having a high storage necessity.

The fourth and fifth places in the reserve index are medical and pharmaceutical necessities such as first-aid medical kits and clothing protection necessities such as uniforms and warm clothes. Medical and pharmaceutical necessities play the role of timely prevention, control, and treatment of unexpected diseases or injuries, and prevent life damage caused by failure to seek medical treatment in time due to special emergencies. Appropriate storage can alleviate the drug demand of special people and special events, and clothing plays an important role as the defense line of the outer skin.

The lowest storage index is aquatic products, edible fungi, fruits, green leafy vegetables, and other non-staple foods. These have high

TABLE 1 Emergency daily necessities single product reserve index.

Category	Subdivision category	Reserve index	Reserve index ranking	Average index
Clothing security category	Daily wear	0.30	13	0.290
	Warm clothing	0.28	14	
Food security category	Processed food	0.40	6	0.274
	Instant food	0.35	10	
	Bottled drinking water	0.40	5	
	Edible oil	0.24	19	
	Salt	0.34	11	
	Leafy greens and other storage-intolerant vegetables	0.18	22	
	Storage-resistant vegetables such as turnips and potatoes	0.39	7	
	Mushrooms	0.18	21	
	Fruits	0.11	23	
	Livestock meat	0.24	18	
	Aquatic products	0.23	20	
	Eggs	0.24	17	
	Liquid milk	0.26	16	
	Milk powder	0.30	12	
Temporary accommodation category	12 m^2 single tent	1.00	1	0.584
	Bedding (bedding, pillows, moisture-proof mats, etc.)	0.83	4	
	Mobile tables and chairs	0.89	3	
Hygiene products	Cleaning and disinfecting products	0.38	8	0.467
	Daily life supplies	0.38	8	
	Hygiene and security supplies	0.97	2	
Medical drugs	First aid medical kits	0.268	15	0.268

TABLE 2 Emergency necessities reserve level.

Category	Subdivision category	Suggested level
Clothing security category	Daily wear	Consider reserves
	Warm clothing	Consider reserves
Food security category	Processed food	Should be reserved
	Instant food	Should be reserved
	Bottled drinking water	Should be reserved
	Edible oil	Consider reserves
	Salt	Consider reserves
	Leafy greens and other storage-intolerant vegetables	Not suitable for storage
	Storage-resistant vegetables such as turnips and potatoes	Should be reserved
	Mushrooms	Not suitable for storage
	Fruits	Not suitable for storage
	Livestock meat	Consider reserves
	Aquatic products	Not suitable for storage
	Eggs	Consider reserves
	Liquid milk	Consider reserves
	Milk powder	Consider reserves
Temporary accommodation category	12 m^2 single tent	Must be reserved
	Bedding	Must be reserved
	Folding bed	Must be reserved
	Pillows	Must be reserved
	Mobile table and chairs	Must be reserved
Hygiene products	Cleaning and disinfecting products	Should be reserved
	Daily life supplies	Should be reserved
	Hygiene and security supplies	Must be reserved
Medical drugs	First aid medical kits	Consider reserves

nutritional value, but their short shelf life and high storage requirements (special storage conditions, high storage cost, and high storage risk) make them less suitable for large-scale reserves.

According to the principle of 3s mathematical statistics, the standard deviation of 1–2 times the average value of different varieties' reserve index is selected. In this study, the reserve grades of different types of daily necessities are classified as managed, which are: must reserve, should reserve, consider reserve, and not suitable for reserve. The specific classification is shown in Table 2.

3.2 Analysis of influencing factors of daily necessities reserve

Daily necessities are closely related to people's daily life. The effective management of daily necessities reserves requires optimizing the role of policy guidance and market mechanism, while also strengthening resource integration to avoid redundant reserves and realizing resource sharing. This approach can better enhance the emergency response capability of daily necessities. To better meet the emergency needs, this paper focuses on the principle of "prevention first, combining peacetime with disasters; government-led and social participation; under the basic principle of hierarchical management and integration of resources (33)." From the perspective of ensuring the most basic living needs of urban residents, the main indicators that affect the reserve quantity of daily necessities include:

Size of regional resident population. The larger the regional population base is, the more people will be affected during crisis and the greater the consumption of daily necessities will be. Under emergency and crisis, local governments usually make detailed material reserve plans according to the size of the resident population, medical resources, and production capacity. Therefore, the size of the regional resident population is an important basis for the reference of daily necessities reserves.

The proportion of urban residents in the region. In areas with a high proportion of rural residents, the self-sufficiency rate of agricultural and sideline products and other necessities is relatively high. Cities with a higher proportion of urban residents have greater dependence on external supplies due to factors like logistics limitations during emergencies. When emergencies occur, there may be situations such as logistics blocking, isolation control, road closure, etc., which hinder the logistics supply, procurement, and retail of daily necessities. Therefore, such areas need to reserve more materials to deal with emergencies, so urban residents' daily necessities are highly dependent on foreign countries.

Probability of disaster occurrence. Emergencies lead to uncertainty and interruption risk in the supply chain environment. In the emergency supply chain, mitigating such risks depends on the efficient distribution of emergency materials (34). Often, the greater the probability of regional disasters, the higher the demand for emergency materials (35), the greater the probability of mobilizing daily necessities reserves, the stronger the necessity of daily necessities reserves, and the more effective the storage of stored materials can be.

Population density. To a certain extent, population density is closely related to the urgency of demand (36). The greater the population density, the higher the urgency of the demand for necessities in an emergency, and the more reserve materials are allocated to this area.

Public budget. A larger public budgets signifies greater economic strength that can be allocated towards reserves. This reflects the government's willingness to support public undertakings.

Regional income level. Varying income levels across regions translate to different consumption structures. In the process of storing daily necessities, it is necessary to accurately match the diversified needs of consumers. In addition to meeting the minimum use value demand, the products and services provided should also consider the diversified and differentiated needs of the people and provide differentiated living materials protection.

4 Results

Taking into account the above influencing factors, combined with the results of the single-variety reserve index for necessities, the key variables are then sequentially identified to measure the number of reserves of necessities. First, determine the per capita demand for

10.3389/fpubh.2024.1402998

TABLE 3 Collation of per capita demand for necessities.

Category	Subdivision category	Per capita demand
Clothing security category	Daily wear	1 set/person
	Warm clothing	1 set/person
Food security category	Processed food	1 kg/person/day
	Instant food	500 g/person/day
	Bottled drinking water	300 g/person/day
	Edible oil	25 g/person/day
	Salt	10 g/person/day
	Leafy greens and other storage-intolerant vegetables	200 g/person/day
	Storage-resistant vegetables such as turnips and potatoes	200 g/person/day
	Mushrooms	200 g/person/day
	Fruits	160 g/person/day
	Livestock meat	45 g/person/day
	Aquatic products	49 g/person/day
	Eggs	43 g/person/day
	Liquid milk	300 g/person/day
	Milk powder	300 g/person/day
Temporary accommodation category	12 m^2 single tent	0.25 tops/person
	Mobile table and chairs	0.25 sets/person
	Folding bed	1 piece/person
	Futon	1 bed/person
	Pillow	1Pc/person
	Moisture-proof mat	1Pc/person
Hygiene products	Cleaning and disinfecting products	1 set/person
	Daily life supplies	1 set/person
	Hygiene and security supplies	0.1 set/person
Medical drugs	First aid medical kits	1 set/person

various types of necessities by the "14th Five-Year Plan" for emergency material security. The food and nutrition development goals in the "China Food and Nutrition Development Program" issued by the State Council determine the per capita intake of food and nutrition. The per capita demand for clothing protection category, temporary accommodation category, hygiene supplies category, and medical drugs category materials refer to policy documents such as Classification and Coding of Emergency Supplies, Classification Catalog of Key Emergency Supplies for Emergency Protection, Suggested List of Emergency Supplies Reserve for Families in Shanghai, and Guidelines on the Standard of Reserve of Disaster Relief Supplies. The final organization is shown in Table 3.

Second, the number of people affected by the disaster is determined. This study determines the affected population according to the minimum value of the number of people in need of emergency relocation or emergency living assistance under the emergency response of the Shanghai Disaster Relief Emergency Plan, and the minimum number of people in need of emergency living assistance under the level I emergency response is 500,000, followed by 300,000 for level II, 100,000 for level III, and 30,000 for level IV. Based on these figures, the reserve quantity of necessities of life under the emergency response at all levels is calculated. The reason for this is that the above-mentioned emergency supplies for the living category are characterized by a large number of demand categories but a small demand, are not consumables, and can be used repeatedly. Compared to dietary protection supplies, the emergency supplies for the living category have longer storage and re-placement cycle. Therefore, the specific emergency supply reserve can be calculated according to the number of people covered in the emergency response plan.

Finally, according to the intensity and coverage of different disaster situations, the dietary protection category of supplies is calculated as the amount to guarantee a 3-day and 7-day supply, respectively. Other categories of materials can be used for a long time without considering the number of days of supply, and the number of days of supply is set to 1. The result of the calculation of the total amount of emergency staples and supplementary foods in Shanghai for all levels and categories is shown in Table 4.

As can be seen from Table 4, among the necessities in the category of dietary security, packaged food and bottled water have the largest quantity of reserves. This is due to two factors: firstly, the high demand—an adult needs to consume 250 g of staple food and 1 kg of water a day as a basic need – with inelastic demand that remain consistent even during emergencies; and secondly, it is concluded from Table 2 that the reserves of these abovementioned necessities have a high priority, and the difficulty of stock-piling them is relatively low. Fresh vegetables, including green leafy vegetables, edible mushrooms, and other perishable vegetables, are not easy to reserve. Vegetable reserves primarily consist of radishes, potatoes, and other vegetables with longer storage life, which coincides with the reality of the emergency supply. The reserve quantities of livestock meat and eggs is not very different, reflecting the difficulty and the cost of maintaining the reserve, and can be considered to mix the reserve. For milk, while liquid milk is more popular than milk powder under normal circumstances, milk powder offers the same protein supply efficiency in a much small volume and a longer shelf life. Therefore, a certain amount of milk powder should be included in reserves, which is consistent with the real-world scenarios. Similarly, for other categories of materials can be used for a long period without considering the number of days of supply, the number of days of supply is set to 1. The results of expanding the reserve of materials from the category of dietary protection to the categories of clothing protection, temporary accommodation, sanitary supplies, and medical drugs under various levels of emergency response are shown in Table 5.

5 Algorithmic test and material distribution

5.1 Algorithmic test

The number of people affected by floods is a key variable in the calculation of the number of reserves of necessities, the more the number of people affected by floods, the higher the demand for

10.3389/fpubh.2024.1402998

TABLE 4 Stockpile of materials in the category of dietary protection under various levels of emergency response (unit: tons).

		Level I emergency response		Level II emergency response		Level III emergency response		Level IV emergency response	
Category	Subdivision category	For 3 Days	For 7 Days	For 3 Days	For 7 Days	For 3 Days	For 7 Days	For 3 Days	For 7 Days
Food security category	Drinking water	1,500	3,500	900	2,100	300	700	90	210
	Processed food	750	1750	450	1,050	150	350	45	105
	Instant food	450	1,050	270	630	90	210	27	63
	Edible oil	37.5	87.5	22.5	52.5	7.5	17.5	2.25	5.25
	Salt	15	35	9	21	3	7	0.9	2.1
	Storable vegetables	300	700	180	420	60	140	18	42
	Livestock meat	67.5	157.5	40.5	94.5	13.5	31.5	4.05	9.45
	Eggs	64.5	150.5	38.7	90.3	12.9	30.1	3.87	9.03
	Milk powder	450	1,050	270	630	90	210	27	63
	Liquid milk	450	1,050	270	630	90	210	27	63

TABLE 5 Stockpiles of clothing protection, temporary accommodation, hygiene supplies and medical drugs under various levels of emergency response.

		Level I emergency response	Level II emergency response	Level III emergency response	Level IV emergency response	
Category	Subdivision category	Reserve				Unit
Clothing security category	Daily wear	500,000	300,000	100,000	30,000	Set
	Warm clothing	500,000	300,000	100,000	30,000	Set
Temporary accommodation category	12 m^2 single tent	125,000	75,000	25,000	7,500	Set
	Mobile table and chairs	125,000	75,000	25,000	7,500	Set
	Folding bed	500,000	300,000	100,000	30,000	Sheet
	Futon	500,000	300,000	100,000	30,000	Piece
	Pillow	500,000	300,000	100,000	30,000	Piece
	Moisture-proof mat	500,000	300,000	100,000	30,000	Piece
Hygiene products	Cleaning and disinfecting products	500,000	300,000	100,000	30,000	Set
	Daily life supplies	500,000	300,000	100,000	30,000	Set
	Hygiene and security supplies	50,000	30,000	10,000	3,000	Set
Medical drugs	First aid medical kits	500,000	300,000	100,000	30,000	Piece

necessities. Therefore, this paper takes the affected population as the basis for the test of the amount of reserves of necessities.

The number of people affected by floods in Shanghai is estimated by the percentage of flood victims in the whole country, and the estimated number of affected people is compared with the number of relief population in the emergency response plan to check whether it can be covered by the number of relief population in the emergency response plan given in this paper, to verify the reliability of the study. According to the data from the National Bureau of Statistics, the number of people affected by natural disasters in 2021 is 107 million, of which 59.01 million people are affected by floods, and the number of people affected by floods accounts for 55.1% of the number of people affected by natural disasters in the country.

$$\text{Percentage of national flooding} = \frac{\text{national flooding}}{\text{national natural disaster}} = \frac{0.0591}{1.07} = 55.1\%\# \quad (4)$$

In 2021, the total population of Shanghai is 24.894 million. The number of people affected by natural disasters in Shanghai is 734,000 people. According to the above Eq. (4) to get the national flood

disaster proportion of the projected number of people affected by floods in Shanghai is 404,400 people.

$$\begin{aligned}&\text{The total population affected by natural}\\&\text{disasters in Shanghai} \times \text{the proportion of national flooding}\\&= 73.4 \times 55.1\% = 404,400 \text{ people}\end{aligned} \quad (5)$$

The minimum number of people who need to be rescued in the level I emergency response to natural disasters in Shanghai is 500,000 people, which can cover the projected value of 404,400 people derived from Eq. (5), so the number of reserves under the level I emergency response calculated in this paper can satisfy the emergency demand for necessities in Shanghai in different scenarios, and the results are informative.

5.2 Construction of a responsive material deployment system

5.2.1 Strengthen the monitoring of supply and demand of daily necessities

In case of emergency, continuously track and monitor the output, stock, and consumption of important emergency necessities, and monitor and collect the demand for daily necessities through multiple channels. Based on factors such as the severity, development trend, and influence range of disasters, the supply and demand of daily necessities are analyzed and predicted using expert analysis, auxiliary decision-making, consultation, and judgment, to accurately guide the preset and financing preparation of daily necessities and transportation capacity.

5.2.2 Improve cross-sectoral and cross-regional redeployment mechanisms

Refine and improve the response procedures for the deployment of daily necessities, and standardize the management of demand submission, allocation approval, instruction issuance, capacity raising, material transportation, reception, and use. At the same time, the centralized management and unified dispatch of daily necessities during emergency response can be strengthened, and daily necessities command and dispatch drills can be carried out regularly to improve the ability of material allocation and coordinated operations.

5.2.3 Improve material transportation capacity

Strengthen the emergency transport capacity reserve. Coordinate passenger transport, freight transport, heavy cargo, cold chain distribution, port shipping, and other emergency transport capacity reserves, and establish an emergency transport vehicle and driver information ledger to do dynamic management. By mobilizing state-owned transport enterprises as the "mopping force" of the urban supply chain, logistics enterprises are selected to join the transportation in the city, and the business is carried out according to the time and place, and the regional multimodal transport is refined, the shared logistics model is promoted, and the application of technologies such as drone transportation is explored to improve the distribution capacity of daily necessities (37).

5.2.4 Strengthen the coordinated support of transportation

Improve the emergency transportation linkage mechanism, including the choice of various materials transportation modes, unified vehicle dispatching plan, and do a good job in emergency transportation guarantees such as emergency transportation of daily necessities, capacity dispatching, and timely repair (38). In case of emergency, a "green passage" for the transportation of daily necessities is set up to realize rapid passage, thus ensuring the priority arrangement and scheduling of daily necessities. Strengthen the coordination with the reserves of daily necessities in adjacent areas, establish channels for material transfer, promote the sharing and linkage of daily necessities across regions, and enhance the ability of mutual assistance and support. Actively mobilize logistics enterprises, enterprises and institutions, social organizations, and volunteers to participate in the delivery, receipt, and distribution of materials, and comprehensively improve the ability of material distribution.

Shanghai's largest material storage warehouse is located in Minhang District, a food material guarantee warehouse established by the government. Shanghai Wusong International Logistics Park, located in Baoshan District, Shanghai, is an international large-scale warehouse. The two areas are located near the city center, with a large area and dense population, which is convenient to support other areas as logistics nodes while rescuing the local area. We can choose the area where the two warehouses are located as the supply point for dispatching in the city to allocate daily necessities to other regions. There is also the Pudong New Area, where the economy is developed and the transportation network is relatively perfect. The total transportation distance to other districts and counties in the community is short, the city's comprehensive support ability is strong, and the logistics cost control options are wide (39). As a densely populated city with a large number of urban areas, Shanghai has a developed traffic network, but it is easy to cause traffic jams. It is also important to take the actual situation of highways into account and plan according to local conditions.

Based on comprehensively improving the above points, taking Shanghai as an example, under the background of flood disasters, we can use the distribution method of daily necessities supply points with the optimal supply and demand distribution model as the core. This method aims at minimizing the total distance to meet the demand. It considers the constraint of Shanghai market reserve points on the guaranteed supply of daily necessities to the original demand points to optimize the distribution of market reserve points for shelter supply. At the same time, based on the real road network, the reliability of road sections is evaluated by using the "degree," "square agglomeration coefficient" and "daily traffic volume of road design" (40), and the road transit time is evaluated by considering the wading speed. With the goal of "shortest path travel time" and "highest path reliability," the optimal distribution path evaluation model between stations is constructed, to compare various algorithms to optimize the distribution path.

6 Discussion

Taking Shanghai as an example, this paper calculates the variety and quantity of urban necessities reserve. Based on the definition and connotation of urban necessities, the model of the urban necessities

reserve index is established. It considers four aspects: market liquidity, production cycle, storage durability, and reserve cost. The subjective and objective combination method of the Delphi method and the entropy weight method is used to determine the weight of evaluation indicators, which solves the problems of subjective interference and the great difference between the results of the objective weighting method and reality. This approach provides a more practical way to categorize emergency supplies: necessities of life that must be stockpiled, should be stockpiled, should be considered for stockpiling, and are not suitable for stockpiling. Furthermore, the model clarify the scientific basis for determining "what to stock" and lays the scientific basis for "how much to stockpile" based on a model for emergency stockpiling of necessities of life. The local government needs to increase the financial guarantee for emergency materials reserves, provide certain policy support and financial subsidies for emergency materials production enterprises and daily necessities production enterprises (41), and pay attention to a stable supply of daily necessities for different groups of people during emergencies. Meanwhile, after settling on "what to store" and "how much to store," we should think deeply about "how to store" and "who will store." We should also establish and improve the emergency storage and transportation mechanism, ensure smooth transportation, increase cooperation between the government and storage enterprises, entrust enterprises to produce, purchase, store, transport and dynamically track the necessary emergency necessities, ensure the use efficiency and allocation speed of materials, and provide stable and reliable inventory and transportation support for emergency work.

Based on the above analysis, this paper puts forward the following suggestions:

First, strengthen monitoring and early warning. (1) Enhance urban risk monitoring: systematically arrange and categorize the demand for emergency materials for natural disasters, accidents, disasters, social security and other emergencies according to Shanghai's urban safety risks and potential hazards, improve the reserve layout, and optimize the reserve scale and structure of emergency necessities; (2) Strengthen market monitoring and supervision: strengthen data sharing, analysis and judgment, establish a linkage mechanism for store managers in surrounding supermarkets, implement dynamic monitoring and timely track and guide scheduling, to provide decision support for timely response to emergencies.

Second, revise and optimize the catalog of daily necessities according to the guiding catalog for storage stipulated by the local government. This will help reduce the storage cost and improve the storage capacity. Implement a multi-level management system for the essential reserves, recommended reserves, the reserves that should be considered, and the reserves of daily necessities that are not suitable for storage to improve the efficiency of emergency reserves.

Third, scientifically plan emergency material reserves. Consider factors like the proportion of urban residents, the number of permanent residents, the probability of disasters, the population density, the public budget, and the per capita disposable income of the region. This will ensure a scientifically and rational plan for the reserve of emergency materials and minimize the waste of reserve materials.

Fourth, improve personnel security, financial security and technical security. First, increase financial investment and allocate a reasonable budget for emergency expenditure, and ensure that emergency funds are in place in time. Second, establish an integrated platform for local risk early warning that enables information sharing. Leverage information technology to understand changes in the consumption demand of public necessities, and establish and improve the database of daily necessities. This allows for timely adjustments to the varieties of daily necessities monitored.

The deficiency of this paper lies in the factors that affect the single variety reserve index and the main indicators that affect the quantity of daily necessities reserve, which can be further enriched and improved. The influencing factors listed in this paper come from the existing literature and research contents, and the more detailed screening of influencing factor indicators is necessary for real-world application. If it is to be applied to practical work, the index system needs to be further improved. Additionally, the research primarily focuses on Shanghai. In future practical work, we will further enrich the width of the evaluation index system by consulting the opinions of staff experts and scholars who have worked in the government extensively, and try to expand the research scope to other cities and countries to deepen the design of logistics models for the distribution of daily necessities.

Data availability statement

The original contributions presented in the study are included in the article/supplementary material, further inquiries can be directed to the corresponding author.

Author contributions

QJ: Conceptualization, Formal analysis, Funding acquisition, Methodology, Project administration, Supervision, Validation, Writing – review & editing. XJ: Conceptualization, Data curation, Formal analysis, Methodology, Project administration, Writing – original draft, Writing – review & editing. ZR: Data curation, Software, Writing – original draft.

Funding

The author(s) declare financial support was received for the research, authorship, and/or publication of this article. This research was funded by "National Social Science Foundation of China: 22BGL274," "2021 Shanghai Philosophy and Social Sciences '14th Five-Year Plan' project: 2021BGL009" and "Modern agricultural system economists of China: CARS-46".

Conflict of interest

The authors declare that the research was conducted in the absence of any commercial or financial relationships that could be construed as a potential conflict of interest.

Publisher's note

References

1. Wei SJ. Building a defense line for normalized emergency preparedness: the list of family emergency supplies attracts attention. *Emerg Manag*. (2021) 11:74–5.

2. Xia JA, Zhai GF. Study on emergency supplies support of Urban Community commercial facilities from the combination of Normal conditions and calamity: experiences of Japan and the United States. *Urban Plan Int*. (2023) 4:21–9. doi: 10.19830/j.upi.2023.282

3. Wang XD. Improving the reserve system for important goods by ensuring both development and security: an analysis from the perspective of agricultural products. *Chin Rural Econ*. (2022) 5:2–19.

4. Gu X, Guo XM, Xiang C, Yuan LH, Hu WS. Design of emergency material management platform for public health emergencies. *Chinese Med Equip J*. (2022) 43:34–9. doi: 10.19745/j.1003-8868.2022226

5. Yang J, Xia Y, Zhao XJ, Yang L. To ensure the supply of major agricultural products in mega cities. *Macroecon Manag*. (2024) 3:75–81. doi: 10.19709/j.cnki.11-3199/f.2024.03.012

6. Luo BJ, Huang J, Yong X, Liu J, Ban C, Chen SD. The construction practice of the emergency supplies support system of COVID-19 of hospital based on information support. *China Digit Med*. (2020) 15:62–4.

7. Zhang H, Tang MJ, Xu SS, Pang Y. The supply of necessities market risk management system. *Logistics Sci-Tech*. (2017) 40:105–9. doi: 10.13714/j.cnki.1002-3100.2017.03.031

8. Shi QY. Study on the supply risk of necessities market. *J Liaoning Teach Coll*. (2020) 2:3–5.

9. Zhao L, Li N, Peng T. Research and application of channel monitoring technology in life necessities emergency reserve. *J Saf Sci Technol*. (2013) 9:150–5.

10. Song HY. Establish a scientific emergency material reserve system. *Labour Protection*. (2020) 4:16–8.

11. Wen WJ, Liu L. Construction of emergency logistics system for daily necessities in Beijing. *Logist Technol*. (2014) 33:157–8.

12. Li H, Zhou Z, Ning Y, Wang Z, Huang H, Tao K. Optimization of emergency allocation of necessities of life based on fractal perspective. *Front Public Health*. (2023) 11:1245415. doi: 10.3389/fpubh.2023.1245415

13. Yang JJ, Zeng ZX. Review and Prospect of situation awareness research on emergency under the background of big data intelligence. *Modern Info Technol*. (2023) 7:21–6. doi: 10.19850/j.cnki.2096-4706.2023.17.004

14. Han NC, Lai Y, Li FJ. Standardization construction of community commerce in China under the digital economy environment: practice, problems and countermeasures. *J Comm Econ*. (2022) 188:245–60. doi: 10.1111/geoj.12436

15. Eldin F, Eileen S, Simon P. Are we all agreed? Consensual methods and the 'necessities of life' in the UK today. *J Soc Policy*. (2015) 44:591–610. doi: 10.1017/S0047279415000033

16. Mäkinen L. Consensus or dissensus? Analysing people's perceptions of the necessities of life in Finland. *J Poverty Soc Justice*. (2018) 26:359–77. doi: 10.1332/175982718X15299593876369

17. Ren HG, Xuan WY. Risk assessment system and empirical research on county territorial spatial planning based on public health emergencies: taking the Main urban area of she county in Handan City as an example. *J Hum Settl West China*. (2023) 38:144–50. doi: 10.13791/j.cnki.hsfwest.20230420

18. Pu MZ, Wu L, Zheng FT. Practice and reflection on China's important agricultural Products' emergency supply system in the COVID-19 pandemic. *J China Agric Univ*. (2020) 5:17–31. doi: 10.13240/j.cnki.caujsse.2020.05.003

19. Chen S. Research on the development path of smart emergency in mega-cities: based on the observation of Shenzhen's practice. *China Emerg Manag*. (2023) 11:74–7.

20. Shi J, Deng H, Wang QS. Organizational adaptation and emergency plan adaptation under "situational gap": an investigation based on urban waterlogging disaster response. *Chinese Public Adm*. (2024) 40:132–43. doi: 10.19735/j.issn.1006-0863.2024.02.13

21. Li TJ, Liu DH. Research of territorial inner principal on material dynamic allocation for sudden public health events based on differential games. *Chinese J Manag Sci*. (2024) 1:1–16. doi: 10.16381/j.cnki.issn1003-207x.2023.1755

22. Lee YH, Kim YC, Seo H. Selecting disaster waste transportation routes to reduce overlapping of transportation routes after floods. *Sustain For*. (2022) 14:2866. doi: 10.3390/su14052866

23. Chai YW, Li CJ. Urban life circle planning: from research to practice. *City Plan Rev*. (2019) 9:5–16.

24. Wu H, Wang L, Zhang Z, Gao J. Analysis and optimization of 15-minute community life circle based on supply and demand matching: a case study of Shanghai. *PLoS One*. (2021) 16:e0256904. doi: 10.1371/journal.pone.0256904

25. Yang XF. The planning and implementation of 15-minute community life circle in communities: a case study of the pilot practice of Xinhua road in Changning District. *Shanghai Urban Plan Rev*. (2020) 3:63–8.

26. Zhao YL. Determination of emergency life necessities in response to outbreak public events: in the case of Pingshan New District of Shenzhen. *Logistics Technol*. (2017) 9:52–4.

27. Yi W, Özdamar L. A dynamic logistics coordination model for evacuation and support in disaster response activities. *Eur J Oper Res*. (2007) 179:1177–93. doi: 10.1016/j.ejor.2005.03.077

28. Wang XF, Jiao YY, Zhang B, Diao SF. Study on the construction of emergency supplies security system on account of supply-storage-usage taking a district in Shenzhen as an example. *City Dis Reduction*. (2023) 6:23–8.

29. Xu YQ, Song JE, Wu QQ. Analysis on management strategy of emergency material Reserve in Electric Power Enterprises. *Money China*. (2021) 14:57–8. doi: 10.19887/j.cnki.cn11-4098/f.2021.14.029

30. Xing H. The optimization model of earthquake emergency supplies collecting with the limited period and double-level multihub. *Math Probl Eng*. (2016) 2016:1–12. doi: 10.1155/2016/4751528

31. Xie RH, Zhang Y. Study on emergency fresh food reserve quantity under major public health emergencies—take Hubei Province as an example. *Logist Res*. (2021) 1:41–7.

32. Yang M, Liu DH, Li DL. Differential game model of material object-production capacity emergency material reserve and purchase pricing of government and enterprises. *Manag Rev*. (2023) 9:274–86. doi: 10.14120/j.cnki.cn11-5057/f.2023.09.016

33. Zhou ZL, Zhao YX, Shen C, Wang ZC. Construction of the whole process prevention and control system of urban major public health risks. *J Xi'an Jiaotong Univ*. (2023) 2023:1–20.

34. Ren X, Tan J. Location allocation collaborative optimization of emergency temporary distribution center under uncertainties. *Math Probl Eng*. (2022) 2022:1–9. doi: 10.1155/2022/6176756

35. Jiang X, Qing ZC, Xin SF. Research on multi-level reserve decision of emergency materials for government and enterprises based on entrusted storage mode. *Syst Eng*. (2024) 1:1–18.

36. Wang FR, Wang XY, He X, Zhou XX. Emergency material Locationand scheduling problem considering demand urgency and comprehensive satisfaction. *Syst Eng*. (2024) 1:37–50.

37. Ma YY. Research on emergency supply chain based on Shanghai epidemic situation. *China Logist Purchas*. (2024) 1:98–9. doi: 10.16079/j.cnki.issn1671-6663.2024.01.021

38. Zhang X. Research on emergency logistics transportation mechanism under abnormal governance. *China Storage Transp*. (2023) 8:164–5. doi: 10.16301/j.cnki.cn12-1204/f.2023.08.105

39. Lv XH, Zhang ZA, Lv CZ, Wang YX. Site selection of secondary distribution Center in Regional Emergency Logistics. *Railway Transp Econ*. (2023) 8:55–61. doi: 10.16668/j.cnki.issn.1003-1421

40. Li YQ, Yu J, Zhou Y, Wu HX, Zhou M, Wen JH. Optimization of the supply and demand allocation and distribution path of food supplies under flood scenarios: a case study in Fengxian District, Shanghai. *Sci Geogr Sin*. (2024) 4:573–85. doi: 10.13249/j.cnki.sgs.20230850

41. Xiong W, Deng XY, Li Q, Hu HT, Zhu XQ. Research on the standardization of emergency materials support in public health emergencies. *China Standard*. (2023) 5:106–10.

frontiers | Frontiers in Earth Science

TYPE Original Research
PUBLISHED 01 August 2024
DOI 10.3389/feart.2024.1419421

OPEN ACCESS

EDITED BY
Lingling Shen,
Beijing Meteorological Information Center, China

REVIEWED BY
Samuele Segoni,
University of Florence, Italy
Chong Xu,
National Institute of Natural Hazards, Ministry of Emergency Management, China
Yaser Ahangari Nanehkaran,
Çankaya University, Türkiye

*CORRESPONDENCE
Yanhui Liu,
lyanhui@mail.cgs.gov.cn
Pinggen Zhou,
bjzhoupg@126.com

RECEIVED 18 April 2024
ACCEPTED 20 June 2024
PUBLISHED 01 August 2024

CITATION
Liu Y, Ma S, Dong L, Xiao R, Huang J and Zhou P (2024), A comparative study of regional rainfall-induced landslide early warning models based on RF、CNN and MLP algorithms.
Front. Earth Sci. 12:1419421.
doi: 10.3389/feart.2024.1419421

A comparative study of regional rainfall-induced landslide early warning models based on RF、CNN and MLP algorithms

Yanhui Liu[1]*, Shiwei Ma[2], Lihao Dong[3], Ruihua Xiao[1], Junbao Huang[4] and Pinggen Zhou[1]*

[1]China Institute of Geo-Environment Monitoring (Technical Guidance Center for Geo-Hazards Prevention of MNR), Beijing, China, [2]Institute of Geology and Geophysics, Chinese Academy of Sciences, Beijing, China, [3]Power China Beijing Engineering Corporation Limited, Beijing, China, [4]Fujian Monitoring Center of Geological Environment, Fuzhou, China

Landslide disasters, due to their widespread distribution and clustered occurrences, pose a significant threat to human society. Rainfall is considered a primary triggering factor, and the frequent clustering of landslides underscores the importance of early warning systems for regional landslide disasters in preventing and mitigating rainfall-induced landslides. Research on early warning models is crucial for accurately predicting rainfall-induced landslides. However, traditional models face challenges such as the complexity of landslide causes, insufficient data, and limited analysis methods, resulting in low accuracy and inadequate precision. This study focuses on Fujian Province, China, proposing a four-step process for building a regional landslide early warning model based on machine learning. The process includes data integration and cleaning, sample set construction, model training and validation, and practical application. By integrating and cleaning the latest and most detailed data, a training sample set (15,589 samples) for the regional landslide disaster early warning model is established. Three machine learning algorithms—Random Forest, Multilayer Perceptron, and Convolutional Neural Network—are employed and compared, the evaluation results indicated that the RF-based warning model achieved an accuracy of 0.930–0.957 and an AUC value of 0.955. The CNN-based warning model demonstrated an accuracy of 0.945–0.948 with an AUC value of 0.940. The MLP-based warning model achieved an accuracy of 0.930–0.953 and an AUC value of 0.930. The results showed comparable accuracy metrics among the three models, with RF exhibiting a significant advantage in AUC values. Finally, the models are applied to the regional landslide disasters induced by heavy rainfall in Fujian Province on 5 August 2021. The results showed that in the binary classification warning strategy, the accuracy of the Random Forest and Convolutional Neural Network was 92.9%, while that of the Multilayer Perceptron was 85.8%, all performing well. In the multi-classification hierarchical warning strategy, the Random Forest excelled, while the performance of the Convolutional Neural Network and Multilayer Perceptron was relatively limited. The findings of this study

contribute to valuable attempts in landslide disaster warning model research, with anticipated further improvements through the gradual accumulation of samples and practical application verification.

KEYWORDS

landslide disaster, machine learning, early warning model, Random Forest, Convolutional Neural Network, Multilayer Perceptron

1 Introduction

Landslide disasters often result in the destruction of houses, disruption of transportation routes, and pose a serious threat to the safety of people's lives and property (Froude and Petly, 2018; Gatto et al., 2023). Given the predominant triggering effect of rainfall and the frequent clustering of landslides in specific regions, early warning systems for regional rainfall-induced landslide disasters have become a critical tool in landslide disaster prevention, often referred to as the primary defense against such disasters. Research on landslide disaster early warning models is essential for accurate predictions. Based on this, numerous scholars both domestically and internationally have conducted extensive research on this matter. For example, Caine studied the rainfall intensity-duration control of shallow landslides and debris flows (Caine, 1980).

The earliest applied model is the statistical critical rainfall threshold model (Cannon, 1985; Au, 1998; Aleotti, 2004; Krøgli et al., 2018; Baum and Godt, 2010; Abraham et al., 2020). Due to its simplicity, this model has been widely referenced and applied in various regions (Liu et al., 2015; Hong et al., 2016a; Ding et al., 2017; Peruccacci et al., 2017; Wei et al., 2018). Other models, such as dynamic warning models, analyze the mechanism of rainfall-infiltration-disaster occurrence, primarily based on the mechanics of infinite slope stability analysis. These models couple rainfall-infiltration hydrogeological models with infinite slope stability mechanics to assess landslide stability (Ponziani et al., 2013; Pennington et al., 2015; Mulyana et al., 2019). Despite their clear physical significance, their complex parameter inputs and uncertainties limit their use to small-scale studies.

In recent years, the vigorous development of artificial intelligence technology has led to the maturation and widespread application of machine learning algorithms across various industries, including geological disaster prevention and control. Machine learning algorithms such as artificial neural networks, decision trees, support vector machines, and Random Forests have been extensively used for landslide spatial evaluation and prediction (Chen et al., 2017; Tien Bui et al., 2016, 2017; Liu et al., 2010; Hong et al., 2016a; Trigila et al., 2015; Dong et al., 2024; Zeng et al., 2024; Luti et al., 2020). For instance, Reichenbach et al. (2018) provided a comprehensive review of statistically-based landslide susceptibility models, while Ado et al. (2022) and Lima et al. (2022) offered extensive literature surveys and bibliometric analyses on machine learning applications in landslide susceptibility mapping. Yilmaz (2009) used frequency ratio, logistic regression, and artificial neural networks to generate landslide susceptibility maps in Tokat County, Turkey, with the artificial neural network model demonstrating superior performance. Micheletti et al. (2014) applied adaptive support vector machines, Random Forests, and AdaBoost for landslide susceptibility mapping in the Canton of Vaud, Switzerland. Thai Pham et al. (2019) used ensemble learning algorithms to assess susceptibility in Pithoragarh, India.

Furthermore, studies have integrated various machine learning techniques with physical models for enhanced accuracy. For instance, Jie Dou et al. (2015) combined the Certainty Factor method with ANN technology for Sado Island, Japan. In Austria, J.N. Goetz et al. (2015) found that Random Forest algorithms yielded the highest accuracy for landslide susceptibility mapping. Miloš Marjanović et al. (2009) and Sameen et al. (2020) used support vector machines, k-nearest neighbors, and Convolutional Neural Networks for regional assessments. Wei et al. (2021) developed a hybrid framework for regional landslide susceptibility mapping that combines physical models with Convolutional Neural Network.

Recent advancements have also focused on hybrid models that integrate machine learning with dynamic rainfall indices for improved early warning systems. Sun et al. (2022) proposed a coupled model using Random Forest susceptibility and precipitation factors, while Zhou et al. (2022) introduced an interpretable model combining SHAP and XGBoost for global and local susceptibility assessment. Yang et al. (2024) explored the CGBOOST deep-learning algorithm, and Liu et al. (2022) validated the feasibility of various machine learning algorithms for regional early warning models. Yuan and Chen (2023) proposed a national-level early warning method using hybrid neural networks and a spatiotemporal transformer.

Additionally, Khan et al. (2022) developed a global landslide forecasting system for hazard assessment and situational awareness. Nocentini et al. (2023) explored the influence of rainfall parameters and model settings on landslide space-time forecasting through machine learning. Ren et al. (2024) combined dynamic rainfall indices with machine learning methods for spatiotemporal landslide susceptibility modeling. Lee et al. (2022) integrated rainfall period, accumulated rainfall, and geospatial information for dynamic landslide susceptibility analysis.

In summary, early warning systems for rainfall-induced landslides are vital for disaster prevention. While traditional models have laid the groundwork, the integration of machine learning algorithms and hybrid models has significantly advanced the field, offering more accurate and scalable solutions for landslide prediction and risk assessment.

However, the aforementioned warning models face challenges such as the complexity of geological disaster causes, insufficient sample data, and limited analysis methods, resulting in low warning accuracy and inadequate precision. To address these issues, this paper introduces a four-step process for constructing a regional landslide early warning model based on machine learning. The steps include data integration and cleaning, construction of training sample sets, model training and validation, and practical application of the model. The study focuses on Fujian Province, one of

the provinces in the southeast of China with a high frequency of landslide disasters, providing a comprehensive demonstration of the four-step process for building landslide warning models using three algorithms: Random Forest (RF), Convolutional Neural Network (CNN), and Multilayer Perceptron (MLP). By applying these algorithms, the paper conducts a comparative study using real-world examples, highlighting the advantages and disadvantages of each model in the context of binary and multiclass landslide disaster early warning strategies. This research represents a valuable attempt to integrate AI technology and machine learning algorithms into the field of landslide disaster early warning.

2 Geological background of the study area

China is one of the countries globally with the most extensive distribution and severe consequences of geological disasters (Liu et al., 2022). Landslide geological disasters are widespread in the mountainous and hilly areas across the country, with nearly a million known occurrences. On average, these landslides cause hundreds of deaths and result in direct economic losses amounting to tens of billions of yuan each year (Geological Hazard Technical Guidance Center, Ministry of Natural Resources, 2019). Fujian Province is one of the provinces in China where landslides occur frequently.

The geographical location of Fujian Province lies mainly in the hilly mountainous area along the southeast coast of China (as shown in Figure 1). Mountainous areas in Fujian Province account for 80.06% of the total land area, plains cover 8.03%, plateaus occupy 1.99%, and hills make up 9.92%. The distribution of terrain in the study area is uneven, with hills and mountains mainly concentrated in the central and western regions of Fujian Province, totaling approximately 106,244 square meters in area. The elevation generally ranges from 5 to 2,180 m. In the western part, the prominent feature is the Wuyi Mountains, which run horizontally and are located near the border between Jiangxi Province and Fujian Province. The Huanggang Mountain, with an altitude of approximately 2,158 m, is one of the main peaks. In the central part, there are mountain ranges such as the Shengfeng Mountain-Daiyun Mountain-Boping Ridge, which run in a north-northeast direction, consistent with the direction of the coastline. In comparison to the central and western regions of Fujian Province, the southeastern coastal area has relatively lower elevations, characterized mainly by terrain features such as hills, plateaus, and plains. The stratigraphy and lithology of Fujian Province are highly developed, with predominant rock types including granite, shale, sedimentary rock, metamorphic rock, sandstone, tuff, and ignimbrite. In the southwestern part of Fujian Province, there are thin layers of relatively soft mudstone and shale, while the central and southern regions are primarily composed of granite. Sedimentary and metamorphic rocks dominate in the western parts, and tuff and ignimbrite are predominant in the eastern parts. Fujian Province experiences a subtropical monsoon climate characterized by warm and humid conditions with abundant rainfall. Summers are hot and humid, autumns are rainy, and winters are relatively dry. The province receives ample precipitation, with an annual average ranging from 1,000 to 2,500 mm, with higher rainfall in summer and autumn and lower in spring and winter. The geological environmental factor map is shown in Figure 2 (modified by Liu et al., 2022).

In recent years, geological disasters have occurred frequently in Fujian Province, with collapses, landslides, debris flows, and ground collapses being the most common types, and the majority of them are of medium and small scale. Among them, landslides are the most significant type of natural disaster. By the end of 2019, a total of 21,176 geological disasters including collapses, landslides, debris flows, and ground collapses had occurred in the province.

3 Research methods and processes

The process of constructing the regional landslide warning model based on machine learning involves four main steps: data integration and cleaning, creation of a training sample set, development and validation of machine learning models, and practical application of the model. The specific structure and workflow are depicted in Figure 3.

3.1 Data integration and cleaning

Building the training sample set for regional landslide warning mainly involves three types of datasets: geological environmental data, historical landslide records, and rainfall-triggering factors. Before constructing the sample set, it is necessary to collect, organize, and clean these three types of data. Data cleaning typically encompasses two categories:

(1) Data Missing and Anomaly Handling: Problems such as human errors, data transmission errors, equipment failures, and ambiguous geological information can impact the integrity of the original dataset. These issues need to be addressed through data preprocessing and cleaning. Typically, this involves dealing with missing values through interpolation or deletion, as well as identifying and correcting outliers.

(2) Feature Attribute Preprocessing: Given the varying scales of input features in the training samples, it is essential to standardize or scale these features uniformly. Different machine learning algorithms react differently to variations in input feature scales, necessitating distinct preprocessing methods for input feature attributes. It is significant to uniformly normalize or scale the input features of training samples before model training to minimize differences in feature ranges. Otherwise, this could directly impact the model's accuracy.

The study focused on Fujian Province, China, and collected and organized historical landslide records, geological environmental data, and rainfall data. The landslide disaster data were sourced from the Fujian Province Landslide Disaster Sample Database spanning from 2010 to 2018. Landslides are distributed across all counties and districts in Fujian, but their frequency varies significantly. In the western, northern, and central regions of Fujian, the number of landslides is higher, mainly due to the rugged terrain and complex geological conditions in these areas, leading to more developed landslides. Specifically, in Youxi County, Datian County, and Dehua County in the central region, landslide occurrences exceed 300

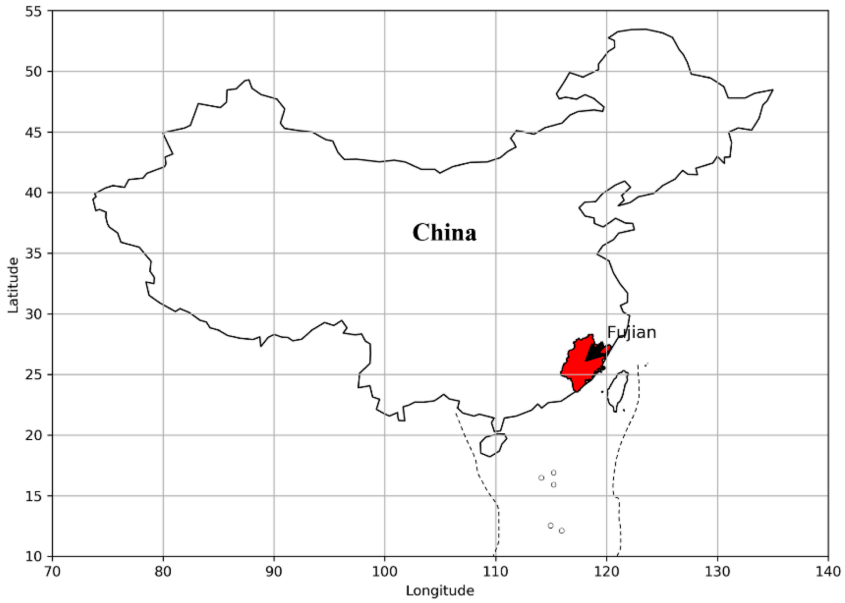

FIGURE 1
The geographical location of Fujian Province.

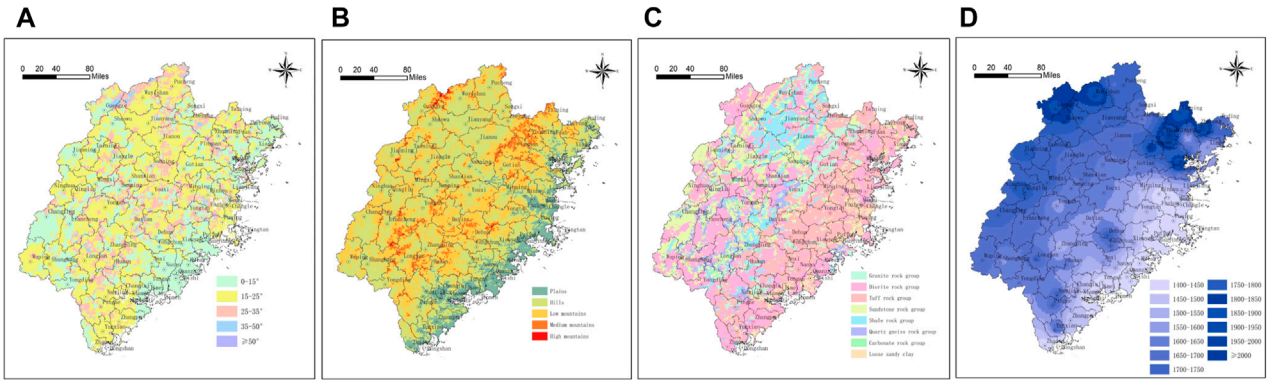

FIGURE 2
Geological environmental factor map **(A)**: grade; **(B)** geomorphic type; **(C)** formation lithology; **(D)**: annual rainfall.

times. In most other areas, the occurrences are below 150 times. However, in the southeastern coastal areas of Fujian, where the terrain is flat with predominantly plains and plateaus, landslide disasters are less likely to occur due to the flat terrain. The highest number of landslides in Fujian Province occurred in 2011, with 2,456 incidents, while the lowest number was in 2018, with only 39 incidents. The number of landslides in 2011 was 63 times that of 2018. Landslides in Fujian are mostly concentrated between May and August, accounting for 76% of the annual total. This is mainly due to Fujian's subtropical monsoon climate, where the rainy season occurs from May to August. Rainfall is a significant factor in landslide disasters as it infiltrates the soil, reducing its strength and making it prone to permeation deformation, leading to soil failure and resulting in landslides. It has been observed that landslide occurrences are primarily influenced by heavy rainfall.

Data cleaning involved standardizing temporal and spatial coordinates, handling erroneous attribute values, and addressing missing fields in the historical landslide data. Geological environmental data were obtained from the 1:20,000 and 1:50,000 geological environment and geological disaster investigation databases of Fujian Province. Besides routine error data cleaning, preprocessing steps such as projection standardization, feature scaling, and normalization were conducted. Rainfall data were sourced from hourly meteorological and hydraulic rainfall station data from 2010 to 2018. Data cleaning tasks primarily included site registration, interpolation of missing data, and elimination of erroneous data. As shown in Table 1.

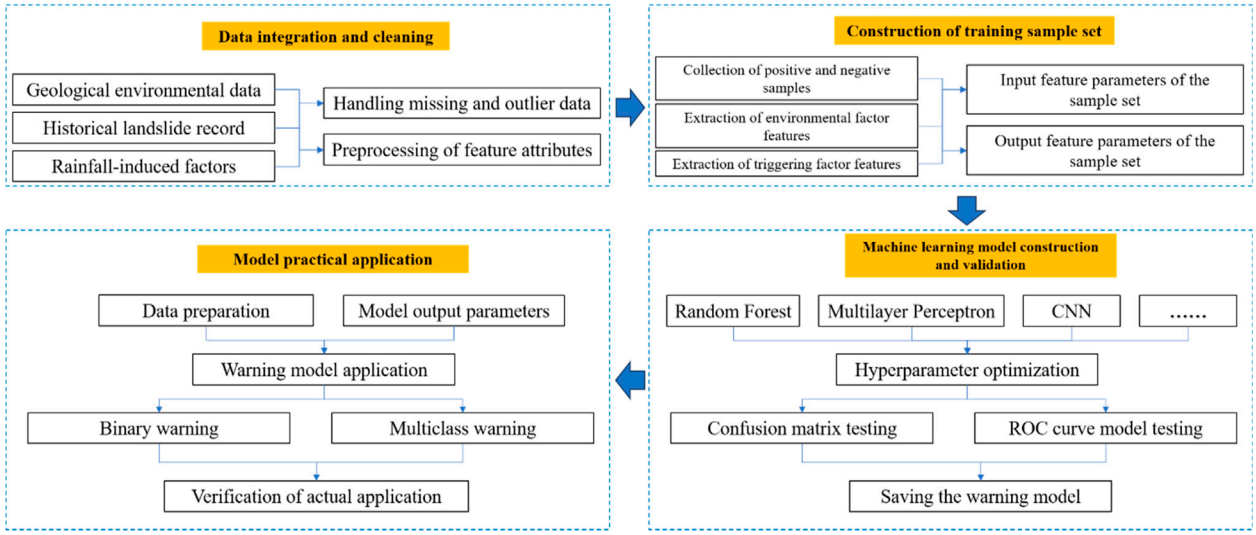

FIGURE 3
Schematic overview of the overall framework.

TABLE 1 Main issues and corresponding solutions for data Existence.

Number	Data type	Main issues	Corresponding solutions
1	Historical Landslide Recorded Data	1. Missing occurrence time; 2. Missing coordinates of occurrence location; 3. Coordinates in latitude and longitude do not match the area described in the field, indicating obvious errors; 4. Other types of disaster data	1. Remove the record; 2. If there is detailed description of the area in the attribute field, supplement by sampling; otherwise, remove the record; 3. If there is detailed description of the area in the attribute field, supplement by sampling; otherwise, remove the record; 4. Remove the record
2	Geological Environmental Data	1. Non-uniform coordinate system; 2. Missing key attributes; 3. Obvious errors in key attributes; 4. Key attributes in different factor layers are qualitatively described; 5. Large quantitative differences in key attributes between different factor layers	1. Projection transformation, uniform coordinate system; 2. Query relevant documents and materials, supplement directly if there is detailed description; otherwise, supplement manually based on relevant materials; 3. Query relevant documents and materials, supplement directly if there is detailed description; otherwise, supplement manually based on relevant materials; 4. Use uncertainty coefficient method for quantization; 5. Conduct feature scaling and normalization
3	Rainfall Data	1. Partial data missing in hourly rainfall station database; 2. Abnormally large hourly rainfall at stations; 3. Blank missing data for hourly rainfall at stations; 4. Large quantitative differences in daily rainfall data for grid units compared to key attributes in other factor layers	1. Interpolate using surrounding station data; 2. Remove outliers, interpolate using surrounding station data; 3. Interpolate using surrounding station data; 4. Conduct feature scaling for rainfall attribute (actual rainfall value/10)

3.2 Construction of training sample set

The construction of the training sample set involves extracting environmental factor features and triggering factor features based on sampling of positive and negative samples, to obtain input and output feature parameters for the model. To construct the warning model, it is necessary to divide the sample data into training and testing sets. The optimized samples are randomly mixed and shuffled

to ensure that the ratio of positive to negative samples in the training and testing sets is nearly consistent, preventing an imbalance in the number of positive and negative samples in either set. This study employs the model_selection module from sklearn using the Python language to divide all the landslide warning samples in the Fujian Province region into training and testing sets at a 4:1 ratio. To maintain consistency in the ratio of positive to negative samples within the training data, a specific percentage of each category's samples is selected as training data. Since the model requires multiple training sessions, and to avoid changes in the training data due to random shuffling of the dataset each time, we use a fixed random_state. This ensures that the division of data remains the same for each training session.

3.2.1 Sampling of positive and negative samples

Positive sample sampling is based on historical landslide record data. According to the requirements of model construction, the selection criteria are as follows: the points must have definite spatial geographic coordinates and time coordinates (accurate to each day). Negative samples refer to points where landslides did not occur, which cannot be directly obtained. Negative sample sampling includes the following steps. See Figure 4 for a schematic diagram.

(1) Negative Sample Collection Outside the Buffer Zone of Positive Samples

Determination of Negative Sample Spatial Location: Negative samples are randomly sampled outside a certain buffer zone around positive samples. The determination of the buffer zone radius should consider both the minimum warning grid unit size in the study area and the distribution of historical landslide points.

Assignment of Time Attributes to Negative Samples: The time attributes of negative samples are typically constrained within the range of time distribution of positive samples. Sampling is conducted using a random function, with the general formula:

$$T = \mathrm{RAND}\,(T_1, T_2)$$

T is the randomly obtained time; T1 is the lower limit of the period for randomly obtaining time; T2 is the upper limit of the period for randomly obtaining time.

(2) Negative Sample Collection Within the Grid of Positive Samples

Determination of Negative Sample Spatial Location: Negative samples are randomly sampled within the grid of positive samples, where the grid represents the warning grid units in the study area. The number of negative samples collected can be determined according to research requirements.

For the sampling of negative samples in this section, it is recommended to use the same number of negative samples as positive samples, meaning a 1:1 sampling ratio within grid units containing positive samples. However, this ratio should be specifically studied based on the particular research question, taking into account the varying number of samples in different study areas. Researchers are advised to collect and construct training sample sets based on different sampling ratios, and then select the optimal positive to negative sample ratio based on the model training results.

Assignment of Time Attributes to Negative Samples: For this portion, the time attributes of negative samples also use the random function shown in formula (1). However, in addition to the upper and lower limits of the period, an additional constraint is added: the time attribute of the sampled negative samples should be different from that of the positive samples.

In this study on early warning research in Fujian Province, the minimum warning grid unit is set to 2 km. In some regions, the density of historical landslide points is relatively high, so the buffer zone radius is set to the size of the warning grid unit, which is 2 km. To ensure the balance between positive and negative samples, the number of negative samples collected outside the buffer zone of positive samples is approximately twice the number of positive samples, while the number of negative samples collected within the grid of positive samples is equal to the number of positive samples. In summary, a total of 15,589 samples covering nearly 9 years

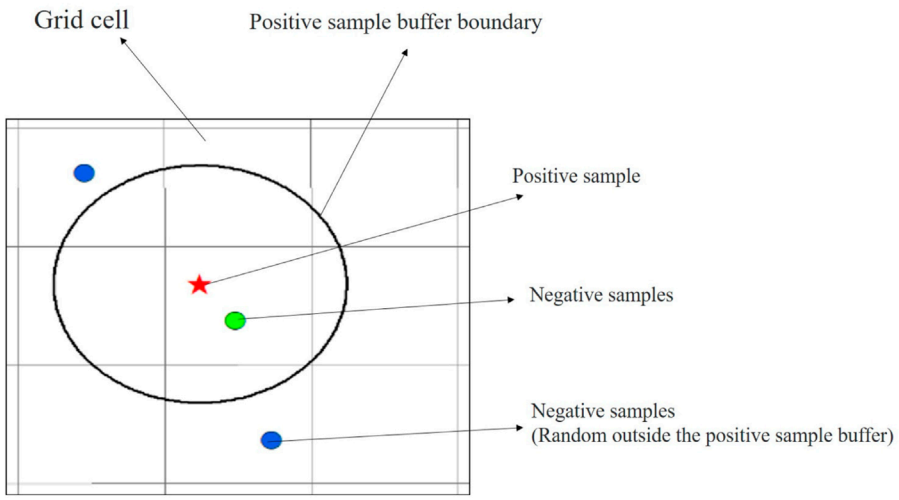

FIGURE 4
Schematic diagram of negative sample spatial sampling based on positive samples (modified by Liu et al., 2022)

(2010–2018) were obtained for Fujian Province. Among them, there are 3,562 positive samples and 12,027 negative samples, resulting in a positive-to-negative sample ratio of approximately 1:3.4. The spatial distribution of positive and negative samples is shown in Figure 5.

3.2.2 Extraction of model input and output feature parameters

The model's input feature parameters primarily encompass geological environmental factors, rainfall-triggering factors, and historical disaster information. The extraction of geological environmental features and rainfall factors is predicated on an analysis of the developmental distribution patterns and influencing factors of landslide disasters in the study area. Geological environmental factors influencing landslide disasters in the region typically comprise topography, lithology, and human activities. Rainfall-triggering factors influencing landslide disasters in the region generally encompass daily rainfall, antecedent rainfall, or antecedent effective rainfall.

Geological environmental factors and rainfall-triggering factors are overlaid and analyzed with the subdivision units of the warning grid (refer to Figure 6) to obtain the geological environmental features and rainfall factors of the warning grid units. The geological environmental feature database contains characteristic attributes of geological environmental factors for each warning grid unit, while the rainfall factor database includes daily rainfall feature attributes or effective rainfall feature attributes for each warning grid unit.

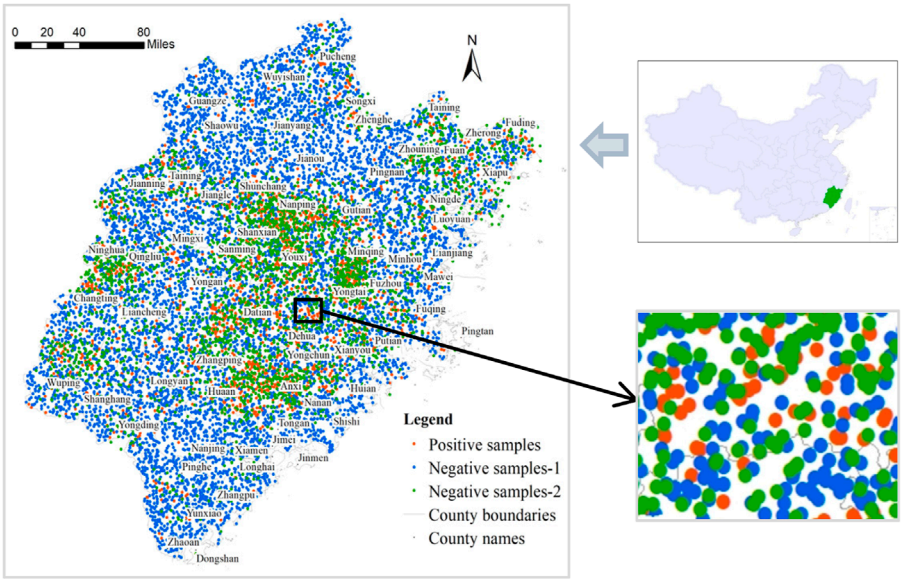

FIGURE 5
Location and training sample set of Fujian province.

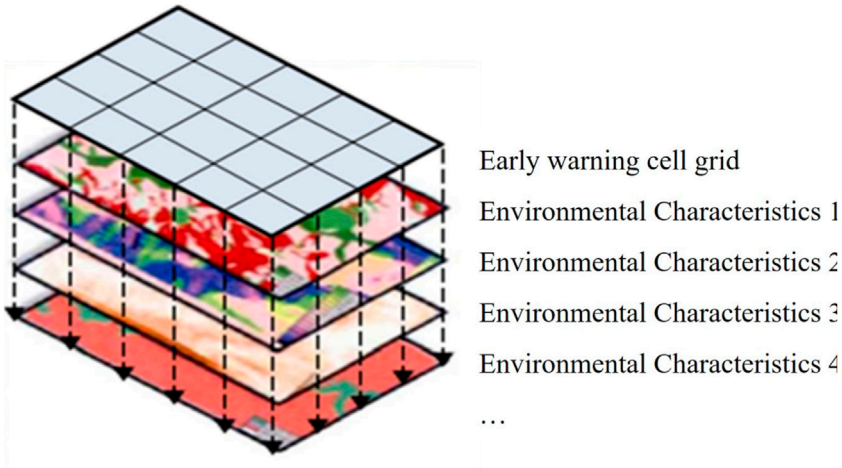

FIGURE 6
Schematic diagram of model input feature parameter extraction (modified by Liu et al., 2022)

TABLE 2 Training sample input and output features and parameters (modified by Liu et al., 2022).

Number	Input feature	Input feature parameters	Data source and processing method
1	Slope/(°)	①0–15; ②15–25; ③25–35; ④35–50; ⑤≥50	Quantification based on Fujian Province 1:100,000 slope map
2	Landform Type	①Plain; ②Hilly Plateau; ③Low Mountains; ④Low-Medium Mountains; ⑤Medium-High Mountains	Quantification based on Fujian Province 1:200,000 landform type map
3	Lithology	①Blocky Hard Granite Formation; ②Blocky Hard - Relatively Hard Diorite Formation; ③Blocky Hard - Relatively Hard Tuff, Tuff Formation; ④Medium to Thick Layer Relatively Hard Sandstone Formation; ⑤Thin Layer Relatively Soft Mudstone, Shale Formation; ⑥Medium Thick Layer Hard Quartz, Schist Formation; ⑦Medium Thick Layer Relatively Hard Carbonate Formation; ⑧Loose Sand, Clay Layer	Quantification based on Fujian Province 1:200,000 lithology map
4	Annual Rainfall/(mm)	①1,400–1,450; ②1,450–1,500; ③1,500–1,550; ④1,550–1,600; ⑤1,600–1,650; ⑥1,650–1700; ⑦1700–1750; ⑧1750–1800; ⑨1800–1850; ⑩1850–1900; ⑪1900–1950; ⑫1950–2000; ⑬>2000	Quantification based on Fujian Province 1:500,000 geological disaster investigation and zoning report, classification quantification
5	Vegetation Type	①South subtropical rainforest area in the east of Daiyun Mountain; ②Daiyun Mountain Yijiufeng Mountain Range; ③Evergreen mulberry-semi-evergreen oak forest area; ④South subtropical rainforest area in southeastern Pingling; ⑤Coastal South Subtropical Rainforest Area; ⑥Evergreen mulberry tree leaf forest area	Quantification based on Fujian Province 1:500,000 vegetation type map, classification quantification
6	Distance to Water System/(m)	①0–500; ②≥500	Extraction of water system distribution layer from Fujian Province 1:500,000 susceptibility map, classification quantification
7	Distance to Roads(m)	①0–500; ②≥500	Extraction of road distribution layer from 1:250,000 DLG data, classification quantification
8	Distance to Buildings/(m	①0–500; ②≥500	Extraction of building distribution layer from 1:250,000 DLG data, classification quantification
9	Population Density (people/km^2)	①50–100; ②100–150; ③150–300; ④300–450; ⑤450–600; ⑥600–750; ⑦>750	Quantification based on the Sixth National Population Census data, classification quantification
10	Historical Disaster Points (count)	The actual number of historical disaster points in each grid unit/10	Scaling based on landslide hazard points from Fujian Province 1:500,000 geological disaster investigation data and National Geological Disaster Database (2010–2008)
11	Daily Rainfall/(mm)	Actual rainfall value/10	Interpolation calculation based on hourly precipitation station data from 2010 to 2018 for meteorology and water resources, scaling
12	Previous Day Rainfall/(mm)	Actual rainfall value/10	
13	Previous 2 Days Rainfall/(mm	Actual rainfall value/10	

(Continued on the following page)

TABLE 2 (*Continued*) Training sample input and output features and parameters (modified by Liu et al., 2022).

Number	Input feature	Input feature parameters	Data source and processing method
		Actual rainfall value/10	
26	Rainfall in the Previous 15 Days/(mm)	Actual rainfall value/10	
27	0 or 1	Positive Sample (1); Negative Sample (0)	Positive samples taken from historical landslide record data are assigned a value of 1; negative samples obtained through sampling are assigned a value of 0

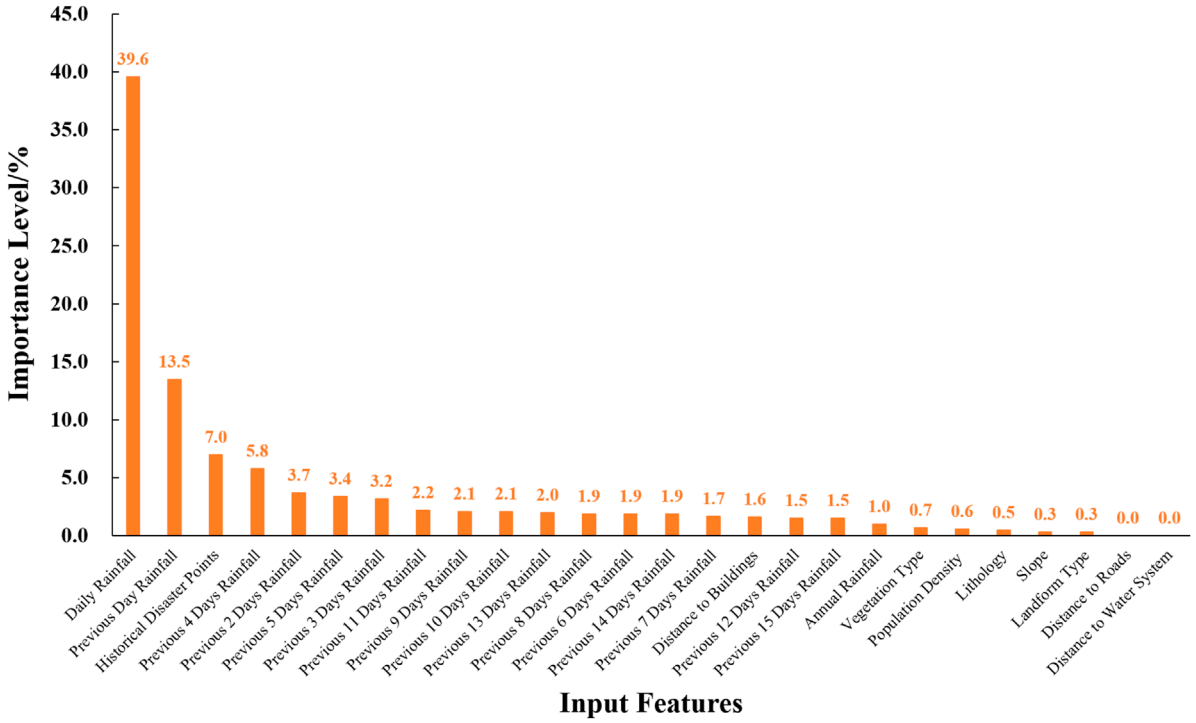

FIGURE 7
The importance of the input features.

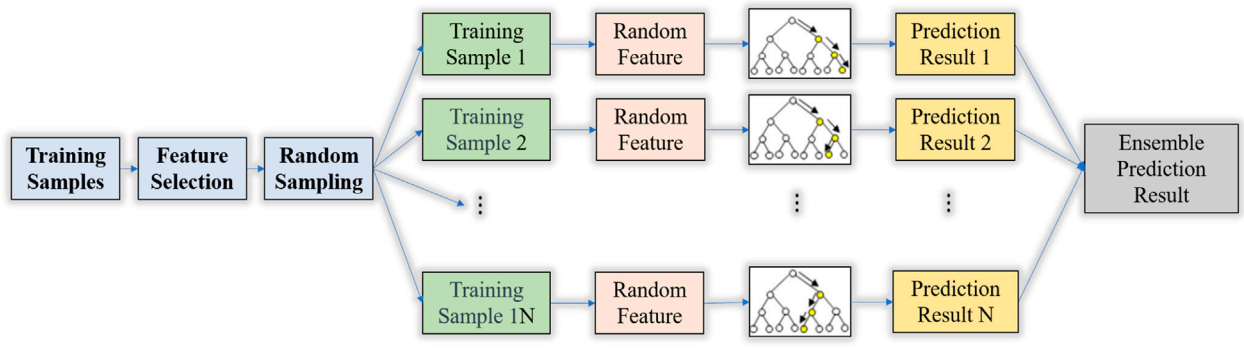

FIGURE 8
Schematic diagram of random forest model.

TABLE 3 Hyperparameters of the random forest model in the study area.

Hyperparameter	Meaning	Optimized value
max_depth	Maximum depth of decision trees	13.8178
max_features	Maximum number of features	0.1
min_samples_split	Minimum number of samples to split	3.1664
'n_estimators	Number of decision trees	165.9397

The model's output feature parameters are determined by the attributes of positive and negative samples. The output feature parameter for positive samples is set to 1, while the output feature parameter for negative samples is set to 0.

In the study area of Fujian Province, China, this paper extracted 10 feature factors including slope, landform type, lithology, annual rainfall, vegetation type, hydrological influence, roads, buildings, and actual occurrences of historical landslides (the actual number of historical disaster points in each grid unit) as input features representing geological environmental conditions. Additionally, 16 rainfall-triggering factors such as daily rainfall and rainfall over the previous 15 days were incorporated as input features for rainfall-triggering factors. This resulted in a total of 26 input feature attributes and one output feature attribute, comprising a training sample set of 15,589 records (see Figure 6; Table 2).

During the process of dividing the sample data into training and testing sets, the optimized samples were randomly mixed to ensure that the ratio of positive and negative samples in both the training and testing sets was consistent. This was done to prevent any imbalance in the number of positive and negative samples in either the training or testing set. The division of the Fujian Province landslide warning sample set into training and testing sets was accomplished using the model_selection module in sklearn, implemented in Python. The dataset was divided in a 4:1 ratio. To ensure a balanced ratio of positive and negative samples in the training data, a specific percentage was extracted from each class of samples as training data. To maintain consistency in data division across multiple training iterations and avoid variations caused by random shuffling of the dataset, a fixed random_state was employed to ensure consistent results in each training division.

The above content selected 26 indicators as input features, but different features have varying levels of importance and impact on the model. To investigate the influence of input features on the model and determine whether the selected input features are appropriate, a study on the importance of input features was conducted using the Random Forest algorithm model as an example.

The process for selecting input features is as follows:

First, calculate the importance of each input feature. The formula for calculating the importance index is as follows:

$$P_k = \frac{\sum_{i=1}^{n}\sum_{j=1}^{t} D_{Gkij}}{\sum_{k=1}^{m}\sum_{i=1}^{n}\sum_{j=1}^{t} D_{Gkij}} \times 100\%$$

Where P_k represents the importance of the k input feature; m is the number of input features; n is the number of decision trees; t is the number of nodes in each decision tree; D_{Gkij} is the decrease in Gini index for the k input feature at the j node of the i decision tree.

The importance of each input feature to the model output was calculated according to the Equation. The ranking of the importance of each input feature is shown in Figure 7.

The importance indices of the 26 input features in the study area can be ranked into six levels:

Level 1: Rainfall on the current day and the previous day, with importance indices of 39.6% and 13.5%, respectively.

Level 2: Distribution of historical disaster points, with an importance index of 7.0%.

Level 3: Rainfall from the second to the fifth day before, with importance indices ranging from 3.2% to 5.8%.

Level 4: Rainfall from the sixth to the 15th day before, distance to houses, and average annual rainfall, with importance indices ranging from 1.0% to 2.2%.

Level 5: Vegetation type, population density, strata lithology, slope, and geomorphological type, with importance indices ranging from 0.3% to 0.7%.

Level 6: Distance to roads and distance to water systems, with the lowest importance indices, both less than 0.1%.

The analysis of the importance ranking of each input feature is closely related to the study scale. At the provincial scale of this study in Fujian (with 2 km * 2 km warning grid units), the input features in Level 5 are larger-scale geological environmental factors with relatively smaller impacts. Additionally, the landslide samples collected are mainly located near residential areas, while landslides along roads were not included, directly resulting in the importance indices of distance to roads and distance to water systems being close to 0. The high importance values of features such as rainfall on the current day, distribution of historical disaster points, rainfall from the first to the fifth day before, and distance to houses align with the recognized patterns of landslide disasters and triggering factors in Fujian Province. Using the recursive elimination method, the input feature with the smallest importance indicator was removed each time, and the optimized Random Forest algorithm was used to calculate the model accuracy. The results showed that the model accuracy remained largely unchanged after removing some features. Considering that the number of input features in this study is not large, all 26 input features were retained for the subsequent model.

3.3 Model construction and validation

This paper develops warning models using three machine learning algorithms: the Random Forest model, the Convolutional Neural Network (CNN) model, and the Multilayer Perceptron

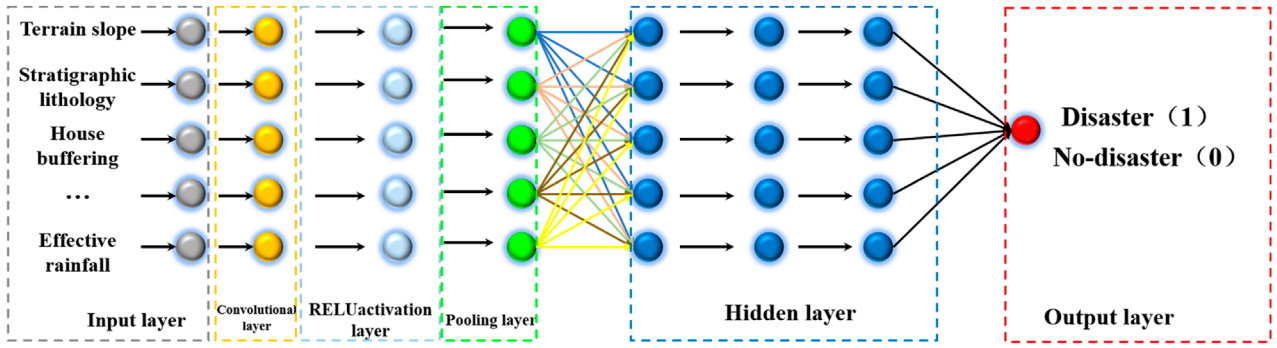

FIGURE 9
Schematic diagram of convolutional neural network (CNN) model.

(MLP) model. The Random Forest model is an ensemble learning technique that combines weak learners (decision trees) by randomly sampling data and aggregating their outputs through voting to produce the final prediction. The Convolutional Neural Network (CNN) is a type of feedforward neural network commonly used in image recognition, speech recognition, and various other applications. It comprises layers such as convolutional layers, pooling layers, fully connected layers, as well as input and output layers. The Multilayer Perceptron (MLP) model consists of multiple layers of neurons, each resembling an artificial neural network layer. Neurons within each layer receive inputs from the preceding layer, apply nonlinear transformations via activation functions, and pass the results to the subsequent layer, enabling effective solutions to nonlinear problems.

3.3.1 Random Forest model

The Random Forest algorithm employs bootstrapping, where n samples are randomly selected with replacement to form k new sample training sets. This ensures that decision trees within the Random Forest can distinguish between each other, thus increasing the diversity of the decision trees and enhancing the reliability of the analysis results, thereby improving model performance. These k-decision trees are then combined into a Random Forest through ensemble algorithms. Subsequently, each of the sample mentioned above sets is used as a training set, and decision tree models are applied to train these samples. By evaluating the output probability values, the best decision tree nodes are selected for splitting. Finally, the results generated by all decision trees are combined using a simple majority voting mechanism to obtain the final result. As shown in Figure 8.

The core of the Random Forest lies in treating any individual decision tree as a base classifier. The samples are trained through decision trees to obtain different classification models *h1(X)*..... *hk(X)*, and the final classification result is obtained through a voting mechanism. The formula for the final classification result is as follows:

$$H(X) = \arg_z^{\max} I(h_i(x) = Z$$

In this context, " $H(x)$" represents the classification output result of the Random Forest model, " h_i"stands foran individual decision tree model, "Z" represents the output variable, and " I(.)" is an indicator function. This indicates that the Random Forest adopts a majority voting decision method to determine the classification.

The study employs the training sample set from the research area (Figure 6; Table 2) to optimize four hyperparameters within the Random Forest model: max_depth, max_features, min_samples_split, and n_estimators. Utilizing the Bayesian optimization algorithm, it searches for the optimal hyperparameter values and outputs the values obtained during each iteration. By rounding these values to integers, the optimal hyperparameter values are determined as follows: {max_depth': 13, 'max_features': 0.1, 'min_samples_split': 3, 'n_estimators': 166}. The refined hyperparameters for the Random Forest algorithm are illustrated in Table 3.

3.3.2 Constructing Convolutional Neural Network (CNN) model

The Convolutional Neural Network (CNN) is a type of deep learning model comprised of components such as convolutional layers, pooling layers, and fully connected layers. The convolutional layer serves as the core of CNN, detecting various features in images, such as edges, textures, or shapes, by applying convolutional operations on input data. These operations utilize learnable filters (also known as kernels) to scan the input data and generate feature maps. Pooling layers typically follow convolutional layers to reduce the size of feature maps and retain the most important information. They achieve this by downsampling the spatial dimensions of the feature maps, either by taking the maximum value (max pooling) or the average value (average pooling) within certain regions of the feature maps. This helps reduce the number of parameters and computational complexity while preserving crucial features. Fully connected layers are usually positioned at the end of CNN and are responsible for mapping the extracted features to the final output categories or predictions. These layers flatten the extracted features from the preceding layers and input them to fully connected neurons in the neural network to perform classification or regression tasks. As shown in Figure 9.

This study utilized the training sample set from the research area (Figure 6; Table 2). The model architecture of the Convolutional Neural Network (CNN) comprises an input layer, an output layer, two convolutional layers, two max-pooling layers, a fully connected layer, and a dropout module aimed at preventing

TABLE 4 Hyperparameters of the convolutional neural network model.

Parameter	Meaning	Optimized value
filters1	Size of the first layer's convolutional kernel	512 × 1
filters2	Size of the second layer's convolutional kernel	32 × 1
dropout rate	Dropout rate for each layer's neurons	0.1
activation1	Activation function for the first layers	relu
activation2	Activation function for the second layers	relu
activation3	Activation function for fully connected layer	sigmoid
lr	The learning rate for model training	0.002

overfitting. Bayesian optimization algorithm was employed to search for partially optimal hyperparameters of the CNN model. This primarily involved determining the number of neurons in certain layers, activation functions for each layer, dropout rates for individual layer neurons, and the learning rate for model training. Specifically, the number of neurons in each layer was set to 512 x 1 for the initial convolutional layer and 32 x 1 for the second convolutional layer. The dropout rate for each layer was set to 0.1, with ReLU as the activation function for the first and second layers. The learning rate was fixed at 0.002. Other parameters were configured to the default settings of the CNN algorithm. The optimized hyperparameters of the Convolutional Neural Network are detailed in Table 4.

3.3.3 Multilayer Perceptron (MLP) model construction

Multilayer Perceptron (MLP) is a fundamental type of feedforward artificial neural network. It consists of multiple layers of neurons, including an input layer, at least one or more hidden layers, and an output layer (Hinton, 2006). In an MLP, each neuron is connected to all neurons in the previous layer, with each connection having an associated weight. Information flows from the input layer through the neurons and layers to the output layer. The presence of hidden layers allows MLP to learn and capture more complex patterns and features. MLP model are often trained using backpropagation algorithms, adjusting weights iteratively to minimize the error between predicted and actual outputs. This model applies to various machine learning tasks such as classification and regression. It is worth noting that MLP is commonly used for processing unstructured data like images, text, or time series data. While MLP is a simple and flexible model, it may suffer from overfitting or require more complex model structures to improve performance when dealing with complex problems.

TABLE 5 Hyperparameters of the multilayer perceptron model.

Parameter	Meaning	Optimized value
units1	Number of neurons in the first layer	64
units2	Number of neurons in the second layer	128
units3	Number of neurons in the third layer	128
units4	Number of neurons in the fourth layer	64
dropout rate1	Dropout rate of neurons in the first layer	0.1
dropout rate2	Dropout rate of neurons in the second layer	0.43
dropout rate3	Dropout rate of neurons in the third layer	0.35
activation1	Activation function of the first layer	relu
activation2	Activation function of the second layer	sigmoid
activation3	Activation function of the third layer	sigmoid
activation4	Activation function of the fourth layer	sigmoid
lr	Learning rate	0.0001

This paper employs the training sample set of the research area (Figure 6; Table 2) to construct a Multilayer Perceptron (MLP) model, comprising one input layer, four hidden layers, and three dropout modules to mitigate overfitting. The optimization of the deep neural network model's hyperparameters is achieved through the Bayesian optimization algorithm, considering factors such as the number of neurons in each layer, activation functions, dropout rates, and the learning rate. Specifically, the first layer has 64 neurons, the second and third layers each have 128 neurons, and the fourth layer has 54 neurons. The dropout rates for the neurons are 0.1, 0.43, and 0.35 for the first, second, and third layers, respectively. ReLU activation is used for the first layer, while sigmoid activation is applied to the subsequent layers, and the learning rate is set to 0.0001. Other parameters adhere to the default settings of the deep neural network algorithm. Table 5 presents the optimized hyperparameters for the Multilayer Perceptron model.

3.3.4 Model optimization

When constructing artificial intelligence models, model training aims to enhance accuracy. Model accuracy relies not only on the learning algorithm's performance but also on the selection of hyperparameters and features. Optimizing the model can also enhance accuracy, thus it is necessary to optimize certain parameters

of each model. Presently, hyperparameter optimization methods can employ automatic tuning techniques. Automatic hyperparameter tuning methods mainly consist of random search, grid search, and Bayesian optimization algorithms. In contrast to grid search and random search, the Bayesian algorithm utilizes Gaussian processes, making full use of prior knowledge. Moreover, Bayesian optimization can attain the optimal solution and is more robust than random search. Consequently, this paper adopts the Bayesian optimization algorithm to adjust the model's hyperparameters (Lee and Min, 2001).

Gaussian Process, also known as Gaussian distribution random process, can represent the distribution of functions. The characteristics of Gaussian distribution are determined by covariance and mean. By calculating the posterior probability of samples, the maximum posterior variance of the model output can be obtained. Generally, Gaussian processes require calculating the probability of each feature and multiplying them. However, due to the large number of feature factors, it is necessary to use a multivariate Gaussian regression model and establish the covariance matrix of features. Finally, the probability "p(χ) is calculated using all feature values.

$$p(\chi) = \prod_{j}^{n} p\left(\chi_j;\mu_j;\sigma^2\right) = \prod_{j}^{n} \frac{1}{\sqrt{2\pi}\sigma_j} \exp\left\{-\left[\frac{\left(\chi_j-\mu_j\right)^2}{2\sigma^2}\right]\right\}$$

Average of all features:

$$\mu_j = \frac{1}{m}\sum_{i=1}^{m} x^i$$

Covariance matrix:

$$\sum = \frac{1}{m}\sum_{i=1}^{m}(\chi^i-\mu)(\chi^i-\mu)^T = \frac{1}{m}(X-\mu)^T(X-\mu)$$

Multivariate Gaussian distribution probability model:

$$p(\chi) = \frac{1}{2\pi^{\frac{\pi}{2}}|\sum|^{\frac{1}{2}}} \exp\left\{-\frac{1}{2}(\chi-\mu)^T\sum^{-1}(\chi-\mu)\right\}$$

During the process of searching for optimal values and optimizing hyperparameters, this process is a Gaussian process.

3.3.5 Model validation

To assess the performance of the model, two metrics, namely, the confusion matrix and ROC curve, were selected to evaluate the effectiveness of the regional landslide warning model. These metrics are used to measure the accuracy and generalization ability of the model, respectively.

(1) Confusion Matrix

The confusion matrix is a matrix used to evaluate the performance of classification models, providing an intuitive reflection of the model's binary classification effectiveness. It categorizes the classification results into four scenarios based on the actual classes (true values) and predicted classes, namely, True Positive (TP), False Positive (FP), True Negative (TN), and False Negative (FN). The specific relationships between these four classification results are depicted in Table 6:

TABLE 6 Confusion matrix.

True values		0	1	Total
Predicted Value	0	TN	FN	TN + FN
	1	FP	TP	FP + TP
Total		TN + FP	FN + FP	TN + FP + FN + FP

As shown in Table 6, TN represents the true negative value, which is the number of samples predicted and not experiencing landslides. FN represents the false negative value, indicating the number of samples predicted as not experiencing landslides but experiencing landslides. FP represents the false positive value, indicating the number of samples predicted as experiencing landslides but not. TP represents the true positive value, which is the number of samples predicted and experiencing landslides. Additionally, other classification metrics can be derived from the confusion matrix, including accuracy, true positive rate (TPR), sensitivity (recall), specificity, and negative predictive value (NPV), aiding in assessing the model's performance. The formulas and meanings are presented in Table 7.

(2) ROC (Receiver Operating Characteristic) curve

The ROC curve is employed to comprehensively assess and evaluate the performance of the model. It is generated by plotting the true positive rate against the false positive rate at various thresholds. The value of AUC (Area Under the ROC Curve) represents the generalization ability of the landslide warning model, serving as an evaluation metric for model performance. AUC ranges from 0.5 to 1.0, with values closer to one indicating better model performance.

3.4 Model application

In practical applications, the pre-trained landslide warning models can be directly accessed using the LOAD function. These models have been previously trained, and saved, and can output the probability of landslide disasters occurring. By adhering to different warning strategies, the warning levels can be systematically determined and classified.

3.4.1 Model input and computation

Acquiring model input parameters by dividing the study area into grid cells of 2 km x 2 km. Each grid cell layer is then associated with 26 input feature parameters. These parameters include slope, terrain type, lithology, annual rainfall, vegetation type, distance to watercourses, distance to roads, distance to buildings, population density, and historical disaster points, which are derived from geological environmental input features trained by the model. The remaining 16 input feature parameters, such as rainfall for the current day, rainfall for the previous 1 day, rainfall for the previous 2 days, and so forth up to rainfall for the previous 15 days, are computed based on the specific time of the day for which the warning calculation is performed. Ultimately, this process generates input data files for each grid cell. These input data files are then fed into the three machine-learning landslide warning models for

TABLE 7 Formulas and meanings of metrics.

Metric	Formula	Meaning
Accuracy	$Accuracy = \frac{TP + TN}{TP + TN + FP + FN}$	The proportion of correctly classified samples among all samples
True Positive Rate (TPR)	$TPR = \frac{TP}{TP + FP}$	The proportion of positive samples correctly identified as positive
Sensitivity (Recall)	$Sensitivity = \frac{TP}{TP + FN}$	The proportion of actual positive samples that are correctly predicted as positive
Specificity	$Specificity = \frac{TN}{TN + FP}$	The proportion of actual negative samples that are correctly predicted as negative
Negative Predictive Value (NPV)	$TNR = \frac{TN}{TN + FN}$	The proportion of negative samples that are correctly identified as negative among all samples predicted as negative

TABLE 8 Binary warning strategy based on machine learning landslide warning models.

Probability threshold range (%)	Output warning level	Risk of geological disaster occurrence
≥50	Warning	High Risk Risky
<50	No Warning	Low Risk

TABLE 9 Multi-class warning strategy based on machine learning landslide warning model.

Probability (%)	Threshold range warning level	Output warning level
>80	Red Warning	very high risk
60–80	Orange Warning	High Risk
40–60	Yellow Warning	Moderate Risk
<40	No Warning	Low Risk

computation, yielding the output of landslide hazard probabilities within each grid cell.

3.4.2 Warning strategy

Based on the probabilities of landslides occurring in each grid cell as output by the model, the final warning level is determined according to the model's output strategy. This paper proposes two warning strategies: binary warning strategy and multiclass warning strategy.

(1) Binary Warning Strategy

The binary warning strategy categorizes the final warning level into two classes based on the probabilities of landslides occurring in each grid cell as output by the model: no warning and warning. We set the threshold for classification at 50% and use this threshold to determine the landslide warning level. When the probability of landslides in each grid cell output by the model is below the 50% threshold, the warning level is classified as "no warning," indicating a low risk of geological disaster occurrence. Conversely, when the probability of landslides in each grid cell output by the model is above the 50% threshold, the warning level is classified as "warning," still indicating a high risk of geological disaster occurrence (Table 8).

(2) Multiple Classification Warning Strategy

The multiple classification warning strategy divides the final warning level into several categories based on the landslide occurrence probability output by the model for each grid cell. This study refers to the industry standard geological disaster meteorological risk warning regulations, using thresholds of 20%, 40%, 60%, and 80% to categorize the warning levels into no warning, yellow warning, orange warning, and red warning. Specifically, when the output probability is below 40%, the warning level is "no warning," indicating a relatively low risk of geological disaster occurrence. When the output probability falls within the range of 40%–60%, the warning level is "yellow warning," suggesting a higher risk of geological disaster occurrence. For output probabilities between 60% and 80%, the warning level is "orange warning," indicating a high risk of geological disaster occurrence. If the output probability exceeds 80%, the warning level is "red warning," indicating a very high risk of geological disaster occurrence (Table 9).

4 Results and comparative analysis of three warning models

4.1 Model validation results

(1) Confusion Matrix Results

According to the confusion matrix output results of the three models (Table 10), it can be observed that when thresholds are set to 0.25, 0.5, and 0.75 respectively, the accuracy of the Random

Forest model is 0.930, 0.953, and 0.957, the accuracy of the Convolutional Neural Network (CNN) model is 0.945, 0.947, and 0.948, and the accuracy of the Multilayer Perceptron (MLP) model is 0.930, 0.937, and 0.953. According to the ROC results of the three models (Figure 10), the AUC value of the Random Forest model is 0.955, the AUC value of the CNN model is 0.940, and the AUC value of the MLP model is 0.930. The test metrics of the three models are very close, demonstrating good generalization ability and accuracy of all three models, proving their reliability. Comparatively, among the three models, the Random Forest model exhibits the highest accuracy (0.957) and the highest AUC value (0.955).

(2) ROC Results

4.2 The effectiveness of model application in early warning

As an example, let's consider 5 August 2021, and apply the model input, model computation, and early warning strategy outlined in Section 2.4. We'll generate the risk warning levels for geological disasters according to both the binary and multiclass warning strategies. The results for the binary warning strategy are shown in Figure 11, while the results for the multiclass warning strategy are shown in Figure 12.

We'll then collect and organize the actual landslide disaster occurrences in the study area on 5 August 2021 (14 newly occurred landslides). By mapping the coordinates of the actual landslide points onto the warning result maps (Figures 11, 12), we'll validate the effectiveness of the model's practical application.

From Figure 11 and Table 11, it is evident that in the results of the binary warning strategy, among all 14 newly occurred landslide points, 13 fall within the "Warning" level range of the Random Forest (RF) model (Figure 11A), achieving a prediction hit rate of 92.9%; 13 newly occurred landslide points fall within the "Warning" level range of the Convolutional Neural Network (CNN) model (Figure 11B), with a prediction hit rate of 92.9%; and 12 newly occurred landslide points fall within the "Warning" level range of the Multilayer Perceptron (MLP) model (Figure 11C), achieving a prediction hit rate of 85.7%.

From Figure 13 and Table 11, in the results of the multiclass warning strategy, the Random Forest model's warning results (Figure 12A) show that among all 14 newly occurred landslide points, 13 (92.9%) fall within the Random Forest model's warning zone, with approximately half falling into the "Yellow Warning" and "Orange Warning" zones and no newly occurred landslide points fall into the "Red Warning" zone. The CNN warning model results (Figure 12B) indicate that among all 14 newly occurred landslide points, 13 (92.9%) fall within the CNN model's warning zone, with no newly occurred landslide points falling into the "Yellow Warning" zone, and approximately 86% fall into the "Red Warning" zone. The MLP warning model results (Figure 12C) show that among all 14 newly occurred landslide points, 12 (85.8%) fall within the MLP model's warning zone, with no newly occurred landslide points falling into the "Orange Warning" zone, and 71.4% fall into the "Red Warning" zone.

Comparative analysis shows that the Random Forest warning model not only performs excellently in accuracy but also exhibits outstanding performance in multi-level hierarchical warning. The warning zones of different levels are distributed more evenly, indicating that the Random Forest model is more suitable for multi-level warnings. The CNN and MLP warning models demonstrate good accuracy, but they perform inadequately in hierarchical warning, with their output results tending toward the two extremes of 0 and 1. Consequently, the majority of the warning zones in the output results of these two models are in the "Red Warning" zone, indicating their limitations in hierarchical warning applications.

4.3 Analysis of results

In the model training and evaluation phase, we employed three machine learning algorithms: Random Forest (RF), Multi-Layer Perceptron (MLP), and Convolutional Neural Network (CNN) for learning, training, and validating the landslide disaster warning models. The dataset was divided into training and testing sets in a 4:1 ratio, and a Bayesian optimization algorithm was used to optimize the model's hyperparameters. The reliability of the models was thoroughly tested on the testing set using confusion matrices and ROC curves. Evaluation results showed that the accuracy of the warning model based on the Random Forest algorithm ranged from 0.930 to 0.957, with an AUC value of 0.955; for the Convolutional Neural Network-based warning model, the accuracy ranged from 0.945 to 0.948, with an AUC value of 0.940; and for the Multi-Layer Perceptron-based warning model, the accuracy ranged from 0.930 to 0.953, with an AUC value of 0.930. The results indicate that the accuracy of the three models' testing metrics is comparable, but the Random Forest algorithm demonstrates a clear advantage in terms of AUC value. All three models exhibit good generalization ability and precision. In terms of model application, methods for obtaining and importing input feature parameters in practical warning scenarios are proposed. Two standardized warning model output feature strategies are suggested: binary classification warning and multi-classification warning. In the binary classification warning strategy, a threshold of 50% is used for the output probability, dividing the warning results into "no warning" and "warning" categories. In the multi-classification warning strategy, thresholds of 40%, 60%, and 80% are utilized, categorizing the warning results into "no warning," "yellow warning," "orange warning," and "red warning" classes. Taking the widespread landslide disasters triggered by heavy rainfall in Fujian Province, China on 5 August 2021, as an example, the practical application of the models in real scenarios was demonstrated. Results revealed that using the binary classification warning strategy, out of the 14 landslide disasters that occurred on 5 August 2021, 13 landslides (accounting for 92.9% of the total) fell within the "warning" areas predicted by the Random Forest and Convolutional Neural Network (CNN) warning models, while 12 landslides (85.7% of the total) fell within the "warning" areas predicted by the Multi-Layer Perceptron (MLP) warning model. This demonstrates the excellent performance of the three warning models in the binary classification warning strategy. When employing the multi-classification warning strategy, within the output results of the Random Forest warning model, seven landslides (50.0% of the total) fell into the "yellow warning" zone, six landslides (42.9% of the total) fell into the "orange warning" zone, and one landslide (7.1% of the total) fell into the "no warning"

TABLE 10 Confusion matrix results of three warning models.

	Threshold			Actual value		
				Landslide	Non-landslide	
RF Model	0.25	Predicted Value	Landslide	2,581	255	Ture Positive Precision:0.910
			Non-Landslide	312	10,124	Ture Negative Precision:0.970
				Recall Rate:0.892	Specificity:0.975	Precision:0.957
	0.5	Predicted Value	Landslide	2,267	29	Ture Positive Precision:0.987
			Non-Landslide	626	10,350	Ture Negative Precision:0.943
				Recall Rate:0.784	Specificity:0.997	Precision:0.953
	0.75	Predicted Value	Landslide	1972	4	Ture Positive Precision:0.998
			Non-Landslide	921	10,375	Ture Negative Precision:0.918
				Recall Rate:0.682	Specificity:1.0	Precision:0.930
CNN Model	0.25	Predicted Value	Landslide	573	57	Ture Positive Precision:0.910
			Non-Landslide	115	2,373	Ture Negative Precision:0.954
				Recall Rate:0.833	Specificity:0.977	Precision:0.945
	0.5	Predicted Value	Landslide	565	40	Ture Positive Precision:0.934
			Non-Landslide	123	2,390	Ture Negative Precision:0.951
				Recall Rate:0.821	Specificity:0.984	Precision:0.948
	0.75	Predicted Value	Landslide	554	30	Ture Positive Precision:0.949
			Non-Landslide	134	2,400	Ture Negative Precision:0.947
				Recall Rate:0.805	Specificity:0.988	Precision:0.947
MLP Model	0.25	Predicted Value	Landslide	556	71	Ture Positive Precision:0.887
			Non-Landslide	124	2,367	Ture Negative Precision:0.950
				Recall Rate:0.818	Specificity:0.971	Precision:0.937
	0.5	Predicted Value	Landslide	547	54	Ture Positive Precision:0.987
			Non-Landslide	133	2,384	Ture Negative Precision:0.943
				Recall Rate:0.784	Specificity:0.997	Precision:0.953
	0.75	Predicted Value	Landslide	540	45	Ture Positive Precision:0.998
			Non-Landslide	140	2,393	Ture Negative Precision:0.918
				Recall Rate:0.682	Specificity:1.0	Precision:0.930

zone. In the output results of the CNN warning model, 12 landslides (85.8% of the total) fell into the "red warning" zone, one landslide (7.1% of the total) fell into the "orange warning" zone, and one landslide (7.1% of the total) fell into the "no warning" zone. In the output results of the MLP warning model, 10 landslides (71.4% of the total) fell into the "red warning" zone, two landslides (14.3% of the total) fell into the "orange warning" zone, and two landslide (14.3% of the total) fell into the "no warning" zone. Comparative analysis indicates that the Random Forest warning model not only demonstrates excellent accuracy but also performs remarkably

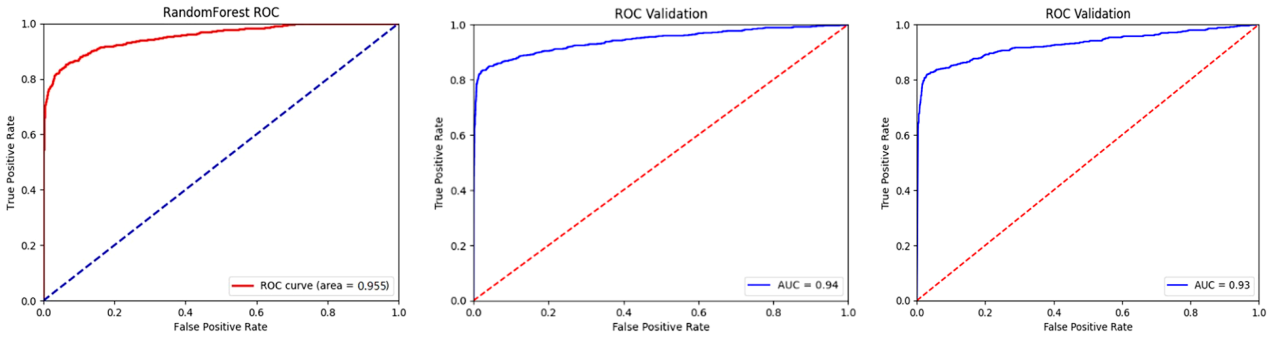

FIGURE 10
ROC Curve Results **(A)**: RF Model; **(B)** CNN Model; **(C)** MLP Model).

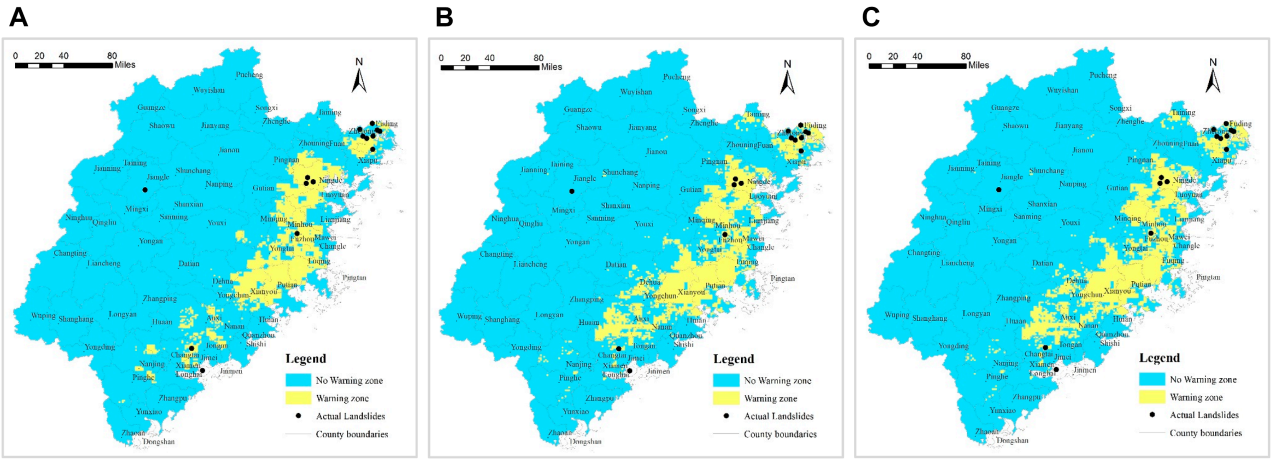

FIGURE 11
Verification Results of Binary Warning Strategy Instance **(A)**: RF Warning Model; **(B)** CNN Warning Model; **(C)** MLP Warning Model).

well in multi-classification hierarchical warning. The CNN and MLP warning models exhibit good accuracy in warning but show limitations in hierarchical warning effectiveness.

5 Discussion

This study uses three machine learning algorithms—Random Forest (RF), Multi-Layer Perceptron (MLP), and Convolutional Neural Network (CNN)—to provide a broader assessment of model performance. The use of multiple algorithms allows for a comparison of different methods, identifying their respective strengths and weaknesses. Previous research typically focused on a single algorithm, limiting the scope of comparative analysis (Hastie et al., 2009). Implementing both binary and multiclass classification strategies enhances the versatility and applicability of the warning models. By categorizing warning results into different risk levels, stakeholders can better prioritize and manage resources. This dual-strategy approach is relatively unique and adds depth to the predictive capability of the models (Breiman, 2001). The models demonstrated strong generalization ability and high accuracy during the testing phase, particularly the Random Forest algorithm, which achieved the highest AUC value. This robustness is crucial for the practical application of landslide prediction, where model reliability is key (Zhou et al., 2020). Previous research on landslide warning models often used single algorithms and simple classification strategies. For example, studies by Dou et al. (2020) and Hong et al. (2016b) mainly used logistic regression and support vector machines, focusing on binary classification. This study employs multiple algorithms and classification strategies, providing a more detailed and comprehensive analysis. It demonstrates the relative advantages of different methods in various contexts. Liu et al. (2022) conducted a study on landslide disaster early-warning models using six machine learning algorithms. Among them, the Random Forest model performed the best, with the highest generalization ability (AUC = 0.955) and no overfitting. The Artificial Neural Network model followed with an AUC of 0.935, then the Nearest Neighbor model, Logistic Regression model, and Support Vector Machine model with AUCs of 0.924, 0.922, and 0.920, respectively. The Decision Tree performed the worst, with an AUC value of 0.904 and an accuracy of 0.937. In comparison, the AUC values of the three early-warning models in this paper are 0.955 for the Random Forest

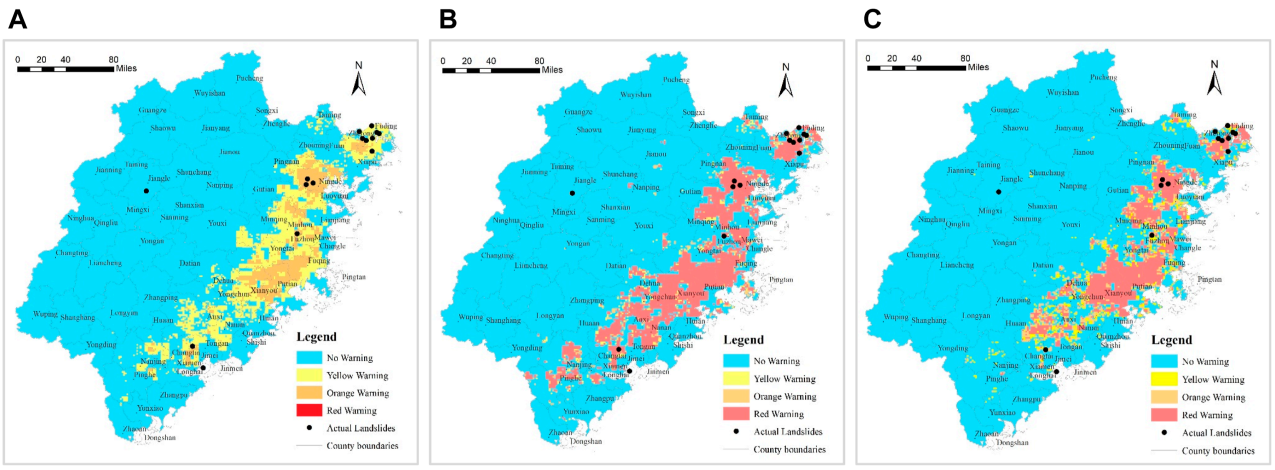

FIGURE 12
Multiclass Warning Strategy Validation Results **(A)**: RF Warning Model; **(B)** CNN Warning Model; **(C)** MLP Warning Model).

TABLE 11 Comparison of the actual application effectiveness of three models in warning.

Model Warning	Binary warning strategy results			Multi-class warning strategy results		
	Warning Level	Landslides (occurrences)	Percentage of Landslides (%)	Warning Level	Landslides (occurrences)	Percentage of Landslides (%)
RF Model	Warning	13	92.9	Red Warning	0	0
				Orange Warning	6	42.9
				Yellow Warning	7	50.0
	No Warning	1	7.1	No Warning	1	7.1
CNN Model	Warning	13	92.9	Red Warning	12	85.8
				Orange Warning	1	7.1
				Yellow Warning	0	0
	No Warning	1	7.2	No Warning	1	7.1
MLP Model	Warning	12	85.7	Red Warning	10	71.4
				Orange Warning	0	0
				Yellow Warning	2	14.3
	No Warning	2	14.3	No Warning	2	14.3

algorithm, 0.940 for the Convolutional Neural Network-based warning model, and 0.930 for the Multi-Layer Perceptron-based warning model. The overall AUC value differences are relatively small, and the values are higher, indicating that the early-warning models established using these three algorithms are more stable.

The Random Forest algorithm typically yields excellent predictive results, even when dealing with complex or high-dimensional datasets. It can effectively handle large datasets and exhibits good robustness towards missing data. Random Forest can also fit nonlinear relationships in data quite well. However, it may perform poorly when dealing with high-dimensional sparse data. CNN excels in processing data with grid-like structures such as images and speech because they can effectively capture local features. Through mechanisms like weight sharing and local connections, CNN reduces the number of parameters, thereby improving the model's training efficiency and generalization ability. However, CNN may not perform well when dealing with sequential data or non-grid structured data, as their architecture assumes input

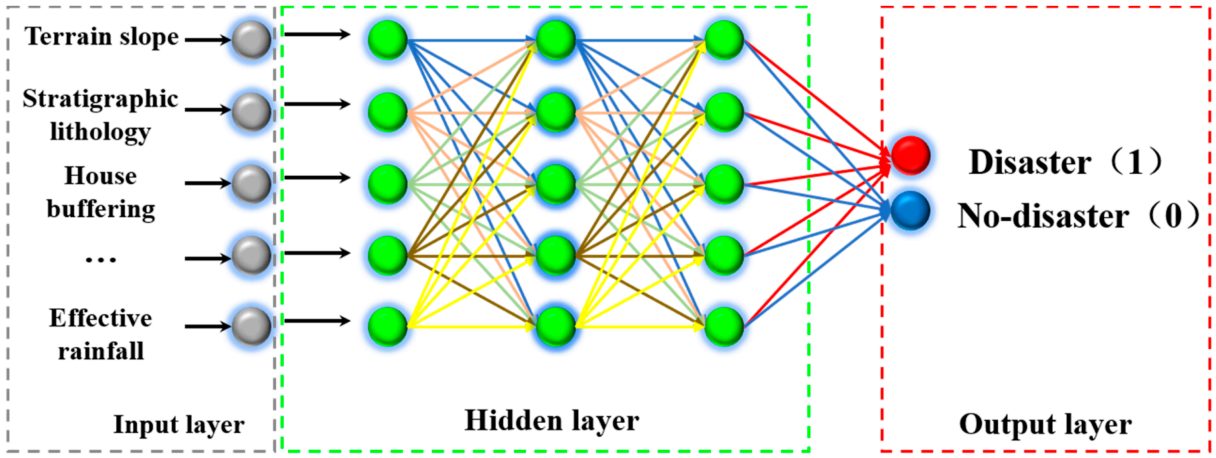

FIGURE 13
Schematic diagram of multilayer perceptron (MLP) model.

TABLE 12 The binary strategy and multiclass strategy.

Feature/Advantage-Disadvantage	Binary strategy	Multiclass strategy
Feature	Simple and intuitive, distinguishes only occurrence or non-occurrence of disasters	Able to detail disaster types and levels, distinguishes multiple disaster states
	Easy to implement and understand	Provides more detailed information on disaster states
	Applicable to various scales and types of geological disaster prediction	Adaptable to complex scenarios, such as multiple types and levels of disasters High prediction accuracy, provides detailed warning strategies
Advantage	High computational efficiency, direct decision-making	
	Able to more accurately reflect actual disaster occurrence and development processes	
Disadvantage	Information loss, relatively lower prediction accuracy and comprehensiveness	High model complexity, requires more data and computational resources
	Unable to handle complex situations	Greater implementation and understanding difficulty

data have a grid-like structure. CNN requires a large amount of data for training to avoid overfitting issues. MLP can adapt to various types of data, including structured and unstructured data. Their model structure is relatively simple, making them easy to understand and implement. However, for high-dimensional or large-scale data, MLP may not be efficient enough as they typically require a large number of parameters to learn complex patterns. However, the dataset established in this study features characteristics such as being large and low-dimensional, making it suitable for the application conditions of Random Forests, CNN, and MLP. This is also why these three models perform well in predicting landslide outcomes.

Although the three models show small numerical differences in validation metrics (such as AUC values and accuracy), these minor differences can lead to significant differences in practical applications. Specifically, we observed the following points:(1) Geographical Distribution Differences: In practical applications, different models show significant differences in the warning areas on geographical distribution maps. Taking the landslide disasters in Fujian Province on 5 August 2021, as an example, although the RF and CNN models are very close in accuracy and AUC values, they exhibit significant differences in the predicted warning areas. The RF model tends to issue warnings in medium-risk areas, while the CNN model issues more warnings in high-risk areas. (2)Reason Analysis: This difference mainly stems from the sensitivity of the models to input features. The RF model performs well in capturing potential risk points due to its ability to handle highly nonlinear relationships in the data. On the other hand, the CNN model effectively captures spatial features through its convolutional layers, leading to more accurate predictions in high-risk areas. (3)Impact Analysis: These small differences in metrics can lead to significant differences in practical applications. For example, the RF model predicts more warnings in “yellow warning” and “orange warning” areas, which is crucial for disaster prevention in medium-risk regions. The high accuracy of the CNN model in “red warning” areas means better preparedness in high-risk regions. The MLP model also provides higher warnings in some low-risk areas, offering additional references for overall risk management. Through the above analysis, we further illustrate that although the three models

have small differences in validation metrics, these differences can translate into significant differences in practical applications. This part of the discussion not only highlights the applicability of the models in different scenarios but also provides valuable insights for practical disaster warning work.

The article employs two warning strategies. The binary warning strategy categorizes the final warning level into two classes: no warning and warning, corresponding to low and high predicted geological disaster risks, respectively. The binary classification strategy is simple and intuitive, well-suited for scenarios requiring direct disaster prediction and emphasizing rapid decision-making. Involving only two categories contributes to high computational efficiency and straightforward decision-making, facilitating swift responses to emergencies. The multiclass warning strategy classifies the final warning level into multiple levels: no warning, yellow warning, orange warning, and red warning. These graded warnings (red, orange, yellow) correspond to very high, high, and relatively high risks of geological disasters. The multiclassification strategy distinguishes between various types or different levels of disaster states, providing more detailed and refined predictive outcomes. This strategy is suitable for regions and situations characterized by diverse types of disasters and higher complexity. It enables more accurate predictions for each potential disaster state and corresponding emergency response measures, thereby enhancing disaster preparedness capabilities. The advantages and disadvantages of these strategies are summarized in the following Table 12.

The application of these models in practical landslide prediction demonstrates their potential. However, limitations such as handling high-dimensional data and the data requirements of CNNs need to be addressed in future research. To further improve the robustness and applicability of landslide warning models, future studies should consider integrating hybrid models that combine the strengths of various algorithms. Additionally, exploring advanced machine learning techniques such as ensemble learning, transfer learning, and unsupervised learning can enhance model performance. Subsequent optimization of input features and validation of models using more diverse datasets will also be beneficial.

6 Conclusion

This study presents a comprehensive approach to constructing regional landslide warning models utilizing machine learning, demonstrated within the context of Fujian Province, China. The outlined four-step process includes data integration and cleaning, construction of training sample sets, machine learning model training and validation, and practical model application. Employing Random Forest (RF), Convolutional Neural Network (CNN), and Multilayer Perceptron (MLP) algorithms, the research showcases the effectiveness of these models in predicting rainfall-induced landslides.

(1) The dataset utilized for model development comprises 15,589 samples, incorporating 10 geological environmental condition factors and 16 rainfall-induced features. This diverse dataset provides a robust foundation for training and testing the models.
(2) The training and evaluation phase highlights the performance of RF, CNN, and MLP algorithms, revealing comparable accuracy metrics. The RF algorithm notably excels with a higher AUC value, indicating superior predictive capability.
(3) In practical model application, two standardized warning strategies are proposed: binary classification and multi-classification. The binary classification strategy distinguishes between "no warning" and "warning" categories based on a 50% threshold, while the multi-classification strategy offers nuanced warnings, dividing predictions into "no warning," "yellow warning," "orange warning," and "red warning" classes using varying thresholds.
(4) Real-world application of the models during the 5 August 2021 landslide disasters in Fujian Province demonstrates their efficacy. In the binary classification strategy, the models successfully predicted the majority of landslide occurrences. In the multi-classification approach, the RF model exhibits superior hierarchical warning effectiveness compared to CNN and MLP models.

In summary, this research significantly contributes to advancing landslide disaster warning models by providing insights into model construction, evaluation, and practical application. Further refinement and validation of these models are anticipated through continued data accumulation and real-world verification.

The paper only conducts statistical analysis on the relationship between various factors and landslide occurrences, lacking sufficient insight into the mechanism and causes of landslides. In the future, it is necessary to employ more rational and complex nonlinear methods for research. Although the sample set used in this study achieves a balance between positive and negative samples through the SMOTE algorithm, the generated synthetic samples are obtained through linear interpolation, which may introduce errors compared to the actual local conditions. Therefore, in future sample dataset construction, it is essential to select positive and negative samples proportionally. The warning methods studied in the paper have implications for broader application. Currently, they are only used in Fujian Province, but they could be applied to other regions in the future. By collecting different disaster-causing factors to construct sample sets, a regional geological disaster meteorological warning model could be developed, thus further verifying its applicability.

Data availability statement

The data analyzed in this study is subject to the following licenses/restrictions: Departmental reasons cannot be fully shared. Requests to access these datasets should be directed to lyanhui@mail.cgs.gov.cn.

Author contributions

YL: Conceptualization, Formal Analysis, Funding acquisition, Investigation, Methodology, Project administration, Resources, Supervision, Validation, Writing–original draft, Writing–review and editing, Data curation, Software, Visualization. SM: Data curation, Investigation, Methodology, Resources, Writing–original

draft, Writing–review and editing. LD: Data curation, Formal Analysis, Investigation, Methodology, Resources, Software, Writing–original draft. RX: Conceptualization, Investigation, Project administration, Resources, Supervision, Writing–original draft. JH: Data curation, Investigation, Resources, Validation, Writing–original draft. PZ: Conceptualization, Funding acquisition, Investigation, Project administration, Resources, Supervision, Validation, Writing–original draft, Methodology, Writing–review and editing.

Funding

The author(s) declare that financial support was received for the research, authorship, and/or publication of this article. This research was financially supported by the National Key Research and Development Program of China (2023YFC3007205) and the National Natural Science Foundation of China(42077440; 41202217).

Acknowledgments

Thanks for the China Institute of Geo-Environment Monitoring and the Fujian Provincial Geological Environmental Monitoring Center for providing the historical landslide records data. We also appreciate the Fujian Meteorological Bureau and the Fujian Water Resources Department for providing the rainfall data.

Conflict of interest

Author LD was employed by Power China Beijing Engineering Corporation Limited.

The remaining authors declare that the research was conducted in the absence of any commercial or financial relationships that could be construed as a potential conflict of interest.

Publisher's note

All claims expressed in this article are solely those of the authors and do not necessarily represent those of their affiliated organizations, or those of the publisher, the editors and the reviewers. Any product that may be evaluated in this article, or claim that may be made by its manufacturer, is not guaranteed or endorsed by the publisher.

References

Abraham, M. T., Satyam, N., Rosi, A., Pradhan, B., and Segoni, S. (2020). The selection of rain gauges and rainfall parameters in estimating intensity-duration thresholds for landslide occurrence: case study from Wayanad (India). *Water* 12 (4), 1000. doi:10.3390/w12041000

Ado, M., Amitab, K., Maji, A. K., Jasińska, E., Gono, R., Leonowicz, Z., et al. (2022). Landslide susceptibility mapping using machine learning: a literature survey. *Remote Sens.* 14 (13), 3029. doi:10.3390/rs14133029

Aleotti, P. (2004). A warning system for rainfall-induced shallow failures. *Eng. Geol.* 73 (3-4), 247–265. doi:10.1016/j.enggeo.2004.01.007

Au, S. W. C. (1998). Rain-induced slope instability in Hong Kong. *Eng. Geol.* 51 (1), 1–36. doi:10.1016/s0013-7952(98)00038-6

Baum, R. L., and Godt, J. W. (2010). Early warning of rainfall-induced shallow landslides and debris flows in the USA. *Landslides* 7, 259–272. doi:10.1007/s10346-009-0177-0

Breiman, L. (2001). Random forests. *Mach. Learn.* 45 (1), 5–32. doi:10.1023/a:1010933404324

Caine, N. (1980). The rainfall intensity-duration control of shallow landslides and debris flows. *Geogr. Ann. Ser. A, Phys. Geogr.* 62 (1-2), 23–27. doi:10.2307/520449

Cannon, S. H. (1985). Rainfall conditions for abundant debris avalanches, San Francisco Bay region, California. *Geology* 38, 267–272.

Chen, W., Xie, X., Wang, J., Pradhan, B., Hong, H., Bui, D. T., et al. (2017). A comparative study of logistic model tree, random forest, and classification and regression tree models for spatial prediction of landslide susceptibility. *Catena* 151, 147–160. doi:10.1016/j.catena.2016.11.032

Ding, G., Wang, Y., Mao, J., et al. (2017). Study on rainfall warning thresholds in debris flow prone areas of beijing. *Hydrogeology Eng. Geol.* 44 (3), 136–142. (in Chinese). doi:10.16030/j.cnki.issn.1000-3665.2017.03.20

Dong, L., Liu, Y., Huang, J., et al. (2024). An early prediction model of regional landslide disasters in Fujian Province based on convolutional neural network. *Hydrogeology Eng. Geol.* 51 (1), 145–153. doi:10.16030/j.cnki.issn.1000-3665.202211018

Dou, J., Yamagishi, H., Pourghasemi, H. R., Yunus, A. P., Song, X., Xu, Y., et al. (2015). An integrated artificial neural network model for the landslide susceptibility assessment of Osado Island, Japan. *Nat. Hazards* 78, 1749–1776. doi:10.1007/s11069-015-1799-2

Dou, J., Yunus, A. P., Merghadi, A., Shirzadi, A., Nguyen, H., and Hussain, Y. (2020). Different sampling strategies for predicting landslide susceptibilities are deemed less consequential with deep learning. *Sci. Total Environ.* 720, 137320. doi:10.1016/j.scitotenv.2020.137320

Froude, M. J., and Petley, D. N. (2018). Global fatal landslide occurrence from 2004 to 2016. *Nat. Hazards Earth Syst. Sci.* 18 (8), 2161–2181. doi:10.5194/nhess-18-2161-2018

Gatto, A., Clò, S., Martellozzo, F., and Segoni, S. (2023). Tracking a decade of hydrogeological emergencies in Italian municipalities. *Data* 8 (10), 151. doi:10.3390/data8100151

Goetz, J. N., Brenning, A., Petschko, H., and Leopold, P. (2015). Evaluating machine learning and statistical prediction techniques for landslide susceptibility modeling. *Comput. geosciences* 81, 1–11. doi:10.1016/j.cageo.2015.04.007

Hastie, T., Tibshirani, R., and Friedman, J. (2009). *The elements of statistical learning: data mining, inference, and prediction*. Germany: Springer.

Hong, H., Pourghasemi, H. R., and Pourtaghi, Z. S. (2016a). Landslide susceptibility assessment in Lianhua County (China): a comparison between a random forest data mining technique and bivariate and multivariate statistical models. *Geomorphology* 259, 105–118. doi:10.1016/j.geomorph.2016.02.012

Hong, H., Pradhan, B., Jebur, M. N., Bui, D. T., Xu, C., and Akgun, A. (2016b). Spatial prediction of landslide hazard at the Luxi area (China) using support vector machines. *Environ. Earth Sci.* 75, 1–14. doi:10.1007/s12665-015-4866-9

Khan, S., Kirschbaum, D. B., Stanley, T. A., Amatya, P. M., and Emberson, R. A. (2022). Global landslide forecasting system for hazard assessment and situational awareness. *Front. Earth Sci.* 10, 878996. doi:10.3389/feart.2022.878996

Krøgli, I. K., Devoli, G., Colleuille, H., Boje, S., Sund, M., and Engen, I. K. (2018). The Norwegian forecasting and warning service for rainfall-and snowmelt-induced landslides. *Nat. hazards earth Syst. Sci.* 18 (5), 1427–1450. doi:10.5194/nhess-18-1427-2018

Lee, J. J., Song, M. S., Yun, H. S., and Yum, S. G. (2022). Dynamic landslide susceptibility analysis that combines rainfall period, accumulated rainfall, and geospatial information. *Sci. Rep.* 12 (1), 18429. doi:10.1038/s41598-022-21795-z

Lima, P., Steger, S., Glade, T., and Murillo-García, F. G. (2022). Literature review and bibliometric analysis on data-driven assessment of landslide susceptibility. *J. Mt. Sci.* 19 (6), 1670–1698. doi:10.1007/s11629-021-7254-9

Liu, C., Liu, Y., Wen, M., et al. (2015). Practice of geological disaster meteorological warning in China: 2003-2012. *J. Geol. Hazards Prev. Res.* 26 (1), 1–8. (in Chinese). doi:10.16031/j.cnki.issn.1003-8035.2015.01.001

Liu, Y., Huang, J., Xiao, R., Ma, S., and Zhou, P. (2022). Research on a regional landslide early-warning model based on machine learning—a case study of Fujian Province, China. *Forests* 13 (12), 2182.doi:10.3390/f13122182

Liu, Y., Yin, K., and Liu, B. (2010). Application of logistic regression and artificial neural network models in spatial prediction of landslide disasters. *Hydrogeology Eng. Geol.* (5), 92–96. (in Chinese). doi:10.16030/j.cnki.issn.1000-3665.2010.05.015

Luti, T., Segoni, S., Catani, F., Munafò, M., and Casagli, N. (2020). Integration of remotely sensed soil sealing data in landslide susceptibility mapping. *Remote Sens.* 12 (9), 1486. doi:10.3390/rs12091486

Marjanovic, M., Bajat, B., and Kovacevic, M. (2009). Landslide susceptibility assessment with machine learning algorithms[C]//2009 international conference on intelligent networking and collaborative systems. *IEEE*, 273–278. doi:10.1109/INCOS.2009.25

Micheletti, N., Foresti, L., Robert, S., Leuenberger, M., Pedrazzini, A., Jaboyedoff, M., et al. (2014). Machine learning feature selection methods for landslide susceptibility mapping. *Math. Geosci.* 46, 33–57. doi:10.1007/s11004-013-9511-0

Ministry of Natural Resources, Geological Hazard Technical Guidance Center (2019). *National geological disaster bulletin (2019) [R]. Beijing: Ministry of natural Resources, geological hazard technical guidance center*.

Mulyana, A. R., Sutanto, S. J., Hidayat, R., et al. (2019). Capability of Indonesian landslide early warning system to detect landslide occurrences few days in advance. *Geophys. Res. Abstr.* 21.

Nocentini, N., Rosi, A., Segoni, S., and Fanti, R. (2023). Towards landslide space-time forecasting through machine learning: the influence of rainfall parameters and model setting. *Front. Earth Sci.* 11, 1152130. doi:10.3389/feart.2023.1152130

Pennington, C., Freeborough, K., Dashwood, C., Dijkstra, T., and Lawrie, K. (2015). The national landslide database of great britain: acquisition, communication and the role of social media. *Geomorphology* 249, 44–51. doi:10.1016/j.geomorph.2015.03.013

Peruccacci, S., Brunetti, M. T., Gariano, S. L., Melillo, M., Rossi, M., and Guzzetti, F. (2017). Rainfall thresholds for possible landslide occurrence in Italy. *Geomorphology* 290, 39–57. doi:10.1016/j.geomorph.2017.03.031

Ponziani, F., Berni, N., Stelluti, M., Zauri, R., Pandolfo, C., Brocca, L., et al. (2013). LANDWARN: an operative early warning system for landslides forecasting based on rainfall thresholds and soil moisture. *Landslide Sci. Pract. Volume 2 Early Warn. Instrum. Monit.*, 627–634. doi:10.1007/978-3-642-31445-2_82

Reichenbach, P., Rossi, M., Malamud, B. D., Mihir, M., and Guzzetti, F. (2018). A review of statistically-based landslide susceptibility models. *Earth-science Rev.* 180, 60–91. doi:10.1016/j.earscirev.2018.03.001

Ren, T., Gao, L., and Gong, W. (2024). An ensemble of dynamic rainfall index and machine learning method for spatiotemporal landslide susceptibility modeling. *Landslides* 21 (2), 257–273. doi:10.1007/s10346-023-02152-1

Sameen, M. I., Pradhan, B., and Lee, S. (2020). Application of convolutional neural networks featuring Bayesian optimization for landslide susceptibility assessment. *Catena* 186, 104249. doi:10.1016/j.catena.2019.104249

Sun, D., Gu, Q., Wen, H., Shi, S., Mi, C., and Zhang, F. (2022). A hybrid landslide warning model coupling susceptibility zoning and precipitation. *Forests* 13 (6), 827. doi:10.3390/f13060827

Thai Pham, B., Shirzadi, A., Shahabi, H., Omidvar, E., Singh, S. K., Sahana, M., et al. (2019). Landslide susceptibility assessment by novel hybrid machine learning algorithms. *Sustainability* 11 (16), 4386. doi:10.3390/su11164386

Tien Bui, D., Tuan, T. A., Hoang, N. D., Thanh, N. Q., Nguyen, D. B., Van Liem, N., et al. (2017). Spatial prediction of rainfall-induced landslides for the Lao Cai area (Vietnam) using a hybrid intelligent approach of least squares support vector machines inference model and artificial bee colony optimization. *Landslides* 14, 447–458. doi:10.1007/s10346-016-0711-9

Tien Bui, D., Tuan, T. A., Klempe, H., Pradhan, B., and Revhaug, I. (2016). Spatial prediction models for shallow landslide hazards: a comparative assessment of the efficacy of support vector machines, artificial neural networks, kernel logistic regression, and logistic model tree. *Landslides* 13, 361–378. doi:10.1007/s10346-015-0557-6

Trigila, A., Iadanza, C., Esposito, C., and Scarascia-Mugnozza, G. (2015). Comparison of logistic regression and random forests techniques for shallow landslide susceptibility assessment in giampilieri (NE sicily, Italy). *Geomorphology* 249, 119–136. doi:10.1016/j.geomorph.2015.06.001

Wei, L. W., Huang, C. M., Chen, H., Lee, C. T., Chi, C. C., and Chiu, C. L. (2018). Adopting the I 3–R 24 rainfall index and landslide susceptibility for the establishment of an early warning model for rainfall-induced shallow landslides. *Nat. Hazards Earth Syst. Sci.* 18 (6), 1717–1733. doi:10.5194/nhess-18-1717-2018

Wei, X., Zhang, L., Luo, J., and Liu, D. (2021). A hybrid framework integrating physical model and convolutional neural network for regional landslide susceptibility mapping. *Nat. Hazards* 109, 471–497. doi:10.1007/s11069-021-04844-0

Yang, Q., Wang, X., Yin, J., Du, A., Zhang, A., Wang, L., et al. (2024). A novel CGBoost deep learning algorithm for coseismic landslide susceptibility prediction. *Geosci. Front.* 15 (2), 101770. doi:10.1016/j.gsf.2023.101770

Yilmaz, I. (2009). Landslide susceptibility mapping using frequency ratio, logistic regression, artificial neural networks and their comparison: a case study from Kat landslides (Tokat—Turkey). *Comput. Geosciences* 35 (6), 1125–1138. doi:10.1016/j.cageo.2008.08.007

Yuan, R., and Chen, J. (2023). A novel method based on deep learning model for national-scale landslide hazard assessment. *Landslides* 20 (11), 2379–2403. doi:10.1007/s10346-023-02101-y

Zeng, T., Linfeng, WANG, Yu, ZHANG, et al. (2024). Landslide susceptibility modeling and interpretability based on CatBoost-SHAP model. *Chin. J. Geol. Hazard Control* 35, 37–50. doi:10.16031/j.cnki.issn.1003-8035.202309035

Zhou, C., Yin, K., Cao, Y., Ahmed, B., Li, Y., and Catani, F. (2020). Landslide susceptibility modeling applying machine learning algorithms: a case study from Longju in the Three Gorges Reservoir area, China. *Comput. Geosciences* 136, 104345. doi:10.1080/10106049.2022.2076928

Zhou, X., Wen, H., Li, Z., Zhang, H., and Zhang, W. (2022). An interpretable model for the susceptibility of rainfall-induced shallow landslides based on SHAP and XGBoost. *Geocarto Int.* 37 (26), 13419–13450. doi:10.1080/10106049.2022.2076928

frontiers | Frontiers in Earth Science

TYPE Original Research
PUBLISHED 08 August 2024
DOI 10.3389/feart.2024.1420425

OPEN ACCESS

EDITED BY
Yanfang Sang,
Institute of Geographic Sciences and Natural Resources (CAS), China

REVIEWED BY
Huajin Li,
Chengdu University, China
Xiang Zhang,
China University of Geosciences Wuhan, China

*CORRESPONDENCE
Chong Xu,
xc11111111@126.com

RECEIVED 20 April 2024
ACCEPTED 30 July 2024
PUBLISHED 08 August 2024

CITATION
Liu J and Xu C (2024) Construction and preliminary analysis of landslide database triggered by heavy storm in the parallel range-valley area of western Chongqing, China, on 8 June 2017.
Front. Earth Sci. 12:1420425.
doi: 10.3389/feart.2024.1420425

Construction and preliminary analysis of landslide database triggered by heavy storm in the parallel range-valley area of western Chongqing, China, on 8 June 2017

Jielin Liu[1,2] and Chong Xu[1,2]*

[1]National Institute of Natural Hazards, Ministry of Emergency Management of China, Beijing, China, [2]Key Laboratory of Compound and Chained Natural Hazards Dynamics, Ministry of Emergency Management of China, Beijing, China

On 8 June 2017, a heavy storm struck the parallel ridge-valley area of western Chongqing, resulting in serious urban waterlogging and landslides, which led to severe impacts on infrastructure and damage to private property. Based on high-resolution optical satellite images, this paper comprehensively identified the landslides triggered by this rainfall event, and established a corresponding landslide database. The database takes the landslide area density and landslide number density as the main indicators, and combines the lithology characteristics to analyze the spatial distribution of landslides. The results show that this event triggered 487 landslides in an area of 583 km^2, involving an area of about 485,587 m^2, accounting for about 0.083% of the study area. The average landslide number density is 0.84 num/km^2, the highest value of landslide number density can reach 55.6 num/km^2, and the maximum landslide area density is about 6.4%. These landslides are mainly distributed in the southern foothills of the Huaying Mountain, especially in the weak interlayer lithology area. The database provides scientific reference and data support for exploring the mechanism of landslides in western Chongqing and reducing the risk of landslide disasters under the background of rapid development of local society.

KEYWORDS

rainfall-triggered landslides, database, parallel range-valley area, satellite imagery, western Chongqing

1 Introduction

Landslide disasters occur frequently, drawing extensive research from numerous scholars (Huang et al., 2022; Huang et al., 2023), with the aim of better addressing this challenge. Particularly in the current scenario of severe global climate change, the impact of climate change on the frequency of landslides has become a matter of great concern (Patton et al., 2019; Kirschbaum et al., 2020). The frequent incidence of extreme events such as heavy rainfall and droughts, caused by climate change, aggravates the erosion and loosening of the earth surface and increases the possibility of landslides occurrence.

As a natural disaster, landslides are extremely destructive, posing a serious threat to both human society and the environment. Between 1 January 2004, and 31 December 2010, there were 2,620 fatal landslide events globally (excluding co-seismic landslides), resulting in a total of 32,322 deaths, with the number of recorded landslides showing an increasing trend each year (Petley, 2012). Landslide disasters can cause direct or indirect damage to local communities (e.g., destruction of infrastructure, power outages, and water supply interruptions), significantly impacting the local economy and social stability. The post-disaster reconstruction costs are enormous, encompassing clearance and reconstruction of facilities, imposing a heavy burden on local governments and social resources (Vranken et al., 2013). Moreover, landslide disasters can change the local landscape. Large-magnitude landslides may result in drastic changes in topography, including collapses, river diversion, etc., bringing profound impacts on surrounding environments and ecosystems (Thapa et al., 2024). Compared to post-disaster remedies, preventive measures beforehand are particularly crucial (World Bank and United Nations, 2010). By upgrading monitoring and warning systems, adjusting land use plans, enhancing infrastructure resilience, etc., thereby the frequency of landslides and the resulting losses and impacts can be effectively reduced.

In recent years, the prominent geographic advantage of the northwest part of Chongqing has garnered attention due to the development of the Chengdu-Chongqing economic circle. Positioned at the intersection of the Belt and Road and the Yangtze River Economic Belt, this region holds a unique geographical advantage in connecting the southwest and northwest of China domestically, and bridging East Asia, Southeast Asia, and South Asia internationally. Not only does this area boast abundant ecological resources and energy, including mineral deposits, but it also features densely populated urban areas and picturesque landscapes. It stands as one of the most densely populated regions in western China, with robust industrial foundations, strong innovative capabilities, broad market potential, and high levels of openness, playing a crucial strategic role in the country's overall development. However, the rapid development of the Chengdu-Chongqing region also brings a series of challenges and risks, including frequent landslide disasters. For instance, an extreme rainfall event could trigger widespread landslides, severely impacting the local socioeconomic and ecological environment. Previous research in the region mainly focused on slope stability assessment (Wang L. et al., 2019; Wu et al., 2023), landslide susceptibility (Sun et al., 2020; Wei et al., 2021) and landslide movement processes (Zhang et al., 2014; Guo et al., 2020), while there is little research on the database of landslide triggered by a single rainfall event.

Compiling a landslide inventory serves as a crucial data foundation for further landslide studies, driven by multiple factors. Firstly, it marks the spatial and temporal occurrences of landslides (Shao et al., 2023a; Chen et al., 2023), providing fundamental data for subsequent research. Through landslide inventory, the mechanism, morphology, and mode controlled by the lithology or geology can be deeply understood (Zhang, 2020; Li et al., 2021). Conducting susceptibility (Ciurleo et al., 2021; Razavi-Termeh et al., 2021) and hazard assessments (Thiery et al., 2020; Lin et al., 2021) are of significant importance for geological disaster management. Developing landslide early warning systems (Lagomarsino et al., 2013; Calvello and Piciullo, 2016; Magrì et al., 2024) and taking proactive measures aids in reducing economic losses and casualties caused by landslides.

The advancement of science leads to technological innovations, offering various methods for landslide detection and inventory compilation. For instance, SAR data, characterized by all-weather capability and low cost, is utilized for landslide identification and displacement monitoring (Handwerger et al., 2022; Zhang et al., 2023). However, rapid deformation rates can lead to decorrelation, rendering it unsuitable for detecting landslides triggered by extreme rainfall events. Field surveys are commonly employed for individual landslides and on-site verification of landslide databases, but with high time and economic costs. Text mining based on big data extracts landslide event locations and times from social media (Franceschini et al., 2022), yielding abundant but potentially redundant and incomplete landslide-related data, posing huge challenges to researchers. Rapid development in optical satellite technology, with high precision, wide coverage, low cost, and multi-temporal, has received extensive attention. Using high-resolution optical satellite images, Sun et al. (2024a) identified 10,968 landslide traces in the Yinshan area; He et al. (2021) found 167 landslides triggered by the Qiaojia Mw5.1 earthquake on 18 May 2020 in Yunnan, China; Huang et al. (2021) established a database of earthquake-triggered landslides in Milin, Tibet, including 3,130 co-seismic landslides. Xie et al. (2023) took an extreme rainfall event in Jiexi County, Guangdong Province in August 2018 as the research subject, and established a database containing 1,844 landslides. Compared with the great progress in earthquake-triggered landslide database construction, the establishment of a rainfall-triggered landslide database using optical satellite images is relatively slow. As of 2022, there are only 16 public databases (Ma et al., 2022) of heavy rainfall-triggered landslides worldwide. Primarily because optical satellites are often hindered by cloud cover during adverse weather conditions, making it challenging to extract rainfall-triggered landslides occurring on cloudy days.

The parallel ridge-valley region in Chongqing, being one of the world's three major fold mountain systems, provides a unique setting for examining how rainfall initiates landslides within its geological context. The area's pronounced geological features greatly intensify the need for research into a database on rainfall-triggered landslide occurrences in this region and its vicinity. This study focused on a localized heavy storm event that occurred in the Huaying Mountains (in the parallel ridge-valley region of western Chongqing) on 8 June 2017. It revealed the spatiotemporal characteristics of this rainfall event. Using satellite images, we extracted landslides triggered by this event to establish a landslide database. This work not only enriches the landslide database of the Chongqing, but also provides accurate data support for subsequent analysis of landslides triggered by the event. It will also directly contribute to the protection of residents' lives and property, reduce potential losses caused by landslide disasters, and thereby ensure the long-term stability and development of the community.

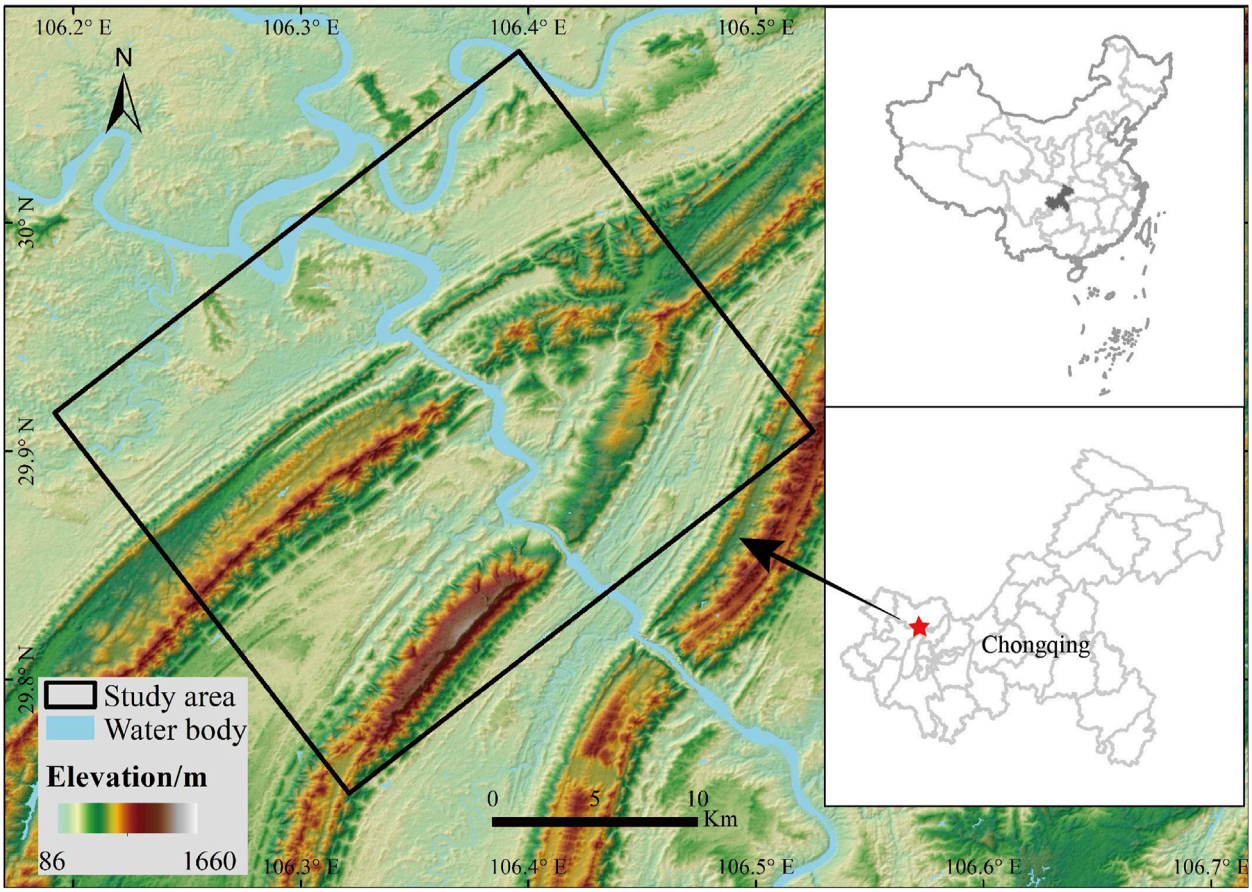

FIGURE 1
Overview of the study area.

2 Study area

The study area is located in the northwest of Chongqing (Figure 1). The coordinates of the study area's corners are: 106.396° E, 30.075° N; 106.192° E, 29.917° N; 106.321° E, 29.75° N; 106.525° E, 29.909° N. The study area covers approximately 583 km^2. The climate in the region is subtropical humid monsoon. It's characterized by early springs, hot summers, rainy autumns, and mild winters. The average annual temperature is 18.2°C. The average annual precipitation is 1156.8 mm, concentrated from May to September each year. The study area is situated at the southern foothills of the Huaying Mountain, which lies within the parallel ridge-valley region adjacent to the eastern Sichuan Basin. The study area exhibits a terrain marked by anticlines forming hills and synclines forming valleys, with elevations ranging from 120 to 1,000 m. Flowing through the heart of the area, the Jialing River provides abundant water resources. The strata of the study area span a wide range from the Jurassic to the Quaternary. Jurassic covers over 50% of the total area, mainly distributed in flat valleys. These areas are composed of mudstone interbedded with siltstone and feldspathic sandstone. In the mountainous regions, the main underlying strata are Triassic, accounting for over 30%, consisting of quartz sandstone, shale, and limestone (Figure 2).

3 Data and method

From June 8th to 10th, 2017, Chongqing experienced an unprecedented rainfall event, resulting in significant economic losses for the region. The severely affected Hechuan District has become the focus of media attention (CCTV, 2017; Lin and Wu, 2017). In response, we utilized the GPM IMERG Final Run product (Huffman et al., 2023) to analyze the precipitation patterns during these three days in Chongqing. Through spatial analysis, we identified the region with the highest precipitation. According to the rainfall distribution, media attention, terrain characteristics, and population density observed from satellite images, we determined the study area, and then carried out research on rainfall-triggered landslides in the study area.

In recent years, the field of landslide identification technology has undergone significant technological innovation, particularly with the application of deep learning techniques (Wang et al., 2021; Yang et al., 2022), which have provided efficient means of identification and high-precision results for disaster emergency response. While the accuracy of deep learning in landslide identification is satisfactory for simple surface environments, its recognition accuracy significantly decreases when dealing with complex surface environments, such as areas near roads. Therefore, at the current stage of technological development,

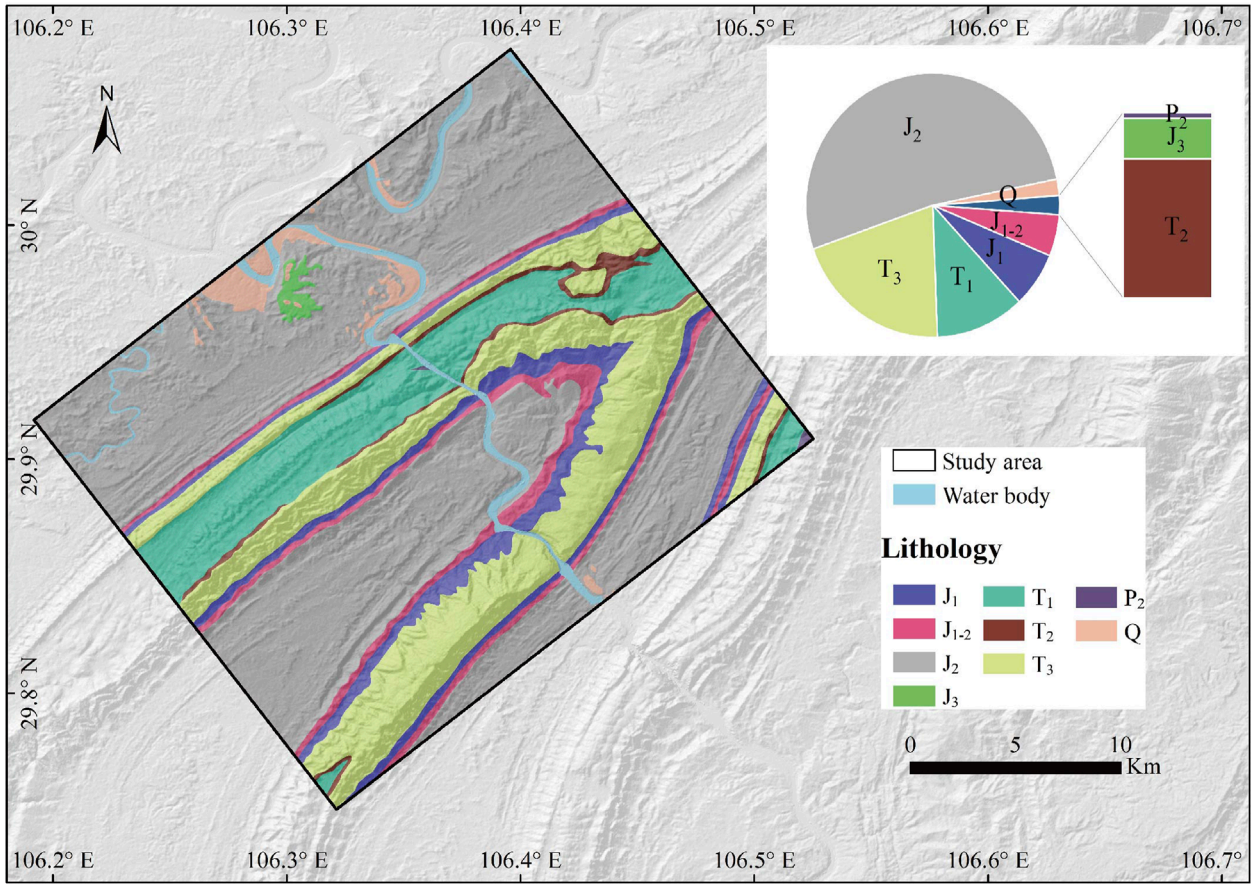

FIGURE 2
Underlying strata map of the study area.

the human-machine interactive method for landslide identification maintains its irreplaceable position.

Our team has made substantial strides in the realm of remote sensing interpretation for event-induced landslides, with a wealth of experience specifically in extracting landslide data from optical remote sensing images. We have successfully developed interpretation criteria for earthquake-induced landslides (Xu et al., 2015; Sun et al., 2024b; Shao et al., 2024) and have also achieved significant breakthroughs in identifying rainfall-induced landslides (Ma et al., 2023a; Cui et al., 2024; Gao et al., 2024). The insights and standards developed for earthquake-induced landslides are readily applicable to the recognition of rainfall-induced landslides in this study, as both types of landslides present marked differences from their surroundings on optical remote sensing images, which is a key indicator for identification. Drawing from our previous research, we have compiled an expert knowledge framework that is a core to the process of landslide interpretation. This framework combines the analysis of optical remote sensing imagery, terrain and geomorphological characteristics, and the mechanisms that trigger landslides, offering a robust scientific foundation for precise landslide identification. Especially for shallow landslides triggered by rainfall events, their distinctive morphological traits (such as compact size and elongated forms) are vital for enhancing the accuracy and efficiency of landslide interpretation.

In this study, based on high-resolution satellite images, all landslide data were extracted by human-computer interaction visual interpretation. We use the Planet satellite image with a resolution of 3 m as the main satellite image. Pre-event imagery dates back to May 2017, captured in a global monthly composite image, while post-event imagery was obtained in July 2017 (Figure 3). Given the spatial resolution of the Planet and extensive traces of human activity in the study area, precautions were taken to avoid misidentifying. For a more accurate identification of landslides, we supplemented the analysis with detailed validation using Google Earth imagery from August 2016 and August 2017 (Figure 4).

The lithology data used in the study are from the China Geological Survey (http://dcc.cgs.gov.cn/, accessed on 19 March 2024).

4 Results

4.1 Rainfall event

This study collected GPM IMERG Final Run daily precipitation products from June 8th to 11 June 2017, to conduct spatial analysis of the rainfall event in Chongqing (Figure 5). The results indicate that the Hechuan District, Beibei District, Bishan District, Yubei District,

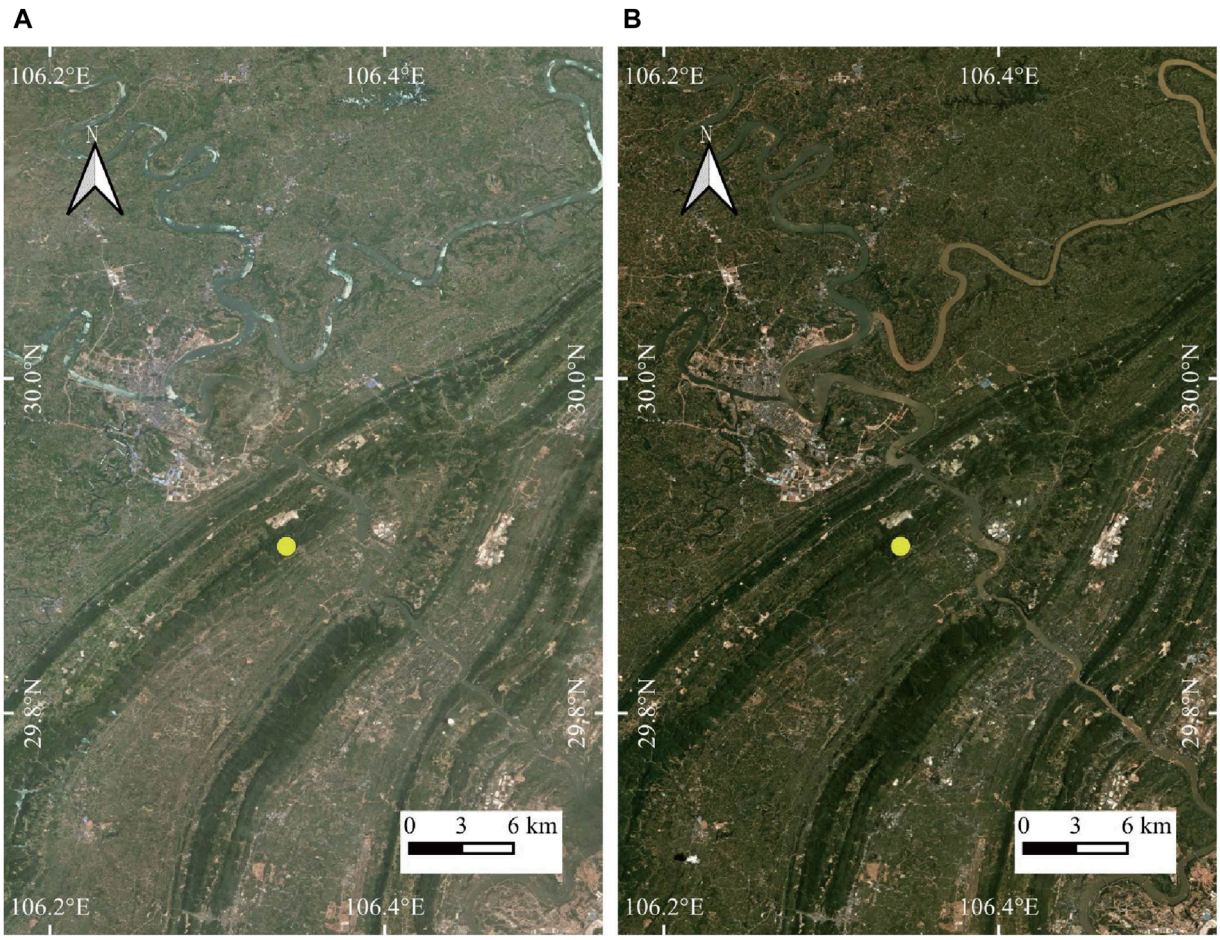

FIGURE 3
The Planet images of the study area pre- and post-rainfall event. **(A)** May 2017 **(B)** July 2017.

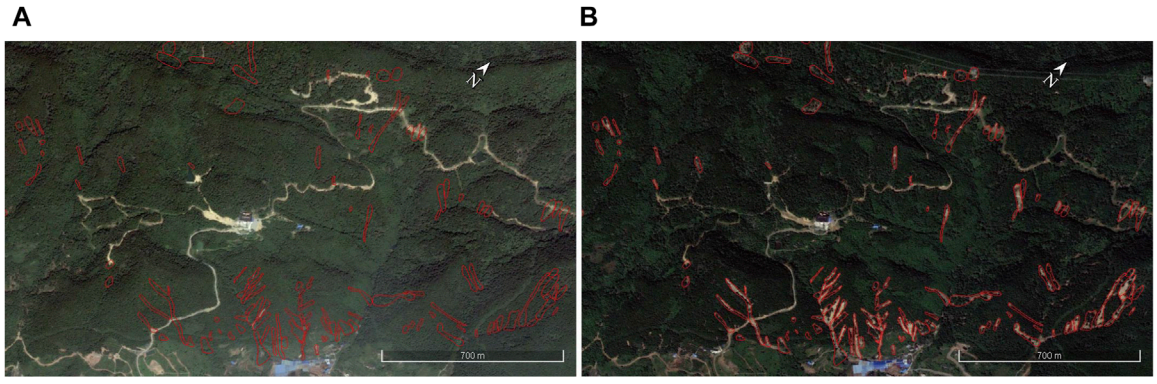

FIGURE 4
The Google Earth image depicts the study area marked in yellow in Figure 3 (29.9°N, 106.341°E) pre- and post-rainfall event. **(A)** August 2016 **(B)** August 2017.

and Tongliang District are the areas with the highest precipitation. This rainfall event caused flooding, leading to waterlogging and road inundation in urban areas. Notably, all 27 towns and streets within Hechuan District experienced significant flooding, resulting in severe submersion of agricultural lands. Due to ongoing river diversion construction in Huangjin Village, river surged, causing 30 workers were trapped (Tianqi Network, 2017). Although all trapped workers were successfully rescued by the firefighters, this incident raised concerns about geological disaster prevention. Hechuan and its surroundings, due to their unique geographical and climatic

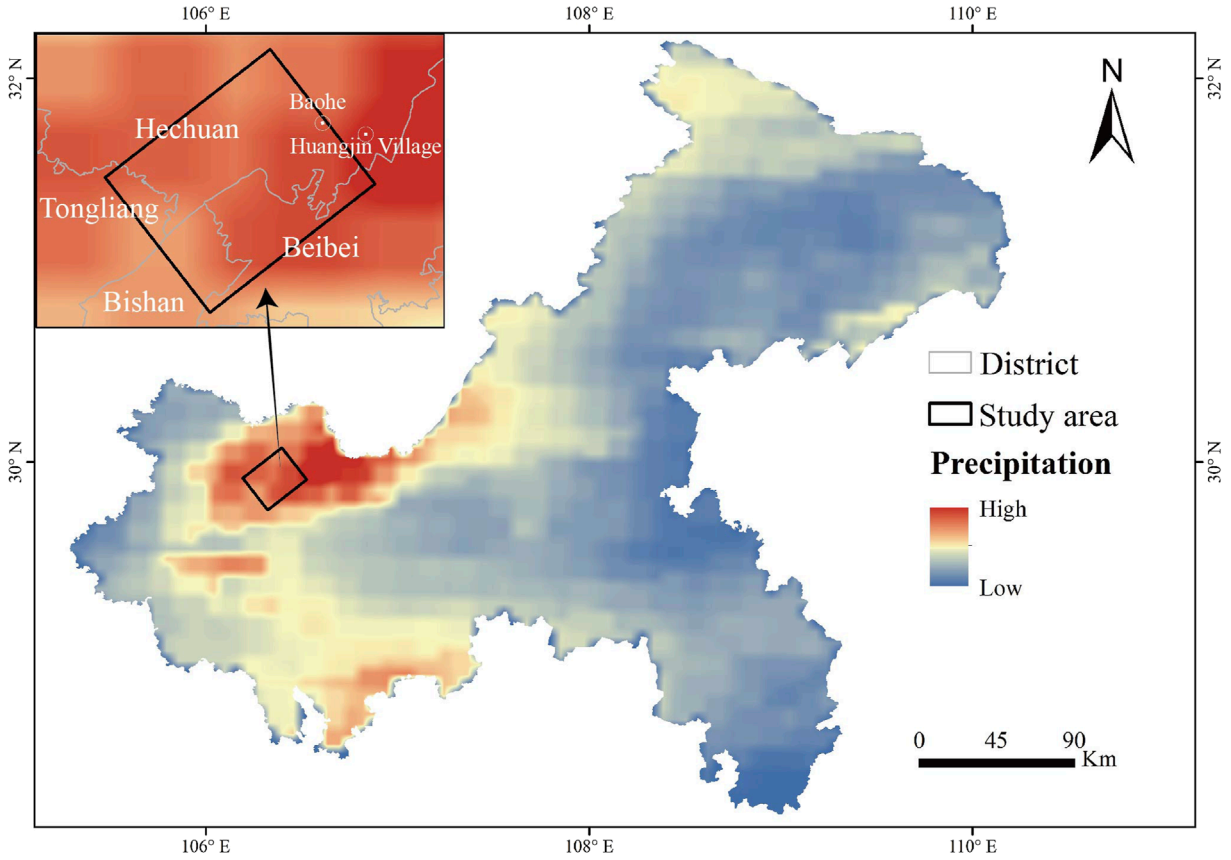

FIGURE 5
Spatial distribution of accumulation precipitation in Chongqing from 8 June 2017 to 10 June 2017.

conditions, are prone to geological disasters. The heavy storm induced landslides pose a serious threat to public safety. Therefore, studying the landslides triggered by this rainfall is critical. Through scientific research and effective prevention measures, authorities can better safeguard lives and property and mitigate the recurrence of such disasters.

The rainfall process of the study area was analyzed temporally using the 0.5-hour rainfall data from the GPM IMERG Final Run. It was observed that the intense rainfall mainly occurred from 3:00 p.m. on 8 June 2017, to 12:00 a.m. on 9 June 2017. According to the standards outlined in the National Standard of the People's Republic of China (GBT28592-2012 Grade of precipitation) and the rainfall intensity classification criteria issued by the China Meteorological Administration (Table 1), the total rainfall on June 8th was approximately 85 mm, reaching the level of a heavy storm. Figure 6 shows that the rainfall intensity reached the maximum at 17: 30 on the 8th, about 30 mm/h. The event spanned three days, with a total precipitation of about 87 mm.

TABLE 1 Precipitation intensity grading standards promulgated by the China Meteorological Administration.

Rainfall classification	Total rainfall in 24 Hours(mm)
Light Rain	<10
Moderate Rain	[10,25)
Heavy Rain	[25,50)
Heavy Strom	[50,100)
Very Heavy Strom	[100,250)
Extremely Heavy Strom	≥250

4.2 Rainfall-induced landslide inventory

The occurrence of rainfall resulted in the initiation of 487 landslides, covering a total area of about 485,587 m^2. This biggest landslide covered an area of about 8,608 m^2, while the smallest was 76 m^2, with an average landslide area of around 997 m^2. Based on the data presented in Figure 7, there was a total of 205 landslides with sizes less than 500 m^2, which represents about 42% of the total area of landslides. There were a total of 227 landslides, with sizes ranging from 500 to 2,000 m^2, which accounted for around 46% of the total. Furthermore, a total of 45 landslides occurred, with sizes varying between 2,000 and 5,000 m^2. There were ten landslides with areas of more than 5,000 m^2, all of which were

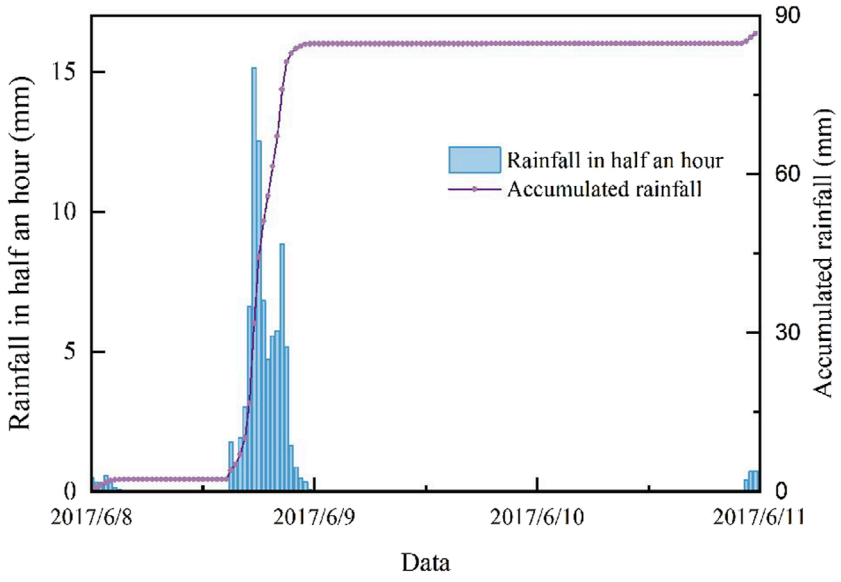

FIGURE 6
Rainfall process curve of the study area from 8 June 2017 to 10 June 2017.

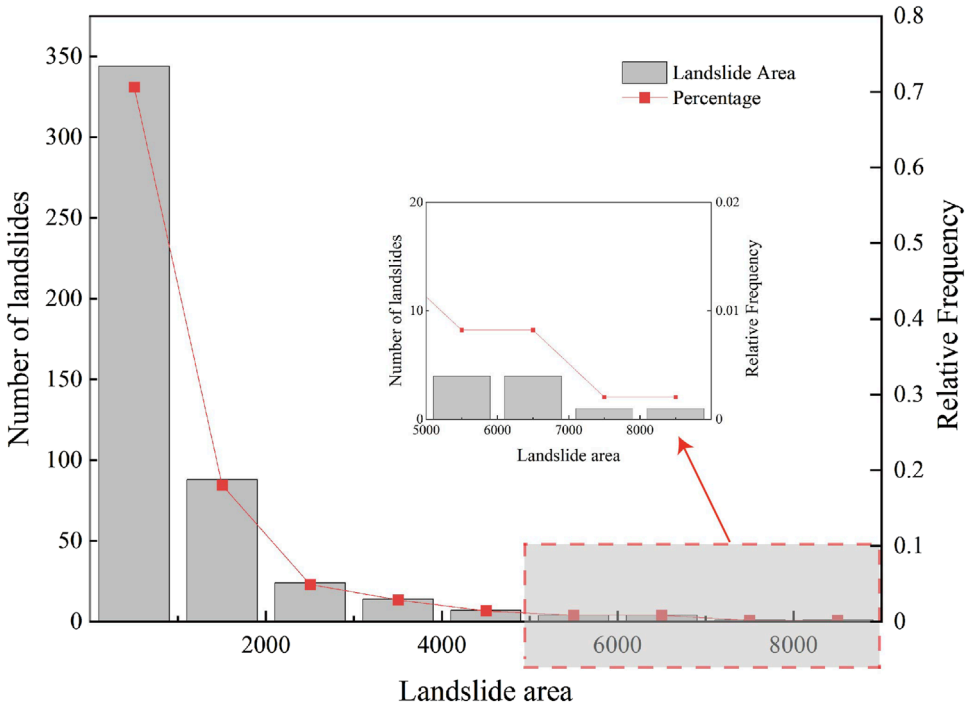

FIGURE 7
Landslide area classification statistics.

situated on the right bank of the Jialing River (Figure 8). Empirical relationships of landslide area-volume proposed by Guzzetti et al. (2009) were utilized for calculations. The findings reveal that the largest volume of an individual landslide was roughly 35,574 m^3, the smallest was around 38 m^3, and the average volume was about 2,197 m^3.

The studied region has an average landslide number density (LND) of 0.84 num/km^2. The area affected by landslides accounts for approximately 0.083%. Based on the search radius of 1 km, the raster resolution was set to 12.5 m, and the Kernel density method was used to plot LND (Figure 9A) and landslide area density(LAD, Figure 9B) maps of landslides. The highest LND

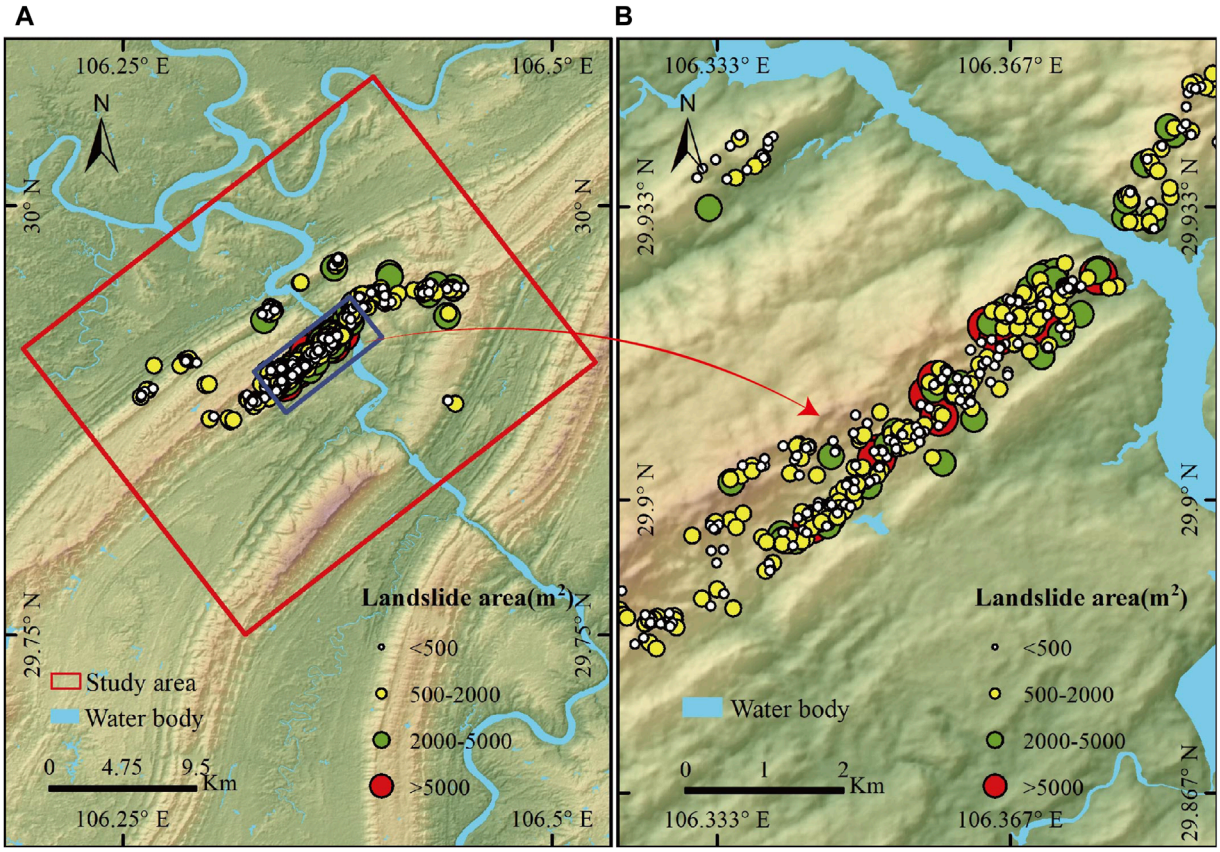

FIGURE 8
(A) Rainfall-induced landslide inventory, **(B)** zooming of the landslide abundance area.

value reaches up to 55.6 num/km^2. According to the distribution of LND, it is divided into six levels. Specifically, the LND of 40–60 num/km^2 covers about 2.5 km^2, which represents 0.43% of the total study area; the 20–40 num/km^2 group takes up an area of about 4 km^2, accounting for 0.67% of the total; the 10–20 num/km^2 group occupies 8.0 km^2, and its proportion is 1.4%; the region of 5–10 num/km^2 is around 10.2 km^2, with a ratio of 1.8%; the area and proportion of 2–5 num/km^2 are 12.6 km^{2}and 2.2%, respectively; the group with less than 2 num/km^2 hold an area of 545.6 km^2 which is 93.6% of all. Correspondingly, the analysis of LAD shows that its maximum is 6.4%. The area where LAD is less than 0.5% covers approximately 562.2 km^2, which accounts for 96.4% of the total study area; the area with LAD between 0.5% and 1% is about 9.0 km^2, representing 1.5% of all; the 1%–2% group takes up 4.8 km^2 in area and 0.82% in proportion; the 2%–4% covers an area of about 3.8 km^2 which is 0.65% of the study area; the area of 4%–6% in LAD is around 3.1 km^2, and its ratio is 0.54%; the region whose LAD is greater than 6% cover approximately 0.3 km^2, accounting for about 0.04%.

In this study, we focused on showcasing localized areas of high landslide density within the research zone, aiming to investigate the phenomenon of rainfall-triggered landslides. As depicted in Figure 10, we presented the topography at two different periods (Planet images from May and July 2017), with locations of landslides triggered by rainfall marked by red dashed lines. Comparing these two images, we observe significant color changes in the marked areas, primarily transitioning from vegetated regions to exposed soil. Upon further observation, unlike deep-seated landslides, rainfall-triggered shallow landslides exhibit elongated fluid-like forms. Additionally, shallow landslides tend to have relatively smaller areas, highlighting distinct differences compared to deep-seated landslides. These observations emphasize the varying impacts of different landslide trigger types on morphology, resulting in different landslide morphologies and distribution characteristics. This diversity serves as crucial evidence for landslide identification, aiding in a deeper understanding of landslide formation mechanisms and their significance in geological hazard management.

5 Discussion

The interplay of various geological structures and climatic backgrounds under different triggering events leads to diversification of landslide phenomena (Tatard et al., 2010). Furthermore, the ongoing warming of the Earth's climate system adds complexity and challenges to the understanding of landslide processes (Gariano and Guzzetti, 2016). In this context, establishing a landslide database is crucial for advancing landslide research. Santangelo et al. (2023) have created a database of landslides triggered by extreme rainfall events in the Marche-Umbria region

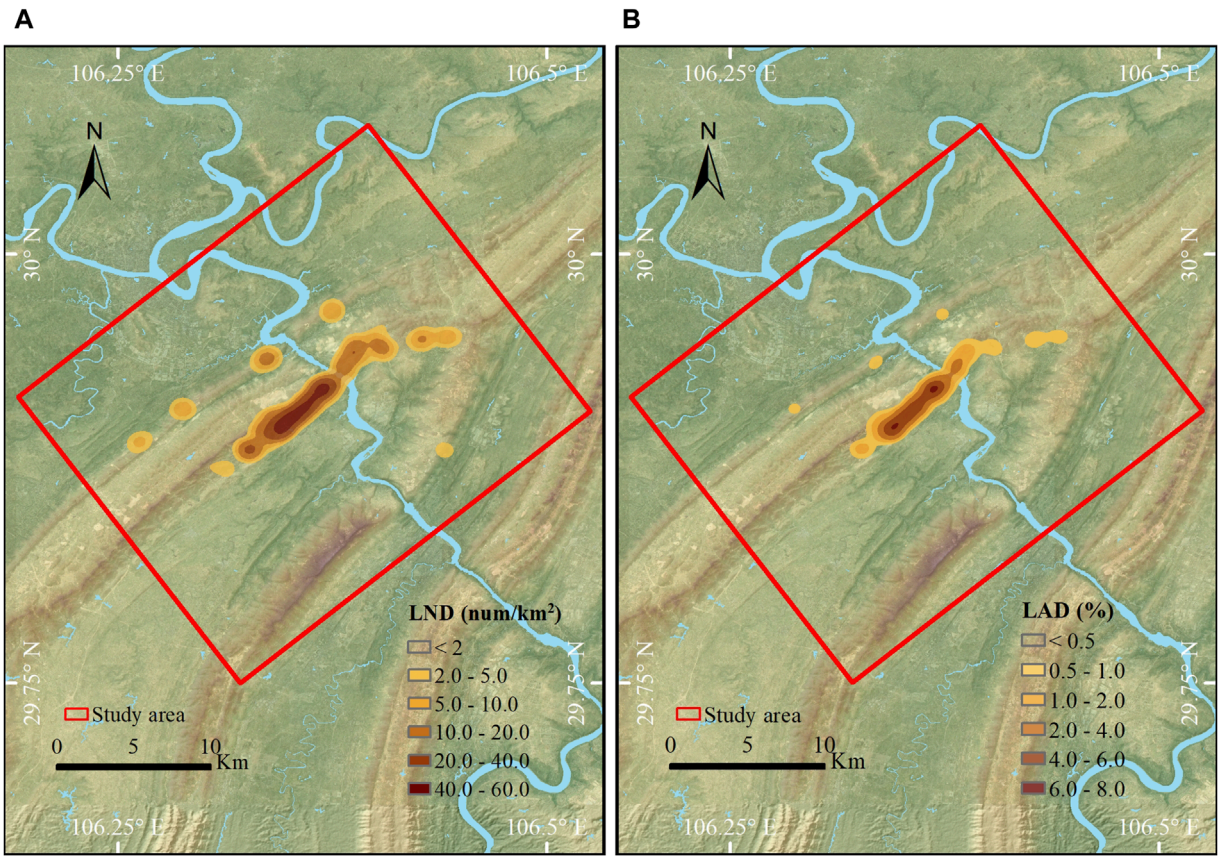

FIGURE 9
Spatial density of landslides triggered by this rainfall event. **(A)** Landslide number density (LND); **(B)** landslide areal density (LAD).

of Italy through field reconnaissance, which includes records of 1,687 landslide events. Martha et al. (2015) mapped a total of 3,472 landslides in the Bhagirathi and Alaknanda river valleys in India following an extreme rainfall event from June 15 to 17, 2013, using satellite remote sensing imagery. This study focuses on the parallel ridge-valley region in Chongqing, one of the world's three major fold mountain systems, which offers a new perspective for landslide research due to its unique geographical location, geological structure, and climatic environment. The rainfall patterns, geological activity, and topographical features of this region significantly differ from other study areas, most notably in the scale of landslides. The establishment of this database not only enhances our understanding of the characteristics of landslides in the parallel ridge-valley region in Chongqing, but also provides valuable data support and theoretical basis for global landslide research, especially in exploring the triggering mechanisms and evolutionary processes of landslides in fold mountain systems.

A preliminary statistical analysis of the rainfall-triggered landslide was conducted, and its spatial distribution characteristics were discussed. During this rainfall event, the maximum precipitation reached 226 mm, which was recorded in the Baohe (Wang Z. et al., 2019). The area with a high incidence of landslides is primarily situated on the right bank of the Jialing River, exhibiting a northeastward distribution trend, consistent with the orientation of the central mountain range in the study area (Figure 8). Despite the higher rainfall in the western region, the relatively gentle terrain resulted in fewer triggered landslides. In contrast, the eastern region, characterized by more rugged terrain, had fewer landslides triggered, possibly due to its greater distance from the rainfall center. The variation in landslide distribution may be influenced by multiple factors, though currently only preliminary speculation can be made. Future research will focus on analyzing the influencing factors of landslides to further elucidate their formation mechanisms.

By Figures 2, 8, landslides are mostly distributed in the Upper Triassic strata. This geological stratigraphy is largely made up of relatively hard quartz sandstone and interbedded shale with poor permeability and lower hardness. The presence of these weak interbeds makes them extremely vulnerable to deformation and failure under external stresses, resulting in slope instability. To further investigate the mechanisms behind rainfall-induced landslides, we selected the western mountainous region as a comparative area. This location is geographically near to the target area, with similar landscape undulations. The geological features of the western mountainous region reveal that the underlying strata are from the Lower Triassic, and are predominantly formed of limestone, marl and other rocks with comparable characteristics. In contrast, these rock layers are more uniform and less prone to significant deformation and damage, thus posing a relatively lower risk of slope instability. By comparing the lithology of these two areas, the distribution of landslides

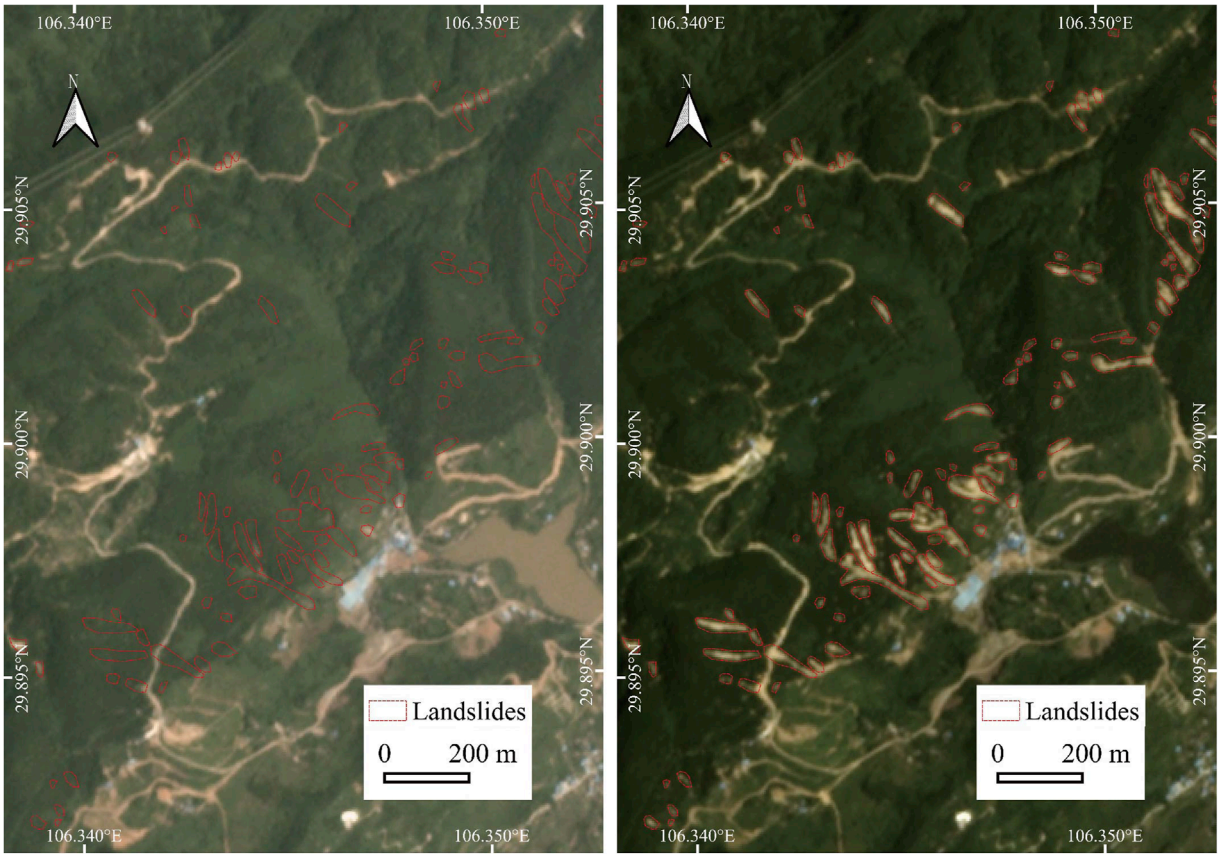

FIGURE 10
The high-density landslide area: **(A)** before rainfall event; **(B)** after rainfall event.

appears to be reasonable. This finding provides an important geological basis for further study of the formation mechanism of rainfall landslides.

In this study, we utilized the GPM IMERG Final Run daily product with a spatial resolution of 0.1°. Pan et al. (2023) assessed the applicability of GPM in the Chinese mainland. Their research revealed that satellite rainfall data exhibited increasing errors compared to national station data under moderate, heavy, and torrential rainfall conditions. Spatially, the GPM IMERG product performed well in the eastern and southern regions but relatively poorly in the western and northern regions. Temporally, the IMERG product could reasonably estimate the seasonal rainfall distribution in China, with the best performance in summer and the worst in winter. Despite the errors in estimating precipitation in the Chinese mainland, these data still hold significant value. The GPM IMERG precipitation product shows good performance in exploring the spatial distribution of three-day cumulative rainfall in Chongqing. However, for our specific area of interest, this spatial resolution is relatively coarse, leading to discrepancies between the rainfall amounts and those recorded by ground-based observation stations. It should be noted that we believe these differences do not hinder the analysis of spatial distribution characteristics and that of rainfall trends.

Satellite technology plays a crucial role in landslide research, among which Planet images, with its 3-meter resolution, provide high accuracy, offering strong support for landslide extraction. However, rainfall-triggered landslides often have small areas, making precise delineation of landslide boundaries a challenging task. Therefore, landslide interpretation personnel are required to have extensive experience. To validate the spatial accuracy of the established landslide database, a series of validation steps were conducted. Firstly, we used sub-meter-level resolution Google Earth images as a reference to carefully inspect the extracted landslide boundaries. The results showed that although there were some errors, they were still within an acceptable range. More importantly, these errors did not significantly affect subsequent analysis and research, ensuring the reliability and usability of the data obtained.

To obtain comprehensive information about the landslide event, we acquired Planet images from one month before and after the event, and introduced Google Earth satellite images on August 26 after the event as auxiliary evidence while considering the time resolution. Despite the at least one-month interval before and after images, we realize that rainfall landslides are usually triggered by extreme rainfall events (Peruccacci et al., 2012; de Oliveira et al., 2016; Zhang et al., 2022). Although the probability of such extreme events is low, it does not rule out the possibility of other rainfall

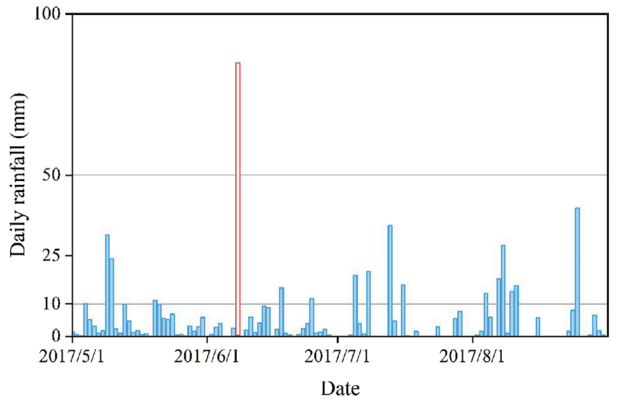

FIGURE 11
The Precipitation in the study area from May to August 2017.

events triggering landslides during this interval. To validate the accuracy of our landslide database, we further utilized the GPM IMERG Final Run daily product from May to August 2017 to investigate the rainfall conditions in the study area (Figure 11). The results show that from May to August, the maximum rainfall occurred on June 8th (approximately 85 mm/day), while the second-highest rainfall (approximately 39.8 mm/day) occurred on August 25th. The rest of the time mainly experienced light rain, with rainfall much lower than the maximum value. In this study, we used Google Earth images to assist in identifying buildings, farmland, and other features. Now, we applied Google Earth images to examine whether landslides were triggered between June 11th and August 25th (the date of the second-highest precipitation). The results indicate that no new landslides were triggered in this period.

Establishing a comprehensive and accurate database of rainfall-induced landslides is crucial for enhancing the precision of landslide risk assessment and optimizing management strategies. The high accuracy of this database not only deepens our understanding of the processes leading to landslides, but also provides critical data support for the establishment of effective early warning systems. A detailed and precise database of rainfall-induced landslides can be used to train more sophisticated landslide semantic segmentation models (Bragagnolo et al., 2021; Li et al., 2023), which play a vital role in disaster emergency response. These models can quickly identify potential landslide areas, issue timely warnings, and guide evacuations, thereby effectively reducing casualties and property damage. This has a long-term and profound impact on safeguarding people's lives and property, as well as the sustained development of the social economy.

In the realm of landslide research, the rainfall-triggered landslide threshold has always been a focal point. In earlier studies, Caine (1980) proposed an empirical formula correlating the intensity and duration of rainfall with the incidence of landslides and debris flows, based on an integrated analysis of literature available at that time. Subsequently, an increasing number of scholars have employed statistical methods to investigate rainfall-triggered landslide thresholds. For instance, Guzzetti et al. (2007) exerted rainfall landslide databases of the Central European Adriatic Danubian South-Eastern Space to establish the relationship between rainfall intensity and duration, inferring threshold curves using Bayesian statistical techniques. They further updated Caine's model by analyzing a database of 2,626 rainfall events worldwide that caused landslides and debris flows (Guzzetti et al., 2008). Rosi et al. (2015) updated 12 rainfall thresholds in Tuscany (Italy) using the MaCumBA software (Segoni et al., 2014). Galanti et al. (2018) derived rainfall thresholds for the Riviera Spezzina region in Italy using least-squares linear fit, quantile regression, and logistic regression, with logistic regression providing the most accurate thresholds. While these studies have made some progress in adjusting the parameters of empirical rainfall threshold formulas, there are still some limitations. Differing from the statistical methods mentioned, Ma et al. (2023b) initially conducted a physics-based spatiotemporal prediction and trigger mechanism analysis of rainfall-induced landslides for four short-duration rainfall events and long-duration intermittent rainfall that occurred from June 19 to 26 July 2013, in the Tianshui area of Gansu Province, China. Building on this, they employed a method based on the TRIGRS physical model, tailored to the specific geological and climatic conditions of the area, to delve into the trigger thresholds for rainfall-induced landslides (Ma et al., 2023c). Additionally, the team conducted an in-depth analysis of the causes of loess landslides triggered by this intense rainfall event (Shao et al., 2023b), which has deepened our understanding of rainfall-induced landslide thresholds. The physics-based modeling approach offers a new perspective for understanding the physical processes of landslides and complements statistical methods, jointly advancing in-depth research in the field. Meanwhile, the advancement of artificial intelligence algorithms has yielded more satisfactory results (Chiang et al., 2022; Distefano et al., 2022).

In exploring the mechanisms behind landslide occurrence, we focuses on the impact of moisture on soil physical properties in this study, particularly the effect of rainfall on soil saturation and shear strength. When rainfall reaches a certain level, the physical properties of the soil undergo significant changes (Moriwaki et al., 2004; Ahmadi-adli et al., 2017), which increases the likelihood of landslides. Based on these observations, the study posits a simplified linear relationship between rainfall volume and the occurrence of landslides. This linear model streamlines the geological processes, making the theoretical framework clearer and easier to operate and validate. At the same time, it provides a foundation for exploring more complex nonlinear relationships, aiding in the understanding of the fundamental conditions for landslide occurrence. The universality of the model makes it applicable across different geological and climatic conditions, facilitating its widespread use and meeting the need for rapid and effective prediction of landslide risk in disaster risk management. Based on the simplified linear model and considering the differences between local observation station data and global satellite precipitation data, it is speculated that the rainfall threshold for the area is much higher than the 39.8 mm/day recorded on August 25th. In fact, there is not a simple linear relationship between precipitation and landslide occurrence. Future research could make use of machine learning models to explore their more complex relationship, aiming to obtain more accurate rainfall thresholds and provide stronger support for landslide hazard assessments and rainfall-induced landslide warning systems.

6 Conclusion

Through preliminary analysis of a localized heavy storm event near the Huaying Mountain in the parallel ridge-valley area of western Chongqing on 8 June 2017, we established a landslide database triggered by this event using high-resolution satellite images. The study revealed that the rainfall event triggered 487 landslides, affecting an area of approximately 4,85,587 m^2, which accounts for 0.083% of the study area. The largest landslide covered an area of about 8,608 m^2, while the smallest was 76 m^2. The maximum volume of a landslide was approximately 35,574 m^3, while the minimum was 38 m^3. The average LND was 0.84 num/km^2, with the highest LND reaching around 55.6 num/km^2, predominantly distributed along the southern foothills of the Huaying Mountain. The maximum LAD was about 6.4%, highlighting the significant impact of extreme climate events on geological disasters. Future research should analyze the factors influencing landslides to reveal their mechanisms. Additionally, more accurate landslide early warning systems could be developed to effectively reduce the occurrence of landslide disasters, thereby ensuring the safety of people's lives and property.

Data availability statement

The raw data supporting the conclusions of this article will be made available by the authors, without undue reservation.

Author contributions

JL: Conceptualization, Investigation, Visualization, Writing–original draft. CX: Conceptualization, Funding acquisition, Resources, Writing–review and editing.

Funding

The author(s) declare that financial support was received for the research, authorship, and/or publication of this article. This study was supported by the National Institute of Natural Hazards, Ministry of Emergency Management of China (2023-JBKY-57) and the National Natural Science Foundation of China (42077259).

Acknowledgments

We would like to express my sincere gratitude to the anonymous reviewers for their professional advice and valuable feedback. Their review not only helped to make the content of this paper more accurate and rigorous but also provided important guidance for its quality improvement. I sincerely appreciate their time and effort devoted to the enhancement of this paper.

Conflict of interest

The authors declare that the research was conducted in the absence of any commercial or financial relationships that could be construed as a potential conflict of interest.

The author(s) declared that they were an editorial board member of Frontiers, at the time of submission. This had no impact on the peer review process and the final decision.

Publisher's note

References

Ahmadi-adli, M., Huvaj, N., and Toker, N. K. (2017). Rainfall-triggered landslides in an unsaturated soil: a laboratory flume study. *Environ. Earth Sci.* 76, 735. doi:10.1007/s12665-017-7049-z

Bragagnolo, L., Rezende, L. R., da Silva, R. V., and Grzybowski, J. M. V. (2021). Convolutional neural networks applied to semantic segmentation of landslide scars. *Catena (Amst)* 201, 105189. doi:10.1016/j.catena.2021.105189

Caine, N. (1980). The rainfall intensity-duration control of shallow landslides and debris flows. *Geogr. Ann.* 62, 23–27. doi:10.1080/04353676.1980.11879996

Calvello, M., and Piciullo, L. (2016). Assessing the performance of regional landslide early warning models: the EDuMaP method. *Nat. Hazards Earth Syst. Sci.* 16, 103–122. doi:10.5194/nhess-16-103-2016

CCTV (2017). Heavy rain strikes Hechuan,: residents trapped, firefighters rescue 149 overnight. Available at: https://tv.cctv.com/2017/06/10/VIDEN5pXhZI8v0DPriFkLLD3170610.shtml (Accessed March 28, 2024).

Chen, Z., Huang, Y., He, X., Shao, X., Li, L., Xu, C., et al. (2023). Landslides triggered by the 10 June 2022 Maerkang earthquake swarm, Sichuan, China: spatial distribution and tectonic significance. *Landslides* 20, 2155–2169. doi:10.1007/s10346-023-02080-0

Chiang, J.-L., Kuo, C.-M., and Fazeldehkordi, L. (2022). Using deep learning to formulate the landslide rainfall threshold of the potential large-scale landslide. *Water (Basel)* 14, 3320. doi:10.3390/w14203320

Ciurleo, M., Ferlisi, S., Foresta, V., Mandaglio, M. C., and Moraci, N. (2021). Landslide susceptibility analysis by applying TRIGRS to a reliable geotechnical slope model. *Geosci. (Basel)* 12, 18. doi:10.3390/geosciences12010018

Cui, Y., Yang, L., Xu, C., and Zheng, J. (2024). Spatial distribution of shallow landslides caused by Typhoon Lekima in 2019 in Zhejiang Province, China. *J. Mt. Sci.* 21, 1564–1580. doi:10.1007/s11629-023-8377-y

de Oliveira, N. S., Rotunno Filho, O. C., Marton, E., and Silva, C. (2016). Correlation between rainfall and landslides in Nova Friburgo, Rio de Janeiro—Brazil: a case study. *Environ. Earth Sci.* 75, 1358. doi:10.1007/s12665-016-6171-7

Distefano, P., Peres, D. J., Scandura, P., and Cancelliere, A. (2022). Brief communication: Introducing rainfall thresholds for landslide triggering based on artificial neural networks. *Nat. Hazards Earth Syst. Sci.* 22, 1151–1157. doi:10.5194/nhess-22-1151-2022

Franceschini, R., Rosi, A., Catani, F., and Casagli, N. (2022). Exploring a landslide inventory created by automated web data mining: the case of Italy. *Landslides* 19, 841–853. doi:10.1007/s10346-021-01799-y

Galanti, Y., Barsanti, M., Cevasco, A., D'Amato Avanzi, G., and Giannecchini, R. (2018). Comparison of statistical methods and multi-time validation for the determination of the shallow landslide rainfall thresholds. *Landslides* 15, 937–952. doi:10.1007/s10346-017-0919-3

Gao, H., Xu, C., Xie, C., Ma, J., and Xiao, Z. (2024). Landslides and debris flows triggered by the "July 2023" extreme rainstorm in the Haihe river basin, China. *Landslides*. doi:10.1007/s10346-024-02322-9

Gariano, S. L., and Guzzetti, F. (2016). Landslides in a changing climate. *Earth Sci. Rev.* 162, 227–252. doi:10.1016/j.earscirev.2016.08.011

Guo, Z., Chen, L., Yin, K., Shrestha, D. P., and Zhang, L. (2020). Quantitative risk assessment of slow-moving landslides from the viewpoint of decision-making: a case study of the Three Gorges Reservoir in China. *Eng. Geol.* 273, 105667. doi:10.1016/j.enggeo.2020.105667

Guzzetti, F., Ardizzone, F., Cardinali, M., Rossi, M., and Valigi, D. (2009). Landslide volumes and landslide mobilization rates in Umbria, central Italy. *Earth Planet Sci. Lett.* 279, 222–229. doi:10.1016/j.epsl.2009.01.005

Guzzetti, F., Peruccacci, S., Rossi, M., and Stark, C. P. (2007). Rainfall thresholds for the initiation of landslides in central and southern Europe. *Meteorology Atmos. Phys.* 98, 239–267. doi:10.1007/s00703-007-0262-7

Guzzetti, F., Peruccacci, S., Rossi, M., and Stark, C. P. (2008). The rainfall intensity–duration control of shallow landslides and debris flows: an update. *Landslides* 5, 3–17. doi:10.1007/s10346-007-0112-1

Handwerger, A. L., Fielding, E. J., Sangha, S. S., and Bekaert, D. P. S. (2022). Landslide sensitivity and response to precipitation changes in wet and dry climates. *Geophys Res. Lett.* 49, e2022GL099499. doi:10.1029/2022GL099499

He, X., Xu, C., Qi, W., Huang, Y., Cheng, J., Xu, X., et al. (2021). Landslides triggered by the 2020 Qiaojia Mw5. 1 earthquake, Yunnan, China: distribution, influence factors and tectonic significance. *J. Earth Sci.* 32, 1056–1068. doi:10.1007/s12583-021-1492-1

Huang, Y., Xu, C., Zhang, X., and Li, L. (2022). Bibliometric analysis of landslide research based on the WOS database. *Nat. Hazards Res.* 2, 49–61. doi:10.1016/j.nhres.2022.02.001

Huang, Y., Xu, C., Zhang, X., Li, L., and Xu, X. (2023). Research in the field of natural hazards based on Bibliometric analysis. *Nat. Hazards Rev.* 24, 04023012. doi:10.1061/NHREFO.NHENG-1739

Huang, Y., Xu, C., Zhang, X., Xue, C., and Wang, S. (2021). An updated database and spatial distribution of landslides triggered by the Milin, Tibet Mw6. 4 Earthquake of 18 November 2017. *J. Earth Sci.* 32, 1069–1078. doi:10.1007/s12583-021-1433-z

Huffman, G. J., Stocker, E. F., Bolvin, D. T., Nelkin, E. J., and Tan, J. (2023). *Final IMERG 1-Month precipitation estimate on global 0.1 x 0.1 degree grid stored in the GeoTIFF format V07*. doi:10.25966/3szv-p092

Kirschbaum, D., Kapnick, S. B., Stanley, T., and Pascale, S. (2020). Changes in extreme precipitation and landslides over high mountain Asia. *Geophys Res. Lett.* 47, e2019GL085347. doi:10.1029/2019GL085347

Lagomarsino, D., Segoni, S., Fanti, R., and Catani, F. (2013). Updating and tuning a regional-scale landslide early warning system. *Landslides* 10, 91–97. doi:10.1007/s10346-012-0376-y

Li, C., Long, J., Liu, Y., Li, Q., Liu, W., Feng, P., et al. (2021). Mechanism analysis and partition characteristics of a recent highway landslide in Southwest China based on a 3D multi-point deformation monitoring system. *Landslides* 18, 2895–2906. doi:10.1007/s10346-021-01698-2

Li, H., He, Y., Xu, Q., Deng, J., Li, W., Wei, Y., et al. (2023). Sematic segmentation of loess landslides with STAPLE mask and fully connected conditional random field. *Landslides* 20, 367–380. doi:10.1007/s10346-022-01983-8

Lin, W., Yin, K., Wang, N., Xu, Y., Guo, Z., and Li, Y. (2021). Landslide hazard assessment of rainfall-induced landslide based on the CF-SINMAP model: a case study from Wuling Mountain in Hunan Province, China. *Nat. Hazards* 106, 679–700. doi:10.1007/s11069-020-04483-x

Lin, X., and Wu, Q. (2017). Hechuan hit hard by June's worst rainfall: flooding, landslides, bridge damage. Available at: http://cq.weather.com.cn/gqtj/2720001.shtml (Accessed March 28, 2024).

Ma, S., Shao, X., and Xu, C. (2022). Characterizing the distribution pattern and a physically based susceptibility assessment of shallow landslides triggered by the 2019 heavy rainfall event in Longchuan County, Guangdong Province, China. *Remote Sens. (Basel)* 14, 4257. doi:10.3390/rs14174257

Ma, S., Shao, X., and Xu, C. (2023a). Landslides triggered by the 2016 heavy rainfall event in Sanming, Fujian Province: distribution pattern analysis and spatio-temporal susceptibility assessment. *Remote Sens. (Basel)* 15, 2738. doi:10.3390/rs15112738

Ma, S., Shao, X., Xu, C., and Xu, Y. (2023b). Insight from a physical-based model for the triggering mechanism of loess landslides induced by the 2013 Tianshui heavy rainfall event. *Water (Basel)* 15, 443. doi:10.3390/w15030443

Ma, S., Shao, X., and Xu, C. (2023c). Physically-based rainfall-induced landslide thresholds for the Tianshui area of Loess Plateau, China by TRIGRS model. *Catena (Amst)* 233, 107499. doi:10.1016/j.catena.2023.107499

Magrì, S., Solimano, M., Delogu, F., Del Giudice, T., Quagliati, M., Cicoria, M., et al. (2024). Modelling rainfall-induced landslides at a regional scale, a machine learning based approach. *Landslides* 21, 573–582. doi:10.1007/s10346-023-02173-w

Martha, T. R., Roy, P., Govindharaj, K. B., Kumar, K. V., Diwakar, P. G., and Dadhwal, V. K. (2015). Landslides triggered by the June 2013 extreme rainfall event in parts of Uttarakhand state, India. *Landslides* 12, 135–146. doi:10.1007/s10346-014-0540-7

Moriwaki, H., Inokuchi, T., Hattanji, T., Sassa, K., Ochiai, H., and Wang, G. (2004). Failure processes in a full-scale landslide experiment using a rainfall simulator. *Landslides* 1, 277–288. doi:10.1007/s10346-004-0034-0

Pan, X., Wu, H., Chen, S., Nanding, N., Huang, Z., Chen, W., et al. (2023). Evaluation and applicability analysis of GPM satellite precipitation over mainland China. *Remote Sens. (Basel)* 15, 2866. doi:10.3390/rs15112866

Patton, A. I., Rathburn, S. L., and Capps, D. M. (2019). Landslide response to climate change in permafrost regions. *Geomorphology* 340, 116–128. doi:10.1016/j.geomorph.2019.04.029

Peruccacci, S., Brunetti, M. T., Luciani, S., Vennari, C., and Guzzetti, F. (2012). Lithological and seasonal control on rainfall thresholds for the possible initiation of landslides in central Italy. *Geomorphology* 139–140, 79–90. doi:10.1016/j.geomorph.2011.10.005

Petley, D. (2012). Global patterns of loss of life from landslides. *Geology* 40, 927–930. doi:10.1130/G33217.1

Razavi-Termeh, S. V., Shirani, K., and Pasandi, M. (2021). Mapping of landslide susceptibility using the combination of neuro-fuzzy inference system (ANFIS), ant colony (ANFIS-ACOR), and differential evolution (ANFIS-DE) models. *Bull. Eng. Geol. Environ.* 80, 2045–2067. doi:10.1007/s10064-020-02048-7

Rosi, A., Lagomarsino, D., Rossi, G., Segoni, S., Battistini, A., and Casagli, N. (2015). Updating EWS rainfall thresholds for the triggering of landslides. *Nat. Hazards* 78, 297–308. doi:10.1007/s11069-015-1717-7

Santangelo, M., Althuwaynee, O., Alvioli, M., Ardizzone, F., Bianchi, C., Bornaetxea, T., et al. (2023). Inventory of landslides triggered by an extreme rainfall event in Marche-Umbria, Italy, on 15 September 2022. *Sci. Data* 10, 427. doi:10.1038/s41597-023-02336-3

Segoni, S., Rossi, G., Rosi, A., and Catani, F. (2014). Landslides triggered by rainfall: a semi-automated procedure to define consistent intensity–duration thresholds. *Comput. Geosci.* 63, 123–131. doi:10.1016/j.cageo.2013.10.009

Shao, X., Ma, S., and Xu, C. (2023a). Distribution and characteristics of shallow landslides triggered by the 2018 Mw 7.5 Palu earthquake, Indonesia. *Landslides* 20, 157–175. doi:10.1007/s10346-022-01972-x

Shao, X., Ma, S., Xu, C., Xie, C., Li, T., Huang, Y., et al. (2024). Landslides triggered by the 2022 Ms. 6.8 Luding strike-slip earthquake: an update. *Eng. Geol.* 335, 107536. doi:10.1016/j.enggeo.2024.107536

Shao, X., Ma, S., Xu, C., and Xu, Y. (2023b). Insight into the characteristics and triggers of loess landslides during the 2013 heavy rainfall event in the Tianshui area, China. *Remote Sens. (Basel)* 15, 4304. doi:10.3390/rs15174304

Sun, D., Wen, H., Wang, D., and Xu, J. (2020). A random forest model of landslide susceptibility mapping based on hyperparameter optimization using Bayes algorithm. *Geomorphology* 362, 107201. doi:10.1016/j.geomorph.2020.107201

Sun, J., Shao, X., Feng, L., Xu, C., Huang, Y., and Yang, W. (2024a). An essential update on the inventory of landslides triggered by the Jiuzhaigou Mw6.5 earthquake in China on 8 August 2017, with their spatial distribution analyses. *Heliyon* 10, e24787. doi:10.1016/j.heliyon.2024.e24787

Sun, J., Xu, C., Feng, L., Li, L., Zhang, X., and Yang, W. (2024b). The Yinshan Mountains record over 10,000 landslides. *Data (Basel)* 9, 31. doi:10.3390/data9020031

Tatard, L., Grasso, J. R., Helmstetter, A., and Garambois, S. (2010). Characterization and comparison of landslide triggering in different tectonic and climatic settings. *J. Geophys Res. Earth Surf.* 115, F04040. doi:10.1029/2009JF001624

Thapa, P. S., Daimaru, H., Ichion, E., and Yanai, S. (2024). Impacts of sediment transported downstream from the 2015 deep-seated landslide in Mt. Hakusan, Japan. *Earth Surf. Process Landf.* 49, 1273–1288. doi:10.1002/esp.5764

Thiery, Y., Terrier, M., Colas, B., Fressard, M., Maquaire, O., Grandjean, G., et al. (2020). Improvement of landslide hazard assessments for regulatory zoning in France: STATE–OF–THE-ART perspectives and considerations. *Int. J. Disaster Risk Reduct.* 47, 101562. doi:10.1016/j.ijdrr.2020.101562

Tianqi Network (2017). 2017 Chongqing rainstorm: Hechuan'precipitation broke the record, and 30 people were trapped. Available at: https://www.tianqi.com/news/189235.html (Accessed March 27, 2024).

Vranken, L., Van Turnhout, P., Van Den Eeckhaut, M., Vandekerckhove, L., and Poesen, J. (2013). Economic valuation of landslide damage in hilly regions: a case study from Flanders, Belgium. *Sci. Total Environ.* 447, 323–336. doi:10.1016/j.scitotenv.2013.01.025

Wang, H., Zhang, L., Yin, K., Luo, H., and Li, J. (2021). Landslide identification using machine learning. *Geosci. Front.* 12, 351–364. doi:10.1016/j.gsf.2020.02.012

Wang, L., Yin, Y., Zhang, Z., Huang, B., Wei, Y., Zhao, P., et al. (2019a). Stability analysis of the Xinlu Village landslide (Chongqing, China) and the influence of rainfall. *Landslides* 16, 1993–2004. doi:10.1007/s10346-019-01240-5

Wang, Z., Hu, C., Wu, S., and Mu, D. (2019b). Diagnostic analysis of a heavy rain process on June 8th in Chongqing. *Mid-low Latit. Mt. Meteorol.* 43, 8–16. (in Chinese). doi:10.3969/j.issn.1003-6598.2019.03.002

Wei, X., Zhang, L., Luo, J., and Liu, D. (2021). A hybrid framework integrating physical model and convolutional neural network for regional landslide susceptibility mapping. *Nat. Hazards* 109, 471–497. doi:10.1007/s11069-021-04844-0

World Bank, and United Nations (2010). *Natural hazards, unnatural disasters: the economics of effective prevention*. Washington, DC: The World Bank. doi:10.1596/978-0-8213-8050-5

Wu, R., Li, Z., Zhang, W., Hu, T., Xiao, S., Xiao, Y., et al. (2023). Stability analysis of rock slope under Sujiaba overpass in Chongqing City based on kinematic and numeric methods. *Front. Earth Sci. (Lausanne)* 11, 181949. doi:10.3389/feart.2023.1181949

Xie, C., Huang, Y., Li, L., Li, T., and Xu, C. (2023). Detailed inventory and spatial distribution analysis of rainfall-induced landslides in Jiexi County, Guangdong Province, China in August 2018. *Sustainability* 15, 13930. doi:10.3390/su151813930

Xu, C., Xu, X., and Shyu, J. B. H. (2015). Database and spatial distribution of landslides triggered by the Lushan, China Mw 6.6 earthquake of 20 April 2013. *Geomorphology* 248, 77–92. doi:10.1016/j.geomorph.2015.07.002

Yang, S., Wang, Y., Wang, P., Mu, J., Jiao, S., Zhao, X., et al. (2022). Automatic identification of landslides based on deep learning. *Appl. Sci.* 12, 8153. doi:10.3390/app12168153

Zhang, Q. X., Wu, Y. P., Ou, G. Z., Fan, X. G., and Zhou, J. H. (2014). Displacement prediction of Liangshuijing landslide based on time series additive model. *Comput. Model. and New Technol.* 18, 215–223. Available at: http://www.cmnt.lv/upload-files/ns_39art37_CMNT1803-16_Zhang.pdf.

Zhang, S., Jiang, Q., Wu, D., Xu, X., Tan, Y., and Shi, P. (2022). Improved method of defining rainfall intensity and duration thresholds for shallow landslides based on TRIGRS. *Water (Basel)* 14, 524. doi:10.3390/w14040524

Zhang, X., Chen, L., and Zhou, C. (2023). Deformation monitoring and trend analysis of reservoir bank landslides by combining time-series InSAR and Hurst Index. *Remote Sens. (Basel)* 15, 619. doi:10.3390/rs15030619

Zhang, Z. (2020). Mechanism of the 2019 Yahuokou landslide reactivation in Gansu, China and its causes. *Landslides* 17, 1429–1440. doi:10.1007/s10346-020-01384-9

frontiers | Frontiers in Earth Science

TYPE Original Research
PUBLISHED 29 August 2024
DOI 10.3389/feart.2024.1444882

OPEN ACCESS

EDITED BY
Lingling Shen,
Beijing Meteorological Information Center, China

REVIEWED BY
Chong Xu,
Ministry of Emergency Management, China
Huiran Gao,
Ministry of Emergency Management, China

*CORRESPONDENCE
Suhua Zhou,
zhousuhua@hnu.edu.cn
Jiuchang Zhang,
zhangjiuchang@foxmail.com

RECEIVED 06 June 2024
ACCEPTED 07 August 2024
PUBLISHED 29 August 2024

CITATION
Zhou S, Li J, Zhang J, Xu Z and Lu X (2024) Exploring Bayesian network model with noise filtering for rainfall-induced landslide susceptibility assessment in Fujian, China. *Front. Earth Sci.* 12:1444882. doi: 10.3389/feart.2024.1444882

Exploring Bayesian network model with noise filtering for rainfall-induced landslide susceptibility assessment in Fujian, China

Suhua Zhou[1,2,3]*, Jinfeng Li[1,2], Jiuchang Zhang[4]*, Zhiwen Xu[1,2] and Xianzhui Lu[5]

[1]College of Civil Engineering, Hunan University, Changsha, Hunan, China, [2]Key Laboratory of Building Safety and Energy Efficiency of Ministry of Education, Changsha, China, [3]Integrated Space-Air-Ground Structural Health Monitoring and Maintenance Center, Hunan University, Changsha, China, [4]Department of Information and Civil Engineering, Yunnan Minzu University, Kunming, Yunnan, China, [5]Key Laboratory for Geological Disaster Prevention and Control in Hilly and Mountainous Areas, Ministry of Land and Resources, Fuzhou, Fujian, China

Machine learning models have been increasingly popular in landslide susceptibility mapping based on the correlations among landslides and their inducing factors. However, mislabeled data in model training sets would deteriorate model accuracy. This study employed a Bayesian network to analyze influencing factors on landslides in Fujian Province, China, prone to typhoons and landslides. An inventory of 5,992 historical landslides informs Bayesian network modeling, with ten geoenvironmental factors as predictors. We introduced a progressive noise filtering method to mitigate the mislabeling effects of non-landslide points. The results show that altitude, wind speed, and lithology are the most important factors of landslides in the study area. The accuracy of the resultant landslide susceptibility map was verified using the area under the receiver operating characteristic curve (AUC) and Moran's I index. The AUC value was improved from 0.838 to 0.931 during the progressive noise filtering. The correlation between historical landslide number density (LND) and resultant landslide susceptibility index (LSI) was evaluated. The Local Indicators of Spatial Association based on Moran's I index shows consistent distribution patterns for high LND and high LSI regions. This study provides a useful reference for reliable landslide susceptibility mapping in the study area and similar areas.

KEYWORDS

landslide susceptibility mapping, GIS, tropical cyclone, Bayesian network model, noise filtering

1 Introduction

Landslides are natural geological phenomena characterized by the gravity-driven downhill movement of earth or rocky materials, with the potential to cause substantial damage to communities, infrastructure, and ecosystems. As per the United Nations, landslides are one of the most destructive and widespread natural hazards on a global scale (United Nations, 2019). Due to the global climate change, the occurrence of extreme weather events such as typhoons and extreme rainfall

has become increasingly frequent. It has notably heightened the potential for landslide incidents. This surge has resulted in a substantial upswing in the rates of mortality associated with landslides (Tian et al., 2020; Yang et al., 2020). In response to this challenge, landslide susceptibility mapping has been positioned as an indispensable instrument to identify landslide-prone areas and mitigate landslide hazards.

In recent years, machine learning techniques have gained increasing popularity in landslide susceptibility modelling (LSM) (Pradhan, 2013). Numerous machine learning (ML) algorithms, including random forest (RF) (Yuan and Chen, 2022), convolutional neural networks (CNN) (Youssef et al., 2022), Bayesian network (BN) (Mihaljevic et al., 2021; Huang, et al., 2022), etc., have been developed and applied in mapping landslide susceptibility. By depicting a collection of stochastic attributes and their conditional dependencies, BN is a probabilistic model widely used in solving problems related to complex systems. The notable features of BN lie in its incremental learning properties (Huang et al., 2022). While getting an acceptable performance, the trained model was applied to predict landslide susceptibility over the whole study area (Cengiz and Ercanoglu, 2022). However, in practical engineering, as new landslides occur in the study area, the landslide dataset undergoes continuous updates over time. Consequently, the training dataset should be adjusted accordingly to incorporate the new knowledge (Huang et al., 2022). Another distinctive characteristic of BN is found in their interpretability (Mihaljevic et al., 2021), as many ML techniques exhibited a black-box nature that was non-transparent to humans. In this regard, BN can furnish decision-makers with a prioritized list of input landslide controlling factors, along with potential interactions among these factors. Given the aforementioned, an increasing number of scholars are employing BN in LSM studies (Cui et al., 2022; Lan et al., 2021).

The establishment of sample sets and the selection of evaluation factors are critical for LSM (Singh et al., 2023). The construction of sample data for machine learning models is typically based on known landslide data (Chakrabortty et al., 2022). To extract more information from limited sample data, many researchers have focused on expanding landslide samples and selecting high-quality non-landslide samples (Sukristiyanti et al., 2020). Yang et al. (2023) have identified landslides from satellite maps to augment the landslide samples. Huang et al. (2022) incorporated the temporal attributes of landslide samples in LSM to analyze the characteristics of landslides over different periods. However, previous studies often randomly chose non-landslide samples from the study area, which can introduce mislabeled samples and uncertainties into the LSM (Abraham et al., 2023; Huang et al., 2020). The inclusion of mislabeled samples can indeed impact the performance of machine learning models, potentially resulting in suboptimal outcomes. In this study, noise is progressively filtered from subsequent training sets using a trained BN model as prior knowledge to identify and filter out mislabeled data.

The triggering effect of tropical cyclones (TCs) on landslides is manifested in the combined action of strong winds and heavy rainfall. On one hand, rainwater infiltration increases the gravitational force on the soil and reduces its shear strength; on the other hand, strong winds increase the instability of slopes by exerting an uplift force on the vegetation (Qi et al., 2023; Zhuang et al., 2022). Therefore, when modeling landslide susceptibility in coastal areas and other regions prone to typhoons, considering only the impact of rainfall on landslide triggering is insufficient. Although some researchers have analyzed landslide characteristics under individual typical typhoon events, they have not proposed a general quantitative assessment method for typhoon impacts to be integrated into LSM (Wu, 2019; Cui et al., 2022).

This study aims to construct a noise filtering method based on a Bayesian Network model to mitigate the mislabeling effects of non-landslide points. Ten geoenvironmental predictors are selected to form the LSM. Additionally, considering the study area is a typhoon-prone region, we used the Rankine vortex model to quantify and assess the impact of historical tropical cyclones and the extreme rainfall.

2 Study area and data sources

2.1 Study area

Fujian Province (115°50′-120°40′E, 23°33′-28°20′N) is situated in the southeast of China (Figure 1). It covers an area of 121,400 km^2 with over 90% of it characterized by hills and mountains with an altitude ranging from −51 m to 2,148 m. Shaped by the new Huaxia structure, the elevational trend ascends towards the northwest and descends towards the southeast (Lin et al., 2021). The geological foundation of Fujian Province is typified by dynamism, with high-angle faults and jointed structures. In the study area, magmatic rocks consist of intrusive rocks alongside Jurassic and Cretaceous volcanic formations. Igneous rocks form a significant component of the lithology, occupying a substantial portion of the province's land area. Metamorphic rocks primarily characterize the northwestern region, while sedimentary rocks constitute a smaller fraction of the landscape, concentrated mainly in the southwest.

Fujian Province is located near the Tropic of Cancer. The prevailing climatic pattern corresponds to a warm and humid subtropical monsoon climate. The region experiences higher levels of precipitation. Facing the Pacific Ocean on the east, Fujian Province is vulnerable to maritime tropical cyclones in the Pacific Ocean. Rainfall distribution displays notable heterogeneity across the region (Ma et al., 2023; Ye et al., 2022). For instance, the coastal plains and mountainous zones of Fujian Province typically encounter an annual average rainfall within the range of 900 mm–1,100 mm. In contrast, the hilly mountain areas experience heightened precipitation levels, with figures approximating 1,500 mm–1,700 mm.

A combination of factors, including heavy rainfall, typhoons, steep terrain, fractured rock, soil formations, and human engineering activities, collectively contribute to geotechnical hazards in the region. Generally, the geohazard profile of Fujian Province is characterized by its widespread occurrence, frequent events, and sudden emergence.

2.2 Data sources

The dataset employed for this study, as outlined in Table 1, encompasses a comprehensive array of variables encompassing the landslide inventory, a spectrum of contributing factors, tropical cyclone data, and the counts of landslides and associated rainfall.

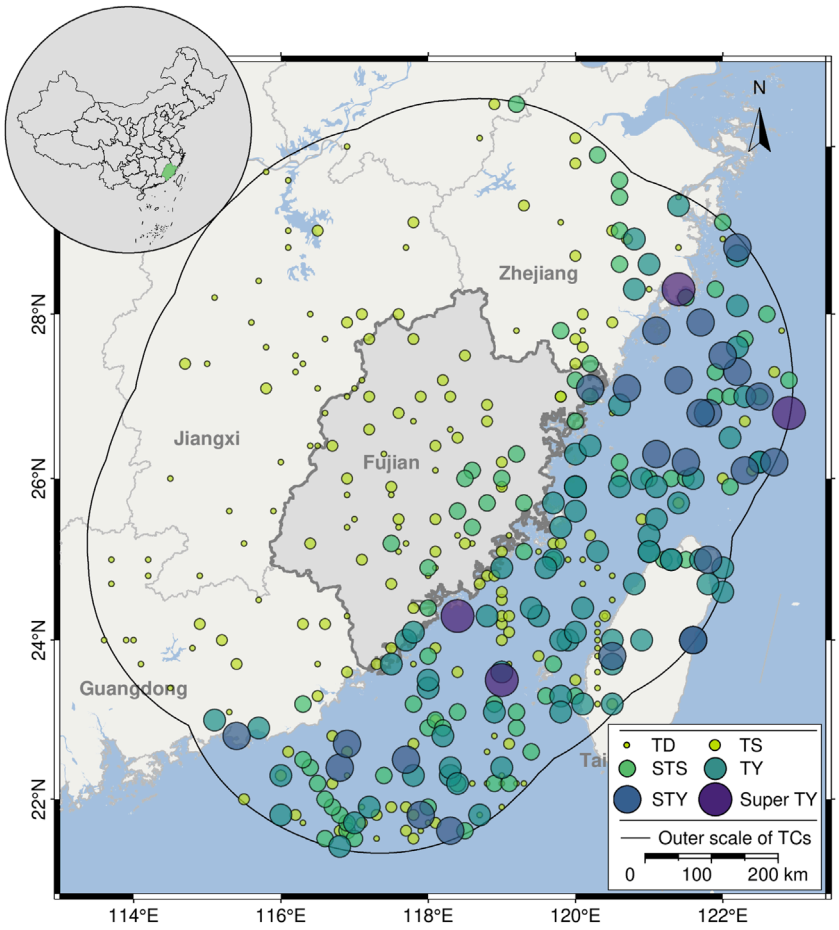

FIGURE 1
Location of the study area and paths of TCs.

The landslide inventory encapsulates historical records detailing 5,992 instances of landslides that have transpired within Fujian Province. A subset of the Digital Elevation Model (DEM), integral to the analysis of landslide susceptibility, was derived via DEM with a spatial resolution of 30 m through ArcGIS 10.6 software. Concurrently, the tropical cyclone dataset encompasses a wealth of information about the geographical location, intensity level, and wind speed of tropical cyclones within the northwest Pacific Ocean. The dataset is sourced primarily from government disaster reports and authoritative websites maintained by scientific institutions.

2.3 Inventory of TCs in the period of 2007–2020

Mature TCs often generate spiral rainbands, which can result in local winds, heavy rainfall, and storm surges (Tang et al., 2018). These convective phenomena can trigger various disasters such as landslides, floods, and urban waterlogging, particularly before and after TC landfall. Situated in the coastal region of southeastern China, the study area is highly susceptible to geological disasters influenced by precipitation patterns. Although annual rainfall offers a general overview of precipitation levels over the year, it may need to accurately reflect the impact of short-term heavy rainfall events associated with TCs. Hence, it is essential to consider TCs when assessing the influence of slope failures.

TCs and their consequent rainfall wield a substantial influence in instigating landslides within Fujian Province (Xiao et al., 2011). The national standard "Grade of tropical cyclones" (GB/T 19201–2006) classifies tropical cyclones into six categories based on wind speed, as shown in Table 2. This study used all TCs from 2007 to 2020, which are within a 250 km buffer from Fujian Province recorded. The 250 km buffer was created as it averages the outer scale of the TCs we used (Qi et al., 2023). Within this buffer zone, TCs were primarily characterized as TY and STY. Over the interval spanning from 2007 to 2020, Fujian Province experienced the landfall of 67 TCs, including 19 instances of TYs and 13 cases of STYs (Lu et al., 2021; Ying et al., 2014). Typically, TCs undergo rapid weakening and gradual dissipation following landfall. As depicted in Figure 1, the intensity of TCs decreases swiftly from TY and STY strength over the sea to TS and TD strength upon landfall. This transition, known as the "after-landfall phase," would extend for several days following landfall. Though the intensity of TCs decreases during this period, heavy rainfall persists, leading to increased runoff and exacerbating landslide risks. As TCs continue to dissipate, the probability of

TABLE 1 Data sources.

Factors	Indicators	Data sources
Topographic and Geomorphic	DEM	Source and Environment Science and Data Center https://www.resdc.cn/
	Slope	Extract from DEM
Land cover	Land-use	Source and Environment Science and Data Center https://www.resdc.cn/
	Vegetation	Source and Environment Science and Data Center https://www.resdc.cn/
	NDVI	Source and Environment Science and Data Center https://www.resdc.cn/
Geological	Earthquake intensity	Source and Environment Science and Data Center https://www.resdc.cn/
	Lithology	National Earth System Science Data Center http://www.geodata.cn/
Human engineering activities	Road density	Source and Environment Science and Data Center https://www.resdc.cn/
Climatic environment	Rainfall	National Earth System Science Data Center http://www.geodata.cn/
	Wind speed	Typhoon online https://www.typhoon.org.cn/
Landslide inventory		Source and Environment Science and Data Center https://www.resdc.cn/
Tropical cyclones		Typhoon online https://www.typhoon.org.cn/
Number of landslides during 2007–2021		Department of Natural Resources of Fujian Province https://zrzyt.fujian.gov.cn/
Rainfall during 2007–2021		Copernicus Climate Change Service (C3S) https://climate.copernicus.eu/

TABLE 2 Tropical cyclone classification table.

Grade of tropical cyclones	Maximum average wind speed near the bottom center (m/s)
Tropical depression (TD)	10.8 ~ 17.1
Tropical storm (TS)	17.2 ~ 24.4
Severe tropical storm (STS)	24.5 ~ 32.6
Typhoon (TY)	32.7 ~ 41.4
Severe typhoon (STY)	41.5 ~ 50.9
Super typhoon (Super TY)	≥51.0

new landslides occurring may decrease, enabling affected areas to commence recovery from the initial impacts.

2.4 Distribution pattern of landslides

2.4.1 Spatial distribution pattern

A total of 5,992 landslides across Fujian Province were detailed and documented. The distribution pattern of landslides in the region shows an apparent spatial characteristic. Most landslides concentrate in the hilly terrains of the central and western areas, extending northeastward through the region. Conversely, landslides occur less frequently in the relatively flat terrain of the southeastern coastal areas. In this study, we employed landslide number density (LND) as a metric to quantify the level of aggregation, providing deeper insights into the spatial distribution of landslide activity. As depicted in Figure 2, landslides in Fujian Province cluster near the mountain belts in central and western Fujian. Significant clustering was observed in cities such as Quanzhou and Sanming, which experienced an accumulation of over 1,000 geological incidents during the specified period. In contrast, southeastern coastal municipalities like Xiamen and Zhangzhou were relatively less affected, recording fewer than 500 geological events within the same timeframe.

The impact of the physical geography on landslides can be categorized into internal and external triggering factors. External triggers such as typhoons and prolonged heavy rainfall are the primary causes of slope failures. Internal factors such as steep slopes and loose soils create a conducive environment for landslide occurrences. These unfavorable conditions are especially pronounced in the hilly areas of the western and central regions.

2.4.2 Temporal distribution characteristics

Since the landslide inventory lacks temporal attributes, this study supplemented by collecting a historical landslide dataset from the Department of Natural Resources of Fujian Province spanning from 2007 to 2021. This additional dataset enabled us to examine the relationship between the frequency of landslides and the prevailing conditions over time.

As depicted in Figure 3C, a consistent correlation is observed between the frequency of landslides and the magnitude of rainfall across varying temporal scales, encompassing monthly and yearly

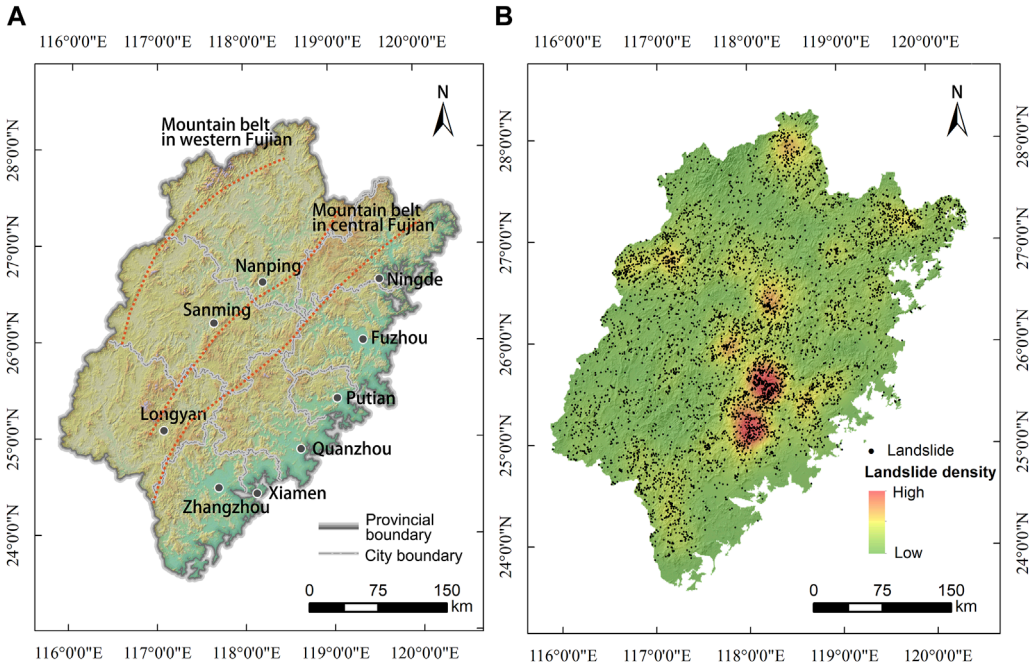

FIGURE 2
(A) Terrian of Fujian province; **(B)** Spatial distribution of landslides and landslide number density.

periods (Figures 3A, B). Monthly data reveals noticeable seasonal variations in both precipitation and landslide occurrences. The incidence of landslides increased during the rainy season from May to August. Over 70% of landslides throughout the entire year occurred during this period. Moreover, monthly average precipitation exceeding 200 mm correlates with a monthly landslide count surpassing 30 instances on average. The incidence of extreme rainfall tends to precipitate a surge in landslide occurrences. Annual data analysis underscores a pronounced positive correlation between rainfall and landslide frequencies. In most instances, peak rainfall coincides closely with the highest landslide events throughout the year. By tracing back to periods with abnormally high numbers of landslides, such as June 2010, May 2015, and July 2016, we found that the study area was indeed affected by typhoons or heavy rainfall during these periods (Figure 3B).

2.5 Thematic layers of landslide-inducing factors

It is crucial to comprehensively consider various inducing factors to achieve an accurate LSA. Therefore, the selection of a wide range of inducing factors is essential. These factors should encompass all relevant environmental variables that may influence landslide occurrence. In this study, we identified ten inducing factors of landslides based on both the natural geographical environment and human engineering activities (Figure 4). These factors were classified into 5 clusters: topography (altitude and slope), land cover (vegetation, NDVI, and land-use), geological (lithology and earthquake intensity), human engineering activities (road density), and climate environment (rainfall and wind speed). Differences in environmental attributes can lead to landslides with different degrees of aggregation, and selecting the inducing factors as comprehensively as possible is a prerequisite for an accurate LSA.

3 Materials and methods

3.1 Modelling of the wind fields

Wind speed is the foundational metric for assessing the intensity of a TC. It encapsulates the broader repercussions of a TC and its associated secondary calamities. Aiming to explore the complexities of TC influence on landslide susceptibility within Fujian Province, we compiled the wind speed of the TCs into an inducing factor and incorporated it into the LSA framework. In this study, the classical Rankine vortex model was used to compute the wind fields of the TCs within the study area. The formula employed to calculate the wind speed is presented in Equation 1:

$$v = \begin{cases} v_m \frac{r}{r_m}, 0 \le r \le r_m \\ \frac{v_m}{r}, r_m \le r \le \infty \end{cases} \quad (1)$$

In the equation, v_m is the maximum wind speed of a TC, r_m is the radial distance from a TC center which is the distance from a TC center to the place of maximum wind speed, and r is the distance to a TC center. The Rankine vortex model conceptualizes a TC as a solid rotating entity, where the allocation of tangential wind speed is governed by two primary parameters: the maximum wind speed and the radial distance from the TC center. At the center of the TC, the tangential wind speed begins at a value of 0 m per

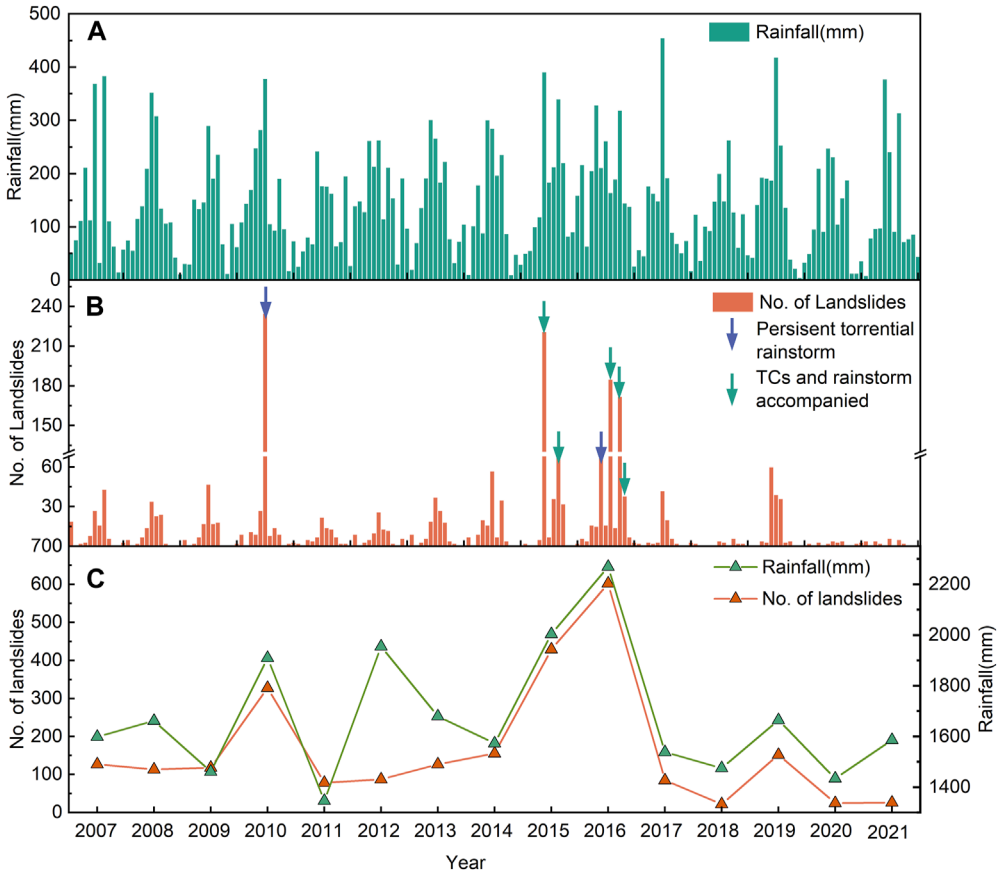

FIGURE 3
The temporal distribution of landslides in Fujian Province **(A)** Monthly rainfall during 2007~2021; **(B)** Monthly landslides; **(C)** Annual rainfall and landslides.

second and linearly increases until it reaches the maximum wind speed at the radius of maximum wind speed. Beyond this radius, the wind speed decreases inversely as the distance from the center increases. Valuable insights from Wu and Lei (2012) provided a compilation of statistics regarding the average maximum wind speed radius of TCs.

The computation of the wind field of TCs within Fujian Province was conducted using ArcGIS 10.7 software. The systematic process was as follows (Figure 5): 1) Selection of Path Collection Points: In the initial phase, path collection points were identified for each TC located within a 250 km radius of Fujian Province. 2) Application of the Classical Rankine Vortex Model: The wind field emanating from each path collection point associated with a specific TC was computed using the classical Rankine Vortex model. 3) Identification of maximum wind field: Within the context of each TC, the maximum wind field magnitude was determined from the array of wind fields generated by the various collection points. This pivotal value represented the characteristic wind field of the respective cyclone. 4) Calculation of Average Wind Speed: The mean value of the maximum wind speed was calculated across all TCs within the study area. This value served as an indicative measure of the mean wind speed. This systematic approach not only facilitated the determination of wind field distribution but also allowed for the quantification of cumulative influences resulting from multiple TCs.

Figure 6 illustrates the wind speed factor derived from the TCs. Wind speed gradually decreases from the southeastern coastal areas of Fujian Province to the northwestern regions. The rapid deterioration and dissipation of the TCs are attributed to several factors, including the gradual depletion of energy sourced from the ocean, an elevation in surface roughness, and alterations in circulation pattern (Ito et al., 2020; Houze, 2010). These factors contribute to the diminished wind speed experienced by TCs as they move away from the coast. In Fujian province, the typhoon is uplifted by the terrain of the inland mountainous areas, so that a typhoon rainstorm center is formed in the east of the mountain belts in central Fujian, which often leads to landslides, debris flows, collapses and other disasters.

3.2 Bayesian network model

A BN model integrates Bayesian theory and graph theory. The inference is based on *a priori* knowledge and objective evidence and belongs to classification models. Its framework comprises two essential elements: the network structure and network parameters, as represented by the equation: $BN = \langle G, \theta \rangle$ (Nie et al., 2019; Song et al., 2012). The network structure, symbolized as G, adopts the form of a Directed Acyclic Graph (DAG), offering a qualitative

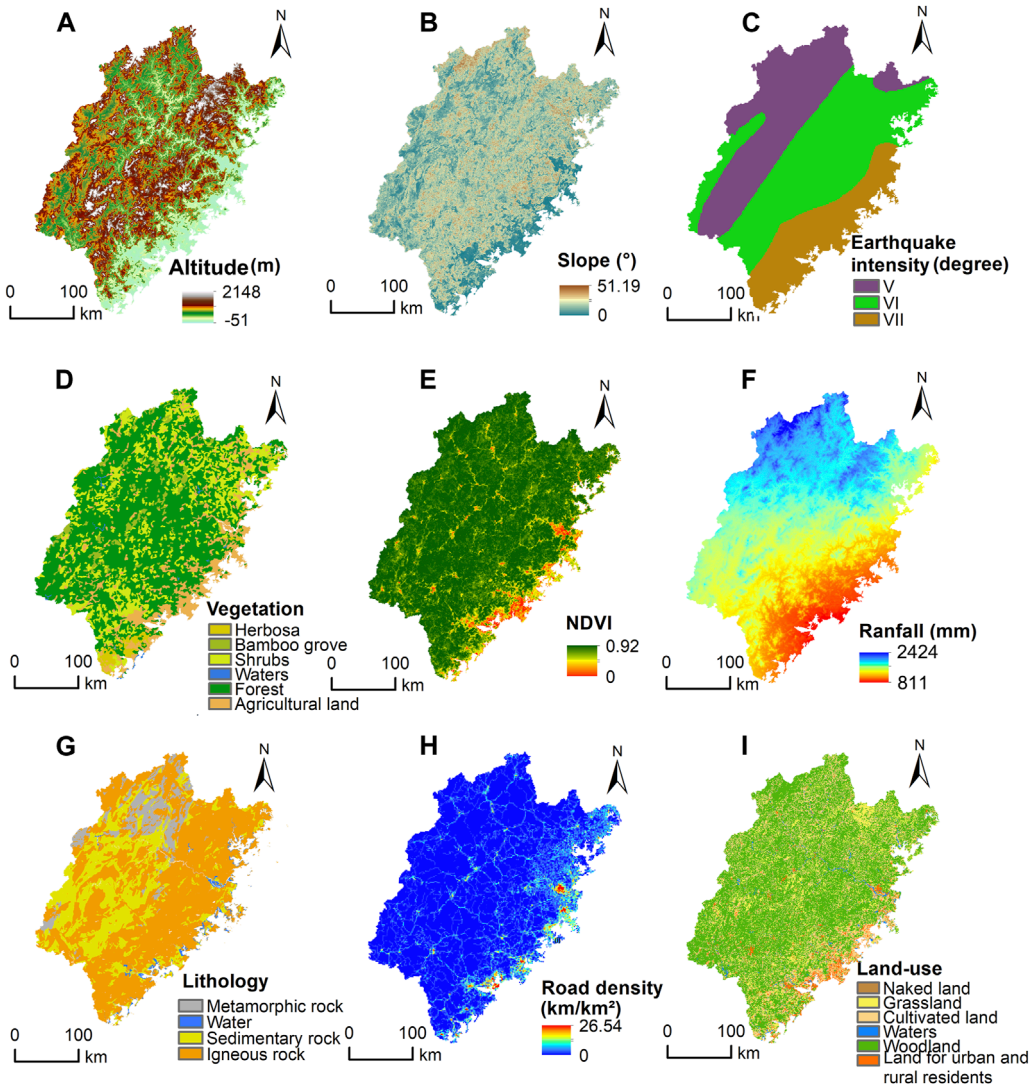

FIGURE 4
Inducing factors map of landslides in Fujian Province: **(A)** Lithology; **(B)** Earthquake intensity; **(C)** Land-use; **(D)** Vegetation; **(E)** NDVI; **(F)** Road density; **(G)** Altitude; **(H)** Rainfall; **(I)** Slope.

examination of the inherent topological relationships among network components. Concurrently, the network parameters encompass the Conditional Probability Table (CPT), quantitatively depicting the joint distribution probability. The joint probability distribution is obtained by multiplying the probability distributions associated with each variable, as expressed in Equation 2:

$$P(X_1, X_2, \ldots, X_n) = \prod_{i=1}^{n} P(X_i | \pi(X_i)) \quad (2)$$

3.2.1 Structure learning

This study determines the structure and parameters of a BN and conducts inference by learning from the available data. The Hill Climbing (HC) search strategy, coupled with the Bayesian Information Criterion (BIC) scoring function, was employed to learn the network relationships among the inducing factors in the process of LSA. The HC algorithm emerges as a strategic choice within structural learning algorithms, particularly when dealing with extensive datasets. Its effectiveness is particularly salient in circumventing the challenges associated with local optima, a common issue encountered by conventional greedy algorithms during structural optimization. It effectively avoids being ensnared in local optima by prioritizing an optimization approach grounded in singular solutions. Simultaneously, the BIC scoring technique is a robust tool for identifying the network structure yielding the most favorable score. Incorporating a complexity penalty term within the BIC framework mitigates overfitting, thereby ensuring that the network structure retains its capacity for generalization. The visual representation of the network structure derived from the structural learning process is depicted in Figure 4.

3.2.2 Parameter learning

Within the context of independent identical distribution, parameter learning commonly employs two principal

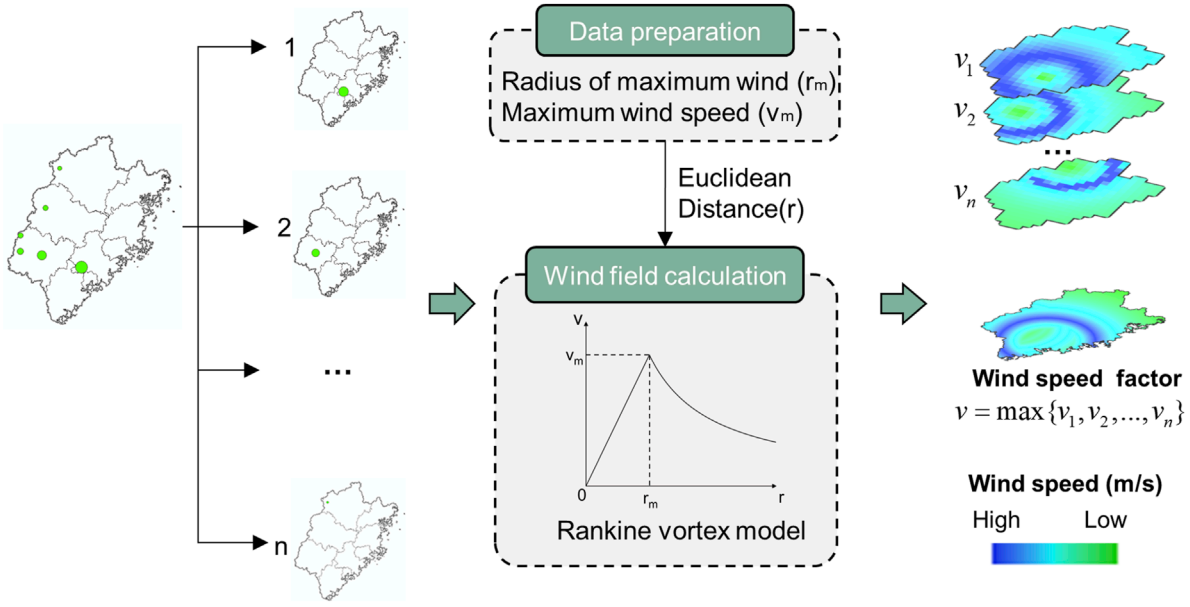

FIGURE 5
Illustration of wind field calculation for a TC in the study area (The illustration shows a TC named bilis that made landfall from Fujian in 2000).

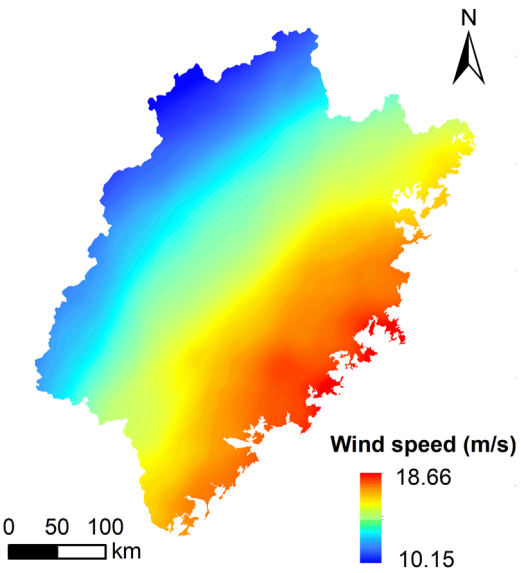

FIGURE 6
Wind speed factor calculated from TCs.

methodologies: Maximum Likelihood Estimation (MLE) and Bayesian Estimation (BE). BE, in particular, stands out as it utilizes prior parameter distribution and selection principles, effectively mitigating the overfitting risks inherent in MLE. The integration of hyperparameters refines BE, rendering it robust and stable even when handling small-sample data.

3.2.3 Inference

Bayesian inference relies on the interaction of the network structure and the Conditional Probability Table (CPT). Within this context, the Variable Elimination (VE) algorithm is a preferred choice, simplifying the calculation process by decomposing the joint distribution. VE's key characteristics of simplicity and generality align well with its exact inference. Moreover, the versatility of VE allows it to handle complex network scenarios effectively. Expanding upon VE's framework, a suite of algorithms, such as the bucket elimination algorithm, further enhances the inference ability by accommodating various optimal elimination orders.

3.3 Noise filtering

We conducted a noise filtering method to filter out mislabeled data and enhance the quality of the model-training dataset. Detailed steps of the noise filtering process are as follows (Figure 7): 1) Dataset partitioning: The dataset was randomly divided into equal subsets, with one segment earmarked for testing and the remaining segments designated for training; 2) Initial training set selection: Initially, one subset was chosen to train a BN model and predict the subsequent subset.; 3) Noise filtering: If the difference between the predicted value and the actual value for an instance within the subset exceeded the predefined threshold "t," the instance would be removed. Conversely, the instance would be included in the training set if the difference fell within the threshold. The threshold value "t" is calculated using the equation: $|LS - Pre| \leq t$, where LS is the actual value; and Pre is the predicted value of an instance. This process was iteratively repeated, progressively introducing clean data samples from each subset into the training data. To update the entire dataset, the study conducted nine rounds of noise filtering, each involving

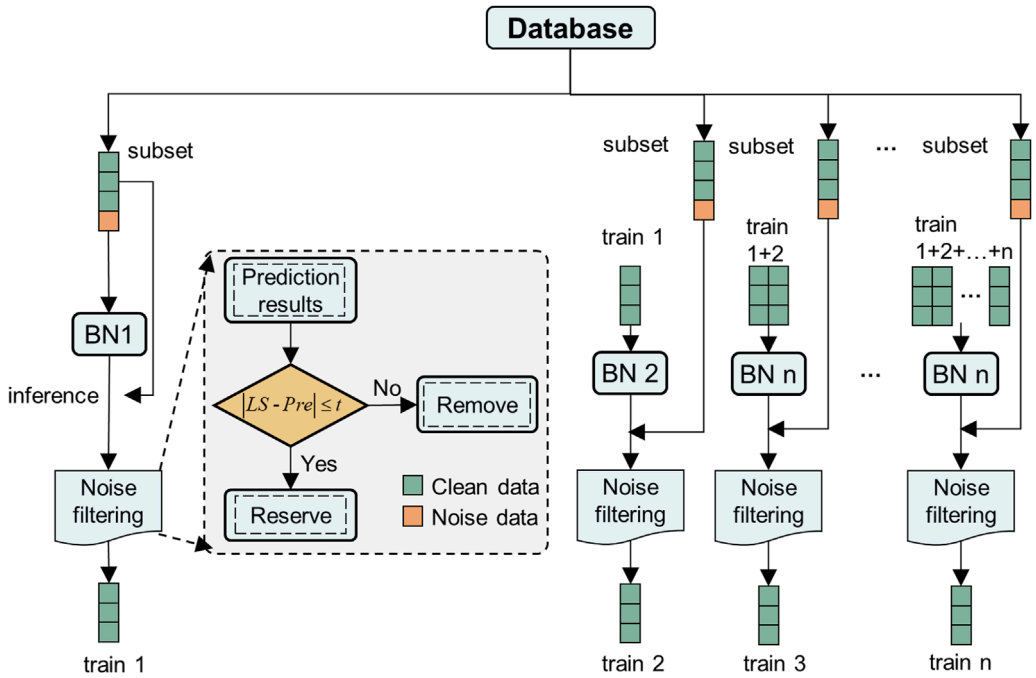

FIGURE 7
Illustration of the noise filtering process.

a thorough evaluation of prediction outcomes. The accuracy of the samples was assessed using the test set after each round of noise filtering.

3.4 Moran's I index

This study utilized Moran's I to investigate the spatial relationship between landslide density and susceptibility. Moran's I is a widely employed metric for assessing spatial autocorrelation, encompassing global and local Moran's I. The computation of global Moran's I yields results within the range of [−1, 1], where a value greater than zero indicates a positive spatial autocorrelation. There is a clustering phenomenon across the entire spatial domain. The magnitude of the index indicates the degree of clustering, with larger values indicating more pronounced clustering. Conversely, a value less than zero suggests a spatial negative correlation, indicating a dispersion pattern in the spatial distribution of the study object. A zero value denotes no spatial autocorrelation or an absence of spatial correlation. The equation of Moran's I is as Equation 3:

$$I = \frac{n\sum_{i=1}^{n}\sum_{j=1}^{n}\left(Y_i-\overline{Y}\right)\left(Y_j-\overline{Y}\right)}{\sum_{i=1}^{n}\sum_{j=1}^{n}w_{ij}\left(Y_i-\overline{Y}\right)^2} \quad (3)$$

In the equation, n represents the total number of samples, w_{ij} denotes the distance weight between i and j, Y_i and Y_j represent the variable values for the i th and jth samples respectively, $\overline{Y}$ representing the mean value across all samples.

Compared to global Moran's I, local Moran's I emphasize assessing local spatial clustering patterns. While global Moran's I indicates overall spatial clustering, it lacks specificity in identifying the regions where clustering phenomena occur. Additionally, even if global Moran's I indicates no overall spatial autocorrelation, local spatial clustering may still manifest in specific areas. The equation of local Moran's I is as Equation 4:

$$I = \frac{Y_i-\overline{Y}}{L^2}\sum_{j\neq i}^{n}w_{ij}\left(Y_j-\overline{Y}\right) \quad (4)$$

In the equation, $L^2 = \frac{1}{n}\sum\left(Y_i-\overline{Y}\right)^2$.

4 Results

4.1 Correlations between landslides and influencing factors

To better analyze the relationships between landslides and inducing factors, the frequency density of landslides and landscape (non-landslide) areas was compared, as shown in Figure 5. A slope is more likely to fail where the frequency density of landslides is higher than the landscape. Regions with a history of frequent landslides are more susceptible to future landslides due to persistent geological and environmental conditions that favor such occurrences.

4.1.1 Topographic and geomorphic factors

Topography, particularly micro-topography, significantly contributes to landslide occurrences within Fujian Province, particularly regarding slope angle and height. Most landslides tend to occur on convex slopes. This study selected altitude and slope as topographic and geomorphic factors. For the analysis

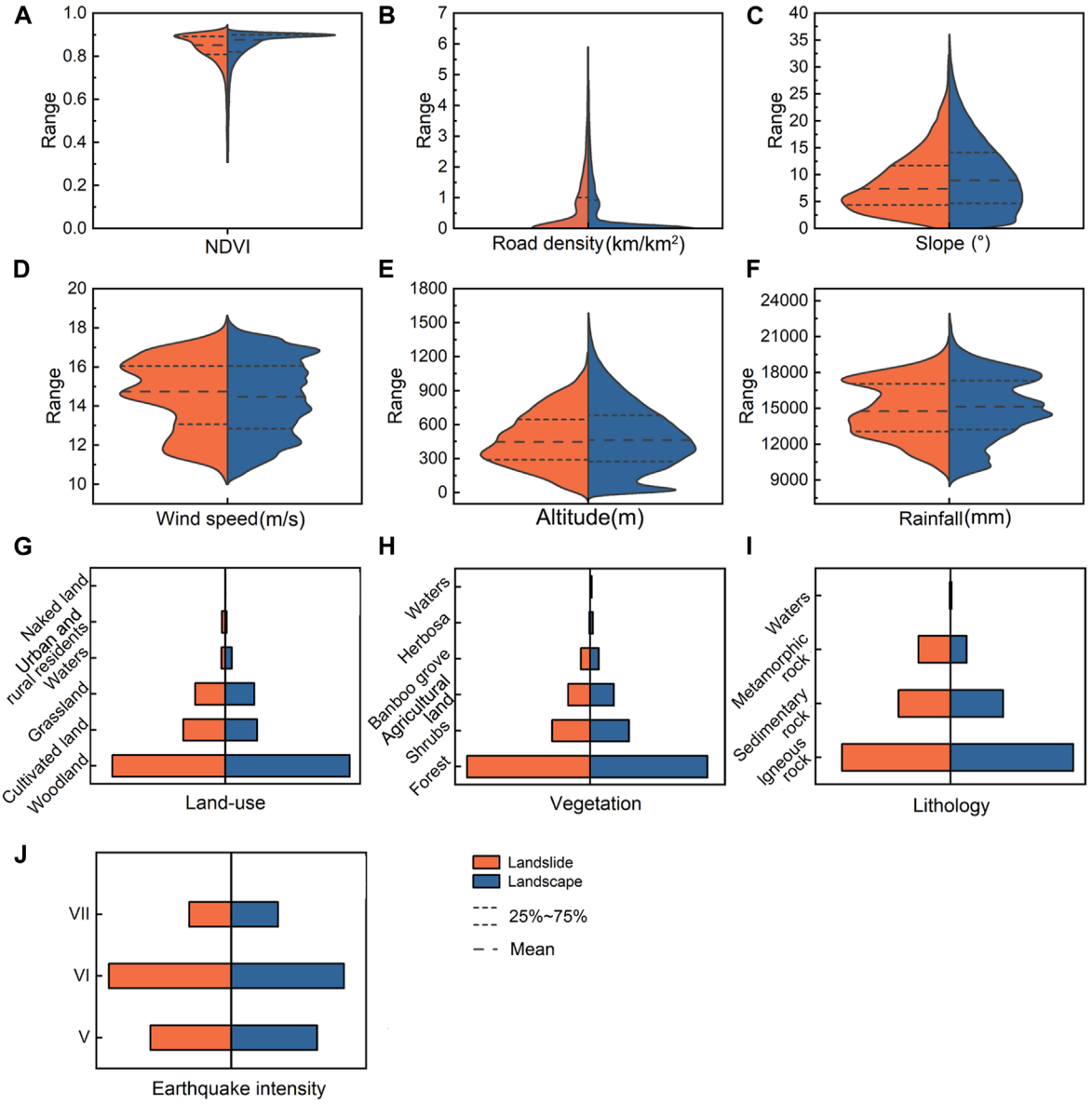

FIGURE 8
Landslide frequency density estimates of the influencing factors; **(A)** NDVI; **(B)** Road density; **(C)** Slope; **(D)** Wind speed; **(E)** Altitude; **(F)** Rainfall; **(G)** Land-use; **(H)** Vegetation; **(I)** Lithology; **(J)** Earthquake intensity.

of altitude (Figure 8E), landslides are more likely to transpire in areas between 200–400 m, as these regions typically feature loose deposits. Concerning slope, landslides are prevalent when the slope ranges between 3°–10° (Figure 8C). Regions within this slope interval tend to possess more loose sediments on the surface. As the slope steepens, although it provides greater energy for sliding, the heightened slope also indicates that the soil or rock has increased strength, which can hinder landslide occurrences (Wu et al., 2021).

4.1.2 Basic geology factors

Geological factors are vital in shaping geomorphic features. Different lithologies exhibit varying degrees of hardness and weathering. The occurrence of landslides is influenced by the lithology and weathering degree of the underlying bedrock. Soft rocks and fragmented rock-soil materials are more prone to landslides. Landslide densities are generally higher on metamorphic rocks (Figure 8I). Earthquakes are usually accompanied by varying collapse, landslides, and debris flow. Classification of earthquake intensity also reflects the distribution of faults. As shown in Figure 8J, landslides in Fujian tend to occur with seismic intensity levels of VI degree or higher.

4.1.3 Land cover factors

In this study, we investigated the impact of land use practices on shallow soil landslides, focusing on vegetation, NDVI, and land use as land cover factors. For NDVI, higher values are commonly associated with lower landslide susceptibility (Figure 8A). However, the analysis results also reveal the complexity of landslide causation.

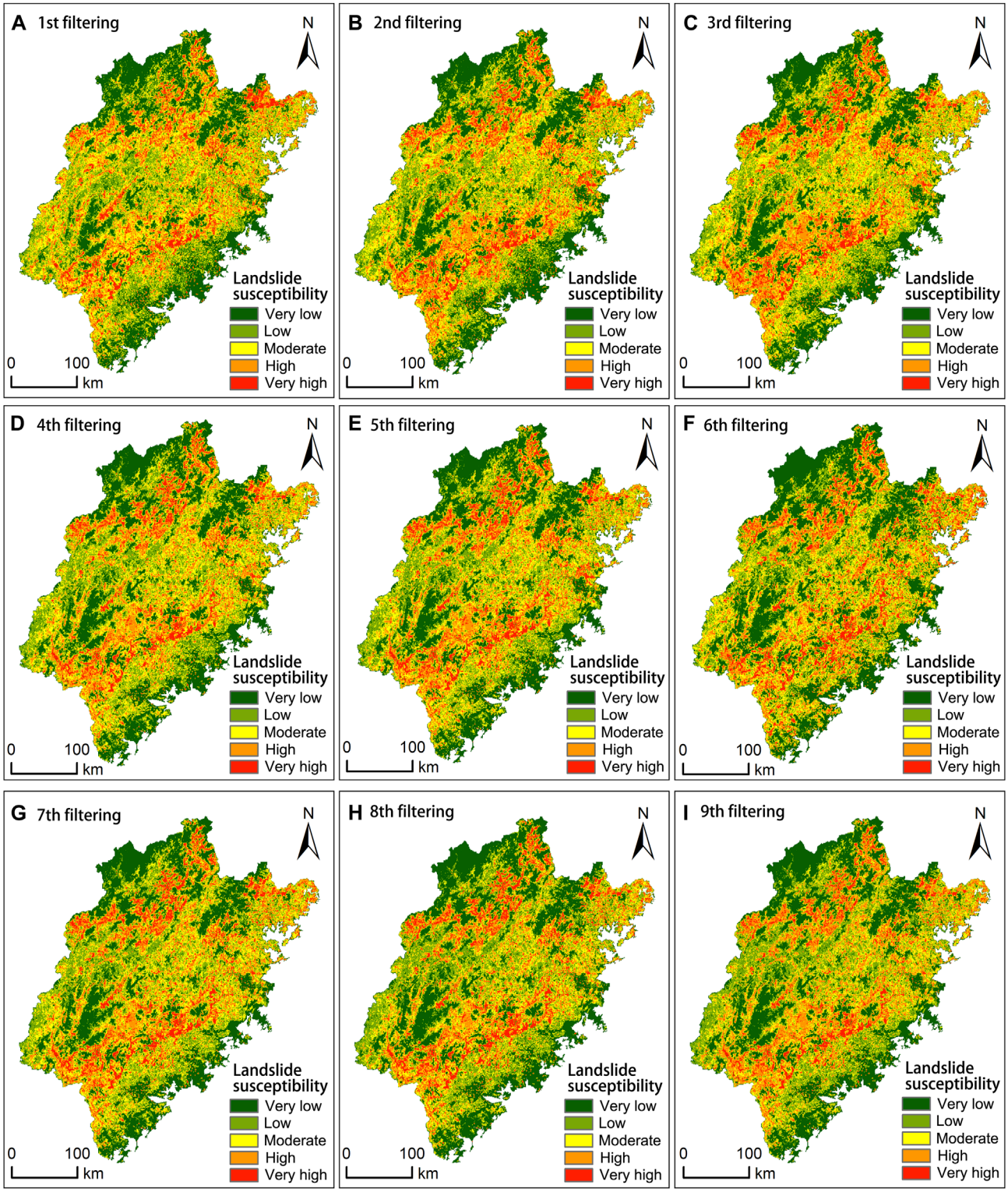

FIGURE 9
Landslide susceptibility map of Fujian Province during the process of noise filtering; **(A)** 1st filtering; **(B)** 2nd filtering; **(C)** 3rd filtering; **(D)** 4th filtering; **(E)** 5th filtering; **(F)** 6th filtering; **(G)** 7th filtering; **(H)** 8th filtering; **(I)** 9th filtering.

Despite the perceived stability related to regions with high NDVI and forests, landslides still occur in these areas. These regions usually feature hilly and mountainous terrain, which are more prone to landslides. Vegetation with well-developed roots stabilizes the slopes, creating a complex network of fibers within the soil, enhancing its shear strength. Thick roots can penetrate deep into

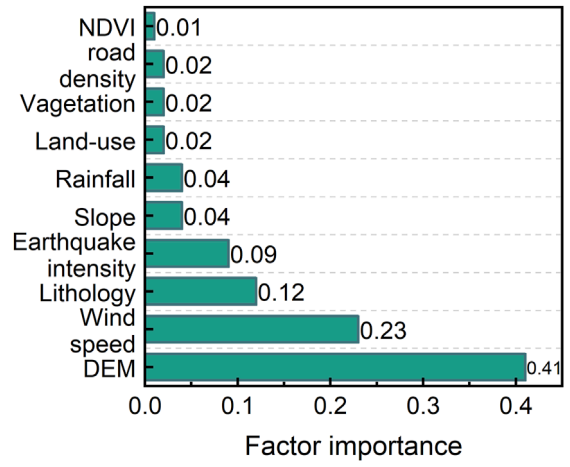

FIGURE 10
Factor importance of wind speed factor.

the bedrock, serving as anchoring elements for the shallow soil. These factors collectively contribute to the slope stability (Bordoloi and Ng, 2020; Pandey et al., 2022). However, the stabilizing effect of trees on slope stability may be limited under certain wind load conditions (Zhuang et al., 2022). This observation may explain why landslides are more prevalent in forested areas when considering the vegetation factor (Figure 8H). Regarding the Land-use factor; landslides are concentrated in cultivated land (Figure 8G). In Fujian Province, where arable land is scarce, many farmers have reshaped slopes for agricultural purposes, leading to numerous unstable cut slopes and an increased risk of landslides.

4.1.4 Human engineering activities factors

As for road density, areas with higher road density generally exhibit higher landslide densities (Figure 8B). The imbalanced alteration of rock and soil mass resulting from construction projects such as housing and road development, including excavation and slope-cutting activities, can increase the susceptibility of mountain slopes to instability and damage. Moreover, the high population density and extensive engineering activities in these areas exacerbate the occurrence of geological disasters. However, regions with the highest road density are less susceptible to landslides due to their high level of urbanization and superior infrastructure management.

4.1.5 Climate environmental factors

Situated adjacent to the Pacific Ocean, Fujian Province and its coastal areas are frequently affected by typhoon rainstorms. The heavy rainfall accompanying typhoons decreases the mechanical strength of the soil, serving as an important triggering factor for landslides. Areas with annual rainfall ranging between 12,000–14,000 mm are more susceptible to landslides than those with higher or lower rainfall levels (Figure 8D). These areas mainly concentrate in central Fujian Province. The rapid uplift of the terrain in the region creates a center of intense rainfall in its vicinity. Additionally, areas with wind speeds in the range of 14–16 m/s also exhibit a higher density of landslides, which can be attributed to the increased erosion and soil instability caused by strong winds (Figure 8F).

4.2 Landslide susceptibility mapping

This study uses the landslide inventory consisting of 5,992 distinct points as a fundamental dataset. These points were identified as positive samples and designated with a value 1. Additionally, an equivalent number of points were randomly selected from the study area, serving as negative samples designated with a value of 0. The dataset of this study consists of both landslide and non-landslide points. The entirety of the modeling procedure proposed a Bayesian Network model to analyze the distribution characteristics of landslide disasters in Fujian Province. Within this method, noise filtering was implemented after the inference of the Bayesian Network model. This iterative process progressively filters noise in the subsets, thereby reducing the impact of mislabeled data on prediction accuracy (Figure 9).

This study incorporated a comprehensive array of factors as inputs for the landslide susceptibility modeling. The variables included altitude, slope, vegetation cover, land-use patterns, NDVI, lithology, earthquake intensity, rainfall patterns, wind speed, and road density. A noise filtering method was adopted to enhance the accuracy of LSA, which served as a primary strategy in this investigation. After the training process with noise filtering, the landslide susceptibility index (LSI) was effectively forecasted. The spatial distribution of landslide susceptibility predicted by noise-filtered samples in Fujian Province is presented in Figure 9. It can be seen from Figure 9 that the high and extremely high susceptibility areas in Fujian Province are mainly located near the mountain belts in central and western Fujian which aligns with the actual spatial distribution pattern of landslide occurrences. The relatively flat areas in the East and southeast coast of the province are mostly low and extremely low susceptibility. With the progress of the noise filtering, the proportion of each susceptibility level changes, the proportion of high and extremely high susceptibility areas increases, and the identifiability of landslide susceptibility mapping gradually increases.

4.3 Results analysis

4.3.1 Factor importance

Altitude, wind speed, and lithology respectively were identified as the main controlling factors of landslides (Figure 10). Wind speed stands out with a factor importance score of 0.23, ranking as the second most influential factor in our landslide susceptibility modelling. This highlights the significant impact of wind speed on landslide occurrences in the study area, emphasizing the necessity of incorporating this factor in landslide risk assessments.

4.3.2 Accuracy analysis

To assess the accuracy, the Area Under the Curve (AUC) metric was adopted as the evaluation criterion for the performance of the machine learning model. A higher AUC value signifies greater accuracy in predictive results. The results of this evaluation are depicted in Figure 11A, where the AUC value steadily increases

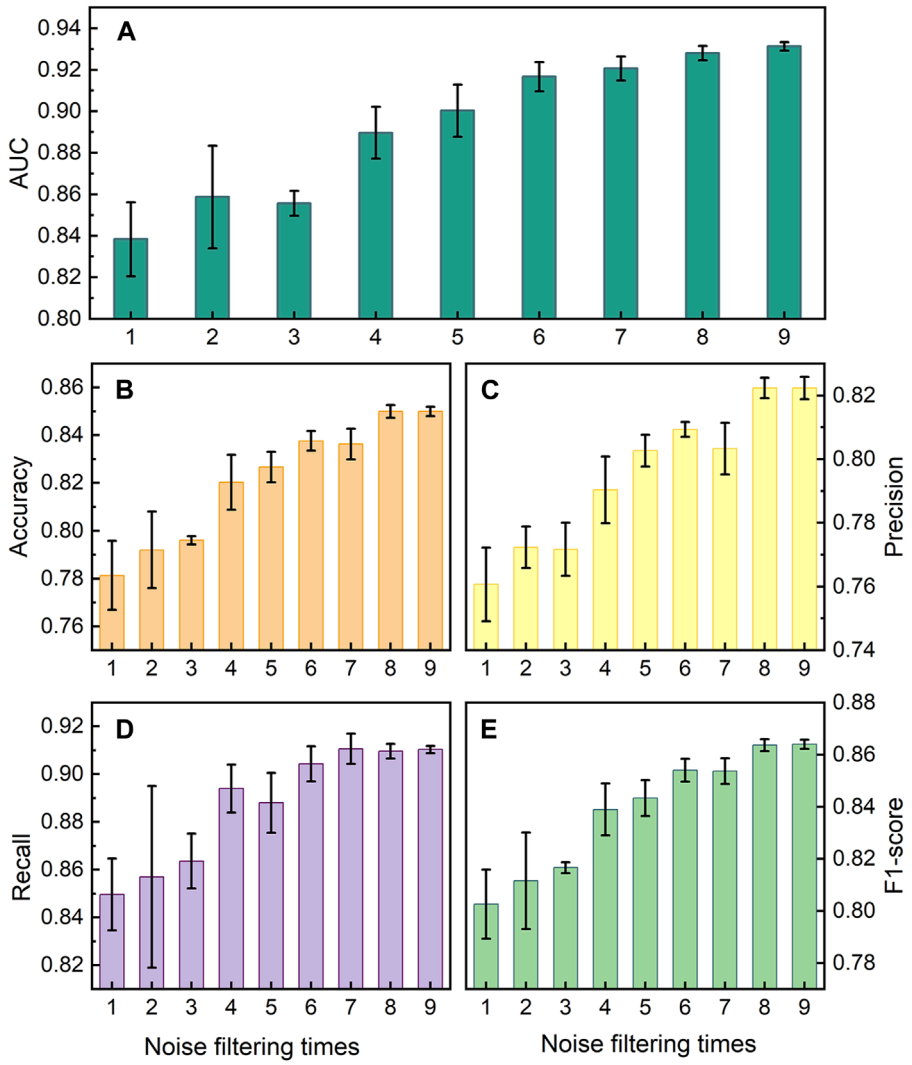

FIGURE 11
Accuracy of each time noise filtering **(A)** AUC; **(B)** Accuracy; **(C)** Precision; **(D)** Recall; **(E)** F1-score.

from 0.838 to 0.931, while the standard deviation gradually decreases. This trend indicates a consistent improvement in model accuracy and reliability, as the model becomes more consistent and dependable in its predictions. This trend highlights the progressive efficacy of the noise filtering approach in enhancing the precision and reliability of the machine learning model for LSA.

Additionally, other key indicators including accuracy, precision, recall, and the F1-score were also involved in the assessment of model classification performance. Higher values of the indicators indicate better classification performance of a model. As shown in Figures 11B–E, these indicators collectively manifest a demonstrably enhanced model performance as the noise filtering times increase. A consistently increasing metric accompanied by a gradually decreasing standard deviation suggests that the model is enhancing and getting more stable throughout the noise filtering process While precision is vital in minimizing false positives, a high recall rate is essential for capturing all instances of landslides. In the context of LSA, prioritizing recall is vital to correctly identify potential landslide-prone areas. According to the results, although both metrics showed improvement during the noise filtering process, the precision reaches a maximum of 0.82 and the recall reaches a maximum of 0.91.

4.3.3 Spatial correlation analysis

The LSI also possesses a high level of accuracy spatially. We employed the GeoDa software to obtain Moran's I and evaluate the spatial correlation between LND and LSI. The calculated values for Moran's I, p-value, and Z-score were 0.335, 0.012, and 529, respectively. At a 95% confidence level, both the p-value and z-value passed the significance tests. These results indicate a positive correlation between LND and LSI, which indicates that the predicted values closely align with actual values.

To further analysing local clustering patterns, we computed the Local Indicators of Spatial Association (LISA) based on the local Moran's I index. Figure 12 depicts the LISA map for LND and LSI.

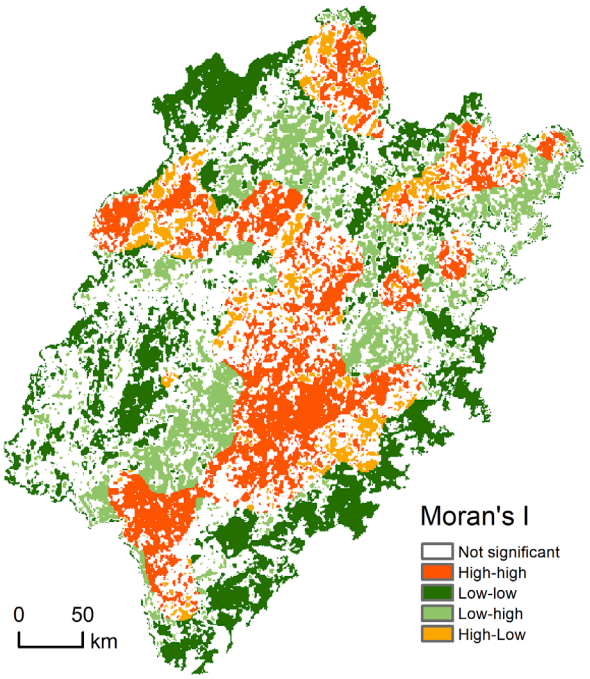

FIGURE 12
Local Moran's I index between LND and LSI.

Elevated high-high regions on the map indicate areas with high LND and LSI values, while low-low regions signify areas with low values for both variables. The predominant distribution of high-high areas closely aligns with regions characterized by high and very high LSI. These regions are mainly in the central and western parts of Fujian Province and run north-east through the province. Similarly, low-low regions correspond to areas with low and very low LSI in the southeastern coastal areas. These findings provide further validation of the predictive accuracy of this study.

4.4 Landslide susceptibility assessment in Fujian

Figure 13 presents the cumulative percentage of landslide susceptibility levels for different cities and counties in Fujian Province. In Figure 13A, the proportion of varying susceptibility intervals within the cities. Correspondence between abbreviations and full names is in Supplementary Table 1. Cities such as QZ and ND have a higher percentage of high and very high susceptibility areas, while cities like XM have a smaller percentage. Figure 13B presents the percentage distribution of different susceptibility levels across various cities. Most areas fall into the low susceptibility category, followed by moderate and very low susceptibility. The high and very high landslide susceptibility is the least prevalent, accounting for less than 10%. Figure 13C displays the distribution of susceptibility levels in subordinate counties and districts across different cities. The susceptibility levels exhibit an uneven distribution among the counties and districts of different cities. Overall, the percentage of landslide susceptibility levels across different cities is controlled by the mountainous regions of central and western Fujian. The cities of SM, NP, and LY, traversed by the mountain belt in western Fujian, have higher susceptibility levels. The southeastern coastal cities of Xiamen and Putian with flatter terrain thus have lower susceptibility levels. In cities such as QZ and FZ, the western regions are characterized by the complex terrain of the mountain belt in central Fujian, while the eastern regions are coastal plains. The complex terrain results in highly uneven susceptibility levels across districts and counties.

5 Discussion

The study of extreme weather and the disasters it brings has been extended through various mathematical and physical methods. In this research work, a wind speed factor was built based on Rankine vortex model and history TCs. We have analyzed the landslide distribution pattern and constructed a noise filtering method based on the BN model to investigate how mislabeled samples impact the model performance.

Mature TCs often produce spiral rainbands that can lead to local winds, heavy rainfall, and storm surges (Tang et al., 2018). This convective effect can cause a series of disasters, including landslides, floods, and urban waterlogging, especially before and after a TC makes landfall (Zhuang et al., 2022). While annual rainfall provides an indication of the level of rainfall in a year, it may not accurately reflect or measure the impact of short-term heavy rainfall brought by TCs. The Rankine vortex model was used to quantify historical tropical cyclone data and derive the wind speed factor (Figure 6). Methods for quantifying the impact of typhoons include: 1) The wind pressure model, which describes the relationship between wind speed and distance from the typhoon center, enabling a more accurate assessment of the damage caused by TCs and serving as crucial tool for evaluating typhoon impacts; 2) Integration of historical typhoons, which characterizes the impact of typhoons by combining the intensity and frequency of historical events (Batke et al., 2014; Qi et al., 2023). Qi et al. (2023) quantified the destructiveness of TCs by this method.

The predictive performance of classification learning algorithms is limited by data quality (Khoshgoftaar and Rebours, 2007; Johnson and Khoshgoftaar, 2022). Non-landslide points in most existing studies were just randomly selected from the entire study area (Wu, 2019; Cui et al., 2022). There's a possibility of mislabeling some points with high landslide susceptibility as non-landslide points, what is known as label noise. Huang et al. (2020) highlighted the issue of selecting non-landslide samples and chose non-landslide points from areas with very low susceptibility under a semi-supervised algorithm. Our study proposes a noise filtering method that gradually eliminates lower-quality samples, which significantly improved the quality of non-landslide samples (Figure 11). The threshold for the noise filtering method is set to 0.7, effectively filtering out samples with large deviations between predicted and actual values. Additionally, adjusting the threshold allows for controlling the balance between the acceptable sample deviation and the number of samples removed (Khoshgoftaar and Rebours, 2007).

It's worth acknowledging that certain limitations might be associated with this study. Landslides are affected by terrain, geology, hydrology, and other factors, leading it impossible to

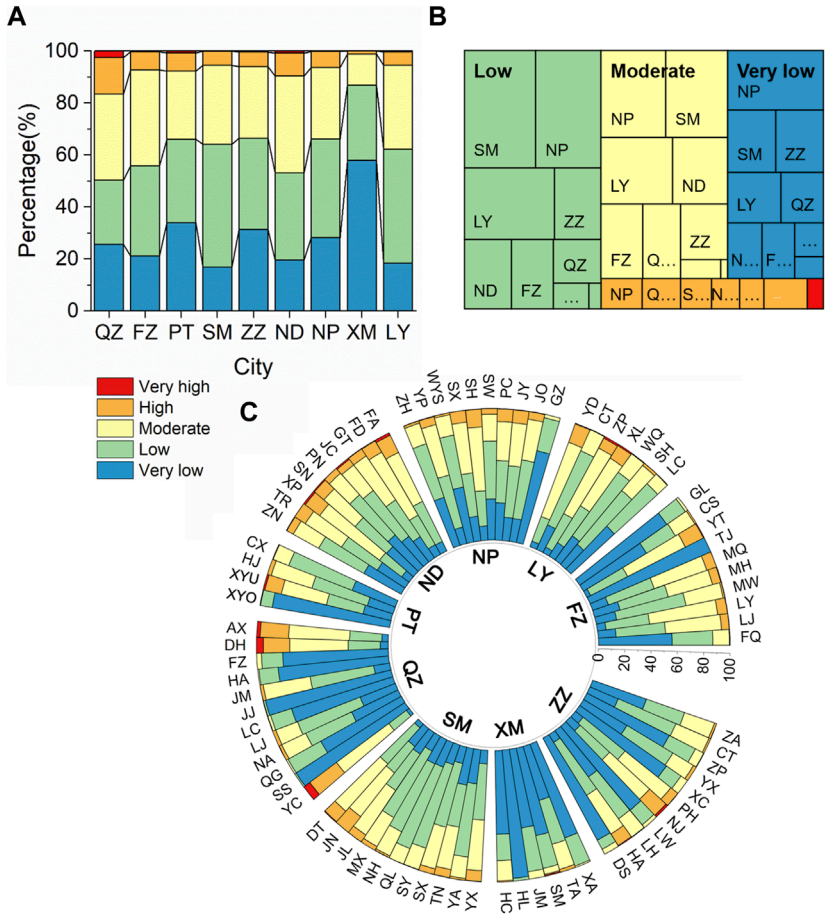

FIGURE 13
Percentage accumulation diagram of landslide susceptibility **(A)** Percentage accumulation diagram of each city; **(B)** Percentage accumulation diagram of susceptibility level; **(C)** Percentage accumulation diagram of each county.

identify areas that will never experience landslides. Selecting non-landslide points that are completely accurate and reliable is challenging. Therefore, we can only work to improve this issue, but we cannot entirely resolve it. The primary focus of our study was to tackle sample noise and amplify the model's classification performance by addressing noise within the samples. The noise instances that get filtered is contingent on the selected threshold value. Although this study did not extensively delve into exploring the optimal threshold value selection, this aspect doesn't detract from the performance enhancement achieved through the noise filtering methodology. Determining the optimal threshold value and further enhancing the methodology may involve employing various search algorithms, such as hill-climbing, simulated annealing, or genetic algorithms.

6 Conclusion

We have analyzed the landslide distribution pattern and constructed a noise filtering method based on the BN model to investigate how mislabeled samples impact the model performance. In the landslide-prone region, landslides are mainly located in the central and western parts of Fujian Province and run north-east through the province. Over 70% of landslides occurred during the rainy season from May to August. In the landslide susceptibility assessment process, 10 geoenvironmental factors have informed the BN model as predictors. Moreover, we have calculated the historical tropical cyclone dataset as a wind speed geoenvironmental factor to consider the impact of tropical cyclones on landslides. And it was proved to be the second most significant factor.

We have also progressively filtered the mislabeled data in non-landslide sets with the noise filtering method in this study. As expected, the AUC value has been improved from 0.838 to 0.931 during the process. Furthermore, the final landslide susceptibility results have been made into a landslide susceptibility map. The reliability was confirmed by Moran's I index. The LISA shows consistent distribution patterns for high LND and LSI regions, further highlighting the reliability. The results demonstrate the ability of the noise filtering method in the quality enhancement of training sets and the performance of machine learning models. The noise filtering method offers a viable approach for enhancing the quality of the non-landslide dataset and a useful reference for reliable landslide susceptibility mapping in the study area and similar areas.

Data availability statement

The original contributions presented in the study are included in the article/Supplementary Material, further inquiries can be directed to the corresponding authors.

Author contributions

SZ: Supervision, Writing–review and editing, Conceptualization, Funding acquisition, Methodology, Project administration, Software. JL: Methodology, Software, Data curation, Formal Analysis, Investigation, Visualization, Writing–original draft. JZ: Supervision, Writing–review and editing. ZX: Methodology, Writing–review and editing. XL: Data curation, Resources, Writing–review and editing.

Funding

The author(s) declare that financial support was received for the research, authorship, and/or publication of this article. The authors declare that financial support was received for the research, authorship, and/or publication of this article. This work has received funding from the Natural Science Foundation of China (Grant No. 12062026), the Science and Technology Infrastructure Program of Guizhou Province (2020-4Y047), Natural Resources Science and Technology Project of Fujian Province (KY-070000-04-2021-025), Natural Science Foundation of Hunan Province, China (2023JJ30135), and Natural Science Foundation of Changsha (kq2208031). All these fundings are greatly acknowledged.

Acknowledgments

We express our appreciation to ChatGPT 3.5 from OpenAI, which we used to improve the readability and language of the manuscript during the writing process. We also extend our gratitude to the reviewers for their constructive comments, which significantly enhanced the quality of the manuscript.

Conflict of interest

The authors declare that the research was conducted in the absence of any commercial or financial relationships that could be construed as a potential conflict of interest.

Publisher's note

All claims expressed in this article are solely those of the authors and do not necessarily represent those of their affiliated organizations, or those of the publisher, the editors and the reviewers. Any product that may be evaluated in this article, or claim that may be made by its manufacturer, is not guaranteed or endorsed by the publisher.

Supplementary material

The Supplementary Material for this article can be found online at: https://www.frontiersin.org/articles/10.3389/feart.2024.1444882/full#supplementary-material

References

Abraham, M. T., Vaddapally, M., Satyam, N., and Pradhan, B. (2023). Spatio-temporal landslide forecasting using process-based and data-driven approaches: a case study from Western Ghats, India. *Catena* 223, 106948. doi:10.1016/j.catena.2023.106948

Batke, S. P., Jocque, M., and Kelly, D. L. (2014). Modelling hurricane exposure and wind speed on a mesoclimate scale: a case study from cusuco NP, Honduras. *Plos One* 9, e91306. doi:10.1371/journal.pone.0091306

Bordoloi, S., and Ng, C. W. W. (2020). The effects of vegetation traits and their stability functions in bio-engineered slopes: a perspective review. *Eng. Geol.* 275, 105742. doi:10.1016/j.enggeo.2020.105742

Cengiz, L. D., and Ercanoglu, M. (2022). A novel data-driven approach to pairwise comparisons in AHP using fuzzy relations and matrices for landslide susceptibility assessments. *Environ. Earth Sci.* 81, 222. doi:10.1007/s12665-022-10312-0

Chakrabortty, R., Pal, S. C., Roy, P., Saha, A., and Chowdhuri, I. (2022). Novel ensemble approach for landslide susceptibility index assessment in a mountainous environment of India. *Geocarto Int.* 37, 13311–13336. doi:10.1080/10106049.2022.2076924

Cui, Y. L., Jin, J. L., Huang, Q. B., Yuan, K., and Xu, C. (2022). A data-driven model for spatial shallow landslide probability of occurrence due to a typhoon in ningguo city, anhui province, China. *Forests* 13, 732. doi:10.3390/f13050732

Houze, R. A., JR (2010). Clouds in tropical cyclones. *Mon. Weather Rev.* 138, 293–344. doi:10.1175/2009mwr2989.1

Huang, F. M., Cao, Z. S., Jiang, S. H., Zhou, C. B., Huang, J. S., and Guo, Z. Z. (2020). Landslide susceptibility prediction based on a semi-supervised multiple-layer perceptron model. *Landslides* 17, 2919–2930. doi:10.1007/s10346-020-01473-9

Huang, F. M., Ye, Z., Zhou, X. T., Huang, J. S., and Zhou, C. B. (2022). Landslide susceptibility prediction using an incremental learning Bayesian Network model considering the continuously updated landslide inventories. *Bull. Eng. Geol. Environ.* 81, 250. doi:10.1007/s10064-022-02748-2

Ito, K., Wu, C.-C., Chan, K. T. F., Toumi, R., and Davis, C. (2020). Recent progress in the fundamental understanding of tropical cyclone motion. *J. Meteorological Soc. Jpn.* 98, 5–17. doi:10.2151/jmsj.2020-001

Johnson, J. M., and Khoshgoftaar, T. M. (2022). A survey on classifying big data with label noise. *Acm J. Data Inf. Qual.* 14, 1–43. doi:10.1145/3492546

Khoshgoftaar, T. M., and Rebours, P. (2007). Improving software quality prediction by noise filtering techniques. *J. Comput. Sci. Technol.* 22, 387–396. doi:10.1007/s11390-007-9054-2

Lan, M., Zhu, J. P., and Lo, S. M. (2021). Hybrid Bayesian network-based landslide risk assessment method for modeling risk for industrial facilities subjected to landslides. *Reliab. Eng. and Syst. Saf.* 215, 107851. doi:10.1016/j.ress.2021.107851

Lin, J., Chen, W., Qi, X., and Hou, H. (2021). Risk assessment and its influencing factors analysis of geological hazards in typical mountain environment. *J. Clean. Prod.* 309, 127077. doi:10.1016/j.jclepro.2021.127077

Lu, X., Yu, H., Ying, M., Zhao, B., Zhang, S., Lin, L., et al. (2021). Western North pacific tropical cyclone database created by the China meteorological administration. *Adv. Atmos. Sci.* 38, 690–699. doi:10.1007/s00376-020-0211-7

Ma, S., Shao, X., and Xu, C. (2023). Landslides triggered by the 2016 heavy rainfall event in sanming, fujian province: distribution pattern analysis and spatio-temporal susceptibility assessment. *Remote Sens.* 15, 2738. doi:10.3390/rs15112738

Mihaljevic, B., Bielza, C., and Larrañaga, P. (2021). Bayesian networks for interpretable machine learning and optimization. *Neurocomputing* 456, 648–665. doi:10.1016/j.neucom.2021.01.138

Nie, W., Feng, D., Lohpaisankrit, W., Li, C., Yuan, J., and Chen, Y. (2019). A dynamic Bayesian network-based model for evaluating rainfall-induced landslides. *Bull. Eng. Geol. Environ.* 78, 2069–2080. doi:10.1007/s10064-017-1221-2

Pandey, H. P., Gnyawali, K., Dahal, K., Pokhrel, N. P., and Maraseni, T. N. (2022). Vegetation loss and recovery analysis from the 2015 Gorkha

earthquake (7.8 Mw) triggered landslides. *Land Use Policy* 119, 106185. doi:10.1016/j.landusepol.2022.106185

Pradhan, B. (2013). A comparative study on the predictive ability of the decision tree, support vector machine and neuro-fuzzy models in landslide susceptibility mapping using GIS. *Comput. and Geosciences* 51, 350–365. doi:10.1016/j.cageo.2012.08.023

Qi, J. D., He, B. J., Cao, Y., Dong, J. Y., and Lin, E. S. (2023). Risk assessment of terrestrial protected areas to extreme wind hazards: a case study in Queensland, Australia. *Landsc. Urban Plan.* 240, 104888. doi:10.1016/j.landurbplan.2023.104888

Singh, A., Chhetri, N. K., Nitesh, Gupta, S. K., and Shukla, D. P. (2023). Strategies for sampling pseudo-absences of landslide locations for landslide susceptibility mapping in complex mountainous terrain of Northwest Himalaya. *Bull. Eng. Geol. Environ.* 82, 321. doi:10.1007/s10064-023-03333-x

Song, Y., Gong, J., Gao, S., Wang, D., Cui, T., Li, Y., et al. (2012). Susceptibility assessment of earthquake-induced landslides using Bayesian network: a case study in Beichuan, China. *Comput. and Geosciences* 42, 189–199. doi:10.1016/j.cageo.2011.09.011

Sukristiyanti, S., Wikantika, K., Sadisun, I. A., Yayusman, L. F., and Pamela, P. (2020). "Utilization of google maps for depicting landslide pattern in Indonesia," in Fifth International Conferences of Indonesian Society for Remote Sensing: The Revolution of Earth Observation for a Better Human Life, West Java, Indonesia, 17-20 September 2019.

Tang, X., Lee, W.-C., and Bell, M. (2018). Subrainband structure and dynamic characteristics in the principal rainband of typhoon hagupit (2008). *Mon. Weather Rev.* 146, 157–173. doi:10.1175/mwr-d-17-0178.1

Tian, Y. Y., Owen, L. A., Xu, C., Shen, L. L., Zhou, Q., and Figueiredo, P. M. (2020). Geomorphometry and statistical analyses of landslides triggered by the 2015 M_W 7.8 gorkha earthquake and the M_W7.3 aftershock, Nepal. *Front. Earth Sci.* 8. doi:10.3389/feart.2020.572449

United Nations (2019). *Asia-pacific disaster report 2019: pathways for resilience, inclusion and empowerment*.

Wu, C. H. (2019). Landslide susceptibility based on extreme rainfall-induced landslide inventories and the following landslide evolution. *Water* 11, 2609. doi:10.3390/w11122609

Wu, J. L., Ma, C., Yang, W. T., Lyu, L. Q., and Miao, L. (2021). Recent expansion of talus slopes in the northern taihang mountain range, China: an example from the xiaowutai region. *Landslides* 18, 3027–3040. doi:10.1007/s10346-021-01715-4

Wu, L. Y., and Lei, X. T. (2012). Preliminary research on the size of inner core and periphery and their relationship with the intensity of tropical cyclones. *J. Trop. Meteorology* 28 (05), 719–725. doi:10.3969/j.issn.1004-4965.2012.05.011

Xiao, F., Yin, Y., Luo, Y., Song, L., and Ye, D. (2011). Tropical cyclone hazards analysis based on tropical cyclone potential impact index. *J. Geogr. Sci.* 21, 791–800. doi:10.1007/s11442-011-0880-3

Yang, H. J., Yang, T. Q., Zhang, S. J., Zhao, F. H., Hu, K. H., and Jiang, Y. H. (2020). Rainfall-induced landslides and debris flows in mengdong town, yunnan province, China. *Landslides* 17, 931–941. doi:10.1007/s10346-019-01336-y

Yang, N., Wang, R., Liu, Z. F., and Yao, Z. J. (2023). Landslide susceptibility prediction improvements based on a semi-integrated supervised machine learning model. *Environ. Sci. Pollut. Res.* 30, 50280–50294. doi:10.1007/s11356-023-25650-0

Ye, P., Yu, B., Chen, W., Liu, K., and Ye, L. (2022). Rainfall-induced landslide susceptibility mapping using machine learning algorithms and comparison of their performance in Hilly area of Fujian Province, China. *Nat. Hazards* 113, 965–995. doi:10.1007/s11069-022-05332-9

Ying, M., Zhang, W., Yu, H., Lu, X., Feng, J., Fan, Y., et al. (2014). An overview of the China meteorological administration tropical cyclone database. *J. Atmos. Ocean. Technol.* 31, 287–301. doi:10.1175/jtech-d-12-00119.1

Youssef, A. M., Pradhan, B., Dikshit, A., Al-Katheri, M. M., Matar, S. S., and Mahdi, A. M. (2022). Landslide susceptibility mapping using CNN-1D and 2D deep learning algorithms: comparison of their performance at Asir Region, KSA. *Bull. Eng. Geol. Environ.* 81, 165. doi:10.1007/s10064-022-02657-4

Yuan, R., and Chen, J. (2022). A hybrid deep learning method for landslide susceptibility analysis with the application of InSAR data. *Nat. Hazards* 114, 1393–1426. doi:10.1007/s11069-022-05430-8

Zhuang, Y., Xing, A. G., Jiang, Y. H., Sun, Q., Yan, J. K., and Zhang, Y. B. (2022). Typhoon, rainfall and trees jointly cause landslides in coastal regions. *Eng. Geol.* 298, 106561. doi:10.1016/j.enggeo.2022.106561

frontiers | Frontiers in Earth Science

TYPE Original Research
PUBLISHED 18 March 2025
DOI 10.3389/feart.2025.1548465

OPEN ACCESS

EDITED BY
Xiya Zhang,
China Meteorological Administration, China

REVIEWED BY
Chong Xu,
Ministry of Emergency Management, China
Yanyan Li,
Beijing University of Technology, China
Qingli Zeng,
University of Chinese Academy of Sciences, China

*CORRESPONDENCE
Lianji Liang,
lianglianji512@163.com
Fuchu Dai,
daifc@bjut.edu.cn

RECEIVED 19 December 2024
ACCEPTED 17 February 2025
PUBLISHED 18 March 2025

CITATION
Liang L, Dai F, Zhu Y and Pan R (2025) Preliminary investigation of hummocky landforms and hyper-mobility of the Bingda landslide, northeastern Tibetan Plateau. *Front. Earth Sci.* 13:1548465. doi: 10.3389/feart.2025.1548465

Preliminary investigation of hummocky landforms and hyper-mobility of the Bingda landslide, northeastern Tibetan Plateau

Lianji Liang[1,2]*, Fuchu Dai[1]*, Yuxuan Zhu[1] and Rongshen Pan[1]

[1]College of Architecture and Civil Engineering, Beijing University of Technology, Beijing, China, [2]State Key Laboratory of Earthquake Dynamics, Institute of Geology, China Earthquake Administration, Beijing, China

Rapid and long-runout landslides characterized by their high speed, long distance mobility, and huge capacity and volume would pose significant threats to infrastructure and life safety. In this study, a rapid and long-runout landslide that occurred in the Bingda village of the northeastern Tibetan Plateau, which was triggered by heavy rainfall in June 2017, was preliminarily investigated. On the basis of detailed field surveys, high-resolution satellite imagery analysis, and laboratory tests, the morphological and sedimentological features of the landslide were described, and the formation mechanism of hummocky landforms and its insight into the extraordinary movement of the Bingda landslide was deduced. The field investigation and satellite imagery analysis showed that there were nearly 200 hummocks, mostly with normal circular bases and with a height of ~0.1 m–7.5 m, distributed in the transfer and accumulation areas of the landslide. The height and number density of the hummocks decreased away from the transfer area to the accumulation area and displayed higher heights at the outer bends of the gully channel than that at the inner bends of it. The characteristics of the spatial distribution and the composition of hummocks indicated that significant generation and dissipation of pore-water pressure within the loose and saturated silty clay layer in the runout path was the most probable reason for the formation of hummocky landforms. This study also provided insights into the hypermobility mechanisms of the Bingda landslide, suggesting that this landslide began with the sliding failure of the weathered colluvium in the source area, and then the landslide debris traveled into the channel and impacted sudden undrained loading and rapid shearing to the underlying silty clay layers in the gully. These processes generated pore-water pressure and reduced the effective stress within the soil particles, resulting in a decrease in the frictional resistance in the substrate, finally facilitating the rapid and long-runout movement of the landslide.

KEYWORDS

rapid and long-runout, landslide, hummock, Tibetan Plateau, rainfall

1 Introduction

Rapid and long-runout landslides are characterized by their extraordinary speed, long distance mobility, and huge capacity and volume, resulting in catastrophic damage to infrastructure and posing grave threats to life safety (Heim, 1882; Legros, 2002; Hungr and Evans, 2004; Hungr et al., 2014). Extensive insights into the kinematic progression of these landslides have been derived from studies on their surface morphology and sedimentological structures (Strom, 2006; Shea and van, 2008; Iverson et al., 2015; Dufresne et al., 2016; Strom and Abdrakhmatov, 2018). The hummock is one of the most striking and common morphological features, seen as isolated or clustered mounds, either rounded or conical in form, which could characterize high-speed sliding. The hummocks have been documented in a wide spectrum of high-energy geological events, including large landslides or rock-debris avalanches (Hewitt, 1999; Linnell et al., 2011; Dai et al., 2019; Wang et al., 2019; Dufresne and Geertsema, 2019; Zeng et al., 2019; Zeng et al., 2021), volcanic edifices (Voight et al., 1981; Ui, 1983; Siebert, 1984; Andrade and van Wyk de Vries, 2010; Yoshida, 2013; 2014; Paguican et al., 2014), and glacier activities (Benn and Evans, 1998; Haeberli et al., 2004; Iturrizaga, 2012; Jermyn and Geertsema, 2015; Reznichenko et al., 2017).

A series of field investigation, laboratory experiments, and model simulations have been conducted in order to explain the formation mechanisms of hummocky landforms. Morphologic studies of hummocks have been conducted on the quantitative and semi-quantitative analyses of the relationship of the elements of hummocks, including the size, orientation, and spacing, with the flow direction of rock-debris avalanches (Yoshida and Sugai, 2010; Yoshida, 2014). Hummocky landforms may appear as blocks ranging in size from a few meters to hundreds of meters in diameter (Ui et al., 2000) or as discrete avalanche blocks interspersed in a matrix of finer materials (Glicken, 1996); the facts that have been explained to be due to the fault formation during mass spreading (Shea and van, 2008; Paguican et al., 2012) or due to basal shear and extensional regimes in the moving mass (Dufresne and Davies, 2009). Paguican et al. (2014) summarized that hummocks form along low-angle basal fault and high-angle normal faults, proposing that the morphology and spatial distribution of hummocks were attributed to the interplay of the number density of normal, thrust, and strike–slip faults (Dufresne and Geertsema, 2019). Shea and van (2008) and Paguican et al. (2012) suggested that the morphology and spatial distribution of hummocks were not only associated with the fault formation during mass spreading but was also related with the basal shear and extensional regimes in the moving mass (Dufresne and Davies, 2009). Prominent elongated, sub-parallel alignments hummocks have also been interpreted as remnants of longitudinal ridges induced by parallel strike–slip faults related to lateral velocity changes (Shea and van, 2008; Dufresne and Davies, 2009; Andrade and van Wyk de Vries, 2010). Undoubtedly, the hummocky landforms and their evolution and formation mechanisms could provide valuable insights into the kinematics and dynamics of landslides (Shea and van, 2008; Paguican et al., 2012; Paguican et al., 2014).

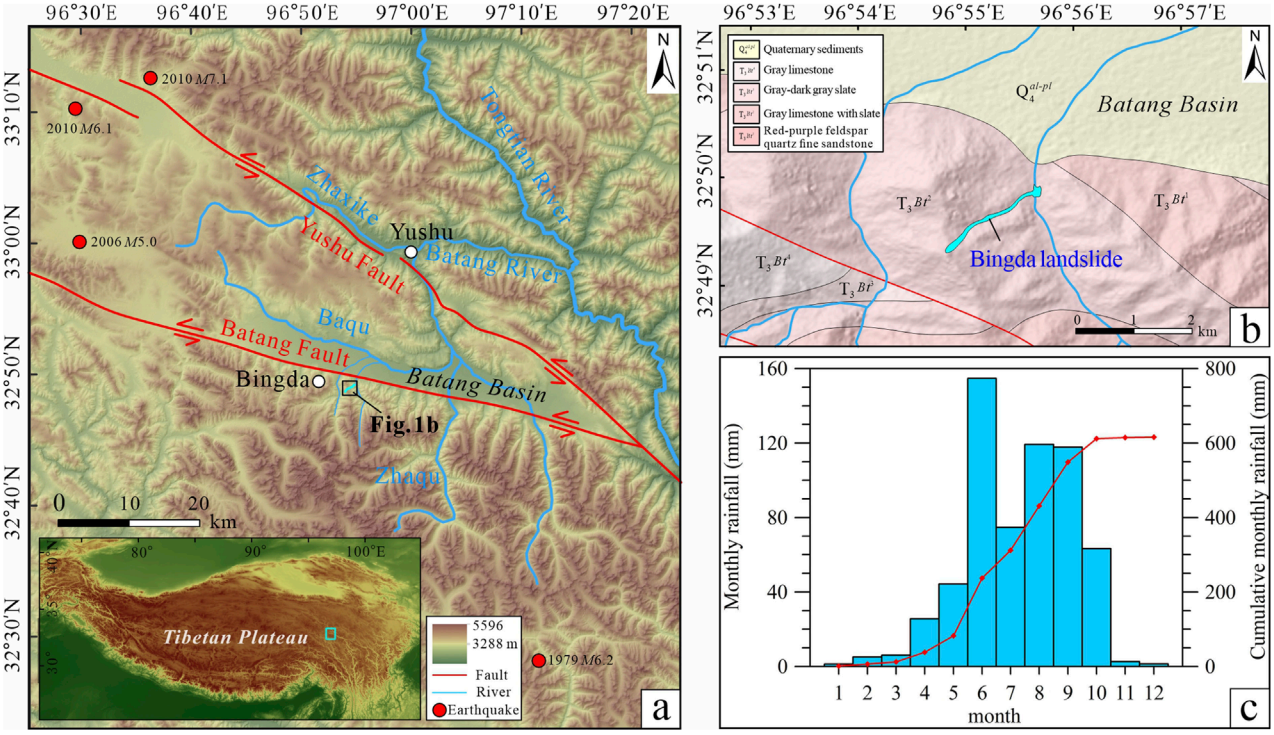

FIGURE 1
(A) Geological background of the study area and the location of the Bingda landslide. **(B)** Geologic sketch setting of the Bingda landslide. **(C)** Rainfall data of the Yushu area in 2017.

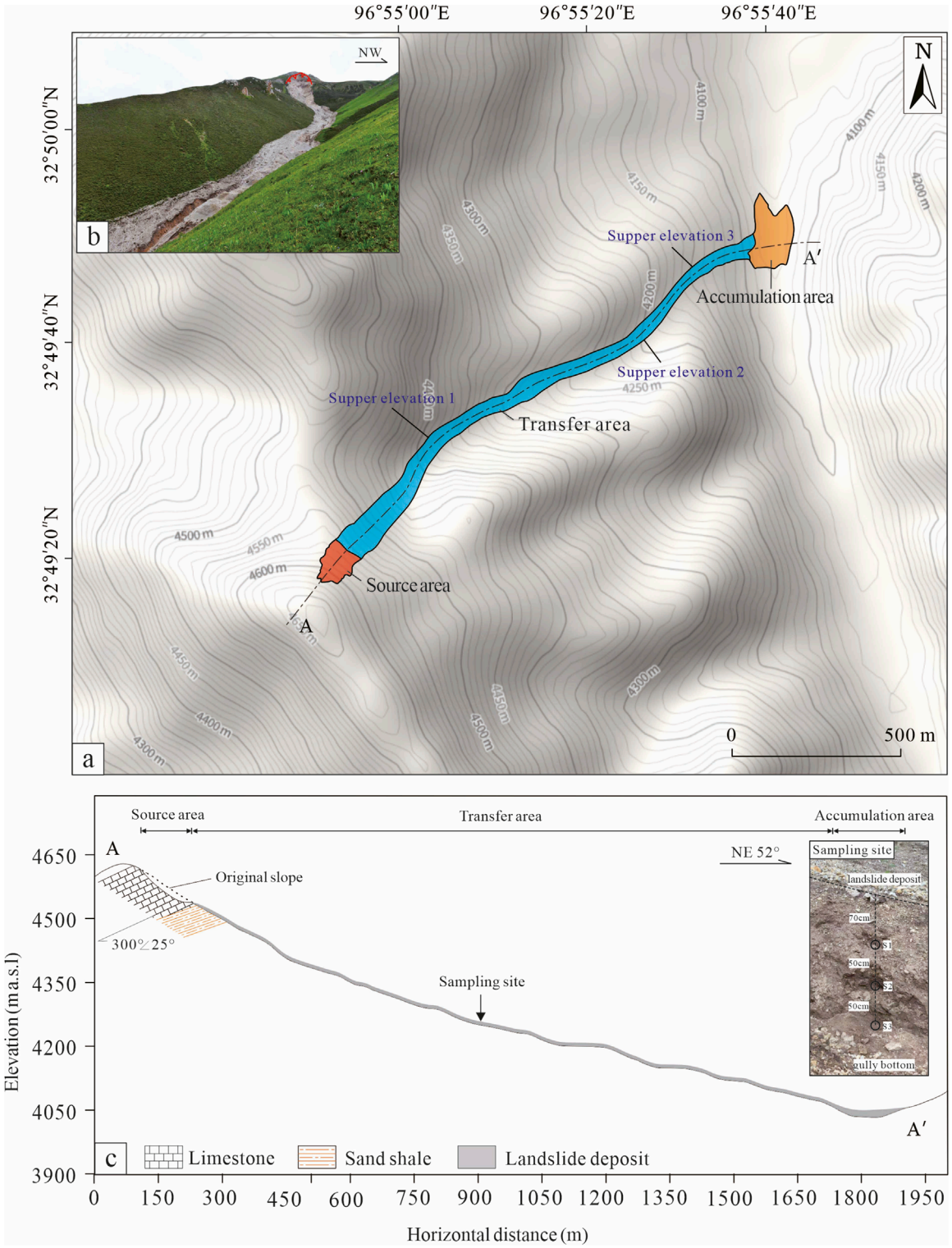

FIGURE 2
(A) Topographic contour map of the Bingda landslide. **(B)** Panorama photo of the Bingda landslide. **(C)** Longitudinal geological profile of the Bingda landslide and the sampling site of the river-cut section in the gully.

In this work, we studied a unique hummocky landform that was well-preserved in a rapid and long-runout landslide in the Bingda village of the northeastern Tibetan Plateau (Zhu et al., 2019; Pan, 2023) (Figure 1). The Bingda landslide was triggered in June 2017 by heavy rainfall, and the average velocity of the landslide mass reached approximately 24 m/s in the transfer area (Zhu et al.,

FIGURE 3
Spatial distribution of hummocks in the Bingda landslide.

2019). On the basis of the field investigation, high-resolution satellite imagery interpretation, and laboratory tests, the morphological and sedimentological features of the landslide were examined with an aim to understand the formation mechanisms of hummocks and shed light on the extraordinary movement of the Bingda landslide. This study contributed novel insights into the dynamic research of rapid and long-runout landslides.

2 Geological setting

The Bingda landslide was located at 32°49′17″N, 96°54′48″E, and 4,645 m above sea level (a.s.l.) in Yushu City in the northeastern Tibetan Plateau of China (Figure 1A). The study area is characterized by its location in the alpine zone, proximal to the Batang basin to the north. The left-lateral Yushu and Batang faults pass through this region and control the regional tectonic activities and earthquake events (Wu et al., 2014). This region mainly contains the Triassic limestone slate and feldspar quartz sandstone with limestone, which constitutes the main lithology of mountainous topography (Peng, 2013; Wu et al., 2014) (Figure 1B). The EW-trending Batang basin is infilled with Quaternary alluvial and diluvial deposits. A drainage channel of the Baqu River tributaries, which is a third-order tributary of the Tongtian River, flows through the front of the valley in the landslide area (Wu et al., 2014). The groundwater and atmospheric precipitation are the primary sources of runoff for these tributaries, contributing to the fragmentation and weathering of the bedrock. The climate of this region is the plateau continental monsoon climate, which is characterized by longer cold seasons and shorter warm seasons. The mean annual temperature fluctuates between - 4.3°C and 4.6°C, while the mean annual rainfall ranges between 419.7 mm and 542.0 mm. Rainfall data from the Yushu meteorological station between 2012 and 2017 indicate that the predominant rainfall period is from June to October, receiving over 70% of the total annual rainfall (Pan, 2023). In 2017, the annual rainfall reached 616.1 mm, with a significant surge in June, recording a monthly total of 154.7 mm over 25 rainfall days (Figure 1C).

3 Methodology

The boundary and zonation of the Bingda landslide were defined and verified utilizing 1.0-m resolution Century Space satellite imagery and were consulted by utilizing 0.3-m resolution Worldview 3 satellite imagery and high-resolution Google Earth imagery. A topographic map of the study area was generated from the Advanced Spaceborne Thermal Emission and Reflection Radiometer (ASTER) digital elevation models (DEMs) at http://www.gscloud.cn/home. Considering the study area's proximity (~20 km) to Batang airport, which is designated as a national no-fly-zone, a detailed field survey focusing on the mapping and orientation of hummocks across various scales was undertaken. Detailed photographic documentation and descriptions of the landslide deposits were recorded, employing a hammer for scale reference. In addition, three samples (named S1 to S3) were systematically collected from the river-cut section exposed in the gully to examine the fundamental physical properties. Undisturbed soil samples were extracted utilizing a ring knife with a diameter of 70 mm and a height of 52 mm. Then, analyses were performed to determine the water content, specific gravity, porosity, saturated and dry density, and grain size distribution. Grain size analysis was carried out on a Mastersizer 3000 laser particle size analyzer equipped at the Hebei Institute of Regional Geology and Mineral Resources Investigation.

4 Basic characteristics of the Bingda landslide

According to the high-resolution satellite image interpretation and topographical field investigation of the landslide, the landslide can be divided into three parts: source area, transfer area, and accumulation area (Figure 2A). The landslide presents a northeastward long and narrow channel shape (Figure 2B). The vertical distance difference (H) and horizontal distance difference (L) of the top and toe of the landslide are ~552 m and ~1,795 m, respectively, and the corresponding equivalent friction coefficient (H/L) is calculated as 0.308 < 0.33 (Heim, 1932; Scheidegger, 1973), exhibiting the rapid and long-runout mobility (Figure 2C).

4.1 Source area

The source area of the landslide presents a spoon shape, with the highest elevation of the main scarp reaching approximately 4,645 m, and the elevation of the toe of the rupture surface assessing

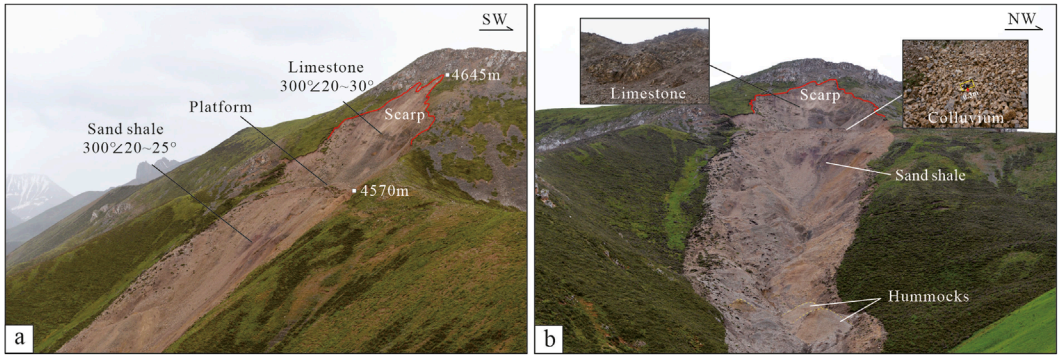

FIGURE 4
(A) Distant view of the source area of the Bingda landslide. **(B)** The front view of the source area of the Bingda landslide, and the limestone bedrock and colluvium deposits in the source area.

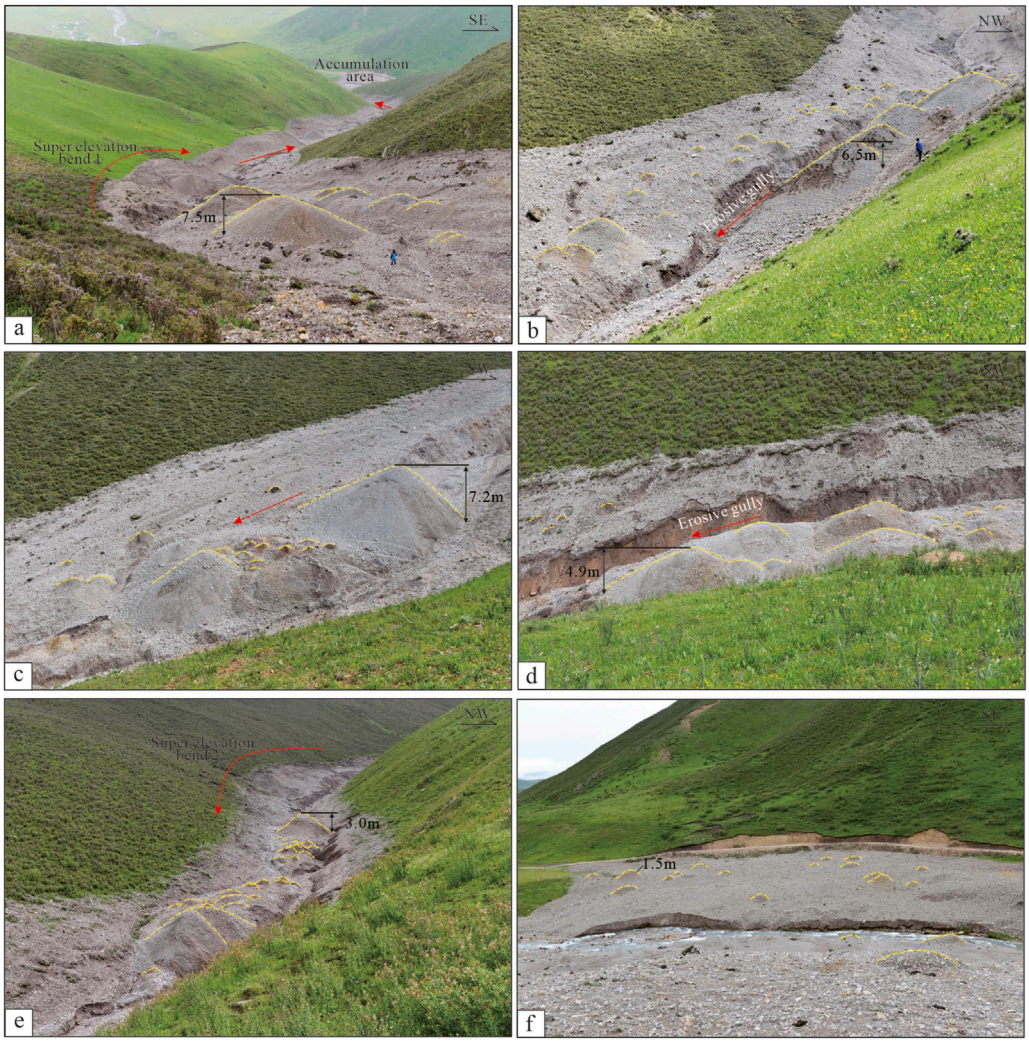

FIGURE 5
Hummocky landforms distributed in the transfer area **(A–E)** and the accumulation area **(F)** of the Bingda landslide.

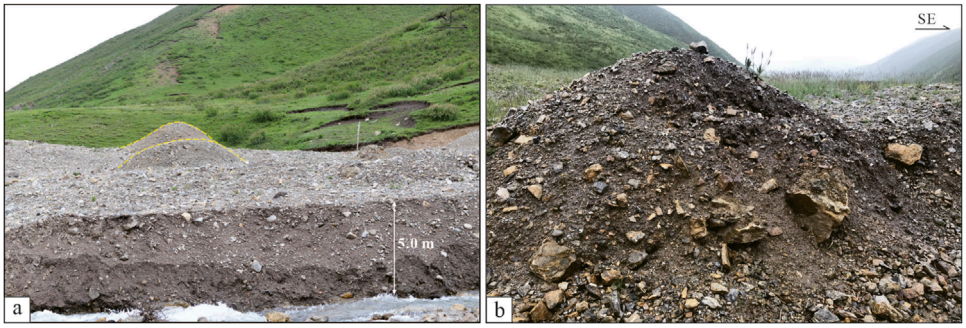

FIGURE 6
(A) Sediment profile of the accumulation area of the Bingda landslide. **(B)** Hummock distributed in the accumulation area of the Bingda landslide.

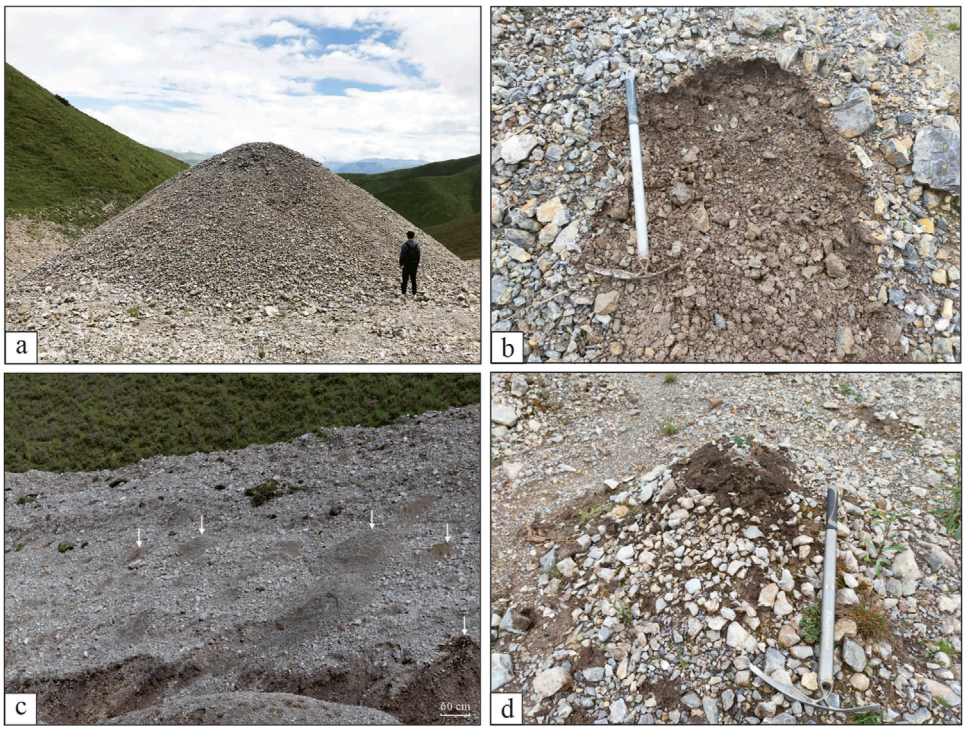

FIGURE 7
(A) Close photograph of a hummock located in the transfer area of the Bingda landslide. **(B)** Inner composition of the hummock in the transfer area. **(C, D)** Liquefaction phenomenon.

approximately 4,570 m (Figures 3, 4A). According to the remote sensing analyses and field surveys, the source area occupies ~8.8 × 10^3 m^2, and the average depth of the rupture surface was ~10 m; thus, the total volume of the main body of the landslide in the source area is approximately 8.8 × 10^4 m^3. The slope of the main scarp measures approximately 40°–50°, and the outcropping bedrock in the source area is anti-dip gray limestone with the predominant attitude of 300°<20°–30°. A platform of length ~96 m and width ~20 m was formed on the lower part of the source area, and the surface was covered by colluvium deposits mainly composed of weathered limestone fragments (Figures 3, 4B). The particle size of the colluvium deposits ranges from 0.1 m to 0.5 m, and the content of the particle size of ~0.1 m–0.3 m occupied approximately 70%. Under the platform, the anti-dip purple sand shale with the attitude of 300°<20°–25° is exposed, and it left distinct scrape marks on the surface of the bedrock. The slope structures with the upper limestone and lower sandy shale controlled the favorable conditions for the differential weathering and the deformation and failure of the slope.

4.2 Transfer area

The transfer area exhibits a long and narrow shape, with the length of ~1,557 m along the sliding axis and the width ranging from approximately 28 m to 100 m (Figure 3). The transfer area occupies a surface area of approximately 99.6 × 10^3 m^2, covering

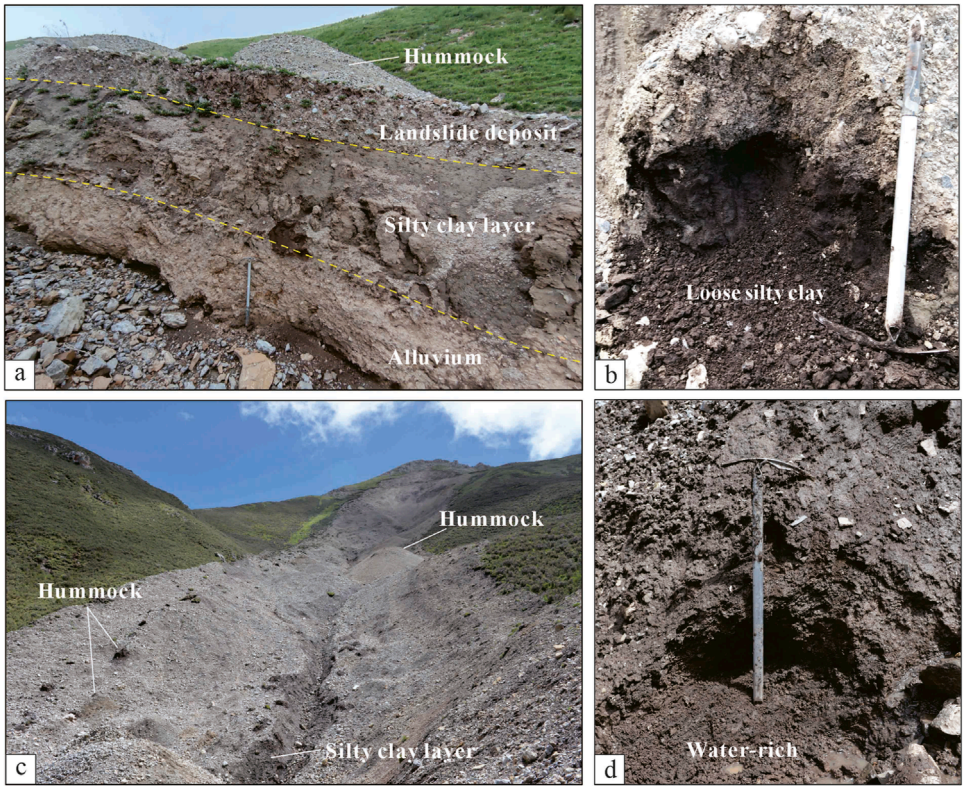

FIGURE 8
(A) Sedimentary structures of the river-cut section in the gully. **(B)** Loose structure of the black silty clay layer. **(C)** Gully profile formed by water erosion. **(D)** Water-rich and saturated silty clay layer.

TABLE 1 Results of the basic physical properties of gully samples.

Sample	d_{50} (μm)	Water (%)	ρ_w (g/cm^3)	ρ_d (g/cm^3)	G_s	e (%)
S1	11.14	20.85	1.2	1	2.62	61.98
S2	7.04	37.76	1.63	1.18	2.63	55.03
S3	7.95	20.89	1.88	1.56	2.69	42.06

over 70% of the total landslide area. The landslide mass eroded and entrained the substrate materials and the surface vegetation in the movement path, forming apparent scrape boundaries at both flanks of the landslide (Figures 5A–E). The upper part of the gully deposits were eroded and entrained by the landslide mass, amplifying the volume of the landslide mass by approximately 7.6×10^4 m^3, while most of them were accumulated in the movement path (Pan, 2023). The average slope of the transfer area is approximately 18°, transitioning from a steep slope of ~30° in the source zone to a gentler slope of ~15° in the front edge of the transfer area (Figure 2C). Due to the transformation of the channel direction, the landslide mass experienced three times the freeboard phenomenon in the curved ways of the channel during the landslide movement (Figure 2A).

4.3 Accumulation area

The accumulation area displays a fan-like shape, occupying approximately 16.8×10^3 m^2 area (Figures 3, 5F). The landslide debris that surged from the gully was hindered by the opposite mountain, causing the decrease in speed and ceasing of the debris. The accumulation area was later eroded by the river, exposing the internal sedimentary structure (Figure 6). The features of the sediment profile indicate that the upper part of the deposits primarily consists of limestone fragments, ranging in particle size from ~0.05 m to 0.5 m, while the lower part comprises silt and silty clay deposits occasionally entrained with individual limestone fragments, demonstrating an inverse grading pattern.

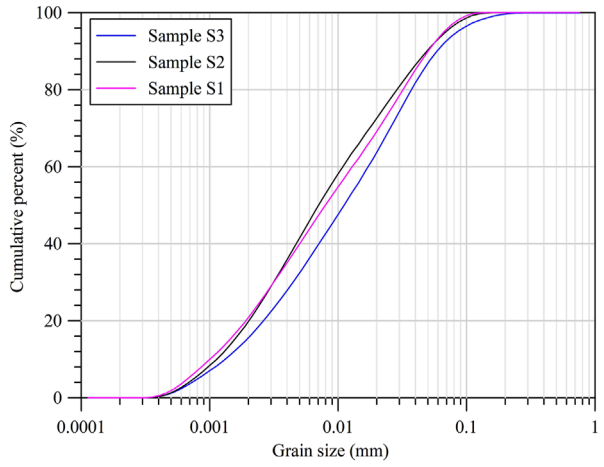

FIGURE 9
Grain size distribution of the samples collected from the gully section.

5 Morphology and sedimentology

5.1 Characteristics of hummocks

The most prominent morphological feature of the Bingda landslide is hummocky landforms, which are mainly distributed in the transfer and accumulation areas (Figures 3, 5, 6). The hummocks generally display as mounds, either individual or clustered, accounting for nearly 200 hummocks with the height of ~0.1 m–7.5 m. There are distributed 12 hummocks that are higher than 3 m, 16 with the height between ~3 m and 1 m, and approximately 171 hummocks that are less than 1 m in height. The hummocks in the transfer area exhibit higher height than those in the accumulation area, showing the decreasing trend along with the downward movement of landslide mass. In the accumulation area, the average height of the hummocks decreased significantly (Figures 3, 5F, 6). Moreover, the hummocks presented higher heights at the outer bends of the gully channel than that at the inner bends of the channel, especially at the places of super elevations (Figure 3). Most hummocks display normal circular shapes and have standard circular bases (Figure 7A), while the hummocks higher than 1 m exhibit elliptical bases due to the slope topography.

The hummocks in the transfer area were primarily covered by the gravelly and sandy limestone fragments, and the inner materials were composed of the gravel–sand fragments and black silty clay that originated from the underlying layers in the gully, which might also be affected by surficial coarseness due to the transferring of fine material by rainfall (Figure 7B). Moreover, in the transfer area, a large amount of mounds with the black silty clay sediments surrounded by limestone fragments are observed, indicating the occurrence of liquefaction in the underlying silty clay layers due to the generation of pore-water pressure (Figures 7C, D). The hummocks in the accumulation area were composed of complicated sand and silt matrices containing single, large boulders, suggesting that the entrainment of the large blocks and silty clay sediments with the landslide mass also happened in this area, influencing the distribution and composition of the hummocks.

5.2 Sedimentological structures of the landslide deposits

The sediment profile of the gully eroded by the surface water well presented the inner structures of landslide and gully deposits (Figure 8). The sedimentary profile exposed in the gully displays a thickness ranging from approximately 1.5 m to 4 m, consisting of three layers, namely, the landslide deposit, silty clay layer, and alluvial deposits from the top to the bottom (Figure 8A). The uppermost landslide deposits, averaging between about 0.2 m and 1.0 m in thickness, primarily consist of sandy and gravelly limestone fragments originating from the source area. The upper landslide fragments outcrop as a thin layer with angular centimeter-to-millimeter-sized blocks supported by a heterogeneous body composed of gravel and sandy and silty clay, presenting an inverse grading (Dufresne et al., 2016).

The black silty clay layer in the gully was distributed with a thickness ranging from approximately 0.5 m to 3 m, displaying a loose structure and water-saturated status (Figures 8B–D). The upper part of the silty clay layer was disturbed and entrained by the landslide deposits, with the entrained thickness of approximately 0.5 m–1.0 m of the silty clay layer. The bottom yellowish alluvial diluvium deposit with a high consolidation degree was exposed intermittently along the gully (Figure 8A). Table 1; Figure 9 presents the laboratory results of the basic physical properties of three samples, which were collected from the gully profile. The results indicate that the S2 sample of the silty clay layer comprises 73% of silt particles (0.005–0.075 mm). The clear trends of dry density, increasing specific gravity, and decreasing porosity from the top to the bottom in the profile are observed.

6 Discussion

6.1 Formation mechanism of hummocks

The hummocky landform is one of the most common morphological features of large landslides or rock–debris avalanches. Previous studies on the formation mechanisms of hummocks mainly focused on extensional regimes during landslide mobility (Dufresne and Davies, 2009) and faulting resulting from landslide mass spreading (Shea and van, 2008; Paguican et al., 2012). A hypothesis had also been proposed that the distribution of large boulders could act as anchors, facilitating the accumulation of debris around them, thereby forming mounds (Andrade and van Wyk de Vries, 2010). These research highlights the relationship between the features of hummock landforms and the kinematic processes of the landslides, suggesting that the perpendicular or parallel orientations of hummocky mounds are attributed to the extrusion or stretching of the landslide mass. Permafrost molards, which are conical mounds of loose debris that result from the degradation of blocks of ice rich in sediments that are mobilized by landslides (Morino et al., 2019; Beck et al., 2024), also display similar shapes with hummocky landforms. However, the hummocky landforms observed in this study exhibited a consistently uniform, round shape without any evident directivity. The composed materials of the hummocks and the inner structures of the gully profile suggested that no fault activity induced by

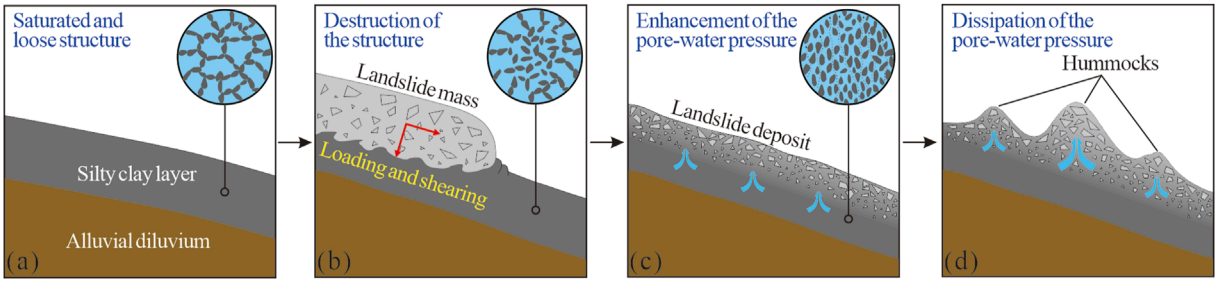

FIGURE 10
Schematic diagram of the formation processes of hummocks. **(A)** Before the landslide event, the silty clay sediments in the gully were in a saturated and loose state. **(B)** During the landslide movement, the sudden undrained loading and rapid shearing surged into the silty clay layer and resulted in the destruction of its loose structure. **(C)** The process of landslide movement induced the enhancement and concentration of the pore-water pressure within the silty clay layer. **(D)** Along with upward dissipation of the pore-water pressure, the hummocks and liquefaction phenomenon formed in the movement path of the landslide.

TABLE 2 Earthquake records in the study area in 2017 (http://data.earthquake.cn).

Date	M	Coordinates	Depth/km
2017/05/06	3.1	32.92°N, 97.18°E	11
2017/05/08	3.3	32.60°N, 97.45°E	9
2017/11/01	3.0	33.38°N, 96.16°E	10
2017/11/01	3.9	33.35°N, 96.18°E	10

the dynamic extension in the landslide mobility had occurred in this area (Paguican et al., 2014). Moreover, the Bingda landslide occurred in June, which was the rainy and high-temperature period in this region, so permafrost molards seem not to have been formed in this case. We supposed that the formation of hummocks in the Bingda landslide is mostly associated with the generation of pore-water pressure, and the loose and saturated silty clay sediments distributed in the movement path played an important role in this process.

During the landslide movement, the saturated and loose silty clay layer in the gully suffered great impact forces from the landslide mass (Figure 10A). The sudden undrained loading and rapid shearing surged into the silty clay layer in the runout path and resulted in the destruction of its loose structures (Figure 10B). This process induced a rapid enhancement and concentration of the pore-water pressure within the substrate and silty clay layer, causing the reduction of the effective stress of soil particles and the shear stress in the basal layer (Figure 10C). This could also be supported by the theoretical model that the high motion of the landslide would contribute to the generation of excess pore-water pressure along the sliding surface and the saturated layer in the movement path (Sassa, 1988). The low permeability of the silty clay layer also promoted the congregation of the pore-water pressure and hindered the timely dissipation of pore-water pressure. Along with the deceleration and stabilization of landslide debris, the pore-water pressure had gradually dissipated through the underlying deposits, forming different scales of hummocks and the liquefaction phenomenon in the movement path (Figures 10D, 7C, D). The morphological features of the hummocks indicated that the height and density of hummocks are likely influenced by factors including, among others, the overlying stress of landslide deposits, movement rate of landslide mass, and the properties of the silty clay layer. The spatial distribution features of hummocks indicated that the stronger loading, higher speed, looser structure, and finer particles of the underlying sediments could benefit the generation of pore-water pressure and the formation of hummocks.

6.2 Insights into the hypermobility of the Bingda landslide

In this study area, the intense tectonic activities and long-term weathering resulted in the steepening of the slope and the formation of a mountainous-valley terrain (Figure 1), which provided a favorable geological background for weakening the bedrock of the slope in strength and the occurrence of landslide hazards. According to the field investigation, the bedrock mainly exposed in the upper part of the source area is anti-dip limestone, and the lower part is anti-dip sand shale (Figure 4). Owing to the gravity forcing and weathering, limestone gradually reduced in strength and fractured intensely, forming thick colluvium deposits in the source area, of which the weathering processes have also been accelerated by the peri-glacial environment and the action of frost weathering in this region. These basic conditions have controlled the deformation and failure of the debris mass slopes in the source area.

According to the regional meteorological and historical earthquake records in this period, this region has experienced overall continuous 25 rainfall days in June 2017 (Figure 1C), but there were no earthquake events recorded (Table 2). Although this region has suffered long-term intense tectonic activities and strong earthquakes, which could affect the fracture development of bedrocks, the earthquake trigger for the Bingda landslide could be excluded. The heavy rainfall increased the high-level groundwater and surface runoff in this region, inducing the stagnation of water at the bottom of the source area and the saturation in the silty clay layers in the transfer and accumulation areas. The Bingda landslide

started from the sliding failure of the colluviums in the steep slope and sheared out from the interface of the limestone and sand shale bedrock. The landslide mass then traveled into the transfer area and entrained the loose silty clay in the runout path and the surface water present in the channel. In this process, the silty clay sediments became subject to sudden undrained loading and rapid shearing, and the substrate underwent a significant increase in pore-water pressure (Sassa, 1985; Hungr et al., 2014) and the reduction of effective stress within the soil particles and frictional resistance in the substrate (Hutchinson and Bhandari, 1971; Wang et al., 2002; Hungr and Evans, 2004; Sassa and Wang, 2005), facilitating the rapid and long-runout mobility of the Bingda landslide.

7 Conclusion

In June 2017, the heavy rainfall triggered a rapid and long-runout landslide with the vertical distance difference of ~552 m, the horizontal distance of ~1,795 m, and an estimated volume of 8.8×10^4 m^3. In the landslide area, we observed the striking hummocky landforms, accounting for nearly 200 hummocks, with the height ranging from ~7.5 m to 0.1 m. The spatial distribution and sedimentary features of hummocks suggested that the formation mechanisms of the hummocks could be attributed to the generation and dissipation processes of pore-water pressure in the saturated and loose silty clay layers in the movement path. This study also generalized that the landslide began with the sliding failure of the weathered colluvium from the steep slope and traveled into the gully channel. In these processes, the silty clay sediments suffered the sudden undrained loading and rapid shearing of the upper landslide mass, causing the generation and concentration of pore-water pressure, and the reduction of the frictional resistance in the substrate, resulting in the rapid and long-runout movement of the Bingda landslide.

Data availability statement

The original contributions presented in the study are included in the article/supplementary material; further inquiries can be directed to the corresponding authors.

Author contributions

LL: conceptualization, data curation, formal analysis, funding acquisition, investigation, methodology, project administration, writing–original draft, and writing–review and editing. FD: conceptualization, investigation, methodology, writing–review and editing, and funding acquisition. YZ: data curation, investigation, and writing–original draft. RP: investigation and writing–original draft.

Funding

The author(s) declare that financial support was received for the research, authorship, and/or publication of this article. This work was supported by the second comprehensive scientific expedition project of the Qinghai–Tibet Plateau (2019QZKK0905-05) and the Open Fund of the State Key Laboratory of Earthquake Dynamics (LED2023B03).

Acknowledgments

The authors express their sincere appreciation to the editor and reviewers for providing insightful and valuable suggestions and improvements to the manuscript.

Conflict of interest

The authors declare that the research was conducted in the absence of any commercial or financial relationships that could be construed as a potential conflict of interest.

The reviewer YL declared a shared affiliation with the authors to the handling editor at time of review.

Generative AI statement

The author(s) declare that no generative AI was used in the creation of this manuscript.

Publisher's note

References

Andrade, S., and van Wyk de Vries, B. (2010). Structural analysis of the early stages of catastrophic stratovolcano flank-collapse using analogue models. *Bull. Volcanol.* 72, 771–789. doi:10.1007/s00445-010-0363-x

Beck, C., Font, M., Conway, S. J., Philippe, M., Clément, J., and Morino, C. (2024). Mountain permafrost landslides: experimental study investigating molard formation processes. *Geomorphology* 461, 109317. doi:10.1016/j.geomorph.2024.109317

Benn, D. I., and Evans, D. J. A. (1998). *Glaciers and glaciation*. London: Arnold, 734.

Dai, Z. L., Wang, F. W., Cheng, Q. G., Wang, Y. F., Yang, H. F., Lin, Q. W., et al. (2019). A giant historical landslide on the eastern margin of the Tibetan Plateau. *Bull. Eng. Geol. Environ.* 78 (3), 2055–2068. doi:10.1007/s10064-017-1226-x

Dufresne, A., Bosmeier, A., and Prager, C. (2016). Sedimentology of rock avalanche deposits-case study and review. *Earth Sci. Rev.* 163, 234–259. doi:10.1016/j.earscirev.2016.10.002

Dufresne, A., and Davies, T. R. H. (2009). Longitudinal ridges in mass movement deposits. *Geomorphology* 105 (3-4), 171–181. doi:10.1016/j.geomorph.2008.09.009

Dufresne, A., and Geertsema, M. (2019). Rock slide–debris avalanches: flow transformation and hummock formation, examples from British Columbia. *Landslides* 17, 15–32. doi:10.1007/s10346-019-01280-x

Glicken, H. (1996). *Rockslide-debris avalanche of may 18, 1980, mount st. Helens volcano*, 96-677. Washington: USGS Open-file Report, 1–90.

Haeberli, W., Huggel, C., Kääb, A., Oswald, S., Polkvoj, A., Zotikov, I., et al. (2004). The Kolka-Karmadon rock/ice slide of 20 September 2002-an extraordinary event of historical dimensions in North Ossetia (Russian Caucasus). *J. Glaciol.* 50, 533–546. doi:10.3189/172756504781829710

Heim, A. (1882). Der Bergsturz von Elm. *Z. Der Dtsch. Geol. Ges.* 34, 74–115.

Heim, A. (1932). "Landslides and human lives (bergsturz and menschenleben)," in *Bi-tech publishers*. Editor N. Skermer (Vancouver, BC), 196.

Hewitt, K. (1999). Quaternary moraines vs catastrophic rock avalanches in the Karakoram Himalaya, Northern Pakistan. *Quat. Res.* 51, 220–237. doi:10.1006/qres.1999.2033

Hungr, O., and Evans, S. G. (2004). Entrainment of debris in rock avalanches: an analysis of a long runout mechanism. *Geol. Soc. Am. Bull.* 116 (9-10), 1240–1252. doi:10.1130/b25362.1

Hungr, O., Leroueil, S., and Picarelli, L. (2014). The Varnes classification of landslide types, an update. *Landslides* 11, 167–194. doi:10.1007/s10346-013-0436-y

Hutchinson, J. N., and Bhandari, R. K. (1971). Undrained loading, A fundamental mechanism of mudflows and other mass movements. *Géotechnique* 21 (4), 353–358. doi:10.1680/geot.1971.21.4.353

Iturrizaga, L. (2012). Hummocky debris landforms in the Chapursan Valley (Karakoram range, Pakistan): a glacio-geomorphological investigation. *Geomorphology* 169-170, 1–16. doi:10.1016/j.geomorph.2011.10.023

Iverson, R. M., George, D. L., Allstadt, K., Reid, M. E., Collins, B. D., Vallance, J. W., et al. (2015). Landslide mobility and hazards: implications of the 2014 Oso disaster. *Earth Planet. Sci. Lett.* 412, 197–208. doi:10.1016/j.epsl.2014.12.020

Jermyn, C., and Geertsema, M. (2015). An overview of some recent large landslide types in Nahanni National Park, Northwest Territories, Canada. Engineering geology for society and territory -volume 1: climate change and. *Eng. Geol.* 1, 315–320. doi:10.1007/978-3-319-09300-0_59

Legros, F. (2002). The mobility of long-runout landslides. *Eng. Geol.* 63, 301–331. doi:10.1016/s0013-7952(01)00090-4

Linnell, T., Brideau, M. A., and Procter, J. (2011). Contrasting the morphology and internal structure of hummocky mounds in two landslide deposits. *EGU Sess. NH3* 3.

Morino, C., Conway, S. J., Helgason, J. K., Hillier, J., Butcher, F. E., Balme, M. R., et al. (2019). Molards as an indicator of permafrost degradation and landslide process. *Earth Planet. Sci. Lett.* 516, 136–147. doi:10.1016/j.epsl.2019.03.040

Paguican, E. M. R., van, W. de V. B., and Lagmay, A. M. F. (2014). Hummocks: how they form and how they evolve in rockslide-debris avalanches. *Landslides* 11, 67–80. doi:10.1007/s10346-012-0368-y

Paguican, E. M. R., van Wyk de Vries, B., and Lagmay, A. M. F. (2012). Volcano-tectonic controls and emplacement kinematics of the Iriga debris avalanches (Philippines). *Bull. Volcanol.* 74, 2067–2081. doi:10.1007/s00445-012-0652-7

Pan, R. S. (2023). "Research on the mechanisms of a rapid and long-runout landslide," in *Yushu Bingda* (Thesis: Beijing University of Technology). (in Chinese with English Abstract).

Peng, L. (2013). *Yushu "4.14" earthquake secondary geological disasters in the development and distribution*. Beijing), Thesis: China University of Geosciences. (in Chinese with English Abstract).

Reznichenko, N. V., Andrews, G. R., Geater, R. E., and Strom, A. (2017). Multiple origins of large hummock deposits in Alai Valley, Northern Pamir: implications for palaeoclimate reconstructions. *Geomorphology* 285, 347–362. doi:10.1016/j.geomorph.2017.02.019

Sassa, K. (1985). "The mechanism of debris flows," in *Proceedings, 11th international conference on* (San Francisco: Soil Mechanics and Foundation Engineering), 1, 1173–1176.

Sassa, K. (1988). "Special lecture: geotechnical model for the motion of landslides," in *Proceedings of the 5th international symposium on landslide* (Rotterdam: A. A. Balkema), 1, 37–55.

Sassa, K., and Wang, G. H. (2005). "Mechanism of landslide-triggered debris flows: liquefaction phenomena due to the undrained loading of torrent deposits," in *Debris-flow hazards and related phenomena*, 81–104.

Scheidegger, A. E. (1973). On the prediction of the reach and velocity of catastrophic landslides. *Rock Mech. Rock Eng.* 5 (4), 231–236. doi:10.1007/bf01301796

Shea, T., and van, W. de V. B. (2008). Structural analysis and analogue modeling of the kinematics and dynamics of rockslide avalanches. *Geosphere* 4 (4), 657–686. doi:10.1130/ges00131.1

Siebert, L. (1984). Large volcanic debris avalanches: characteristics of source areas, deposits, and associated eruptions. *J. Volcanol. Geotherm. Res.* 22, 163–197. doi:10.1016/0377-0273(84)90002-7

Strom, A. (2006). "Morphology and internal structure of rockslides and rock avalanches: grounds and constraints for their modeling," in *Landslides from massive rock slope failure, NATO Sciences Series, IV. Earth and environmental Sciences*. Editor S. G. Evans 49, 305–326.

Strom, A., and Abdrakhmatov, K. (2018). *Rockslides and rock avalanches of Central Asia: distribution, morphology, and internal structure*. Elsevier, 458.

Ui, T. (1983). Volcanic dry avalanche deposits: identification and comparison with non-volcanic debris stream deposits. *J. Volcanol. Geotherm. Res.* 18, 135–150. doi:10.1016/0377-0273(83)90006-9

Ui, T., Takarada, S., and Yoshimoto, M. (2000). "Debris avalanches," in *Encyclopedia of volcanoes*. Editors H. Sigurdsson, B. F. Houghton, S. R. McNutt, H. Rymer, and J. Stix (San Diego: Academic Press), 617–626.

Voight, B., Glicken, H., Janda, R. J., and Douglas, P. M. (1981). "Catastrophic rockslide avalanche of May 18," in *The 1980 eruptions of mount st. Helens*. Editors P. W. Lipman, and D. R. Mullineaux, 347–377.

Wang, F. W., Sassa, K., and Wang, G. H. (2002). Mechanism of a long-runout landslide triggered by the August 1998 heavy rainfall in Fukushima Prefecture, Japan. *Eng. Geol.* 63, 169–185. doi:10.1016/s0013-7952(01)00080-1

Wang, Y. F., Cheng, Q. G., Shi, A. W., Yuan, Y. Q., Qiu, Y. H., and Yin, B. M. (2019). Characteristics and transport mechanism of the Nyixoi Chongco rock avalanche on the Tibetan Plateau, China. *Geomorphology* 343 (Oct.15), 92–105. doi:10.1016/j.geomorph.2019.07.002

Wu, Z. H., Zhou, C. J., Feng, H., Zhang, K. Q., Lin, J. C., Ye, P. S., et al. (2014). Active faults and earthquake around Yushu in eastern Tibetan Plateau. *Geol. Bull. China* 33 (4), 419–469. doi:10.3969/j.issn.1671-2552.2014.04.003

Yoshida, H. (2013). Decrease of size of hummocks with downstream distance in the rockslide-debris avalanche deposit at Iriga volcano, Philippines: similarities with Japanese avalanches. *Landslides* 10, 665–672. doi:10.1007/s10346-013-0414-4

Yoshida, H. (2014). Hummock alignment in Japanese volcanic debris avalanches controlled by pre-avalanche slope of depositional area. *Geomorphology* 223, 67–80. doi:10.1016/j.geomorph.2014.06.024

Yoshida, H., and Sugai, T. (2010). Quantitative examination of hummock alignment in debris avalanche deposits: zenkoji debris avalanche, Usu volcano, Japan. *Geogr. Rev. Jpn. Ser. B* 83, 64–72. doi:10.4157/geogrevjapanb.83.64

Zeng, Q. L., Wei, R. Q., Mcsaveney, M., Ma, F. S., Yuan, G. X., and Liao, L. Y. (2021). From surface morphologies to inner structures: insights into hypermobility of the Nixu rock avalanche, Southern Tibet, China. *Landslides* 18, 125–143. doi:10.1007/s10346-020-01503-6

Zeng, Q. L., Zhang, L. Q., Davies, T. R. M., Yuan, G. X., Xue, X. Y., Wei, R. Q., et al. (2019). Morphology and inner structure of Luanshibao rock avalanche in Litang, China and its implications for long-runout mechanisms. *Eng. Geol.* 260, 105216. doi:10.1016/j.enggeo.2019.105216

Zhu, Y. X., Dai, F. C., and Liang, L. J. (2019). Analysis on the formation mechanism of rapid and long runout landslides in liquefaction-type in Tibetan plateau. *Adv. Eng. Sci.* 52 (6), 10–21. (in Chinese with English Abstract). doi:10.15961/j.jsuese.202000282

Frontiers in Earth Science

Investigates the processes operating within the major spheres of our planet

Advances our understanding across the earth sciences, providing a theoretical background for better use of our planet's resources and equipping us to face major environmental challenges.

Discover the latest Research Topics

See more →

Frontiers

Avenue du Tribunal-Fédéral 34
1005 Lausanne, Switzerland
frontiersin.org

Contact us

+41 (0)21 510 17 00
frontiersin.org/about/contact